Rada Naukowa Dyscypliny Inżynieria Materiałowa
Politechniki Warszawskiej
Ul. Wołoska 141
02-507
za pośrednictwem:
Rady Doskonałości Naukowej
pl. Defilad 1
00-901 Warszawa
(Pałac Kultury i Nauki, p. XXIV, pok. 2401)

Dr inż. Agnieszka Teresa Krawczyńska
.....
(imię i nazwisko wnioskodawcy)

Politechnika Warszawska Wydział Inżynierii Materiałowej
.....
(miejsce pracy/jednostka naukowa)

Wniosek

z dnia 15.09.2023

o przeprowadzenie postępowania w sprawie nadania stopnia doktora habilitowanego w dziedzinie **nauk inżynieryjno-technicznych** w dyscyplinie[1] **inżynieria materiałowa**.

Określenie osiągnięcia naukowego będącego podstawą ubiegania się o nadanie stopnia doktora habilitowanego jest **jednotematyczny cykl 9 publikacji zatytułowany „Zjawiska zachodzące w materiałach o strukturze nanometrycznej podczas ekspozycji na różne warunki środowiskowe".**

Wnioskuję – na podstawie art. 221 ust. 10 ustawy z dnia 20 lipca 2018 r. Prawo o szkolnictwie wyższym i nauce (Dz. U. z 2021 r. poz. 478 zm.) – aby komisja habilitacyjna podejmowała uchwałę w sprawie nadania stopnia doktora habilitowanego w głosowaniu ~~**tajnym**~~**/jawnym***[2]

Zostałem poinformowany, że:

Administratorem w odniesieniu do danych osobowych pozyskanych w ramach postępowania w sprawie nadania stopnia doktora habilitowanego jest Przewodniczący Rady Doskonałości Naukowej z siedzibą w Warszawie (pl. Defilad 1, XXIV piętro, 00-901 Warszawa).

Kontakt za pośrednictwem e-mail: kancelaria@rdn.gov.pl , tel. 22 656 60 98 lub w siedzibie organu.

Dane osobowe będą przetwarzane w oparciu o przesłankę wskazaną w art. 6 ust. 1 lit. c) Rozporządzenia UE 2016/679 z dnia z dnia 27 kwietnia 2016 r. w związku z art. 220 - 221 oraz art. 232 – 240 ustawy z dnia 20 lipca 2018 roku - Prawo o szkolnictwie wyższym i nauce, w celu przeprowadzenie postępowania o nadanie stopnia doktora habilitowanego oraz realizacji praw i obowiązków oraz środków odwoławczych przewidzianych w tym postępowaniu.

Szczegółowa informacja na temat przetwarzania danych osobowych w postępowaniu dostępna jest na stronie www.rdn.gov.pl/klauzula-informacyjna-rodo.html

.....A. Krawczyńska.....
(podpis wnioskodawcy)

---

[1] Klasyfikacja dziedzin i dyscyplin wg. rozporządzenia Ministra Nauki i Szkolnictwa Wyższego z dnia 20 września 2018 r. w sprawie dziedzin nauki i dyscyplin naukowych oraz dyscyplin w zakresie sztuki (Dz. U. z 2018 r. poz. 1818).

[2] * Niepotrzebne skreślić.

Załączniki:

1. Kopia dyplomu potwierdzająca uzyskanie stopnia doktora nauk technicznych
2. Dane wnioskodawcy
3. Autoreferat
4. Wykaz osiągnięć naukowych
5. Analiza cytowań z Biblioteki Głównej PW
6. Oświadczenia współautorów publikacji
7. Publikacje ujęte w cyklu
8. Dokumenty potwierdzające kierowanie projektami
9. Dokumenty potwierdzające odbyte staże

Załącznik 1

Odpis

RZECZPOSPOLITA POLSKA

POLITECHNIKA WARSZAWSKA

WYDZIAŁ INŻYNIERII MATERIAŁOWEJ

DYPLOM

mgr inż. AGNIESZKA TERESA KRAWCZYŃSKA

urodzon.a dnia [redacted] r. w [redacted]

na podstawie przedstawionej rozprawy doktorskiej "Zmiany mikrostruktury i właściwości mechanicznych nanostrukturalnej stali austenitycznej 316LVM pod wpływem wygrzewania w różnych warunkach"

oraz po złożeniu wymaganych egzaminów uzyska.ła stopień naukowy

DOKTORA

nauk technicznych

w zakresie inżynierii materiałowej

nadany uchwałą Rady Wydziału Inżynierii Materiałowej Politechniki Warszawskiej

z dnia 26 października 2012 r.

Promotor w przewodzie doktorskim: prof. dr hab. inż. Małgorzata Lewandowska

Recenzenci w przewodzie doktorskim: prof. dr hab. inż. Wojciech Przetakiewicz
prof. dr inż. Andrzej Szummer

Warszawa, 7 listopada 2012r.

DZIEKAN

Jarosław Mizera

dr hab.inż.Jarosław Mizera,prof.PW

mp.

REKTOR

prof.dr hab.inż.Jan Szmidt

Załącznik 2

Dane wnioskodawcy

1. Imię i Nazwisko:

   Agnieszka Teresa Krawczyńska

2. Miejsce pracy:

   Politechnika Warszawska
   Wydział Inżynierii Materiałowej

3. Adres korespondencyjny:

   Agnieszka Teresa Krawczyńska
   Wydział Inżynierii Materiałowej PW
   Ul. Wołoska 141
   02-507 Warszawa

4. Nr telefonu:

   [redacted]

5. Adres e-mail:

   agnieszka.krawczynska@pw.edu.pl

6. Numer PESEL:

   [redacted]

7. Numer i seria dokumentu tożsamości w przypadku braku nadania numeru PESEL: -

A. Krawczyńska
.....
(podpis wnioskodawcy)

Załącznik 3

Załącznik nr 3

Autoreferat

Dr inż. Agnieszka Krawczyńska

Autoreferat

1. Imię i nazwisko.

Agnieszka Teresa Krawczyńska

2. Posiadane dyplomy, stopnie naukowe lub artystyczne – z podaniem podmiotu nadającego stopień, roku ich uzyskania oraz tytułu rozprawy doktorskiej.

DOKTOR NAUK TECHNICZNYCH	**2012** r., Wydział Inżynierii Materiałowej, Politechnika Warszawska *Zmiany mikrostruktury i właściwości mechanicznych nanostrukturalnej stali austenitycznej 316LVM pod wpływem wygrzewania w różnych warunkach* Promotor: Prof. dr hab. inż. Małgorzata Lewandowska
MAGISTER INŻYNIER	**2006** r., Wydział Inżynierii Materiałowej, Politechnika Warszawska *Kompozyty Al_2O_3-SiC_w* Promotor: Prof. dr hab. inż. Andrzej Olszyna

3. Informacja o dotychczasowym zatrudnieniu w jednostkach naukowych lub artystycznych.

18.02.2009 – 31.12.2014	starszy referent ds. administracyjnych, Wydział Inżynierii Materiałowej, Politechnika Warszawska
01.12.2012 – 30.06.2013	post-dok Centre d'Elaboration des Matériaux et d'Etudes Structurales (Toulouse, France)
02.02.2015 – 31.07.2020	specjalista naukowo-techniczny Wydział Inżynierii Materiałowej, Politechnika Warszawska
01.08.2020 – aktualnie	adiunkt badawczy Wydział Inżynierii Materiałowej, Politechnika Warszawska

4. Omówienie osiągnięć, o których mowa w art. 219 ust. 1 pkt. 2 ustawy z dnia 20 lipca 2018 r. Prawo o szkolnictwie wyższym i nauce (Dz. U. z 2021 r. poz. 478 z późn. zm.).

4.1 Cykl publikacji wchodzących w skład osiągnięcia naukowego

Osiągnięciem, o których mowa w art. 219 ust. 1 pkt. 2 ustawy z dnia 20 lipca 2018 r. Prawo o szkolnictwie wyższym i nauce (Dz. U. z 2021 r. poz. 478 z późn. zm.) jest jednotematyczny cykl 9 publikacji zatytułowany **„Zjawiska zachodzące w materiałach o strukturze nanometrycznej podczas ekspozycji na różne warunki środowiskowe”.**

Przedstawiony cykl publikacji nie ma charakteru chronologicznego, a ujęty jest zagadnieniowo. Wynika to z faktu, że równolegle do analizy wpływu defektów powstałych w mikrostrukturze w wyniku procesów SPD na zjawiska zachodzące podczas wygrzewania pod wysokim ciśnieniem hydrostatycznym (ang. high hydrostatic pressure annealing (HPA), prowadziłam badania wpływu defektów mikrostruktury powstałych w wyniku procesów SPD na warstwy powstające w wyniku procesu niskotemperaturowego azotowania jarzeniowego stali austenitycznej oraz na zdolność odbicia naświetlonych luster z molibdenu do zastosowań w reaktorach termojądrowych.

Dla każdej publikacji wskazano całkowitą liczbę cytowań wg. bazy Web of Science (Z_{WOS}) i Scopus (Z_S) - w nawiasach liczba cytowań po odrzuceniu cytowań własnych, impact factor (IF) czasopisma obowiązujący w roku opublikowania artykułu oraz liczbę punktów zgodnie z listą Ministerstwa Nauki i Szkolnictwa Wyższego obowiązującą w roku opublikowania artykułu MNiSW. Sumaryczny impact factor cyklu publikacji wynosi **36,737**.

1H. **A.T. Krawczyńska**, Ł. Ciupinski, M. Gloc, D. Setman, M. Spychalski, P. Suchecki, M.O. Liedke, M. Butterling, A. Wanger, E. Hirschmann, P. Petersson, Impact of high pressure torsion processing on helium ion irradiation resistance of molybdenum, Mater. Charact. 191 (2022). https://doi.org/10.1016/j.matchar.2022.112151.

Z_{WOS}: 0(0), Z_S:0(0), IF(2022): 4,7, pkt. MNiSW: 100

W tym artykule pełniłam rolę autora wiodącego i byłam wykonawcą projektu w ramach którego powstała publikacja (Projekt międzynarodowy EUROFUSION, zadanie „Irradiation testing of mirrors: microscopy studies of surface"). Po pierwsze mój udział w pracy polegał na stworzeniu koncepcji przeprowadzanych badań. Koncepcja ta pojawiła się w wyniku wcześniejszej pracy w dwóch projektach: (1) w projekcie Sonata, w którym zajmowałam się materiałami o rozdrobnionej mikrostrukturze oraz (2) w projekcie Eurofusion, w którym zajmowałam się mikrokrystalicznymi lustrami do zastosowania w reaktorach termojądrowych. W celu poprawy zdolności odbicia luster, zaproponowałam rozdrobnienie ich mikrostruktury metodą skręcania pod wysokim ciśnieniem hydrostatycznym (ang. high pressure torsion (HPT)). W celu szczegółowej analizy defektów obecnych w warstwie optycznie czynnej nawiązałam współpracę z dr Maciejem Liedke z Institute of Radiation Physics, Helmholtz-Zentrum Dresden-Rossendorf, gdzie zostały wykonane badania spektroskopii anihilacji pozytronów. Dodatkowo w artykule byłam odpowiedzialna za:

- opracowanie metodyki badań,
- przeprowadzenie procesów HPT,
- wykonanie badań mikrotwardości wraz z analizą wyników,
- analizę wyników nanotwardości, gęstości dyslokacji, rodzaju i rozmieszczenia defektów oraz zdolności odbicia luster w kontekście przedstawionego tematu badań,
- przeprowadzenie obserwacji mikrostruktury przy użyciu skaningowej i transmisyjnej mikroskopii elektronowej oraz mikroskopii jonowej wraz z analizą uzyskanych wyników,
- całościowe opracowanie publikacji wraz z korekcją po recenzji.

2H. **A.T. Krawczyńska**, M. Lewandowska, A.T. Fry, Microstructural characterization and residual stress distribution in a nanostructured austenitic stainless steel, Int. J. Mater. Res. (2018). https://doi.org/10.3139/146.111672.

Z_{WOS}: 1(1), Z_S:2(2), IF(2018): 0,851, pkt. MNiSW: 30

W tym artykule pełniłam rolę autora wiodącego i byłam wykonawcą projektu, w ramach którego powstała publikacja (projekt OPUS finansowany przez NCN „Tworzenie dyfuzyjnych warstw azotowanych na stali austenitycznej o strukturze nanometrycznej"). Po pierwsze byłam pomysłodawcą pomiaru rozkładu naprężeń na średnicy prętów odkształconych w wyniku procesu hydroektruzji (ang. hydrostatic extrusion (HE)) przy

użyciu metody dyfrakcji rentgenowskiej cosα, ponieważ nie możliwe było zastosowanie w przypadku tak steksturowanych materiałów metod konwencjonalnych. Dodatkowo byłam odpowiedzialna za:

- opracowanie metodyki badań,
- wykonanie badań mikrotwardości wraz z analizą wyników,
- wykonanie badań naprężeń wraz z analizą wyników w kontekście tematu badań,
- przeprowadzenie obserwacji mikrostruktury przy użyciu transmisyjnej mikroskopii elektronowej wraz z analizą uzyskanych mikrostruktur,
- całościowe opracowanie publikacji wraz z korekcją po recenzji.

3H. **A.T. Krawczyńska**, W. Chromiński, E. Ura-Bińczyk, M. Kulczyk, M. Lewandowska, Mechanical properties and corrosion resistance of ultrafine grained austenitic stainless steel processed by hydrostatic extrusion, Mater. Des. 136 (2017). https://doi.org/10.1016/j.matdes.2017.09.050.

Z_{WOS}: 34(28), Z_S:33(27), IF(2017): 4,525, pkt. MNiSW: 35

W tym artykule pełniłam rolę autora wiodącego i byłam wykonawcą projektu, w ramach którego powstała publikacja (projekt OPUS finansowany przez NCN „Tworzenie dyfuzyjnych warstw azotowanych na stali austenitycznej o strukturze nanometrycznej").

W tym artykule byłam odpowiedzialna za:

- opracowanie całościowej koncepcji artykułu,
- opracowanie metodyki badań mikrostruktury i właściwości mechanicznych,
- wykonanie obserwacji mikrostruktury przy użyciu transmisyjnej mikroskopii elektronowej oraz analizę uzyskanych mikrostruktur,
- analizę wyników badań wytrzymałościowych,
- dyskusję wyników bez części dotyczącej korozji,
- zredagowanie i przygotowanie publikacji.

4H. **A.T. Krawczyńska**, J. Zdunek, R. Sitek, M. Lewandowska, Formation of the Nitrided Layers on an Austenitic Stainless Steel with Different Grain Structures, Adv. Eng. Mater. (2018). https://doi.org/10.1002/adem.201701049

Z_{WOS}: 3(2), Z_S:4(3), IF(2018): 2.906, pkt. MNiSW: 30

W tym artykule pełniłam rolę autora wiodącego i byłam wykonawcą projektu, w ramach którego powstała publikacja (projekt OPUS finansowany przez NCN „Tworzenie dyfuzyjnych warstw azotowanych na stali austenitycznej o strukturze nanometrycznej").
W tym artykule byłam odpowiedzialna za:

- opracowanie całościowej koncepcji artykułu,
- opracowanie metodyki badań,
- wykonanie obserwacji mikrostruktury przy użyciu transmisyjnej i skaningowej mikroskopii elektronowej oraz mikroskopii jonowej, analizę uzyskanych mikrostruktur,
- analizę wyników badań składu fazowego i składu chemicznego warstw w kontekście tematu badań,
- zredagowanie i przygotowanie publikacji (włączając dyskusję wyników).

5H. **A.T. Krawczyńska**, M. Kerber, P. Suchecki, B. Romelczyk-Baishya, M. Oskar, M. Butterling, E. Hirschmann, A. Wagner, M. Lewandowska, D. Setman, The impact of high hydrostatic pressure maintenance after high-pressure torsion on phenomena during high hydrostatic pressure annealing, Mater. Sci. Eng. A. 840 (2022) 142874.
https://doi.org/10.1016/j.msea.2022.142874

Z_{WOS}: 1(1), Z_S:2(2), IF(2022): 6,4, pkt. MNiSW: 140

Byłam pomysłodawcą i kierownikiem projektu, w ramach którego powstała publikacja (projekt Sonata finansowany przez NCN „Rekrystalizacja i rozrost ziaren w silnie odkształconej stali austenitycznej").
W tej pracy odpowiedzialna byłam za:

- opracowanie całościowej koncepcji artykułu,
- opracowanie metodyki badań,
- asystowanie podczas modernizacji urządzenia HPT w celu przeprowadzenia procesów HPT i HPA,
- przeprowadzenie procesów HPT i HPA,
- wykonanie badań mikrotwardości oraz analizę uzyskanych wyników,

- analizę wyników uzyskanych podczas statycznej próby rozciągania w kontekście tematu badawczego,
- analizę rodzaju i rozmieszczenia defektów w kontekście tematu badawczego,
- przeprowadzenie obserwacji mikrostruktury przy użyciu skaningowej i transmisyjnej elektronowej mikroskopii, mikroskopii jonowej oraz analizę uzyskanych mikrostruktur,
- całościowe opracowanie publikacji wraz z korekcją po recenzji.

6H. **A.T. Krawczyńska**, S. Gierlotka, P. Suchecki, D. Setman, B. Adamczyk-Cieslak, M. Lewandowska, M. Zehetbauer, Recrystallization and grain growth of a nano/ultrafine structured austenitic stainless steel during annealing under high hydrostatic pressure, J. Mater. Sci. (2018). https://doi.org/10.1007/s10853-018-2459-1.

Z_{WOS}: 13(9), Z_S:16(11), IF(2018): 3,442, pkt. MNiSW: 30

Byłam pomysłodawcą i kierownikiem projektu, w ramach którego powstała publikacja (projekt Sonata finansowany przez NCN „Rekrystalizacja i rozrost ziaren w silnie odkształconej stali austenitycznej").
W tej pracy odpowiedzialna byłam za:

- opracowanie całościowej koncepcji artykułu,
- opracowanie metodyki badań,
- przeprowadzenie procesów HPT,
- wykonanie badań mikrotwardości wraz z analizą wyników,
- analizę składu fazowego stali po procesie HPT w kontekście tematu badawczego,
- przeprowadzenie obserwacji mikrostruktury przy użyciu skaningowej i transmisyjnej mikroskopii elektronowej oraz analizę uzyskanych mikrostruktur,
- przygotowanie i zredagowanie publikacji (włączając dyskusję wyników).

7H. **A.T. Krawczyńska**, S. Gierlotka, P. Suchecki, D. Setman, B. Adamczyk-Cieslak, M. Gloc, W. Chromiński, M. Lewandowska, M. Zehetbauer, Phenomena Occurring in Nanostructured Stainless Steel 316LVM during Annealing under High Hydrostatic Pressure, Adv. Eng. Mater. (2019). https://doi.org/10.1002/adem.201800101.

Z_{WOS}: 3(1), Z_S:4(1), IF(2019): 3,217, pkt. MNiSW: 100

Byłam pomysłodawcą i kierownikiem projektu, w ramach którego powstała publikacja (projekt Sonata finansowany przez NCN „Rekrystalizacja i rozrost ziaren w silnie odkształconej stali austenitycznej").
W tej pracy odpowiedzialna byłam za:

- opracowanie całościowej koncepcji artykułu,
- opracowanie metodyki badań,
- przeprowadzenie procesów HPT,
- analizę tekstury stali po procesie HPT oraz wyników korozji w kontekście tematu badawczego,
- przeprowadzenie obserwacji mikrostruktury przy użyciu skaningowej i transmisyjnej mikroskopii elektronowej oraz analizę uzyskanych mikrostruktur wraz z analizą składu chemicznego wydzieleń,
- przygotowanie i zredagowanie publikacji (włączając dyskusję wyników).

8H. **A.T. Krawczyńska**, P. Suchecki, B. Adamczyk-Cieslak, B. Romelczyk-Baishya, M. Lewandowska, Influence of high hydrostatic pressure annealing on the recrystallization of nanostructured austenitic stainless steel, Mater. Sci. Eng. A. (2019). https://doi.org/10.1016/j.msea.2019.138381.

Z_{WOS}: 9(8), Z_S:11(9), IF(2019): 4,652, pkt. MNiSW: 140

Byłam pomysłodawcą i kierownikiem projektu, w ramach którego powstała publikacja (projekt Sonata finansowany przez NCN „Rekrystalizacja i rozrost ziaren w silnie odkształconej stali austenitycznej").
W tej pracy odpowiedzialna byłam za:

- opracowanie całościowej koncepcji artykułu,
- opracowanie metodyki badań,
- wykonanie badań mikrotwardości wraz z analizą wyników,
- analizę wyników tekstury oraz wyników ze statycznej próby rozciągania w kontekście tematu badań,
- przeprowadzenie obserwacji mikrostruktury przy użyciu skaningowej i transmisyjnej mikroskopii elektronowej oraz analizę uzyskanych mikrostruktur,
- przygotowanie i zredagowanie publikacji (włączając dyskusję wyników).

9H. **A.T. Krawczyńska**, M. Kerber, P. Suchecki, B. Romelczyk-Baishya, M. Lewandowska, D. Setman, The impact of the stacking fault energy of nanostructured metals on phenomena during annealing at the high hydrostatic pressure, Mater. Sci. Eng. A. 808 (2021) 140913. https://doi.org/10.1016/j.msea.2021.140913.

Z_{WOS}: 3(3), Z_S:4(3), IF(2021), 6,044, pkt. MNiSW: 140

Byłam pomysłodawcą i kierownikiem projektu, w ramach którego powstała publikacja (projekt Sonata finansowany przez NCN „Rekrystalizacja i rozrost ziaren w silnie odkształconej stali austenitycznej").
W tej pracy odpowiedzialna byłam za:

- opracowanie całościowej koncepcji artykułu,
- opracowanie metodyki badań,
- asystowanie podczas modernizacji urządzenia HPT w celu przeprowadzenia procesów HPT i HPA,
- przeprowadzenie procesów HPT i HPA,
- analizę wyników uzyskanych w statycznej próbie rozciągania oraz badań kalorymetrycznych w kontekście tematu badawczego,
- przeprowadzenie obserwacji mikrostruktury przy użyciu skaningowej i transmisyjnej elektronowej mikroskopii, mikroskopii jonowej oraz analizę uzyskanych mikrostruktur,
- przygotowanie i zredagowanie publikacji (włączając dyskusję wyników).

4.2 Wstęp

Materiały otrzymywane metodami dużego odkształcenia plastycznego (ang. severe plastic deformation, SPD) cieszą się dużym zainteresowaniem świata nauki od wielu lat, co widać choćby w liczbie artykułów publikowanych w tej tematyce. Jeszcze w 2000 roku liczba publikacji wynosiła poniżej 100, teraz sięga 1000 rocznie. Wynika to z faktu, że metody SPD umożliwiają wytworzenie objętościowych materiałów nanostrukturalnych, które definiowane są wg NanoSPD Steering Commitee jako ultradrobnoziarniste materiały o wielkości ziarna poniżej 1 mikrometra (wymiary w skali submikronowej i nanometrycznej) zawierające głównie granice ziaren o dużym kącie dezorientacji. Takie materiały mają w swojej mikrostrukturze dodatkowo także nanowydzielenia, czy nanobliźniaki, ale przede wszystkim charakteryzują się dużą gęstością defektów. Właśnie ta duża gęstość defektów tzn. wakansów, dyslokacji, błędów ułożenia, bliźniaków czy granic ziaren odpowiada za wyjątkowe właściwości tych materiałów takie jak niespotykana do tej pory wytrzymałość, nadplastyczność oraz właściwości absorbcji i desorpcji wodoru, odporności na korozję czy właściwości magnetyczne.

Duża gęstość defektów charakterystyczna dla tych materiałów jest także kluczowa dla zjawisk zachodzących podczas eksploatacji i/lub kolejnych etapów przetwarzania, w tym obróbek cieplnych i cieplno-chemicznych. W ten wątek rozwoju materiałów nanostrukturalnych wytwarzanych metodami SPD wpisuje się prezentowane przeze mnie osiągnięcie. **Celem ogólnym prowadzonych badań było zrozumienie wpływu defektów mikrostruktury utworzonych w wyniku dużego odkształcenia plastycznego na zjawiska zachodzące w materiałach podczas takich procesów jak naświetlanie jonami He, niskotemperaturowe azotowanie jarzeniowe czy wygrzewanie pod wysokim ciśnieniem hydrostatycznym.** Osiągnięcie dotyczy trzech zagadnień szczegółowych:

- **Określenie wpływu defektów mikrostruktury powstałych w wyniku procesów SPD na zdolność odbicia naświetlonych luster z molibdenu do zastosowań w reaktorach termojądrowych, (1H)**
- **Określenie wpływu defektów mikrostruktury powstałych w wyniku procesów SPD na tworzenie warstw procesie niskotemperaturowego azotowania jarzeniowego stali austenitycznej, (2H-4H)**
- **Określenie wpływu defektów mikrostruktury powstałych w wyniku procesów SPD na zjawiska zachodzące podczas wygrzewania pod wysokim ciśnieniem hydrostatycznym (5H-9H).**

Specyficzna mikrostruktura materiałów wytwarzanych metodami SPD wymaga zastosowania do jej opisu zaawansowanych metod mikroskopii elektronowej. Doświadczenie w tym zakresie zdobywałam w mojej macierzystej instytucji (na Wydziale Inżynierii Materiałowej Politechniki Warszawskiej), jak również podczas stażu postdoktorskiego w Centre d'Elaboration des Matériaux et d'Etudes Structurales w ramach współpracy z dr hab. inż. Frederic Mompiou, a także podczas realizacji projektu Polonium w ramach współpracy z prof. dr hab. inż. Karine Masenelli-Varlot z INSA Lyon. Ta współpraca międzynarodowa znacznie wzbogaciła mój warsztat badawczy, m.in. o analizę defektów powstałych podczas rozciągania in situ w oparciu o analizę projekcji stereograficznej a także umiejętność zbierania danych i analizy zdjęć dyfrakcyjnych w celu określenia orientacji ziaren przy użyciu oprogramowania ASTAR. W swojej pracy wykorzystywałam szereg urządzeń dostępnych na Wydziale Inżynierii Materiałowej Politechniki Warszawskiej, takich jak:

- skaningowy transmisyjny mikroskop elektronowy (STEM) firmy Hitachi model HD2700,
- skaningowy transmisyjny mikroskop elektronowy (STEM) firmy Hitachi model S 5500,
- skaningowy mikroskop elektronowy (SEM) firmy Hitachi model SU 8000,
- mikroskop jonowy (FIB) firmy Hitachi model NB5000 nanoDUET,
- mikroskop jonowy (FIB) firmy Hitachi model FiB NB-2100,
- transmisyjny mikroskop elektronowy (TEM) firmy Jeol model 1200.

Dodatkowo swoje badania wsparłam innymi metodami badawczymi, takimi jak dyfrakcja rentgenowska, różnicowa kalorymetria skaningowa, jak również spektroskopia anihilacji pozytronów.

Badania w ramach przedstawionego cyklu publikacji realizowałam we współpracy z ośrodkami krajowymi i zagranicznymi, wśród których pragnę wymienić:

- Instytut Wysokich Ciśnień PAN (współpraca z dr hab. inż. Mariuszem Kulczykiem oraz dr inż. Stanisławem Gierlotką),
- Wydział Fizyki Uniwersytetu Wiedeńskiego, Wiedeń, Austria (współpraca z prof. Michaelem Zehetbauerem, dr Darią Setman i dr Michaelem Kerberem)
- Institute of Radiation Physics, Helmholtz-Zentrum Dresden-Rossendorf, Drezno, Niemcy (współpraca z dr Maciejem Liedke)
- Department of Fusion Plasma Physics, KTH Royal Institute of Technology, Uppsala, Szwecja (współpraca z prof. Markiem Rublem oraz dr Per Pettersonem)
- National Physical Laboratory, Teddington, Wielka Brytania (współpraca z prof. Anthonym Fry'em).

4.3 Motywacja

Jedną z nietypowych właściwości materiałów otrzymywanych metodami SPD jest ich podwyższoną odporność na naświetlanie jonami w stosunku do materiałów o mikrometrycznej wielkości ziarna. Badania pokazują, że naświetlanie energetycznymi cząstkami prowadzi najpierw do przemieszczenia atomów, po którym następuje rekombinacja defektów, aż do powstawania skupisk wakansów, pęcherzyków a następnie pustki. W końcowej fazie naświetlania w zależności od dawki promieniowania obserwuje się również powstawanie pęcherzy czy ubytków materiałów na powierzchni. Chociaż proponowane są różne sposoby zwiększenia odporności na naświetlanie, to wytwarzanie materiałów metodami SPD o dużej gęstości defektów wykazuje spory potencjał. Wynika to stąd, że dwuwymiarowe defekty takie jak nierównowagowe granice ziaren są miejscami gdzie gromadzą się powstałe w wyniku naświetlania defekty i emitowane są atomy międzywęzłowe, które mogą rekombinować z wakansami powstałymi podczas naświetlania we wnętrzu ziaren [1]. Daje to zatem materiałom uzyskanym w wyniku procesów SPD zdolność do samoregeneracji w wyniku naświetlania. Warto zauważyć, że na powierzchni wytworzonego w procesie HPT nanostrukturalnego wolframu po naświetlaniu jonami He $1{,}0x10^{23}$ m^{-2} nie pojawiły się pęcherze w przeciwieństwie do mikrostrukturalnego wolframu [2]. Biorąc te fakty pod uwagę, podjęłam się zbadania wpływu rozdrobnionej mikrostruktury molibdenu uzyskanej w wyniku procesu HPT na zdolność odbicia naświetlonych luster z molibdenu. Zagadnieniu temu poświęcona jest publikacja 1H. W reaktorach termojądrowych ważnym elementem są lustra diagnostyczne wytworzone z molibdenu, które prowadzą plazmę na drodze odbicia do systemu kontroli plazmy. Istotne jest aby ich powierzchnia nie uległa degradacji w wyniku naświetlania jonami helu czy wodoru [3], do czego dochodzi podczas pracy reaktora.

Kolejną istotną właściwością materiałów uzyskiwanych metodami SPD jest ich zwiększona dyfuzyjność. Wynika to głównie z faktu, że w tych materiałach występuje duża gęstość granic ziaren oraz innych defektów, które pełnią rolę dróg szybkiej dyfuzji. Ma to szczególne znaczenie w wielu procesach technologicznych, w których dyfuzja odgrywa znaczącą rolę, jak podczas tworzenia warstw dyfuzyjnych np. warstw azotowanych. Proces azotowania jarzeniowego ma na celu zwiększenie odporności na zużycie przez tarcie i korozję. Jest on często stosowany w celu poprawy właściwości stali austenitycznych. W wyniku azotowania stali austenitycznych powstaje dyfuzyjna warstwa austenitu azotowego

tzw. faza S. Tworzenie warstw azotowanych w materiałach mikrokrystalicznych jest dobrze poznane, jednak w przypadku materiałów otrzymywanych metodami SPD pozostaje jeszcze wiele kwestii do wyjaśnienia. Wyniki niektórych badań wykazują, że w krótszym czasie można uzyskać w nich znacznie grubszą warstwę dyfuzyjną [4]. Jednak ze na ich niską stabilność cieplną niezbędne jest zastosowanie azotowania niskotemperaturowego, a więc w przedziale temperatur 300-450°C.

Różne metody SPD prowadzą do uzyskania różnych mikrostruktur, różnych granic ziaren, więc różny jest ich wpływ na szybkość dyfuzji azotu w głąb materiału. Zatem podjęłam wątek badawczy polegający na analizie wpływu różnych granic ziaren utworzonych w wyniku metod SPD w stali austenitycznej na zachodzenie procesów azotowania. Dokładne zrozumienie tego zjawiska może prowadzić do wytworzenia materiałów o optymalnej gęstości defektów służącej do otrzymania odpowiedniej grubości warstwy azotowanej w odpowiednio krótkim czasie. Zagadnieniu temu są poświęcone publikacje 2H-4H.

Zwiększona dyfuzyjność granic ziaren materiałów otrzymywanych metodami SPD z jednej strony umożliwia obniżenie temperatury i skrócenie czasu procesów technologicznych jak azotowanie, a z drugiej strony jest wadą tych materiałów, gdyż prowadzi do ich znacznie obniżonej stabilności cieplnej. W szczególności czyste metale rozdrobnione metodami SPD charakteryzują się niską stabilnością cieplną, co powoduje, że rozrost ziarna obserwujemy w nich już w temperaturze pokojowej. Z tego wynika, że konieczna jest dalsza stabilizacja ich mikrostruktury np.: stosując wygrzewanie lub przeprowadzając procesy SPD w podwyższonej temperaturze. Konwencjonalne metody wygrzewania nie przynoszą zadowalających efektów, gdyż prowadzą często do znacznego zmniejszenia wytrzymałości. Z tej przyczyny coraz popularniejsze staje się zastosowanie niekonwencjonalnych metod wygrzewania. W swoich badaniach zaproponowałam metodę HPA (ang. high hydrostatic pressure annealing (HPA)). Metoda ta, w przeciwieństwie do innych metod jak np. wygrzewania prądem czy impulsami prądowymi, spowalnia procesy dyfuzji w materiale, co daje lepszą możliwość kontroli nad przemianami, które zachodzą w mikrostrukturze. Dodatkowo, możliwość zastosowania wysokiego ciśnienia hydrostatycznego (między ciśnienia) bezpośrednio po procesie SPD, a przed HPA, daje możliwość utworzenia mikrostruktur niemożliwych do wytworzenia metodami konwencjonalnymi. Przyczynia się to do znacznego poszerzenia wiedzy na temat materiałów otrzymywanych metodami SPD oraz niekonwencjonalnego wygrzewania HPA. Wyróżnieniem moich prac jest zastosowanie do przeprowadzenia procesów HPA urządzenia

do przeprowadzenia procesów HPT. W tym celu we współpracy z dr Darią Setman i dr Michaelem Kerberem zmodyfikowaliśmy i doposażyliśmy urządzenie HPT.

Wiadomo, że w przypadku konwencjonalnego wygrzewania pod ciśnieniem atmosferycznym stopień odkształcenia plastycznego, od którego zależy gęstość wprowadzonych defektów, znacznie wpływa na uzyskaną mikrostrukturę po procesie wygrzewania. Podczas wygrzewania materiałów uzyskanych metodami SPD zachodzą procesy zdrowienia, rekrystalizacji i rozrostu ziarna, jednak mają one inny przebieg, niż w przypadku materiałów odkształconych metodami konwencjonalnymi. Dzieje się tak dlatego, że przeważają w nich granice o dużym kącie dezorientacji, a o małym kącie dezorientacji stanowią około 20% wszystkich granic. Trudno zatem wyróżnić etap tworzenia się zarodków rekrystalizacji, tj. segmentów granic ziaren o dużym kącie dezorientacji. W dużym uproszczeniu podczas wygrzewania materiałów odkształconych metodami SPD można wyróżnić częściową anihilację defektów na granicach ziaren i wewnątrz ziaren, czemu towarzyszy relaksacja naprężeń, a następnie migrację nierównowagowych granic ziaren, co może prowadzić do anormalnego rozrostu ziaren. Dodatkowe zastosowanie wysokiego ciśnienia hydrostatycznego podczas wygrzewania spowalnia procesy dyfuzji związane bezpośrednio z ruchem wakansów, a więc spowalnia ruchliwość granic ziaren. Wobec tego należałoby się spodziewać, że wprowadzając dużą gęstość wakansów metodami SPD, wpływ ciśnienia będzie mniejszy, niż stosując konwencjonalne metody odkształcenia plastycznego. Jest to jednak znaczne uproszczenie, ponieważ wpływ zastosowanego wysokiego ciśnienia hydrostatycznego w podwyższonej temperaturze w zróżnicowany sposób wpływa na ruch różnych granic ziaren. Do ruchu granic nachylonych typu <110> niezbędny jest skoordynowany ruch wielu atomów, a do ruchu granic nachylonych typu <100> i <111> wystarczą przeskoki pojedynczych atomów [5, 6]. Dodatkowo ruch granic o małym kącie dezorientacji, odbywający się w wyniku migracji wakansów granic ziaren, może być całkowicie wstrzymany przy odpowiednio wysokim ciśnieniu [7]. Biorąc pod uwagę fakt, że w materiałach uzyskanych metodami SPD udział granic o dużym kącie dezorientacji jest znaczny, wpływ wysokiego ciśnienia hydrostatycznego podczas wygrzewania będzie szczególnie istotny. Do tej pory, poza własnymi badaniami, badania nad wpływem wysokiego ciśnienia hydrostatycznego zastosowanego podczas wygrzewania, koncentrowały się na badaniu materiałów odkształconych do nieznacznych stopni odkształcenia. Zagadnieniu temu są poświęcone publikacje 5H-9H.

4.4 Opis merytoryczny osiągnieć

4.4.1 Określenie wpływu defektów mikrostruktury powstałych w wyniku procesów SPD na zdolność odbicia naświetlonych luster z molibdenu do zastosowań w reaktorach termojądrowych

Istotnym tematem, jakim się zajęłam, była weryfikacja możliwości zastosowania nanostrukturalnego molibdenu otrzymanego metodą HPT na lustra diagnostyczne w reaktorach termojądrowych w celu poprawy odporności luster na naświetlanie jonami He. Temat ten nie został wcześniej poruszony w literaturze, zatem moje badania mają oryginalny wkład w rozwój dyscypliny. To właśnie defekty utworzone podczas procesów SPD warunkują poprawę odporności na naświetlanie jonami. Dodatkowo uzyskana nanostruktura zapewnia dużo niższą chropowatość powierzchni po procesie czyszczenia luster niż konwencjonalna mikrostruktura o wielkości ziaren z zakresu mikrometrycznego, co z kolei zapewnia pożądaną kierunkową zdolność odbicia luster. Czyszczenie luster jest niezbędnym procesem w reaktorach, gdyż oprócz uszkodzenia powierzchni luster na skutek naświetlania jonami ich zdolność odbicia może ulec pogorszeniu w wyniku osadzania zanieczyszczeń obecnych w plazmie [8]. Osadzanie zanieczyszczeń jest niemożliwe do uniknięcia podczas działania reaktora, dlatego czyszczenie in-service jest konieczne. Podczas 10-cyklowego czyszczenia plazmą zauważono znaczny wzrost chropowatości luster z powłoką Mo o mikroziarnach, podczas gdy powłoki nanostrukturalne pozostały o praktycznie niezmienionej chropowatości [9]. Jednak zastosowanie powłok w reaktorach nie jest optymalnym rozwiązaniem z uwagi na możliwość ich delaminacji, co w efekcie może doprowadzić do zanieczyszczenia plazmy.

W celu weryfikacji poszerzenia możliwości zastosowania nanostrukturalnego Mo w reaktorach termojądrowych przeprowadziłam analizę wpływu mikrostruktury nanostrukturalnego lustra otrzymanego w wyniki HPT na zdolność odbicia naświetlonych luster. Potencjalne lustra zostały odkształcone w procesie HPT w wyniku zastosowania jednego i pięciu obrotów. Procesy HPT zostały przeprowadzone w ramach współpracy z dr Darią Setman z Wydziału Fizyki, Uniwersytetu Wiedeńskiego. W wyniku odkształcenia znacznie zmniejszyła się średnia wielkość ziarna z 2.00 μm do 500 i 100 nm, odpowiednio po jednym i pięciu obrotach (**Rys. 1**).

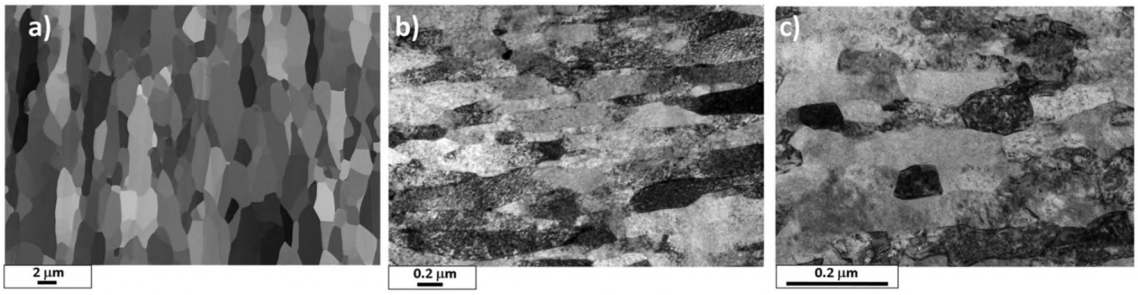

Rys. 1 Mikrostruktury luster z Mo a) lustro nieodkształcone, b) lustro po procesie HPT, jeden obrót (lamelka FIB), c) lustro po procesie HPT, pięć obrotów (lamelka FIB) – przekroje poprzeczne; a) BSE-SEM (SU8000 Hitachi) b), c) TEM, kierunek naświetlania jest równoległy do krótszej krawędzi zdjęcia; SEM Hitachi Su8000, FIB Hitachi NB5000, TEM Jeol 1200 [1H]

Naświetlanie luster jonami He oraz badania zdolności odbicia luster przeprowadzono we współpracy z dr Per Petersonem i prof. Markiem Rublem z Department of Fusion Plasma Physics, KTH Royal Institute of Technology w Szwecji w ramach projektu Eurofusion – zadanie Irradiation testing of mirrors: microscopy studies of surface. Badania całkowitej zdolności odbicia luster mikrokrystalicznych i nanostrukturalnych przed procesem naświetlania wykazały identyczne wartości. Następnie lustra zostały naświetlone jonami He 2keV, dawką o wartości $8x10^{16}$ cm^{-2} w Ion Technology Center, Uppsala University. Warunki naświetlania zostały dobrane na podstawie modelowania Stopping and Range of Ions in Matter (SRIM) tak, aby naświetlić optycznie aktywną warstwę wynoszącą 15-20 nm. Dawka została dobrana na podstawie wcześniejszych eksperymentów, które pozwoliły na znalezienie takiej dawki progowej, przy której po naświetlaniu widoczne zmiany w mikrostrukturze luster można zaobserwować przy użyciu transmisyjnego mikroskopu elektronowego. Chociaż w rzeczywistych warunkach lustra będą naświetlane przez neutrony, izotopy wodoru i jony He, w niniejszym eksperymencie zbadano tylko naświetlanie jonami He. Powszechnie wiadomo, że naświetlanie neutronami prowadzi do powstania wakansów czy atomów międzywęzłowych. Biorąc pod uwagę, że istnieje silna interakcja He z defektami oraz że HPT może również doprowadzić do powstania dużej gęstości wakansów, zrezygnowano z jakiekolwiek wcześniejszego naświetlenia neutronami. Badania całkowitej zdolności odbicia luster po naświetlaniu wykazały spodziewane zmniejszenie zdolności odbicia luster. Zaskakującym jednak było nieznaczne obniżenie zdolności odbicia luster nanostrukturalnych w porównaniu do luster mikrokrystalicznych o 2,5%. Wskazuje to na nieznaczne pogorszenie odporności na naświetlanie jonami He luster nanostrukturalnych w porównaniu do mikrokrystalicznych.

W swoich dalszych badaniach skupiłam się na wyjaśnieniu obserwowanego zjawiska przede wszystkim w oparciu o analizę mikrostruktury przy użyciu transmisyjnej mikroskopii elektronowej. W celu lepszego zrozumienia różnic w mikrostrukturze luster trudnych do zobrazowania w oparciu o mikroskopię elektronową zastosowałam spektroskopię anihilacji pozytronów. Nawiązałam współpracę z dr Maciejem Liedke z Institute of Radiation Physics, Helmoltz-Zentrum Dresden-Rassendorf. Na podstawie przeprowadzonych badań udowodniłam, że w przypadku luster odkształconych jak i nieodkształconych powstają w wyniku naświetlania nanopęcherzyki do głębokości 20 nm pod powierzchnią luster. Ponieważ ich wielkość i gęstość jest porównywalna między sobą, nie są one przyczyną różnic we współczynniku odbicia między lustrami odkształconymi a nieodkształconymi.

W wyniku rozdrobnienie ziarna w wyniku HPT doszło do znacznego zwiększenia powierzchni względnej granic ziaren. Podczas naświetlania jonami He jony te są pułapkowane w granicach ziaren. Aglomeracja jonów He prowadzi do zarodkowania pęcherzyków w granicach ziaren. Wskutek aglomeracji pęcherzyków w granicach ziaren tworzą się nanopęknięcia w warstwie optycznie aktywnej (**Rys. 2**). To właśnie te nanopęknięcia mogą być odpowiedzialne za zmniejszenie zdolności odbicia luster nanostrukturalnych w porównaniu do luster mikrokrystalicznych, ponieważ w przypadku luster nanostrukturalnych występuje większa gęstość granic ziaren, a więc jest więcej miejsc do zarodkowania nanopęknięć. Nanopęknięcia pojawiają się tylko w/przy w niektórych granicach ziaren, co może wynikać z wielu czynników, wśród których warto wymienić m.in. dezorientację granic ziaren, charakter granic ziaren i lokalne odkształcenia.

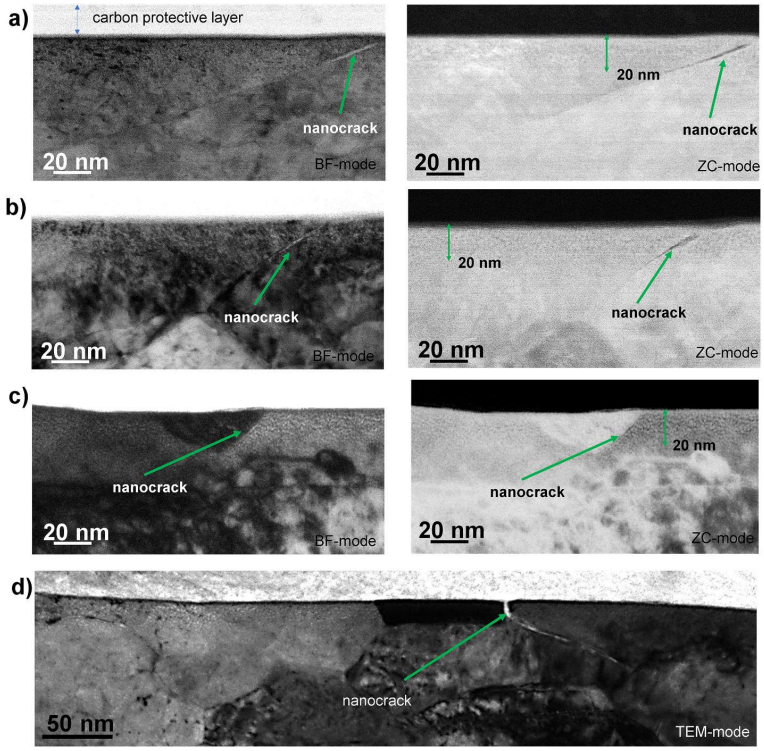

Rys. 2 Przekrój poprzeczny przez lustra naświetlone jonami He: a) lustro nieodkształcone, b) lustro po procesie HPT, jeden obrót (lamelka FIB), c) lustro po procesie HPT, pięć obrotów (lamelka FIB) – przekroje poprzeczne; FIB Hitachi NB5000, TEM Jeol 1200, STEM Hitachi HD2700 [1H]

Niewielka różnica współczynnika odbicia pomiędzy naświetlonymi lustrami różniącymi się znacznie stopniem odkształcenia może wynikać ze sposobu przygotowania powierzchni próbek do eksperymentów. Przed naświetlaniem powierzchnia luster została wyszlifowana i wypolerowana mechanicznie. Mechaniczne przygotowanie powierzchni próbek prowadzi do powstania defektów w warstwie przypowierzchniowej, która to warstwa odgrywa kluczową rolę podczas odbicia promieniowania. Wyraźne zmiany w mikrostrukturze były widoczne nawet do 1 μm w głąb próbki. Przeprowadzając badania Doppler broadening variable energy positron annihilation spectroscopy (DB-VEPAS) wyznaczono parametr S w funkcji głębokości materiału. Precyzując, parametr S określa wkład w widmie powstały w wyniku anihilacji elektronów o niskich pędach w związku z tym jest on bardzo czuły na obecność wakansów i ich skupisk. Parametr ten osiągnął najwyższą wartość na głębokości 20 nm poniżej powierzchni luster nieodkształconych i po procesie HPT. Sugeruje to, iż pomimo, że próbki różnią się znacznie stopniem odkształcenia, są podobne pod względem gęstości defektów typu wakansów. Wobec tego to właśnie granice ziaren odgrywają najistotniejszą rolę w obserwowanych różnicach w zdolności odbicia mikrokrystalicznych i nanostrukturaluch luster. Dodatkowo przeprowadzono badania variable energy positron

annihilation lifetime spectroscopy (VEPALS), które udowodniły, że w lustrach po HPT występują większe skupiska wakansów w granicach ziaren niż w lustrach nieodkształconych. Powoduje to, że w takich granicach jest wyższe prawdopodobieństwo powstania nanopęknięć.

Pomimo iż moje badania wykazały, że nanostrukturalne lustra Mo po naświetlaniu jonami He $8x10^{16}cm^{-2}$ wykazują mniejszą zdolność odbicia niż lustra mikrokrystaliczne, należy się spodziewać, że ta tendencja odwróci się dla wyższych dawek naświetlania. Będzie to spowodowane faktem, że nanopeknięcia utworzone na granicach ziaren tworzą porowatość otwartą, która może przyczynić się do uwolnienia jonów He z luster i opóźnić formowanie pęcherzy, których pojawienie się drastycznie obniża zdolność odbicia. Przeprowadzone badania nie wykluczają możliwości zastosowania nanostrukturalych luster w reaktorach termojądrowych, wskazują natomiast na istotne różnice powstające w mikrostrukturze materiałów nanostrukturalnych i mikroziarnistych w wyniku naświetlania jonami He.

4.4.2 Określenie wpływu defektów mikrostruktury powstałych w wyniku procesów SPD na tworzenie warstw w procesie niskotemperaturowego azotowania jarzeniowego stali austenitycznej

Kolejny podjęty przez mnie wątek badawczy dotyczył określenia wpływu charakteru granic ziaren utworzonych podczas procesów HE na zimno i na gorąco w stali austenitycznej na grubość warstwy azotowanej powstającej podczas niskotemperaturowego azotowania jarzeniowego. W wyniku procesu HE na zimno i na gorąco uzyskane sumaryczne odkształcenie rzeczywiste wynosiło 1,4. Dane literaturowe wskazywały, że wprowadzone defekty podczas odkształcenia plastycznego zapewnią wysoką dyfuzyjność tak otrzymanych materiałów, co z kolei może przyczynić się do zwiększenia wydajności procesów azotowania jarzeniowego. Jako metodę rozdrobnienia ziarna wybrałam HE, gdyż w przeciwieństwie do innych stosowanych technik SPD umożliwia otrzymanie dużych objętości materiału w postaci prętów, które łatwo mogą znaleźć zastosowanie w przemyśle [10]. Procesy HE zostały przeprowadzone w Instytucie Wysokich Ciśnień PAN przez dr hab. inż. Mariusza Kulczyka, a procesy niskotemperaturowego azotowania jarzeniowego zostały przeprowadzone w Politechnice Rzeszowskiej.

W wyniku procesu HE uzyskujemy bardzo duże rozdrobnienie mikrostruktury materiału, jednak mikrostruktury próbek odkształcanych w niskiej i wysokiej temperaturze różniły się znacząco. Mikrostruktura próbki po procesie HE na zimno składa się głównie z

nanobliźniaków odkształcenia oraz pasm ścinania [2H, 3H], co przedstawia **Rys. 3**. Inaczej wygląda mikrostruktura stali austenitycznej po procesie HE prowadzonym na gorąco (**Rys. 4**). W tej mikrostrukturze można zauważyć obszary w orientacji <111> i <100>. Obszary w orientacji <111>, są to obszary o wysokiej gęstości dyslokacji, gdzie dyslokacje tworzą granice dyslokacyjne. Natomiast obszary w orientacji <100> składają się z podziaren o niskiej gęstości dyslokacji, a także wyróżnić tu można pojedyncze całkowicie zrekrystalizowane ziarna [2H, 3H].

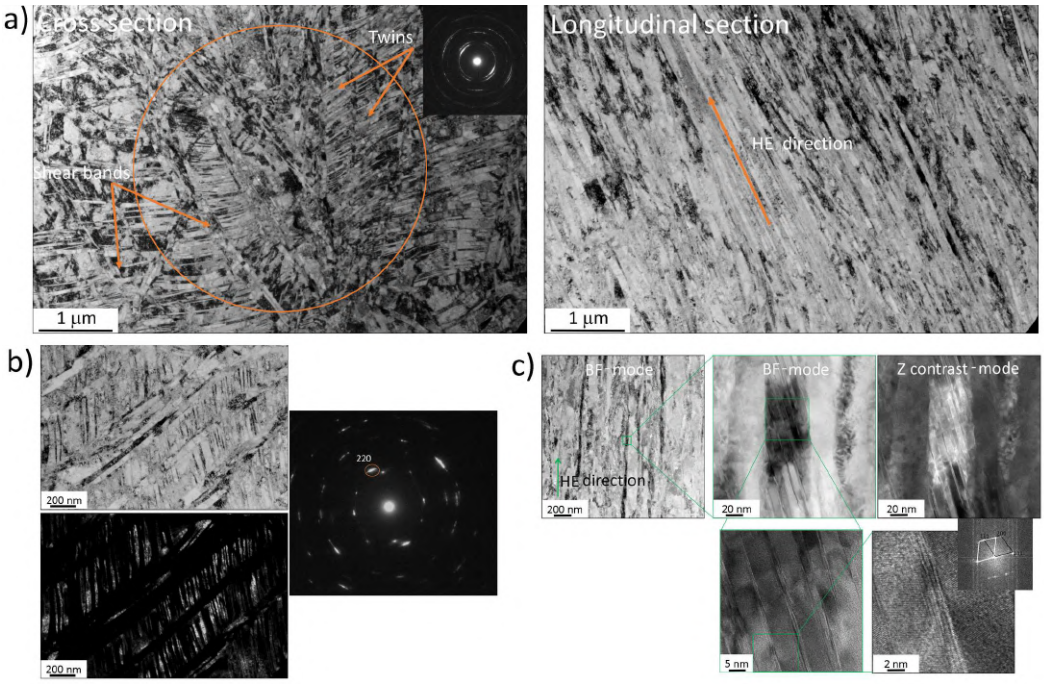

Rys. 3 Mikrostruktury próbki po procesie HE na zimno a) przekrój poprzeczny i wzdłużny, b) bliźniaki odkształcenia w jasnym i ciemnym polu wraz z dyfrakcją, c) nanobliźniaki widoczne na przekroju wzdłużnym wraz z transformatą Fouriera w orientacji [011] osnowy i [0-1-1] nanobliźniaków; TEM Jeol 1200, STEM Hitachi 2700 [2H]

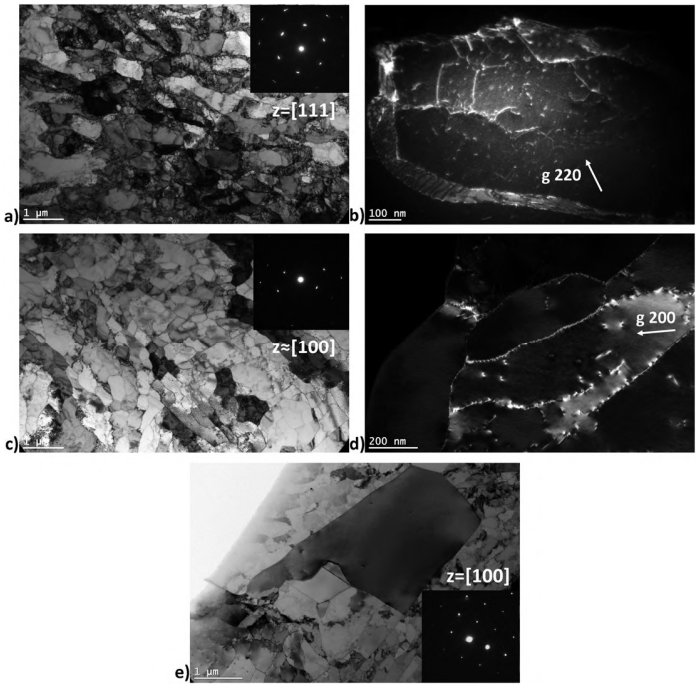

Rys. 4 Mikrostruktury próbki po procesie HE na gorąco przedstawiające obszary w orientacji <111> (a,b) i <100> (c, d, e); obserwacje podstruktur przy użyciu słabej wiązki b) i d); TEM Jeol 1200 [3H]

Ponieważ materiały nanostrukturalne charakteryzują się niższą stabilnością cieplną niż materiały mikrokrystaliczne, azotowanie zostało przeprowadzone w odpowiednio niskiej temperaturze 430°C tak, aby zachować rozdrobnienie mikrostruktury. Analiza mikrostruktury podłoża nie ujawniła istotnych zmian w porównaniu do stanu przed azotowaniem, co oznacza, że zastosowane warunki azotowania zapewniają stabilność nanometrycznej struktury podłoża i utrzymanie wysokich właściwości mechanicznych (**Rys. 5**). Zaobserwowałam w próbce wyżarzonej i po HE na gorąco bliźniaki utworzone w fazie S [4H].

Analiza grubości warstw (obserwacje w skaningowym mikroskopie elektronowym) pozwoliła stwierdzić, że w próbkach po wyżarzaniu średnia grubość warstw wynosi nieco poniżej 5 μm, natomiast po HE na zimno i gorąco ta grubość wzrasta nieco powyżej 5 μm, co oznacza, że rozdrobnienie mikrostruktury nie powoduje wzrostu szybkości dyfuzji. Jest to wynik znacząco różny od doniesień literaturowych, które wskazują na istotny wzrost grubości warstw w przypadku próbek o rozdrobnionym ziarnie. Należy jednak zwrócić uwagę, że mikrostruktura podłoża w przypadku próbek po HE (duży udział granic bliźniaczych w przypadku próbki po HE na zimno i struktura subziarnowa z dużą gęstością dyslokacji w przypadku próbki po HE na gorąco) znacząco różniła się od mikrostruktury próbek badanych

w literaturze, gdzie mikrostruktura składała się z dobrze wykształconych ziaren o dużym udziale granic o dużym kącie dezorientacji.

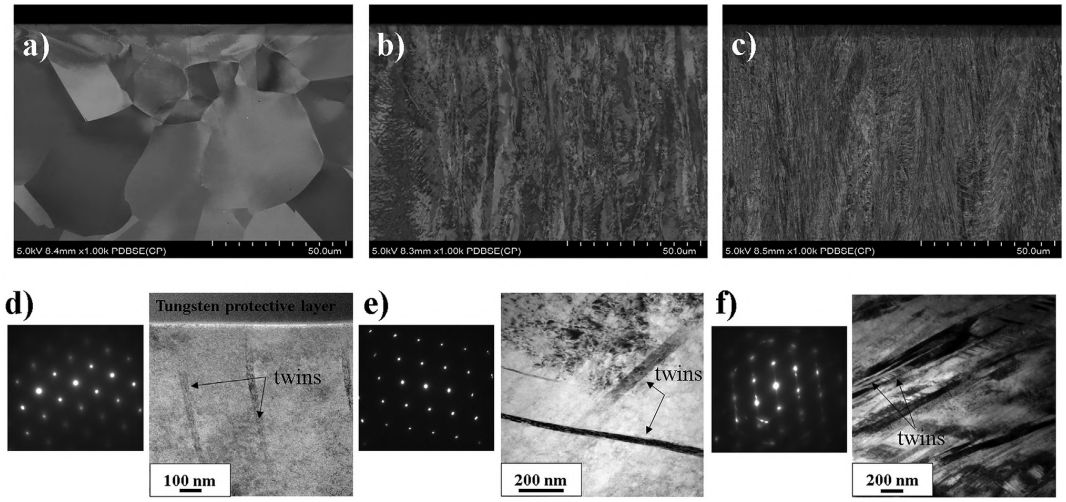

Rys. 5 Mikrostruktury warstw azotowanych i podłoża próbki: a) wyżarzonej, b) po procesie HE na gorąco, c) po procesie HE na zimno (SEM-BSE); mikrostruktury fazy S w próbkach d) wyżarzonej, e) po procesie HE na gorąco, f) po procesie HE na zimno wraz z dyfrakcją w orientacji [110]; SEM Hitachi Su 8000, TEM Jeol 1200 [4H]

Analiza głębokości, na jaką wnika azot, przy użyciu spektroskopii elektronów Auger'a pozwoliła zauważyć znaczne różnice w profilach stężenia azotu w zależności od mikrostruktury podłoża. Głębokość, na którą wnika azot, wynosi w przypadku próbki wyżarzonej i po HE na gorąco 8 μm, a na zimno 7 μm. Największe stężenie azotu przy powierzchni zaobserwowano w próbce po HE na zimno (w przybliżeniu 50%at.), najniższe w próbce po wyżarzaniu (w przybliżeniu 25%at.). Stężenie azotu we wszystkich próbkach zmniejsza się od powierzchni w głąb materiału, jednak kształt profili znacznie różnił się w zależności od mikrostruktury podłoża. Taki wynik eksperymentu wskazuje, że we wszystkich przypadkach wzrost warstw azotowanych kontrolowany jest dyfuzją objętościową. Brak różnic w kinetyce wzrostu warstw przypisano specyficznej mikrostrukturze podłoża. Granice specjalne, jakimi są granice bliźniacze lub dyslokacyjne, chętnie pułapkują azot, przez co nie stanowią dróg łatwej dyfuzji, a dyfuzja zachodzi w objętości materiału.

Przeprowadzone przeze mnie badania dowodzą, że rozdrobnienie mikrostruktury w wyniku procesów SPD nie zawsze doprowadza do przyspieszonej dyfuzji, gdyż zależy ona od rodzaju defektów i ich rozmieszczenia.

4.4.3 Określenie wpływu defektów mikrostruktury powstałych w wyniku procesów SPD na zjawiska zachodzące podczas HPA

W tym wątku badawczym postawiłam sobie za cel zrozumienie zjawisk zachodzących podczas HPA i określenie możliwości optymalizacji właściwości nanomateriałów tą drogą. Dokonałam więc szczegółowej analizy mikrostruktur powstałych w wyniku procesów SPD w różnych materiałach i jej wpływ na uzyskane mikrostruktury i właściwości materiałów w wyniku procesu HPA. Jak zostanie przedstawione poniżej, kombinacja procesów SPD i HPA daje możliwość wytworzenia takich mikrostruktur, które są niemożliwe do otrzymania konwencjonalnymi metodami wygrzewania [5H], co daje wymierny wkład w rozwój dyscypliny inżynierii materiałowej (**Rys.6**). W efekcie możliwe staje się wytworzenie materiałów o wysokiej wytrzymałości i zadowalającej plastyczności (**Rys. 7**). Wyniki pokazują że między ciśnienie zastosowane między HPT i HPA doprowadziło do wzrostu wytrzymałości z niewielkim zmniejszeniem plastyczności w porównaniu do odciążonej próbki po HPT. Zjawisko to można wytłumaczyć większym udziałem objętościowym ziarna o mniejszej średnicy które warunkują większą wytrzymałość.

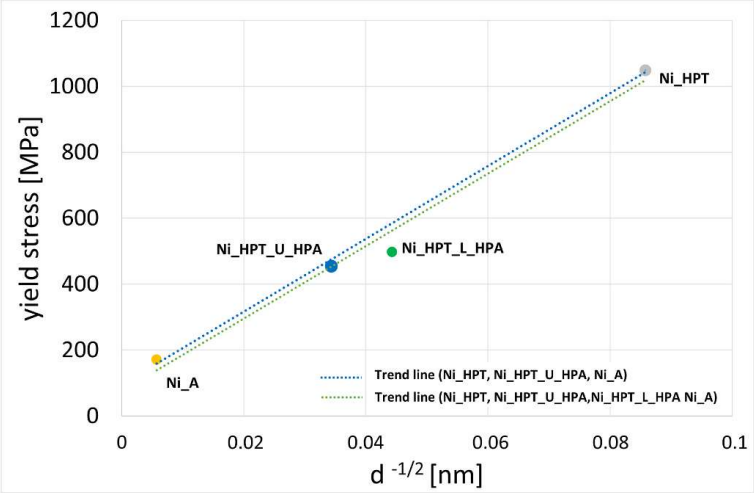

Rys. 6 Zależność Hall-Petch dla próbek Ni po różnych obróbkach cieplno-plastycznych; punkt Ni_HPT_L_HPA nie leży na linii trendu; wygrzanie konwencjonalne (Ni_A), po procesie HPT (Ni_HPT), oraz dodatkowo po procesie HPA z zastosowaniem między ciśnienia (Ni_HPT_L_HPA) oraz bez zastosowania między ciśnienia (Ni_HPT_U_HPA) [5H]

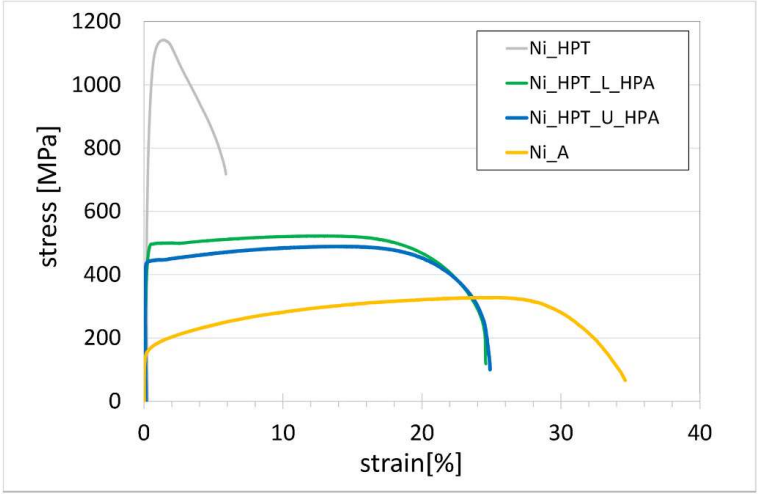

Rys. 7 Wykresy naprężenie-odkształcenie dla próbek Ni: wygrzanych konwencjonalnie (Ni_A), odkształconych w procesie HPT (Ni_HPT), oraz dodatkowo po procesie HPA z zastosowaniem między ciśnienia (Ni_HPT_L_HPA) oraz bez zastosowania między ciśnienia (Ni_HPT_U_HPA) [5H]

Warto też nadmienić, że prezentowane w tej części wyniki powstały w wyniku realizacji projektów, których byłam kierownikiem: SONATA finansowany przez NCN UMO-2014/15/D/ST8/00532 i WTZ PL 11/2018 finansowany przez Ministerstwo Nauki i Szkolnictwa Wyższego oraz Austrian Federal Ministry of Education, Science and Research. Procesy HPA stali austenitycznej zostały przeprowadzone w Instytucie Wysokich Ciśnień UNIPRESS PAN dzięki uprzejmości dr inż. Stanisława Gierlotki. Procesy HPA pozostałych materiałów omawianych w dalszej części autoprezentacji zostały po raz pierwszy na świecie przeprowadzone przy użyciu urządzenia do HPT. Było to możliwe dzięki modernizacji urządzania do HPT, której to modernizacji dokonałam wraz dr Darią Setman i dr Michael Kerber z Wydziału Fizyki Uniwersytetu Wiedeńskiego. Warunki procesów HPA zostały dobrane w wyniku wielu eksperymentów.

4.4.3.1 Określenie wpływu mikrostruktury powstałej w wyniku SPD na przemiany zachodzące w mikrostrukturze podczas wygrzewania konwencjonalnego i HPA

W pierwszym etapie badań skoncentrowałam się na określeniu wpływu mikrostruktury stali austenitycznej powstałej w wyniku procesu HPT na zmiany zachodzące w jej mikrostrukturze podczas wygrzewania konwencjonalnego i HPA tj. na rozroście ziarna, procesach wydzieleniowych oraz dominujących orientacjach. Procesy HPT przeprowadziłam osobiście na Wydziale Fizyki Uniwersytetu Wiedeńskiego. Takie badanie porównawcze

wnosi istotne informacje na temat możliwości, jakie niesie zastosowanie wysokiego ciśnienia hydrostatycznego podczas wygrzewania dla materiałów nanostrukturalnych.

W pierwszym etapie badań scharakteryzowałam mikrostrukturę stali austenitycznej po HPT. Moje badania dowiodły, że stal austenityczna po procesie HPT charakteryzuje się średnią wielkością ziarna poniżej 100 nm oraz dużą gęstością dyslokacji. Moje dalsze badania wykazały, że po procesie HPA przeprowadzonym w temperaturze 900°C w czasie 10 minut pod ciśnieniem 2 GPa i 6 GPa średnia wielkość ziarna d_2 wynosząca odpowiednio 1,4 i 0,6 μm jest zdecydowanie mniejsza niż w wyniku konwencjonalnego wygrzewania w tej samej temperaturze, która wynosiła 2,0 μm (**Rys. 7**) [6H]. Zastosowane wysokiego ciśnienia hydrostatycznego podczas wygrzewania znacznie utrudnia migrację granic ziaren mimo wytworzenia w materiale dużej gęstości defektów w wyniku procesu HPT. Co ciekawe, wraz ze wzrostem ciśnienia wzrasta współczynnik zmienności rozkładu wielkości ziarna $CV(d_2)$, definiowany jako stosunek odchylenia standardowego do wartości średniej wielkości ziarna. Oznacza to, że coraz trudniejszy jest ruch wakansów, a wraz z nim ruch granic wymagających skoordynowanego ruchu wakansów.

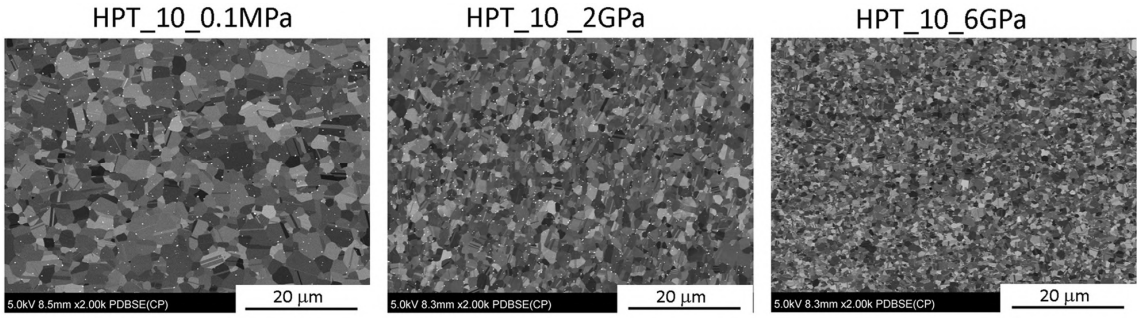

Rys. 8 Mikrostruktury stali austenitycznej po procesie HPT oraz wygrzewaniu konwencjonalnym (HPT_10_0.1MPa) i HPA (HPT_10_2GPa i HPT_10_6GPa) ; SEM Hitachi Su8000 [6H]

Kolejnym istotnym aspektem, jaki poruszyłam, były badania wpływu ciśnienia zastosowanego podczas wygrzewania na procesy wydzieleniowe [7H]. Analiza wpływu ciśnienia zastosowanego podczas wygrzewania na wielkość ziarna pozwoliła stwierdzić, że HPA zdecydowanie zahamowało rozrost ziarna, więc należałoby się spodziewać, że spowolnione będą również procesy wydzieleniowe, których szybkość zależy bezpośrednio od szybkości dyfuzji. Niezależnie od zastosowanego ciśnienia zaobserwowałam obecność wydzieleń. Wydzielenia powstały na granicach ziaren jak również w ziarnach. Udowodniłam, że HPA nie zatrzymało całkowicie procesów wydzieleniowych, ale zastosowane ciśnienia 6 GPa wyraźnie zahamowało wzrost wielkości wydzieleń. Dodatkowo zwiększyła się liczba wydzieleń, co wykazałam poprzez analizę wielkości komórek Woronoja. Zwiększona

wyraźnie liczba wydzieleń w porównaniu do wygrzewania pod ciśnieniem atmosferycznym może być spowodowana przez zmniejszenie tempa wspinania i poślizgu dyslokacji, co umożliwia obcym atomom segregację na liniach dyslokacji. W przypadku stali austenitycznej istotny jest również skład chemiczny powstających wydzieleń a szczególnie weryfikacja obecności wydzieleń bogatych w chrom typu $Cr_{23}C_6$. Wydzielenia te powstają podczas wygrzewania stali austenitycznej pod ciśnieniem atmosferycznym w zakresie temperatur 480-815°C i prowadzą do uczulenia stali na korozję międzykrystaliczną. Weryfikacja składu chemicznego wydzieleń została przeprowadzona poprzez wykonanie przyspieszonego testu korozyjnego podatności na korozję międzykrystaliczną. Po teście korozyjnym na powierzchni próbek można zauważyć wytrawienia. Wytrawienia są efektem korozji osnowy w sąsiedztwie wydzieleń zawierających Cr. Zatem korozja międzykrystaliczna jest tu w początkowym stadium. Przyspieszony test korozyjny pozwolił stwierdzić, że wygrzewanie pod ciśnieniem 6 GPa doprowadziło do powstania wydzieleń bogatych w Cr. Zauważyłam więc, że podczas HPA zaszły procesy tworzenia wydzieleń bogatych w Cr, które podczas konwencjonalnego wygrzewania pojawiłyby się w znacznie niższej temperaturze.

Dowiodłam również, że w przypadku materiałów nanostrukturalnych wysokie ciśnienie zastosowane podczas wygrzewania ma istotny wpływ na tworzące się dominujące orientacje i teksturę [7H]. Jest to bardzo istotny wkład w rozwój wiedzy na temat czynników kształtujących teksturę materiałów, gdyż do tej pory wpływ ciśnienia podczas wygrzewania był zaniedbywany. Do tej pory uważano, że na teksturę mają wpływ głównie takie czynniki jak wielkość ziarna, tekstura odkształcenia, stopień odkształcenia, czas wygrzewania, temperatura wygrzewania czy szybkość nagrzewania. W przypadku materiałów o strukturze krystalicznej regularnej ściennie centrowanej po odkształceniu konwencjonalnym i wygrzewaniu obserwuje się pojawienie się tekstury kubicznej ({001}<100>). Jednak w przypadku stali austenitycznej odkształconej w procesie HPT, a następnie wyżarzonej konwencjonalnie w temperaturze 900°C, dominuje orientacja <111>. Dzieje się tak dlatego, że podczas wygrzewania następuje ruch granic o dużym kącie dezorientacji utworzonych podczas HPT, a wiadomo, że granice o pewnych orientacjach 40°<111> wykazują dużo większą ruchliwość niż pozostałe. Natomiast można zauważyć, że po HPA, pojawia się oprócz dominującej orientacji <111> orientacja <100>. To zjawisko wyjaśniłam w sposób następujący: podczas wygrzewania pod ciśnieniem atmosferycznym granice o dużym kącie dezorientacji migrują i w rezultacie mikrostruktura stali austenitycznej po wygrzewaniu składa się z ziaren w orientacji <111>, gdyż granice <111> mają najwyższą mobilność. Jednakże pod podwyższonym ciśnieniem podczas wygrzewania ruch granic jest bardziej

ograniczony. Z tego powodu dostarczana energia podczas wygrzewania może umożliwić zarodkowanie nowych zrekrystalizowanych ziaren w orientacji <100>.

Kwestię wpływu wysokiego ciśnienia hydrostatycznego na zmiany w teksturze zgłębiłam dokładnie na przykładzie stali austenitycznej odkształconej w procesie walcowania profilowego (ang. profile rolling PR) [8H]. Dowiodłam, że HPA doprowadza do pojawienia się nowych komponentów tekstury {111}<11-2>, oprócz tych wykształconych po wygrzewaniu konwencjonalnym {001}<100>, <111>, <001>.

4.4.3.2 Określenie wpływu różnych metod odkształcenia plastycznego na zjawiska zachodzące podczas procesu HPA

W swoich badaniach skoncentrowałam się również na porównaniu wpływu różnych metod odkształcenia plastycznego na zjawiska zachodzące podczas HPA [6H]. Wybrałam dwie metody odkształcenia plastycznego: PR i HPT, dla których to metod całkowite odkształcenie wynosiło 3,4 i 79 i przeprowadziłam obrazowanie i analizę tak uzyskanych mikrostruktur. Mikrostruktury tak odkształconych stali znacznie się różnią. Odkształcenie metodą HPT prowadzi do utworzenia w materiale większej gęstości defektów niż stosując metodę PR. Mikrostruktura stali uzyskana podczas procesu HPT jest jednorodna i składa się z ziaren o średniej wielkości poniżej 100 nm. Natomiast mikrostruktura stali po procesie PR jest niejednorodna i składa się z wydłużonych pasm odkształcenia plastycznego podzielonych na podziarna o szerokości 50-100 nm i długości 100-300 nm. Występują tu nanobliźniaki odkształcenia o średniej szerokości 5-10 nm oraz granice o małym kącie dezorientacji.

Proces HPA przeprowadzony w temperaturze 900°C przez 10 min prowadzi do powstania mniejszej średniej wielkości ziarna w przypadku stali odkształconej metodą PR niż HPT zarówno po zastosowaniu ciśnienia 2 jak i 6 GPa. Co ciekawe, stosując ciśnienie atmosferyczne zależność jest odwrócona i mniejsze ziarno uzyskamy po procesie HPT (**Rys. 8**). Wyjaśniłam to zjawisko koncentrując się na wpływie niejednorodności mikrostruktury uzyskanej po procesie odkształcenia jak i wpływem granic bliźniaczych. Niejednorodna mikrostruktura uzyskana w procesie PR prowadzi do powstania uprzywilejowanych miejsc zarodkowania ziaren podczas wygrzewania pod ciśnieniem atmosferycznym, które następnie szybko rosną, co prowadzi do anormalnego rozrostu ziarna. W jednorodnej mikrostrukturze utworzonej w wyniku HPT na początku procesu wygrzewania następuje zdrowienie nierównowagowych granic ziaren, których mobilność w ten sposób zmniejsza się, zapewniając równomierną migrację granic ziaren. W sytuacji zastosowania wysokiego

ciśnienia podczas wygrzewania obecne w próbce PR granice bliźniacze rozumiane jako nachylone granice 70.5° <110>, do których ruchu wymagany jest skoordynowany ruch grupy atomów, na skutek niewystraczającego stężenia wakansów wykazują utrudnioną migrację pod wysokim ciśnieniem hydrostatycznym. Dodatkowo w próbce PR utrudniony jest ruch granic o małym kącie dezorientacji. W przypadku próbki po HPT stężenie wakansów podczas HPA jest wystarczająca, aby zapewnić dużo większą mobilność granic ziaren.

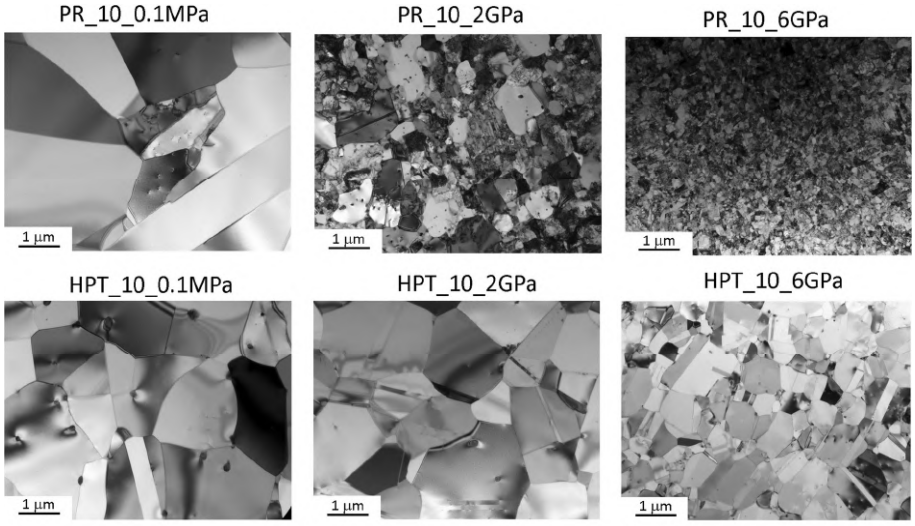

Rys. 9 Mikrostruktury stali austenitycznej po procesie PR, HPT oraz wygrzewaniu konwencjonalnym i HPA; TEM Jeol 1200 [6H]

Podsumowując, aby można było efektywnie kształtować mikrostrukturę w wyniku zastosowania procesu HPA, materiał wyjściowy powinien zawierać jak najmniejszy udział bliźniaków odkształcenia, gdyż granice bliźniacze wykazują dużą stabilność cieplną podczas HPA. W celu zweryfikowania wyciągniętych wniosków w następnej kolejności zbadałam wpływ energii błędu ułożenia (EBU) na zjawiska zachodzące w mikrostrukturze materiałów podczas procesu HPA.

4.4.3.3 Wpływ EBU na zjawiska zachodzące w mikrostrukturze materiałów podczas procesu HPA

W celu zbadania wpływu EBU na zjawiska zachodzące w mikrostrukturze materiałów podczas procesu HPA wytypowałam dwa materiały znacznie różniące się EBU: Ni o EBU=125 mJm^{-2} oraz Ag o EBU=16 mJm^{-2} [9H]. Materiały te charakteryzowały się tą samą czystością, aby nie wprowadzać dodatkowego czynnika, który mógłby utrudnić interpretację wyników. Materiały po procesie HPT, w którym to zostały odkształcone do tego samego

stopnia odkształcenia, zostały poddane procesowi HPA w tej samej temperaturze homologicznej, $0{,}4T_m$. Bezpośrednio po procesie HPT obserwacje mikroskopowe pozwoliły zauważyć, że mikrostruktury Ni i Ag różniły się znacznie. Średnia wielkość ziarna Ni wynosiła 140 nm, a Ag 120 nm. Dodatkowo w przypadku Ni nie zaobserwowano żadnych bliźniaków odkształcenia. Bliźniaki odkształcenia o średniej szerokości 10 nm były obecne w Ag.

Obserwacje mikrostruktury po procesie HPA pozwoliły zauważyć, że EBU spowodowała w różnym stopniu spowolnienie rozrostu ziarna. HPA znacznie utrudnia rozrost ziarna w porównaniu z wygrzewaniem konwencjonalnym. W przypadku Ni w wyniku HPA uzyskaliśmy średnią wielkość ziarna po HPA wynoszącą 70% tej po wygrzewaniu konwencjonalnym, a w przypadku Ag wynoszącą 13% tej po wygrzewaniu konwencjonalnym (**Rys. 9**). Co więcej, HPA także wpłynęło na jednorodność uzyskanych mikrostruktur biorąc pod uwagę wielkość ziarna. Niejednorodność mikrostruktury Ni po HPA w porównaniu do wygrzewania konwencjonalnego wzrosła, a niejednorodność mikrostruktury Ag zmniejszyła się. Te obserwowane przemiany w mikrostrukturze można wyjaśnić wpływem gęstości defektów utworzonych podczas HPT w materiałach różniących się EBU.

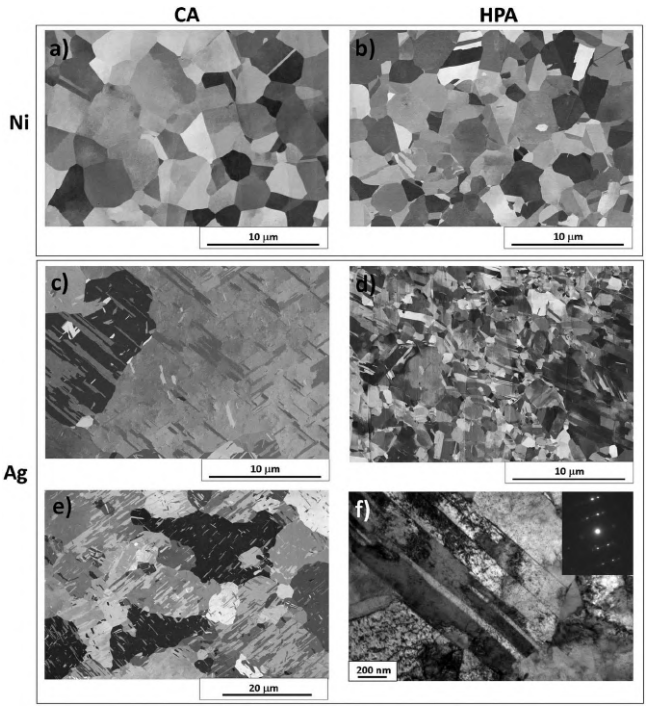

Rys. 10 Mikrostruktury Ag i Ni po procesie HPT oraz po procesie HPT i wygrzewaniu konwencjonalnym (CA) (a), c), e)) lub HPA (b), d), f)); a)-e) SEM Hitachi Su8000, f) TEM Jeol 1200 z dyfrakcją w orientacji [011] [9H]

Pomimo, że w materiale o niskiej EBU gęstość dyslokacji jest wyższa niż w materiale o wysokiej EBU, co znacznie ułatwia rozrost ziaren podczas konwencjonalnego

wygrzewania, stężenie wakansów jest niższe. Jest to efektem dwóch równolegle zachodzących procesów generacji i anihilacji wakansów. Ponieważ entalpia migracji wakansów jest niższa dla Ag niż dla Ni, oznacza to, że gęstość wakansów po procesie HPT jest wyższa w materiale o wyższej EBU. W efekcie większa gęstość wakansów podczas HPA znacznie ułatwia w Ni migracje granic ziaren. Dodatkowym czynnikiem utrudniającym rozrost ziarna w materiale o niskiej EBU jest duża gęstość nanobliźniaków. Jeśli traktować te granice jak nachylone 70,5° <110>, które do ruchu wymagają zsynchronizowanego ruchu wielu atomów, można łatwo wyjaśnić ich utrudniony ruch podczas HPA. Podobne zjawisko obserwowałam podczas procesu HPA stali austenitycznej odkształconej w wyniku PR.

4.4.3.4 Określenie wpływu wysokiego cienienia hydrostatycznego zadanego pomiędzy procesem HPT a HPA na zjawiska zachodzące w mikrostrukturze materiałów podczas procesu HPA

Kolejnym moim istotnym wkładem w rozwój wiedzy w dyscyplinie inżynieria materiałowa jest wykazanie ważnego wpływu wysokiego ciśnienia hydrostatycznego zadanego pomiędzy HPT a HPA na przemiany zachodzące w mikrostrukturze, jak również właściwości mechaniczne tak otrzymanych materiałów [5H]. To zagadnienie nie zostało nigdy wcześniej podjęte, gdyż do tej pory nie stosowano tego samego urządzenia do przeprowadzenia procesu HPT i HPA. Wiadomo, że podczas odciążania próbki po procesie HPT znaczna ilość defektów ulega anihilacji szczególnie w materiałach o niskiej stabilności cieplnej [11,12]. Zatem zastosowanie między ciśnienia, aby zachować defekty powstałe w materiale w wyniku HPT, prowadzi do uzyskania nowych mikrostruktur po procesie HPA (**Rys. 10**). W przeprowadzonym eksperymencie wykazałam, że zastosowane między ciśnienie pozwala na zachowanie pewnej gęstości wygenerowanych w procesie HPT Ni wakansów. Fakt, że większa gęstość kompleksów monowakans-dyslokacja była wykrywalna w próbce z zastosowanym między ciśnienia, potwierdziły badania variable energy positron lifetime spectroscopy (VEPALS) (**Rys. 10**).

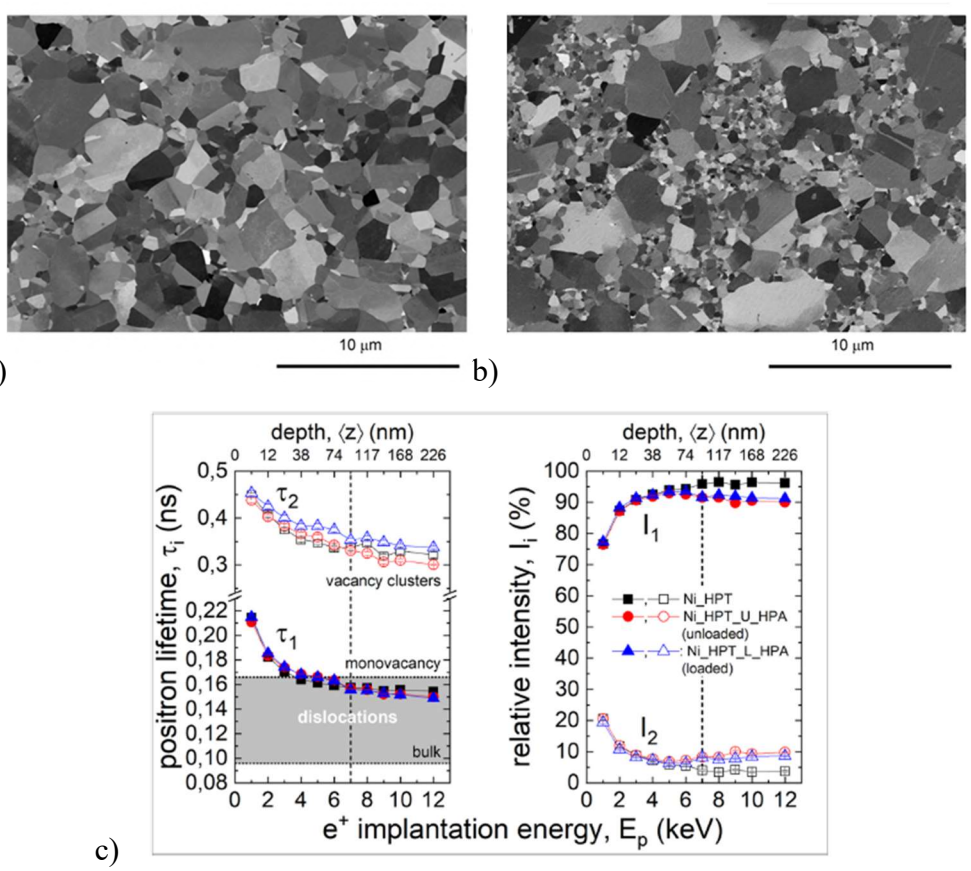

Rys. 11 a) Mikrostruktura Ni po HPA a) bez między ciśnienia b) z między ciśnieniem, c) długość życia pozytronów i względna intensywność w funkcji głębokości wnikania i energii implantacji [5H]

Co więcej, zastosowane między ciśnienie spowodowało utrudniony ruch wakansów do granic ziaren. Takie warunki pozwoliły na utworzenie większych aglomeratów wakansów niż w próbce bez zastosowanego między ciśnienia, co również potwierdziły badania VEPALS. Oznacza to, że pomimo większej gęstości wakansów w materiale poddanym działaniu między ciśnienia ich migracja do granic ziaren jest utrudniona. W rezultacie utrudniony jest ruch granic ziaren podczas HPA, co skutkuje mniejszą średnią wielkością ziarna po tej obróbce cieplno-mechanicznej. Zastosowanie między ciśnienia jest dodatkowym czynnikiem pozwalającym na kształtowanie optymalnych mikrostruktur o niespotykanych wcześniej właściwościach.

4.5 Podsumowanie wkładu naukowego w rozwój dyscypliny Inżynieria Materiałowa

Mój wkład naukowy w rozwój dyscypliny inżynieria materiałowa można podsumować następująco:

- *Określenie wpływu defektów mikrostruktury powstałych w wyniku procesów SPD na zdolność odbicia naświetlonych luster z molibdenu do zastosowań w reaktorach termojądrowych*

  Dowiodłam, że powstanie nanopęknięć na granicach ziaren luster z Mo po naświetlaniu jonami He, 2keV dawką $8x10^{16}$ [cm^{-2}], skutkuje obniżoną o 2,5% zdolnością odbicia nanostrukturalnych luster z Mo w porównaniu z lustrami mikrokrystalicznymi. Jest to związane z utworzeniem większej liczby nanopęknięć w przypadku luster nanostrukturalnych niż mikrokrystalicznych, co wynika z większej powierzchni względnej granic ziaren w lustrach nanostrukturalnych. Nie wynika to z różnic w gęstości defektów, gdyż ta jest zbliżona w warstwie optycznie aktywnej z powodu stosowania konwencjonalnego szlifowania i polerowania do przygotowania powierzchni luster.

- *Określenie wpływu defektów mikrostruktury powstałych w wyniku procesów SPD na tworzenie warstw powstałych w procesie niskotemperaturowego azotowania jarzeniowego stali austenitycznej*

  Wykazałam brak wyraźnych różnic w grubości warstw azotowanych w stali austenitycznej po procesie wygrzewania, HE na zimno i gorąco. Brak różnic w kinetyce wzrostu warstw przypisałam specyficznej mikrostrukturze podłoża, mianowicie granicom bliźniaczym i dyslokacyjnym, które chętnie pułapkują azot, przez co nie stanowią dróg łatwej dyfuzji, a dyfuzja zachodzi w objętości materiału.

- *Określenie wpływu defektów mikrostruktury powstałych w wyniku procesów SPD na zjawiska zachodzące podczas HPA*

  Dowiodłam, że HPA utrudnia zajście procesów rekrystalizacji i rozrostu ziarna w stali austenitycznej odkształconej przy użyciu HPT i PR. Opóźnienie to jest dużo bardziej wyraźne w przypadku próbek poddanych obróbce PR. Wynika to z większego stężenia wakansów, większej gęstości dyslokacji, mniejszego udziału granic o małym kącie dezorientacji i bliźniaczych a większym udziale

nierównowagowych granic ziaren w próbce po HPT. Wszystkie te czynniki zwiększają mobilność granic ziaren podczas HPA.

Podczas HPA stali austenitycznej po HPT pojawia się oprócz dominującej orientacji <111> orientacja <100>, nieobecna podczas wygrzewania konwencjonalnego. Wynika to z faktu, że podczas HPA ruch granic jest bardziej ograniczony, również i tych o najwyższej mobilności w temperaturze pokojowej. Z tego powodu dostarczana energia podczas wygrzewania może umożliwić zarodkowanie nowych zrekrystalizowanych ziaren w orientacji <100>.

HPA sprzyja zarodkowaniu wydzieleń w stali austenitycznej po HPT i utrudnia ich wzrost, co skutkuje wyższą liczbą $Cr_{23}C_6$ węglików podczas HPA pod ciśnieniem 6 GPa, niż stosując wygrzewanie konwencjonalne. Zwiększona wyraźnie liczba wydzieleń w porównaniu do wygrzewania pod ciśnieniem atmosferycznym może być spowodowana przez zmniejszenie tempa wspinania i poślizgu dyslokacji, co umożliwia obcym atomom segregację na liniach dyslokacji.

HPA opóźnia procesy rozrostu ziarna wyraźniej w materiałach o niskiej wyraźniej niż w materiałach o wysokiej EBU. Jest to odmienny wpływ w porównaniu do wygrzewania konwencjonalnego. Wolniejsze tempo wzrostu ziarna podczas HPA w przypadku Ag (w porównaniu z Ni) przypisałam większej powierzchni względnej granic bliźniaczych i mniejszemu stężeniu wakansów.

Zastosowane między ciśnienie pomiędzy HPT a HPA powoduje utrudniony ruch wakansów do granic ziaren i doprowadza do powstania mniejszej średniej wielkości ziarna niż w materiale bez zastosowania między ciśnienia. Takie warunki pozwoliły na utworzenie większych aglomeratów wakansów niż w próbce bez zastosowanego między ciśnienia. Oznacza to, że pomimo większego stężenia wakansów w materiale poddanym działaniu między ciśnienia, ich migracja do granic ziaren jest utrudniona. **Zastosowanie między ciśnienia jest dodatkowym czynnikiem pozwalającym na kształtowanie optymalnych mikrostruktur o niespotykanych wcześniej właściwościach.**

Dodatkowo podczas badań powstało nowatorskie rozwiązanie technologiczne, umożliwiające zastosowanie między ciśnienia pomiędzy procesem HPT a HPA.

4.6 Realizowane aktualnie i w najbliższej przyszłości badania

Przeprowadzone badania dotyczące wygrzewania pod wysokim ciśnieniem hydrostatycznym są kontynuowane w obecnie trwającym projekcie WEAVE_UNISONO (UMO-2021/03/Y/ST5/00253) „Kształtowanie nanomateriałów w wyniku wygrzewania pod wysokim ciśnieniem", który w 2022 dostałam w ramach konkursów w organizowanych przez NCN. Projekt ten ma charakter międzynarodowy. Umożliwia mi on kontynuowanie już rozpoczętych prac wraz z zespołem austriackim, a także utworzenie zespołu badawczego. Po stronie polskiej zespól składa się z ze mnie jako kierownika, doktoranta i post-doka. Jednocześnie zostałam promotorem pomocniczym pracy doktorskiej mgr inż. Tanmay Engineer „Designing Novel Nanomaterials by High Pressure Annealing". Dodatkowo tę tematykę kontynuuję w ramach przyznanego w 2022 roku GRANTU przez Radę Naukową Dyscypliny na Wydziale Inżynierii Materiałowej „Kształtowanie nanostruktury stopu aluminium w procesie starzenia pod wysokim ciśnieniem hydrostatycznym", w ramach którego student mgr inż. Tanmay Engineer realizuje swoją pracę magisterską.

Badanie wpływu defektów mikrostruktury na właściwości materiałów rozszerzyłam o wątek dotyczący wpływu defektów na właściwości antybakteryjne. Realizację tego zagadnienia badawczego umożliwia mi uzyskany w roku 2022 projekt SONATA BIS (UMO-2021/42/E/ST5/00118) „Kształtowanie mikrostruktury materiałów metalicznych w celu poprawy ich właściwości antybakteryjnych" przyznany w ramach konkursów organizowanych przez NCN. W ramach tego projektu stworzyłam zespół badawczy składający się ze mnie jako kierownika oraz dwóch doktorantów: mgr inż. Karoliny Budniak oraz mgr Anny Michalichy. Jednocześnie zostałam promotorem pomocniczym w pracy doktorskiej mgr inż. Karoliny Budniak.

Literatura:

1. X.M. Bai, A.F. Voter, R.G. Hoagland, M. Nastasi, B.P. Uberuaga, Efficient annealing of radiation damage near grain boundaries via interstitial emission, Science (80-.). (2010), https://doi.org/10.1126/science.1183723.
2. O. El-Atwani, J.A. Hinks, G. Greaves, S. Gonderman, T. Qiu, M. Efe, J.P. Allain, Insitu TEM observation of the response of ultrafine- and nanocrystalline-grained tungsten to extreme irradiation environments, Sci. Rep. (2014), https://doi.org/10.1038/srep04716.

3. A. Litnovsky, V.S. Voitsenya, R. Reichle, M. Walsh, A. Razdobarin, A. Dmitriev, N. Babinov, L. Marot, L. Moser, R. Yan, M. Rubel, A. Widdowson, S. Moon, S.G. Oh, Y. An, P. Shigin, I. Orlovskiy, K.Y. Vukolov, E. Andreenko, A. Krimmer, V. Kotov, P. Mertens, Diagnostic mirrors for ITER: research in the frame of international tokamak physics activity, Nucl. Fusion. (2019), https://doi.org/10.1088/1741-4326/ab1446.
4. H. Ferkel, M. Glatzer, Y. Estrin, R.Z. Valiev, RF plasma nitriding of a severely deformed high alloyed steel, Scr. Mater. 46 (2002) 623–628. https://doi.org/10.1016/S1359-6462(02)00031-3.
5. W. Lojkowski, D.A. Molodov, G. Gottstein, L. S. Shvidlerman, The mechanism of grain boundary migration in aluminium bicrystals. Mater Sci Forum (1996) 207–209:537–540
6. L. S. Shvindlerman, U. Czubayko, G. Gottstein, D. A. Molodov, High pressure effect on grain boundary migration and mechanism of grain boundary migration. Mater Sci Forum (1996) 204–206:45–54
7. V. Sursaeva, S. Protasova, W. Lojkowski et al, Microstructure evolution during normal grain growth under high pressure in 2-D aluminium foils. Texture Mictrostruct (1999) 32:175–185
8. A.T. Krawczynska, Ł. Ciupiński, P. Petersson, Impact of material migration and radiation damage on the reflectivity of molybdenum mirrors: Laboratory test for DEMO. Phys Scr, (2020). https://doi.org/10.1088/1402-4896/ab3e81.
9. L. Moser, L. Marot, R. Steiner, R. Reichle, F. Leipold, C. Vorpahl, F. Le Guern, U. Walach, S. Alberti, I. Furno, R. Yan, J. Peng, M. Ben Yaala, E. Meyer, Plasma cleaning of ITER first mirrors, in, Phys. Scr. (2017), https://doi.org/10.1088/1402-4896/aa8f30.
10. W. Pachla, J. Skiba, M. Kulczyk, S. Przybysz, M. Przybysz, M. Wróblewska, R. Diduszko, R. Stepniak, J. Bajorek, M. Radomski, W. Fafara, Nanostructurization of 316L type austenitic stainless steels by hydrostatic extrusion, Mater. Sci. Eng. A. 615 (2014) 116–127. https://doi.org/10.1016/j.msea.2014.07.069.
11. E. Schafler, Strength response upon pressure release after high pressure torsion deformation, Scripta Mater. (2011), https://doi.org/10.1016/j.scriptamat.2010.09.026.
12. E. Schafler, Effects of releasing the hydrostatic pressure on the nanostructure after severe plastic deformation of Cu, Scripta Mater. (2010), https://doi.org/10.1016/j.scriptamat.2009.12.004.

5. Informacja o wykazywaniu się istotną aktywnością naukową albo artystyczną realizowaną w więcej niż jednej uczelni, instytucji naukowej lub instytucji kultury, w szczególności zagranicznej.

5.1 Podczas studiów doktoranckich, które realizowałam na Wydziale Inżynierii Materiałowej Politechniki Warszawskiej odbyłam dwumiesięczny (09.-10.2010) staż naukowy w **Erich Schmid Institute of Materials Science w Leoben w Austrii** w ramach programu **KMM-VIN RESEARCH FELLOWSHIPS**. Staż odbyłam pod opieką **Prof. Rainhard Pippan**. Podczas stażu przygotowywałam próbki do procesów HPT, przeprowadzałam procesy HPT, wykonywałam pomiary mikrotwardości oraz badania właściwości wytrzymałościowych. W efekcie współpracy powstał artykuł:

A.T. Krawczynska, M. Lewandowska, R. Pippan, K.J. Kurzydlowski, The effect of high pressure torsion on structural refinement and mechanical properties of an austenitic stainless steel, J. Nanosci. Nanotechnol. (2013). https://doi.org/10.1166/jnn.2013.7468.

5.2 Bezpośrednio po obronie doktoratu odbyłam 7-miesięczny staż podoktorski (12.2012-06.2023) w **Centre d'Elaboration des Matériaux et d'Etudes Structurales** w Tuluzie we Francji w ramach projektu Strategy for Tailoring Multiscale Microstructures. Mechanical Properties and Micromechanical Modelling (MIMIC). Staż odbył się pod opieką **dr hab. inż. Frederic Mompiou**. Podczas stażu badałam mechanizmy odkształcenia plastycznego w nanokrystalicznym/ultradrobnoziarnistym niklu przy użyciu transmisyjnej mikroskopii elektronowej Jeol 2010. Przeprowadzałam zarówno badania in-situ rozciągania próbek jak i obserwacje post-mortem próbek po konwencjonalnych statycznych próbach rozciągania w transmisyjnym mikroskopie elektronowym. W efekcie współpracy powstały dwa artykuły:

L. Farbaniec, G. Dirras, **A. T. Krawczynska**, F. Mompiou, H. Couque, F. Naimi, F. Bernard, D. Tingaud, Powder metallurgy processing and deformation characteristics of bulk multimodal nickel, Mater. Charact. (2014). https://doi.org/10.1016/j.matchar.2014.05.008.

D. Tingaud, P. Jenei, **A. T. Krawczynska**, F. Mompiou, J. Gubicza, G. Dirras, Investigation of deformation micro-mechanisms in nickel consolidated from a bimodal

powder by spark plasma sintering, Mater. Charact. (2015). https://doi.org/10.1016/j.matchar.2014.11.025.

5.3 Podczas realizacji projektu **SONATA** (UMO-2014/15/D/ST8/00532), którego byłam kierownikiem, nawiązałam współpracę z **Prof. Michaelem Zehetbauerem** oraz **dr Darią Setman** i **dr Michaelem Kerberem**, umożliwiającą mi odbycie tygodniowego stażu na **Wydziale Fizyki Uniwersytetu Wiedeńskiego**. Podczas stażu przygotowałam próbki do procesów HPT, przeprowadzałam procesy HPT oraz badałam właściwości wytrzymałościowe próbek. W efekcie współpracy powstały trzy artykuły:

A.T. Krawczynska , M. Kerber, P. Suchecki, B. Romelczyk-Baishya, M. Oskar, M. Butterling, E. Hirschmann, A. Wagner, M. Lewandowska, D. Setman, The impact of high hydrostatic pressure maintenance after high-pressure torsion on phenomena during high hydrostatic pressure annealing, Mater. Sci. Eng. A. 840 (2022) 142874. https://doi.org/10.1016/j.msea.2022.142874.

A.T. Krawczynska, S. Gierlotka, P. Suchecki, D. Setman, B. Adamczyk-Cieslak, M. Lewandowska, M. Zehetbauer, Recrystallization and grain growth of a nano/ultrafine structured austenitic stainless steel during annealing under high hydrostatic pressure, J. Mater. Sci. (2018). https://doi.org/10.1007/s10853-018-2459-1.

A.T. Krawczynska, S. Gierlotka, P. Suchecki, D. Setman, B. Adamczyk-Cieslak, M. Gloc, W. Chrominski, M. Lewandowska, M. Zehetbauer, Phenomena Occurring in Nanostructured Stainless Steel 316LVM during Annealing under High Hydrostatic Pressure, Adv. Eng. Mater. (2018). https://doi.org/10.1002/adem.201800101.

Współpracę z dr inż. Darią Setman kontynuowałam w ramach projektu WTZ PL 11/2018 finansowanego przez Ministerstwo Nauki i Szkolnictwa Wyższego oraz Austrian Federal Ministry of Education, Science and Research, którego byłam kierownikiem po stronie polskiej. W ramach tego projektu odbyłam dwa staże naukowe na **Wydziale Fizyki Uniwersytetu Wiedeńskiego** (01.02-31.03.2019 i 10.02-13.03.2020), z których drugi został przerwany z powodu wybuchu epidemii koronawirusa. Podczas stażu modernizowałam urządzenie HPT wraz z dr Michaelem Kerberem, aby możliwe było przeprowadzenie eksperymentów HPA, a następnie przeprowadziłam takie eksperymenty na materiałach różniących się EBU. Dodatkowo przeprowadziłam eksperymenty z zastosowaniem między ciśnienia, które jednoczenie

były badaniami wstępnymi do projektu WEAVE-UNISONO. W efekcie tej współpracy powstał jeden artykuł:

A.T. Krawczynska, M. Kerber, P. Suchecki, B. Romelczyk-Baishya, M. Lewandowska, D. Setman, The impact of the stacking fault energy of nanostructured metals on phenomena during annealing at the high hydrostatic pressure, Mater. Sci. Eng. A. 808 (2021) 140913. https://doi.org/10.1016/j.msea.2021.140913.

5.4 W ramach projektu **Polonium** 2018-2019, finansowanym przez Ministerstwo Nauki i Szkolnictwa Wyższego oraz Les Ministères de l'Europe et des Affaires étrangères et de l'Enseignement Supérieur et de la Recherche, którego byłam kierownikiem po stronnie polskiej, odbyłam w ciągu dwóch lat cztery tygodniowe staże w **INSA Lyon**. Podczas staży przeprowadzałam badania plastyczności tlenku aluminium w różnej skali podczas eksperymentów in situ w mikroskopach elektronowych. W okresie stażu współpracowałam z **Prof. K. Masenelli-Varlot**. Próbki do badań przygotowywałam przy użyciu FIB NB5000.W efekcie współpracy została przedstawiona na konferencji Nanomechanical Testing in Materials Research and Development 29.10-04.112019 w Malaga, Hiszpanii:

prezentacja ustna: *Nanomechanical Testing in Materials Research and Development,* L. Joly-Pottuz, **A.T. Krawczynska**, T. Plocinski, I. Issa, V. Garnier, S. Le Foch, D. Machon, K. Masenelli-Varlot

5.5 W dniach 13.06.-18.06.2023 odbyłam staż w **Helmholtz-Zentrum Dresden-Rossendorf**, podczas którego przeprowadzałam eksperymenty DB-VEPAS i VEPALS otrzymując finansowanie z ramach konkursu **Mobility PW**. Współpracę z **dr M. Liedke** rozpoczęłam już w 2020 roku, jednak z powodu epidemii koronawirusa nie mogłam uczestniczyć w badaniach w Instytucie osobiście. Od 2020 roku współpraca zaowocowała dwoma artykułami:

A.T. Krawczynska, Ł. Ciupinski, M. Gloc, D. Setman, M. Spychalski, P. Suchecki, M.O. Liedke, M. Butterling, A. Wanger, E. Hirschmann, P. Petersson, Impact of high pressure torsion processing on helium ion irradiation resistance of molybdenum, Mater. Charact. 191 (2022). https://doi.org/10.1016/j.matchar.2022.112151.

A.T. Krawczynska, M. Kerber, P. Suchecki, B. Romelczyk-Baishya, M. Oskar, M. Butterling, E. Hirschmann, A. Wagner, M. Lewandowska, D. Setman, The impact of high hydrostatic pressure maintenance after high-pressure torsion on phenomena

during high hydrostatic pressure annealing, Mater. Sci. Eng. A. 840 (2022) 142874. https://doi.org/10.1016/j.msea.2022.142874.

5.6 Aktywnie współpracowałam z Prof. Markiem Rublem i z dr inż. Perem Peterssonem z Royal Institute of Technology (KTH) jako wykonawca międzynarodowego projektu EUROFUSION, zadanie „Irradiation testing of mirrors: microscopy studies of surface". Analizowałam defekty powstałe w wyniku naświetlania luster z molibdenu przy użyciu FIB Hitachi NB5000, TEM Jeol 1200, STEM Hitachi HD2700. W wyniku tej współpracy powstały trzy artykuły:

A.T. Krawczyńska, Ciupiński, M. Gloc, D. Setman, M. Spychalski, P. Suchecki, B. Adamczyk-Cieślak, M.O. Liedke, M. Butterling, A. Wanger, E. Hirschmann, P. Petersson, Impact of high pressure torsion processing on helium ion irradiation resistance of molybdenum, Mater. Charact. 191 (2022). https://doi.org/10.1016/j.matchar.2022.112151.

A.T. Krawczyńska, Ł. Ciupiński, P. Petersson, Impact of material migration and radiation damage on the reflectivity of molybdenum mirrors: Laboratory test for DEMO, in: Phys. Scr., 2020. https://doi.org/10.1088/1402-4896/ab3e81.

M. Rubel, S. Moon, P. Petersson, A. Garcia-Carrasco, A. Hallén, **A. T. Krawczyńska**, E. Fortuna-Zaleśna, M. Gilbert, T. Płociński, A. Widdowson, Metallic mirrors for plasma diagnosis in current and future reactors: Tests for ITER and DEMO, in: Phys. Scr., 2017. https://doi.org/10.1088/1402-4896/aa8e27.

W ramach projektu Techmatstrateg III „Nowe powłoki zwiększające trwałość narzędzi w procesach kucia i wyciskania", którego byłam wykonawcą, współpracowałam z Prof. Tomaszem Mościckim z IPPT PAN i badałam mikrostrukturę powłok WBrTi/Ta magnetronowo nałożonych na podłoże stalowe przy użyciu SEM Su8000. W ramach współpracy powstał artykuł:

M. Maździarz, R. Psiuk, **A.T. Krawczyńska**, M. Lewandowska, T. Mościcki, Effect of zirconium doping on the mechanical properties of W1-xZrxB2 on the basis of first-principles calculations and magnetron sputtered films, Arch. Civ. Mech. Eng. 4 (2022) http://dx.doi.org/10.1007/s43452-022-00513-6

W ramach współpracy z Prof. Agnieszką Kowalkowską z Wydziału Biologii Uniwersytetu Gdańskiego obserwowałam procesy wydzieleniowe w storczykach przy użyciu TEM Jeol 1200. W ramach współpracy powstały trzy artykuły:

A.K. Kowalkowska, **A.T. Krawczyńska**, Anatomical features related with pollination of Neottia ovata (L.) Bluff & Fingerh. (Orchidaceae), Flora Morphol. Distrib. Funct. Ecol. Plants. (2019). https://doi.org/10.1016/j.flora.2019.03.015.

N. Wiśniewska, A.K. Kowalkowska, M. Kozieradzka-Kiszkurno, **A.T. Krawczyńska**, J. Bohdanowicz, Floral features of two species of Bulbophyllum section Lepidorhiza Schltr.: B. levanae Ames and B. nymphopolitanum Kraenzl. (Bulbophyllinae Schltr., Orchidaceae), Protoplasma. 255 (2018) 485–499. https://doi.org/10.1007/s00709-017-1156-2.

A.K. Kowalkowska, M. Pawłowicz, P. Guzanek, **A.T. Krawczyńska**, Floral nectary and osmophore of Epipactis helleborine (L.) Crantz (Orchidaceae), Protoplasma. (2018). https://doi.org/10.1007/s00709-018-1274-5.

6. Informacja o osiągnięciach dydaktycznych, organizacyjnych oraz popularyzujących naukę lub sztukę.

6.1 Osiągnięcia dydaktyczne

Z uwagi na charakter mojego zatrudnienia w Politechnice Warszawskiej – na stanowisku adiunkta w grupie pracowników badawczych, a wcześniej specjalisty naukowo-technicznego – moje doświadczenie dydaktyczne jest nieduże. Tym niemniej w miarę możliwości staram się włączać w proces kształcenia studentów i doktorantów. Moje osiągnięcia w tym zakresie są następujące.

6.1.1 Opieka nad dyplomantami i doktorantami

Pod moją opieką oraz w ramach prowadzonych przeze mnie projektów zostały zrealizowane/są realizowane następujące prace inżynierskie i magisterskie:

- Praca inżynierska: Dawid Fura „Wpływ wyżarzania na mikrostrukturę i właściwości stali nanokrystalicznej” – w ramach mojego projektu Sonata, 2017
- Praca magisterska: Paweł Wolanowski, tytuł: „Wpływ energii błędu ułożenia na zjawiska zachodzące w materiałach ultradrobnoziarnistych podczas wyżarzania pod wysokim ciśnieniem” – w ramach mojego projektu WTZ, 2020

- Tanmay Engineer, tytuł: „Nanostructure design in aluminium alloy duringageing under high hydrostatic pressure” – w ramach mojego grantu Rady Naukowej Dyscypliny Inżynieria Materiałowa PW, praca w trakcie realizacji, promotor

Promotor pomocniczy podczas realizacji pracy doktorskiej.

- Mgr inż. Karolina Budniak, tytuł: „Kształtowanie mikrostruktury materiałów metalicznych w celu poprawy ich właściwości antybakteryjnych”, data rozpoczęcia 2022, w ramach mojego projektu Sonata bis
- Mgr inż. Tanmay Engineer, tytuł: „Designing Novel Nanomaterials by High Pressure Annealing”, data rozpoczęcia 2023, w ramach mojego projektu Weave-Unisono

6.1.2 Od 2013 roku pomagam prowadzić zajęcia ze studentami w Laboratorium Elektronowej Mikroskopii Skaningowej. Tematyka zajęć dotyczy obrazowania mikrostruktur przy użyciu SEM i TEM oraz badania składu chemicznego materiałów przy użyciu spektroskopii z dyspersją energii.

6.2 Osiągnięcia organizacyjne

Byłam kierownikiem pięciu projektów finansowanych przez MNiSW i NCN oraz jednego grantu Rady Naukowej Dyscypliny Inżynieria Materiałowa PW.

1) **SONATA 8** o tytule „Rekrystalizacja i rozrost ziaren w silnie odkształconej stali austenitycznej” (2014/15/D/ST8/00532) finansowany przez NCN. W wyniku realizacji tego projektu powstały trzy artykuły:

A.T. Krawczynska, S. Gierlotka, P. Suchecki, D. Setman, B. Adamczyk-Cieslak, M. Lewandowska, M. Zehetbauer, Recrystallization and grain growth of a nano/ultrafine structured austenitic stainless steel during annealing under high hydrostatic pressure, J. Mater. Sci. (2018). https://doi.org/10.1007/s10853-018-2459-1.

A.T. Krawczynska, S. Gierlotka, P. Suchecki, D. Setman, B. Adamczyk-Cieslak, M. Gloc, W. Chrominski, M. Lewandowska, M. Zehetbauer, Phenomena Occurring in Nanostructured Stainless Steel 316LVM during Annealing under High Hydrostatic Pressure, Adv. Eng. Mater. (2018). https://doi.org/10.1002/adem.201800101

A.T. Krawczynska, P. Suchecki, B. Adamczyk-Cieslak, B. Romelczyk-Baishya, M. Lewandowska, Influence of high hydrostatic pressure annealing on the

recrystallization of nanostructured austenitic stainless steel, Mater. Sci. Eng. A. (2019). https://doi.org/10.1016/j.msea.2019.138381.

2) **WTZ PL 11/2018** o tytule „ The impact of the stacking fault energy of nanomaterials on phenomena during annealing at high hydrostatic pressure" finansowany przez Ministerstwo Nauki i Szkolnictwa Wyższego oraz Austrian Federal Ministry of Education, Science and Research. W wyniku realizacji projektu opublikowałam jeden artykuł:

A.T. Krawczynska, M. Kerber, P. Suchecki, B. Romelczyk-Baishya, M. Lewandowska, D. Setman, The impact of the stacking fault energy of nanostructured metals on phenomena during annealing at the high hydrostatic pressure, Mater. Sci. Eng. A. 808 (2021) 140913. https://doi.org/10.1016/j.msea.2021.140913.

3) **Polonium 2018-2019** o tytule „Badanie plastyczności tlenku aluminium w różnej skali podczas eksperymentów in-situ w różnej skali", finansowany przez Ministerstwo Nauki i Szkolnictwa Wyższego oraz Les Ministères de l'Europe et des Affaires étrangères et de l'Enseignement Supérieur et de la Recherche. Wyniki projektu zostały przedstawione na konferencji Nanomechanical Testing in Materials Research and Development 29.10-04.112019 w Malaga, Hiszpanii:

referat: *Nanomechanical Testing in Materials Research and Development,* L. Joly-Pottuz, **A.T. Krawczynska**, T. Plocinski, I. Issa, V. Garnier, S. Le Foch, D. Machon, K. Masenelli-Varlot

4) **SONATA BIS 11** (UMO-2021/42/E/ST5/00118) o tytule „Kształtowanie mikrostruktury materiałów metalicznych w celu poprawy ich właściwości antybakteryjnych" finansowany przez NCN. Projekt w realizacji od roku 2022.

5) **WEAVE-UNISONO** (UMO-2021/03/Y/ST5/00253) o tytule „Kształtowanie nanomateriałów w wyniku wygrzewania pod wysokim ciśnieniem" finansowany przez NCN. Projekt w realizacji od roku 2022.

6) **GRANT Rady Naukowej Dyscypliny** o tytule „Kształtowanie nanostruktury stopu aluminium w procesie starzenia pod wysokim ciśnieniem hydrostatycznym"

6.2.2 Organizacja konferencji naukowych

- Członek Komitetu Organizacyjnego XVI Konferencji Mikroskopii Elektronowej, Jachranka, wrzesień 2017.
- Udział w organizacji konferencji EMRS Fall Meeting w latach 2007-2011.

6.2.3 Inne

- Członek Polskiego Towarzystwa Materiałoznawczego od 2022 roku
- Członek Zespołu ds. Opracowania Kryteriów Oceny Nauczycieli Akademickich na Wydziale Inżynierii Materiałowej PW

6.3 Osiągnięcia popularyzujące naukę

W latach 2017-2019 reprezentowałam Politechnikę Warszawską w ramach organizowanego w INSA Lyon „International Partner Day". Celem mojego udziału w tym wydarzeniu było zachęcenie studentów z INSA Lyon do podjęcia studiów w Politechnice Warszawskiej. Studenci INSA Lyon muszą podczas studiów spędzić minimum jeden semestr na uczelni zagranicznej.

7. Oprócz kwestii wymienionych w pkt. 1-6, wnioskodawca może podać inne informacje, ważne z jego punktu widzenia, dotyczące jego kariery zawodowej.

7.1 W roku 2015 odbyłam dwumiesięczny staż 09.-10.2015 w **National Physical Laboratory w Teddington** w Anglii w ramach programu Skills (121/US/SKILLS/2015) organizowanego przez Fundację na rzecz Nauki Polskiej w celu podniesienia kwalifikacji związanych z zarządzaniem badaniami naukowymi oraz zarządzaniem zespołami naukowymi.
7.2 W roku 2021 dostałam Nagrodę zespołową I stopnia Rektora Politechniki Warszawskiej za osiągnięcia w latach 2019-2020.

Wynikiem mojej dotychczasowej działalności naukowej jest 54 publikacji, z czego 45 zostało opublikowanych w czasopismach z listy JCR. Po uzyskaniu stopnia doktora brałam udział w 15 konferencjach krajowych i międzynarodowych. Byłam kierownikiem 6 projektów, z czego 3 finansowanych przez NCN i 2 finansowanych przez MNiSW oraz odpowiednio Les Ministères de l'Europe et des Affaires étrangères et de l'Enseignement Supérieur et de la

Recherche i Austrian Federal Ministry of Education, Science and Research a także 1 grantu Rady Naukowej Dyscypliny Inżynierii Materiałowej PW. Brałam udział jako wykonawca w realizacji 10 projektów finansowanych przez NCN, NCBR i fundusze europejskie. Jako ekspert byłam recenzentem 4 wniosków o finansowanie i recenzentem 12 artykułów z bazy JCR. Dodatkowo jestem współautorem 2 patentów i jednego wdrożenia. W **Tabeli 1** przedstawiam swoje wskaźniki bibliometryczne.

Tabela 1 Moje wskaźniki bibliometryczne

Wskaźniki bibliometryczne		
Baza / Wskaźnik	Wg Scopus (opcja Basic Search and Secondary Documents)	Wg Web of Science (opcja Researchers and Cited Reference)
Indeks Hirsha bez autocytowań	13	13
Liczba publikacji	54	48
Liczba cytowań	590	556
Liczba cytowań bez autocytowań	523	487
Liczba publikacji jako pierwszy autor	21	21

A. Krawczyńska
.....
(podpis wnioskodawcy)

Załącznik 4

Wykaz osiągnięć naukowych albo artystycznych, stanowiących znaczny wkład w rozwój określonej dyscypliny

Informacje zawarte w poszczególnych punktach tego dokumentu powinny uwzględniać podział na okres przed uzyskaniem stopnia doktora oraz pomiędzy uzyskaniem stopnia doktora a uzyskaniem stopnia doktora habilitowanego.

I. WYKAZ OSIĄGNIĘĆ NAUKOWYCH ALBO ARTYSTYCZNYCH, O KTÓRYCH MOWA W ART. 219 UST. 1. PKT 2 USTAWY

1. Cykl powiązanych tematycznie artykułów naukowych, zgodnie z art. 219 ust. 1. pkt 2b ustawy;

Tytuł: Zjawiska zachodzące w materiałach o strukturze nanometrycznej podczas ekspozycji na różne warunki środowiskowe

1H. **A.T. Krawczyńska**, Ł. Ciupinski, M. Gloc, D. Setman, M. Spychalski, P. Suchecki, M.O. Liedke, M. Butterling, A. Wanger, E. Hirschmann, P. Petersson, Impact of high pressure torsion processing on helium ion irradiation resistance of molybdenum, Mater. Charact. 191 (2022). https://doi.org/10.1016/j.matchar.2022.112151.
IF(2022): 4,7, pkt. MNiSW: 100

2H. **A.T. Krawczyńska**, M. Lewandowska, A.T. Fry, Microstructural characterization and residual stress distribution in a nanostructured austenitic stainless steel, Int. J. Mater. Res. (2018). https://doi.org/10.3139/146.111672.
IF(2018): 0,851, pkt. MNiSW: 30

3H. **A.T. Krawczyńska**, W. Chromiński, E. Ura-Binczyk, M. Kulczyk, M. Lewandowska, Mechanical properties and corrosion resistance of ultrafine grained austenitic stainless steel processed by hydrostatic extrusion, Mater. Des. 136 (2017). https://doi.org/10.1016/j.matdes.2017.09.050.
IF(2017): 4,525, pkt. MNiSW: 35

4H. **A.T. Krawczyńska**, J. Zdunek, R. Sitek, M. Lewandowska, Formation of the Nitrided Layers on an Austenitic Stainless Steel with Different Grain Structures, Adv. Eng. Mater. (2018). https://doi.org/10.1002/adem.201701049.
IF(2018): 2.906, pkt. MNiSW: 30

5H. **A.T. Krawczyńska**, M. Kerber, P. Suchecki, B. Romelczyk-baishya, M. Oskar, M. Butterling, E. Hirschmann, A. Wagner, M. Lewandowska, D. Setman, The impact of high hydrostatic pressure maintenance after high-pressure torsion on phenomena during high hydrostatic pressure annealing, Mater. Sci. Eng. A. 840 (2022) 142874. https://doi.org/10.1016/j.msea.2022.142874

IF(2022): 6,4, pkt. MNiSW: 140

6H. **A.T. Krawczyńska**, S. Gierlotka, P. Suchecki, D. Setman, B. Adamczyk-Cieslak, M. Lewandowska, M. Zehetbauer, Recrystallization and grain growth of a nano/ultrafine structured austenitic stainless steel during annealing under high hydrostatic pressure, J. Mater. Sci. (2018). https://doi.org/10.1007/s10853-018-2459-1.

IF(2018): 3,442, pkt. MNiSW: 30

7H. **A.T. Krawczyńska**, S. Gierlotka, P. Suchecki, D. Setman, B. Adamczyk-Cieslak, M. Gloc, W. Chrominski, M. Lewandowska, M. Zehetbauer, Phenomena Occurring in Nanostructured Stainless Steel 316LVM during Annealing under High Hydrostatic Pressure, Adv. Eng. Mater. (2018). https://doi.org/10.1002/adem.201800101.

IF(2019): 3,217, pkt. MNiSW: 100

8H. **A.T. Krawczyńska**, P. Suchecki, B. Adamczyk-Cieslak, B. Romelczyk-Baishya, M. Lewandowska, Influence of high hydrostatic pressure annealing on the recrystallization of nanostructured austenitic stainless steel, Mater. Sci. Eng. A. (2019). https://doi.org/10.1016/j.msea.2019.138381.

IF(2019): 4,652, pkt. MNiSW: 140

9H. **A.T. Krawczyńska**, M. Kerber, P. Suchecki, B. Romelczyk-Baishya, M. Lewandowska, D. Setman, The impact of the stacking fault energy of nanostructured metals on phenomena during annealing at the high hydrostatic pressure, Mater. Sci. Eng. A. 808 (2021) 140913. https://doi.org/10.1016/j.msea.2021.140913

IF(2021), 6,044, pkt. MNiSW: 140

II. WYKAZ AKTYWNOŚCI NAUKOWEJ ALBO ARTYSTYCZNEJ

1. Wykaz opublikowanych monografii naukowych (z zaznaczeniem pozycji niewymienionych w pkt I.1).

Brak

2. Wykaz opublikowanych rozdziałów w monografiach naukowych.

Brak

3. Wykaz członkostwa w redakcjach naukowych monografii.

Brak

4. Wykaz opublikowanych artykułów w czasopismach naukowych (z zaznaczeniem pozycji niewymienionych w pkt I.2).

Publikacje przed uzyskaniem stopnia doktora:

Publikacje z bazy JCR:

1) M. Lewandowska, **A.T. Krawczyńska**, M. Kulczyk, K.J. Kurzydłowski, Structure and properties of nano-sized Eurofer 97 steel obtained by hydrostatic extrusion, J. Nucl. Mater. (2009). doi:10.1016/j.jnucmat.2008.12.166.
   IF(2009): 1,933 pkt. MNiSW: 30
2) **A.T. Krawczyńska**, M. Lewandowska, K.J. Kurzydlowski, Thermal stability of hydrostatically extruded EUROFER 97 steel, Fusion Eng. Des. (2009). doi:10.1016/j.fusengdes.2008.12.108.
   IF(2009): 1,122, pkt. MNiSW: 25
3) P. Czarkowski, **A.T. Krawczyńska**, R. Slesinski, T. Brynk, J. Budniak, M. Lewandowska, K.J. Kurzydlowski, Low temperature mechanical properties of 316L type stainless steel after hydrostatic extrusion, Fusion Eng. Des. (2011). doi:10.1016/j.fusengdes.2010.12.067.
   IF(2011): 1,49, pkt. MNiSW: 25

Publikacje spoza bazy JCR:

1) **A.T. Krawczyńska**, K. Biesiada, A. Olszyna, Kompozyty Al2O3-SiCw, Kompozyty, 2006, 6, 38-43
   IF(2006): 0 pkt. MNiSW: 0
2) **A.T. Krawczyńska**, M. Lewandowska, K.J. Kurzydlowski, Nanomaterials by Severe Plastic Deformation, Nanomaterials by Severe Plastic Deformation IV, Pts 1 and 2 (2008) 173-178

IF(2008): 0, pkt. MNiSW: 0

3) **A.T. Krawczyńska**, M. Lewandowska, K.J. Kurzydlowski, Fabrication of nanostructured stainless steel via hydrostatic extrusion, Conference Proceedings 6th European Stainless Steel Conference Science and Market Helsinki (2008) 239-243
   IF(2008): 0, pkt. MNiSW: 0
4) **A.T. Krawczyńska**, M. Lewandowska, K.J. Kurzydlowski, Nanostructure formation in austenitic stainless steel, in: Solid State Phenom., 2008. https://doi.org/10.4028/www.scientific.net/SSP.140.173.
   IF(2008): 0, pkt. MNiSW: 0
5) **A.T. Krawczyńska**, M. Lewandowska, K.J. Kurzydlowski, Recrystallization in nanostructured austenitic stainless steel, in: Mater. Sci. Forum, 2008. doi:10.4028/www.scientific.net/msf.584-586.966.
   IF(2008): 0, pkt. MNiSW: 0
6) **A.T. Krawczyńska**, M. Lewandowska, R. Kuziak, K.J. Kurzydłowski, Recrystallization and grain growth in nano-structured austenitic stainless steel under electric current heating, Phys. Status Solidi C. (2010). https://doi.org/10.1002/pssc.200983377.
   IF(2010): 0, pkt. MNiSW: 0
7) P.M. Kozikowski, **A.T. Krawczyńska**, M. Kulczyk, M. Lewandowska, K.J. Kurzydłowski, Tailoring mechanical properties of nano-structured Eurofer 97 steel for fusion applications, Phys. Status Solidi C. (2010). https://doi.org/10.1002/pssc.200983382.
   IF(2010): 0, pkt. MNiSW: 0
8) **A.T. Krawczyńska**, T. Brynk, M. Rosinski, A. Michalski, S. Gierlotka, E. Grzanka, S. Stelmakh, B. Palosz, M. Lewandowska, K.J. Kurzydlowski, Improving mechanical properties of nanometals by annealing, Proceedings of the 33rd Risoe International Symposium on Materials Science: Nanometals - Status and Perspective (2012)
   IF(2010): 0, pkt. MNiSW: 0

Publikacje po uzyskaniu stopnia doktora:

Publikacje z bazy JCR:

1) S. Gierlotka, E. Grzanka, **A.T. Krawczyńska**, S. Stelmakh, B. Palosz, M. Lewandowska, C. Lathe, K.J. Kurzydlowski, Strain relaxation and grain growth in 316LVM stainless steel annealed under pressure, Zeitschrift Für Krist. Proc. 1 (2013) 281–286. doi:10.1524/zkpr.2011.0042.
   IF(2013): 1,255, pkt. MNiSW: 20
2) **A.T. Krawczyńska**, M. Gloc, K. Lublinska, Intergranular corrosion resistance of nanostructured austenitic stainless steel, in: J. Mater. Sci., 2013. doi:10.1007/s10853-013-7283-z.
   IF(2013): 2,305, pkt. MNiSW: 30
3) **A.T. Krawczyńska**, T. Brynk, S. Gierlotka, E. Grzanka, S. Stelmakh, B. Palosz, M. Lewandowska, K.J. Kurzydlowski, Mechanical properties of nanostructured 316LVM stainless steel annealed under pressure, Mech. Mater. 67 (2013) 25–32. doi:10.1016/j.mechmat.2013.07.017.
   IF(2013): 2,225, pkt. MNiSW: 40
4) **A.T. Krawczyńska**, M. Lewandowska, R. Pippan, K.J. Kurzydlowski, The effect of high pressure torsion on structural refinement and mechanical properties of an austenitic stainless steel, J. Nanosci. Nanotechnol. (2013). doi:10.1166/jnn.2013.7468.
   IF(2013): 1,339, pkt. MNiSW: 20
5) P. Czarkowski, **A.T. Krawczyńska**, T. Brynk, M. Nowacki, M. Lewandowska, K.J. Kurzydłowski, Strength of nanostructured austenitic steel 316LN at cryogenic temperatures, in: J. Phys. Conf. Ser., 2014. doi:10.1088/1742-6596/568/3/032007.
   IF(2014): 0, pkt. MNiSW: 5
6) L. Farbaniec, G. Dirras, **A.T. Krawczyńska**, F. Mompiou, H. Couque, F. Naimi, F. Bernard, D. Tingaud, Powder metallurgy processing and deformation characteristics of bulk multimodal nickel, Mater. Charact. (2014). doi:10.1016/j.matchar.2014.05.008.
   IF(2014): 1,845, pkt. MNiSW: 45
7) P. Czarkowski, **A.T. Krawczyńska**, T. Brynk, M. Nowacki, M. Lewandowska, K.J. Kurzydłowski, Cryogenic strength and microstructure of a hydrostatically extruded austenitic steel 1.4429 (AISI 316LN), Cryogenics (Guildf). (2014). doi:10.1016/j.cryogenics.2014.07.014.

IF(2014): 1,168, pkt. MNiSW: 25

8) D. Tingaud, P. Jenei, **A.T. Krawczyńska**, F. Mompiou, J. Gubicza, G. Dirras, Investigation of deformation micro-mechanisms in nickel consolidated from a bimodal powder by spark plasma sintering, Mater. Charact. (2015). doi:10.1016/j.matchar.2014.11.025.
   IF(2015): 2,383 pkt. MNiSW: 45
9) M. Andrzejczuk, A. Roguska, M. Michalska, L. Lipińska, A. Czerwiński, M. Cantoni, **A.T. Krawczyńska**, M. Lewandowska, STEM study of Li4Ti5O12 anode material modified with Ag nanoparticles, J. Microsc. (2016). doi:10.1111/jmi.12414.
   IF(2016): 1,692, pkt. MNiSW: 35
10) ***A.T. Krawczyńska***, *W. Chromiński, E. Ura-Binczyk, M. Kulczyk, M. Lewandowska, Mechanical properties and corrosion resistance of ultrafine grained austenitic stainless steel processed by hydrostatic extrusion, Mater. Des. 136 (2017). https://doi.org/10.1016/j.matdes.2017.09.050.*
   IF(2017): 4,525, pkt. MNiSW: 35
11) M. Michalska, D.A. Ziółkowska, M. Andrzejczuk, **A.T. Krawczyńska**, A. Roguska, A. Sikora, New synthesis route to decorate Li4Ti5O12 grains with GO flakes, J. Alloys Compd. 719 (2017) 210–217. doi:10.1016/j.jallcom.2017.05.173.
   IF(2017): 3,779, pkt. MNiSW: 35
12) B. Wysocki, P. Maj, **A. T. Krawczyńska**, K. Rożniatowski, J. Zdunek, K.J. Kurzydłowski, W. Święszkowski, Microstructure and mechanical properties investigation of CP titanium processed by selective laser melting (SLM), J. Mater. Process. Technol. (2017). doi:10.1016/j.jmatprotec.2016.10.022.
   IF(2017): 3,647, pkt. MNiSW: 40
13) M. Rubel, S. Moon, P. Petersson, A. Garcia-Carrasco, A. Hallén, **A. T. Krawczyńska**, E. Fortuna-Zaleśna, M. Gilbert, T. Płociński, A. Widdowson, Metallic mirrors for plasma diagnosis in current and future reactors: Tests for ITER and DEMO, in: Phys. Scr., 2017. doi:10.1088/1402-4896/aa8e27.
   IF(2017): 1,902 pkt. MNiSW: 25
14) B. Kucharska, **A.T. Krawczyńska**, K. Rozniatowski, J. Zdunek, K. Poplawski, J.R. Sobiecki, The effect of current types on the microstructure and corrosion properties of Ni/NanoAl2O3 composite coatings, Mater. Tehnol. (2017). doi:10.17222/mit.2015.347.

IF(2017): 0,59 pkt. MNiSW: 15

15) Z. Oksiuta, Z. Mazurkiewicz, E. Romanczuk, M. Andrzejewicz, **A. T. Krawczyńska**, Analysis of microstructural aspects of a hip stem failure made of the REX 734 stainless steel, Eng. Fail. Anal. (2017). doi:10.1016/j.engfailanal.2016.11.012.
IF(2017): 2,157, pkt. MNiSW: 35

16) ***A.T. Krawczyńska***, *M. Lewandowska, A.T. Fry, Microstructural characterization and residual stress distribution in a nanostructured austenitic stainless steel, Int. J. Mater. Res. (2018). https://doi.org/10.3139/146.111672.*
IF(2018): 0,851, pkt. MNiSW: 30

17) ***A.T. Krawczyńska***, *J. Zdunek, R. Sitek, M. Lewandowska, Formation of the Nitrided Layers on an Austenitic Stainless Steel with Different Grain Structures, Adv. Eng. Mater. (2018). https://doi.org/10.1002/adem.201701049.*
IF(2018): 2.906, pkt. MNiSW: 30

18) ***A.T. Krawczyńska***, *S. Gierlotka, P. Suchecki, D. Setman, B. Adamczyk-Cieslak, M. Lewandowska, M. Zehetbauer, Recrystallization and grain growth of a nano/ultrafine structured austenitic stainless steel during annealing under high hydrostatic pressure, J. Mater. Sci. (2018). https://doi.org/10.1007/s10853-018-2459-1.*
IF(2018): 3,442, pkt. MNiSW: 30

19) N. Wiśniewska, A. Kowalkowska, M. Kozieradzka-Kiszkurno, **A.T. Krawczyńska**, J. Bohdanowicz, Floral features of two species of Bulbophyllum section Lepidorhiza Schltr.: B. levanae Ames and B. nymphopolitanum Kraenzl. (Bulbophyllinae Schltr., Orchidaceae), Protoplasma (2018). doi:10.1007/s00709-017-1156-2.
IF(2018): 2,633, pkt. MNiSW: 30

20) A.K. Kowalkowska, M. Pawłowicz, P. Guzanek, **A.T. Krawczyńska**, Floral nectary and osmophore of Epipactis helleborine (L.) Crantz (Orchidaceae), Protoplasma. (2018). doi:10.1007/s00709-018-1274-5.
IF(2018): 2,633, pkt. MNiSW: 30

21) ***A.T. Krawczyńska***, *S. Gierlotka, P. Suchecki, D. Setman, B. Adamczyk-Cieslak, M. Gloc, W. Chrominski, M. Lewandowska, M. Zehetbauer, Phenomena Occurring in Nanostructured Stainless Steel 316LVM during Annealing under High Hydrostatic Pressure, Adv. Eng. Mater. (2018). https://doi.org/10.1002/adem.201800101.*

IF(2019): 3,217, pkt. MNiSW: 100

22) ***A.T. Krawczyńska****, P. Suchecki, B. Adamczyk-Cieslak, B. Romelczyk-Baishya, M. Lewandowska, Influence of high hydrostatic pressure annealing on the recrystallization of nanostructured austenitic stainless steel, Mater. Sci. Eng. A. (2019). https://doi.org/10.1016/j.msea.2019.138381.*
IF(2019): 4,652, pkt. MNiSW: 140

23) A.K. Kowalkowska, **A.T. Krawczyńska,** Anatomical features related with pollination of Neottia ovata (L.) Bluff & Fingerh. (Orchidaceae), Flora Morphol. Distrib. Funct. Ecol. Plants. (2019). doi:10.1016/j.flora.2019.03.015.
IF(2019): 1,591, pkt. MNiSW: 40

24) M. Wachowski, R. Kosturek, L. Śniezek, S. Mróz, M. Gloc, **A.T. Krawczyńska**, M. Malek, Analysis of the microstructure of an Az31/Aa1050/Aa2519 laminate produced using the explosive-welding method, Mater. Tehnol. (2019). doi:10.17222/mit.2018.151.
IF(2019): 0,697, pkt. MNiSW: 40

25) E. Ura-Bińczyk, **A. T. Krawczyńska**, R. Sitek, M. Lewandowska, Mechanical properties and corrosion resistance of hydrostatically extruded 316 LVM stainless steel after low-temperature plasma nitriding, Surf. Coatings Technol. (2019). doi:10.1016/j.surfcoat.2019.07.035.
IF(2019): 3,784, pkt. MNiSW: 100

26) Ł. Żrodowski, B. Wysocki, R. Wróblewski, **A.T. Krawczyńska**, B. Adamczyk-Cieślak, J. Zdunek, P. Błyskun, J. Ferenc, M. Leonowicz, W. Święszkowski, New approach to amorphization of alloys with low glass forming ability via selective laser melting, J. Alloys Compd. (2019). doi:10.1016/j.jallcom.2018.08.075.
IF(2019): 4,65, pkt. MNiSW: 100

27) T. Brynk, **A.T. Krawczyńska**, D. Setman, Z. Pakieła, 3D DIC-assisted residual stress measurement in 316 LVM steel processed by HE and HPT, Arch. Civ. Mech. Eng. (2020). doi:10.1007/s43452-020-00068-4.
IF(2020): 4,369, pkt. MNiSW: 140

28) P. Czarniak, K. Szymanowski, B. Kucharska, **A.T. Krawczyńska**, J.R. Sobiecki, J. Kubacki, P. Panjan, Modification of tools for wood based materials machining with TiAlN/a-CN coating, Mater. Sci. Eng. B Solid-State Mater. Adv. Technol. (2020). doi:10.1016/j.mseb.2020.114540.
IF(2020): 4,051, pkt. MNiSW: 100

29) A. Majchrowicz, A. Roguska, **A.T. Krawczyńska**, M. Lewandowska, J. Martí-Muñoz, E. Engel, O. Castano, In vitro evaluation of degradable electrospun polylactic acid/bioactive calcium phosphate ormoglass scaffolds, Arch. Civ. Mech. Eng. (2020). doi:10.1007/s43452-020-00052-y.
IF(2020): 4,369, pkt. MNiSW: 140

30) **A.T. Krawczyńska**, Ł. Ciupiński, P. Petersson, Impact of material migration and radiation damage on the reflectivity of molybdenum mirrors: Laboratory test for DEMO, in: Phys. Scr., 2020. doi:10.1088/1402-4896/ab3e81.
IF(2020): 2,487, pkt. MNiSW: 40

31) M. Michalska, M. Andrzejczuk, **A.T. Krawczyńska**, A. Roguska, K. Nikiforow, P. Żurek, A. Sikora, P. Peikertová, The effect of MWCNT modification on structural and morphological properties of Li4Ti5O12, Diam. Relat. Mater. (2021). https://doi.org/10.1016/j.diamond.2021.108276.
IF(2021): 3,800, pkt. MNiSW: 100

32) A. Chmielewska, A. Dobkowska, E. Kijeńska-Gawrońska, M. Jakubczak, **A. T. Krawczyńska**, E. Choińska, A. Jastrzębska, D. Dean, B. Wysocki, W. Święszkowski, Biological and corrosion evaluation of in situ alloyed NiTi fabricated through laser powder bed fusion (LPBF), Int. J. Mol. Sci. (2021). https://doi.org/10.3390/ijms222413209.
IF(2021): 6,208, pkt. MNiSW: 140

33) K. Kwatek, W. Ślubowska, J.L. Nowiński, **A.T. Krawczyńska**, I. Sobrados, J. Sanz, Electrical and structural properties of Li1.3Al0.3Ti1.7(po4)3-based ceramics prepared with the addition of Li4SiO4, Materials (Basel). (2021). https://doi.org/10.3390/ma14195729.
IF(2021): 3,748, pkt. MNiSW: 140

*34) **A.T. Krawczyńska**, M. Kerber, P. Suchecki, B. Romelczyk-Baishya, M. Lewandowska, D. Setman, The impact of the stacking fault energy of nanostructured metals on phenomena during annealing at the high hydrostatic pressure, Mater. Sci. Eng. A. 808 (2021) 140913. https://doi.org/10.1016/j.msea.2021.140913.*
IF(2021), 6,044, pkt. MNiSW: 140

*35) **A.T. Krawczyńska**, Ł. Ciupinski, M. Gloc, D. Setman, M. Spychalski, P. Suchecki, M.O. Liedke, M. Butterling, A. Wanger, E. Hirschmann, P. Petersson, Impact of high pressure torsion processing on helium ion irradiation resistance of*

molybdenum, Mater. Charact. 191 (2022). https://doi.org/10.1016/j.matchar.2022.112151.
IF(2022): 4,7, pkt. MNiSW: 100

36) ***A.T. Krawczyńska**, M. Kerber, P. Suchecki, B. Romelczyk-baishya, M. Oskar, M. Butterling, E. Hirschmann, A. Wagner, M. Lewandowska, D. Setman, The impact of high hydrostatic pressure maintenance after high-pressure torsion on phenomena during high hydrostatic pressure annealing, Mater. Sci. Eng. A. 840 (2022) 142874. https://doi.org/10.1016/j.msea.2022.142874.*
IF(2022): 6,4, pkt. MNiSW: 140

37) M. Maździarz, R. Psiuk, **A.T. Krawczyńska**, M. Lewandowska, T. Mościcki, Effect of zirconium doping on mechanical properties of W1−xZrxB2 on the base of ab initio calculations and magnetron sputtered films, Arch. Civ. Mech. Eng. (2022) https://doi.org/10.48550/arXiv.2203.13728
IF(2022): 4,4, pkt. MNiSW: 140

38) A. Chmielewska, B. Wysocki, P. Kwaśniak, M.J. Kruszewski, B. Michalski, A. Zielińska, B. Adamczyk-Cieślak, **A.T. Krawczyńska**, J. Buhagiar, W. Święszkowski, Heat Treatment of NiTi Alloys Fabricated Using Laser Powder Bed Fusion (LPBF) from Elementally Blended Powders, Materials (Basel). (2022). https://doi.org/10.3390/ma15093304.
IF(2022): 3,4, pkt. MNiSW: 140

39) B. Kucharska, P. Czarniak, K. Kulikowski, **A.T. Krawczyńska**, K. Rożniatowski, J. Kubacki, K. Szymanowski, P. Panjan, J.R. Sobiecki, Comparison Study of PVD Coatings: TiN/AlTiN, TiN and TiAlSiN Used in Wood Machining, Materials (Basel). (2022). https://doi.org/10.3390/ma15207159.
IF(2022): 3,4, pkt. MNiSW: 140

40) E. Ura-Bińczyk, A. Dobkowska, P. Bazarnik, J. Ciftci, **A.T. Krawczyńska**, W. Chromiński, T. Wejrzanowski, R. Molak, R. Sitek, T. Płociński, J. Jaroszewicz, J. Mizera, Effect of annealing on the mechanical and corrosion properties of 316L stainless steel manufactured by laser powder bed fusion, Mater. Sci. Eng. A. (2022). https://doi.org/10.1016/j.msea.2022.144263.
IF(2022): 6,4, pkt. MNiSW: 140

41) Ł. Żrodowski, R. Wróblewski, M. Leonowicz, B. Morończyk, T. Choma, J. Ciftci, W. Święszkowski, A. Dobkowska, E. Ura-Bińczyk, P. Błyskun, J. Jaroszewicz, **A. T. Krawczyńska**, K. Kulikowski, B. Wysocki, T. Cetner, G. Moneta, X. Li, L.

Yuan, A. Malachowska, P.J. Masset, R. Chulist, C. Żrodowski, How to Control the Crystallization of Metallic Glasses During Laser Powder Bed Fusion? Towards Part-Specific 3d Printing of in Situ Composites, SSRN Electron. J. (2022). https://doi.org/10.2139/ssrn.4239108.
IF(2022): 0, pkt. MNiSW: 5

42) K. Kwatek, W. Ślubowska-Walkusz, E. Kwiatkowska, J.L. Nowiński, **A.T. Krawczyńska**, I. Sobrados, V. Diez-Gómez, J. Sanz, Lithium mobility along conduction channels of ceramic LiTa2PO8, J. Eur. Ceram. Soc. (2023). https://doi.org/10.1016/j.jeurceramsoc.2023.05.013.
IF(2023): 5,7, pkt. MNiSW: 200

43) P. Dubey, V. Shrivastav, P.H. Maheshwari, M. Hołdyński, **A. T. Krawczyńska**, S. Sundriyal, Comparative study of different metal-organic framework electrodes synthesized using waste PET bottles for supercapacitor applications, J. Energy Storage. (2023). https://doi.org/10.1016/j.est.2023.107828.
IF(2023): 9,4, pkt. MNiSW: 100

Publikacje spoza bazy JCR:

1) M. Lewandowska, **A.T. Krawczyńska**, A. Panigrahi, E. Schafler, M. Zehetbauer, Precipitation processes in nanostructured 7475 aluminium alloy, in: PTM 2015 - Proc. Int. Conf. Solid-Solid Phase Transform. Inorg. Mater. 2015, 2015.
IF(2015): 0, pkt. MNiSW: 0

5. Wykaz osiągnięć projektowych, konstrukcyjnych, technologicznych (z zaznaczeniem pozycji niewymienionych w pkt I.3).

Brak

6. Wykaz publicznych realizacji dzieł artystycznych (z zaznaczeniem pozycji niewymienionych w pkt I.3).

Brak

7. Wykaz wystąpień na krajowych lub międzynarodowych konferencjach naukowych lub artystycznych, z wyszczególnieniem przedstawionych wykładów na zaproszenie i wykładów plenarnych.

Wystąpienia w postaci prezentacji ustnych:

1) Wykład zaproszony: 16.06.2023 Institute of Radiation Physics Helmholtz-Zentrum Dresden – Rossendorf,

Tytuł wystąpienia: Impact of high pressure torsion processing on helium ion irradiation resistance of molybdenum mirrors,

A.T.Krawczyńska, Ł. Ciupinski, D. Setman, M. O. Liedke, M. Butterling, A.Wanger, E. Hirschmann, P. Petersson, M. Rubel

Konferencje:

Po uzyskaniu stopnia doktora:

1) *Euromat 2023, Frankfurt, Niemcy, 03.09.-07.09.2023*

Tytuł wystąpienia: The impact of high hydrostatic pressure maintenance after high-pressure torsion on phenomena during high hydrostatic pressure annealing

A.T. Krawczyńska, D. Setman, M. Butterling, E. Hirschmann, M. Kerber, M. Liedke, B. Romelczyk-Baishya, P. Suchecki, A. Wagner, M. Lewandowska

2) *Euromat 2021, virtual, 13.09.-17.09.2021*

Tytuł wystąpienia: The impact of the stacking fault energy of nanostructured metals on phenomena during annealing at the high hydrostatic pressure

A. T. Krawczyńska, M. Kerber, P. Suchecki, B. Romelczyk-Baishya, M. Lewandowska, D. Setman

3) EMRs 2019, Warsaw, Poland, 16.09.-19.09.2019

Tytuł wystąpienia: A detailed microstructural analysis of He bubbles and blisters formed in irradiated Mo mirrors

A. T. Krawczyńska, Ł. Ciupiński, P. Petersson, M. Rubel

4) *Yucomat 2018, Herceg Novi, Serbia, 03.09-07.09.2018*

Tytuł wystąpienia: Microstructure characterization of a nanostructured austenitic steel annealed under high hydrostatic pressure

A.T. Krawczyńska, S. Gierlotka, P. Suchecki, D. Setman, B. Adamczyk-Cieslak, M. Gloc, W. Chrominski, M. Lewandowska, M. Zehetbauer

5) Euromat 2017, Saloniki, Greece, 18.09. – 22.09.2017

Tytuł wystąpienia: Recrystallization in nanograined stainless steel 316LVM annealed under high hydrostatic pressure

A.T. Krawczyńska, S. Gierlotka, D. Setman, M. Lewandowska, M. Zehetbauer

6) *International Conference on Structural Integrity 2017, Funchal, Portugal, 04.09. - 07.09.2017*

Tytuł wystąpienia: Improvement of corrosion resistance of AZ-91E magnesium alloy by plasma electrolytic oxidation

A. T. Krawczyńska, M. Spychalski, B. Morończyk, N. Piotrowska, Ł. Nieużyła, M. Wojucki, R. M. Molak

7) *EMRS Spring Meeting 2016, Lille, France, 2016-05-02 - 2016-05-06*

Tytuł wystąpienia: The effect of microstructural features on the formation of nitrided layers in an austenitic stainless steel

A.T. Krawczyńska, R. Sitek, M. Lewandowska, K.J. Kurzydłowski

8) *European Stainless Steel and Duplex Steel Conference 2015, Graz, Austria, 28.04-30.04.2015*

Tytuł wystąpienia: Nitriding a nanostructured austenitic steel - processing, properties and characterisation

A.T. Krawczyńska, R. Sitek, M. Lewandowska, K.J. Kurzydłowski

Przed uzyskaniem stopnia doktora:

9) *33rd Risø International Symposium on Materials Science: Nanometals - Status and perspective 2012, Riso, Denmark, 03.09. - 07.09.2012*

Tytuł wystąpienia: Improving mechanical properties of nanometals by annealing,

A.T. Krawczyńska, T. Brynk, M. Rosiński, A. Michalski, S. Gierlotka, E. Grzanka, S. Stelmakh, B. Pałosz, M. Lewandowska, K.J. Kurzydłowski,

10) *Stainless Steel Conference, Science and Market 2011, Como, Italy, 21.09.- 23.09.2011*

Tytuł wystąpienia: Effects of electropulsing on the annealing behaviour of nanostructured austenitic stainless steel,

A.T.Krawczyńska, M.Rosiński, A.Michalski, Lewandowska, K.J.Kurzydłowski

11) *E-MRS 2011 Fall Meeting 2011, Poland, Warsaw, 19.09.-23.09.2011*

Tytuł wystąpienia: Mechanical properties of nanostructured stainless steel 316LVM annealed under pressure

A.T. Krawczyńska, T. Brynk, S. Gierlotka, E. Grzanka, S.Stelmakh, B. Pałosz, M. Lewandowska, K.J. Kurzydłowski

12) *29th Risø International Symposium on Materials Science 2008, Denmark Riso, 01.09.-05.09.2008*

Tytuł wystąpienia: Microstructure characterization of nanostructured Eurofer 97 steel, **A.T. Krawczyńska**, M. Rasiński, M. Lewandowska, K. J. Kurzydłowski

Wystąpienia w postaci prezentacji posterowych:

Po uzyskaniu stopnia doktora:

1) *20th International Conference of Fusion Reactor Materials, virtual, 24.10.-29.10.2021*

poster: Microstructure study of irradiation resistance of nanostructured Mo mirrors

A. T. Krawczyńska, Ł. Ciupiński, M. Gloc, D. Setman, M. Spychalski, P. Petersson

2) *17th International Conference on Plasma-Facing Materials and Components for Fusion Applications, Holandia, Einhoven, 20.05.-24.05.2019*

poster: Impact of Material Migration and Radiation Damage on the Reflectivity of Molybdenum Mirrors: Laboratory test for DEMO

A. T. Krawczyńska, Ł. Ciupiński, M. Gloc, M. Spychalski, D. Setman, P. Petersson, M. Rubel

3) *XVI International Conference on Electron Microscopy, Polska, Jachranka, 10.09.-13.09.2017*

poster: Microstructure characterization of nanograined stainless steel 316LVM annealed under high hydrostatic pressure

A.T. Krawczyńska, S. Gierlotka, D. Setman, W. Chromiński, M. Lewandowska, M. Zehetbauer

4) *The 16th Electron Microscopy Congress, Lyon, Francja , 28.08-02.09.2016*

poster: The comparison of grain boundaries in a nanostructured austenitic stainless steel annealed conventionally and under high hydrostatic pressure

A.T. Krawczyńska, S. Gierlotka, M. Lewandowska

5) *Euromat 2015, Warszawa, Polska, 20.09-24.09.2015,*

poster: Diversity of microstructures of the austenitic stainless steel produced by hydrostatic extrusion

A.T. Krawczyńska, M. Kulczyk , M. Lewandowska

6) *SCANDEM 2015, Jyvaskyla, Finlandia, 9-11.06.2015,*

poster: STEM analysis of modified LiMnO powder for application in lithium-ion batteries

A. T. Krawczyńska, M. Andrzejczuk, M. Lewandowska, M. Michalska, L. Lipińska, A. Czerwiński

7) *XV International Conference on Electron Microscopy EM2014, Kraków, Polska, 15-18.09. 2014,*

poster: STEM characterization of LiMn2O4 powder modified by metal oxides

A.T. Krawczyńska, M. Andrzejczuk, P. Bazarnik, M. Lewandowska, M. Michalska, L. Lipińska, A. Czerwiński

Przed uzyskaniem stopnia doktora:

8) *E-MRS 2012 Fall Meeting, Warszawa, Polska, 17-21.09.2012,*

poster: Intergranular corrosion resistance of nanostructured austenitic stainless steel,

A.T.Krawczyńska, M. Gloc, K. Lublinska

9) *E-MRS 2011 Spring Meeting Nicea, Francja, 9-13.05.2011,*

poster: The effect of high pressure torsion on structural refinement and mechanical properties of an austenitic stainless steel,

A.T.Krawczyńska, M. Lewandowska, R. Pippan, K.J. Kurzydłowski

10) *E-MRS 2009 Fall Meeting, Warszawa, Polska, 14-18.09.2009,*

poster: Recrystallization and Grain Growth in Nano-structured Austenitic Stainless Steel under Electric Current Heating,

A.T.Krawczyńska, M. Lewandowska, R. Kuziak. K.J. Kurzydłowski

11) *The 10th European Congress of Stereology and Image Analysis, Mediolan, Włochy, 22-26.06.2009,*

poster: Quantitative description of the nano-structures in 316LVM austenitic stainless steel,

A.T.Krawczyńska, M. Lewandowska, K.J. Kurzydłowski

12) *25th Symposium on Fusion Technology (SOFT 2008), Rostock, Dania, 15-19.09.2008*

poster: Thermal stability of nanostructured Eurofer 97 steel,

A.T.Krawczyńska, M. Rasiński, M. Lewandowska, K.J. Kurzydłowski

13) *NanoSPD4, Goslar, Niemcy, 18-22.08.2008,*

poster: Recrystallization in nanostructured austenitic stainless steel,

A.T.Krawczyńska, M. Lewandowska, K.J. Kurzydłowski

14) *Stainless Steel Conference, Science and Market, Helsinki, Finlandia, 10-13.06.2008,*

poster: Fabrication of nanostructured stainless steel via hydrostatic extrusion,

A.T.Krawczyńska, M. Lewandowska, K.J. Kurzydłowski

15) *E-MRS 2007 Fall Meeting, Warszawa, Polska, 17-21.09.2007,*

poster: Nanostructure Formation in Austenitic Stainless Steel,

A.T.Krawczyńska, M. Lewandowska, K.J. Kurzydłowski

16) *Euromat 2007, Norymberga, Niemcy, 10-13.09.2007,*

poster: Microstructure and mechanical properties of Eurofer 97 steel subjected to hydrostatic extrusion,

A.T.Krawczyńska, M. Rasiński, M. Lewandowska, K.J. Kurzydłowski

Wystąpienia posterowe w których miałam współudział:

1) *EMRS Spring Meeting 2023,*

poster: Deposition of superhard WB2 based coatings using HiPIMS

A. T. Krawczyńska, M. Ciemiorek, T. Moscicki, M. Lewandowska

2) *23rd International Conference on Plasma Surface Interactions in Controlled Fusion Devices, Princeton, USA, 17-22.2018*

poster: Impact of low-Z and high-Z ion-induced damage on the reflectivity molybdenum mirrors and sub-surface distribution of gas bubbles

Ł. Ciupiński, **A. T. Krawczyńska**, P. Petersson, M. Rubel

3) *XV International Conference on Electron Microscopy EM2014, Kraków, Polska, 15-18.09. 2014,*

poster: STEM characterization of LiMn2O4 powder modified by metal oxides

M. Andrzejczuk, **A. T. Krawczyńska**, P. Bazarnik, M. Lewandowska, M. Michalska, L. Lipińska, A. Czerwiński,

8. Wykaz udziału w komitetach organizacyjnych i naukowych konferencji krajowych lub międzynarodowych, z podaniem pełnionej funkcji.

8.1 Członek Komitetu Organizacyjnego XVI Konferencji Mikroskopii Elektronowej, Jachranka, wrzesień 2017 rok.

9. Wykaz uczestnictwa w pracach zespołów badawczych realizujących projekty finansowane w drodze konkursów krajowych lub zagranicznych, z podziałem na projekty zrealizowane i będące w toku realizacji, oraz z uwzględnieniem informacji o pełnionej funkcji w ramach prac zespołów.

Lp	Numer projektu	Tytuł projektu	Rola pełniona w projekcie	Nazwa programu i źródło finansowania
realizowane				
1.	UMO-2021/03/Y/ ST5/00253	Kształtowanie nanomateriałów w wyniku wygrzewania pod wysokim ciśnieniem	**Kierownik**	Weave-Unisono NCN
2.	UMO-2021/42/ E/ST5/00118	Kształtowanie mikrostruktury materiałów metalicznych w celu poprawy ich właściwości antybakteryjnych	**Kierownik**	Sonata bis NCN
zrealizowane				
3.	Polonium 2018-2019	Badanie plastyczności tlenku aluminium w różnej skali podczas eksperymentów in situ w mikroskopach elektronowych	**Kierownik**	Polonium, MNiSW
4.	UMO-2014/15/D/ ST8/00532	Rekrystalizacja i rozrost ziaren w silnie odkształconej stali austenitycznej	**Kierownik**	SONATA, NCN
5.	WTZ 2018-2019	Wpływ energii błędu ułożenia nanomateriałów na zjawiska zachodzące podczas wyżarzania pod wysokim ciśnieniem	**Kierownik**	WTZ, MNiSW
realizowane				
6.	TECHMATSTRATEG -III/0017/2019-00	Nowe powłoki zwiększające trwałość narzędzi w procesach kucia i wyciskania	Wykonawca	Techmatstrateg III, NCBiR
7.	EUROFUSION nr.633053	Implementation of activities described in the Roadmap to Fusion during Horizon 2020 through a joint programme of the member of the EUROfusion consortium	Wykonawca	Euratom 2014-20, 2021-2023 fundusze europejskie
zrealizowane				
8.	LIDER/003/ 097/L-5/13/ NCBR/2014	Opracowanie nowych powłok antykorozyjnych dla stopu magnezu AZ-91E stosowanego na elementy silników i przekładni lotniczych	Wykonawca	LIDER, NCBiR
9.	POIR.04.01.01-00-0052/18	Opracowanie technologii nieniszczącego diagnozowania gazociągów w oparciu o magnetyczną metodę bezkontaktową i sensory zintegrowane z wykorzystaniem algorytmów uczenia maszynowego	Wykonawca	INGA, NCBiR
10.	PBS1/A5/27/2012	Nowe polimerowe ogniwa fotowoltaiczne: Badanie wpływu budowy polimeru, architektury ogniwa oraz rodzaju domieszki na sprawność polimerowych ogniw słonecznych opartych na poliazometinach i politiofenach	Wykonawca	PBS 1, NCBiR
11.	PBS1/A1/4/2012	Badania i rozwój nowoczesnych technologii polimerowych baterii litowo-jonowych o podwyższonym bezpieczeństwie eksploatacji	Wykonawca	PBS 1, NCBiR
12.	UMO-2016/23/B/ ST8/02097	Płytki o strukturze ultra drobnoziarnistej, małej anizotropii, zdolności do głębokiego tłoczenia i odkształcenia nadplastycznego	Wykonawca	OPUS, NCN

		przy dużej szybkości odkształcenia		
13.	UMO-2013/11/ BST8/03641	Tworzenie dyfuzyjnych warstw azotowanych na stali austenitycznej o strukturze nanometrycznej	Wykonawca	OPUS, NCN
14.	POIG.01.03.01-00-015/08	NANOMET - Nowe materiały metaliczne o strukturze nanometrycznej do zastosowań w nowoczesnych gałęziach gospodarki	Wykonawca	POIG, NCBiR

Udział w projektach jako kierownik/wykonawca po uzyskaniu stopnia doktora: 1-13
Udział w projektach jako kierownik/wykonawca przed uzyskaniem stopnia doktora: 14

10. Wykaz członkostwa w międzynarodowych lub krajowych organizacjach i towarzystwach naukowych wraz z informacją o pełnionych funkcjach.

10.1. Członek Polskiego Towarzystwa Materiałoznawczego od 2022 roku

11. Wykaz staży w instytucjach naukowych lub artystycznych, w tym zagranicznych, z podaniem miejsca, terminu, czasu trwania stażu i jego charakteru.

11.1. *13.-18.06.2023,* ***Institute of Radiation Physics Helmholtz-Zentrum Dresden – Rossendorf*** *– staż naukowy* w ramach Mobility PW, współpraca z dr O. Liedke, przeprowadzenie badania defektów przy użyciu doppler broadening variable energy positron annihilation spectroscopy (DB-VEPAS) i variable energy positron annihilation lifetime spectroscopy (VEPALS)

11.2. *Cztery tygodniowe staże w ciągu 2018 i 2019 roku w* ***INSA Lyon*** w ramach projektu POLONIUM MNiSW, współpraca z Prof. K. Masenelli-Varlot w obszarze badań plastyczności tlenku aluminium w różnej skali podczas eksperymentów in situ w mikroskopach elektronowych

11.3 *10.02-13.03.2020* ***Uniwersytet Wiedeński, Wydział Fizyki*** *– staż naukowy* w ramach projektu WTZ MNiSW, współpraca z Prof. M. Zehetbauer i dr Darią Setman w dziedzinie nanomateriałów i wyżarzania pod wysokim ciśnieniem hydrostatycznym

11.4. *01.02-31.03.2019* ***Uniwersytet Wiedeński, Wydział Fizyki*** *– staż naukowy* w ramach projektu WTZ MNiSW, współpraca z Prof. M. Zehetbauer i dr Darią Setman w dziedzinie nanomateriałów i wygrzewania pod wysokim ciśnieniem hydrostatycznym

11.5. *18.01-22.01.2016* ***Uniwersytet Wiedeński, Wydział Fizyki*** *– staż naukowy* w ramach projektu Sonata, współpraca z profesorem M. Zehetbauer w dziedzinie nanomateriałów

11.6. *09.-10.2015* ***National Physical Laboratory (Teddington, Anglia)*** *– staż* w ramach programu Skills organizowanego przez Fundację na rzecz Nauki Polskiej w celu podniesienia kwalifikacji związanych z zarządzaniem badaniami naukowymi oraz zarządzaniem zespołami naukowymi

11.7. *12.2012-06.2013* ***Centre d'Elaboration des Matériaux et d'Etudes Structurales (Toulouse, France) – post-dok***, współpraca dr hab. Inż. F. Mompiou w dziedzinie mechanizmów odkształcenia nanokrystalicznego/ultradrobnoziarnistego niklu

11.8. *09.-10.2010* ***Erich Schmid Institute of Materials Science (Leoben, Austria)*** *– staż naukowy* w ramach projektu KMM.VIN, współpraca z profesorem R. Pippanem w dziedzinie nanomateriałów

12. Wykaz członkostwa w komitetach redakcyjnych i radach naukowych czasopism wraz z informacją o pełnionych funkcjach (np. redaktora naczelnego, przewodniczącego rady naukowej, itp.).

Brak

13. Wykaz recenzowanych prac naukowych lub artystycznych, w szczególności publikowanych w czasopismach międzynarodowych.

13.1. Wykaz recenzowanych prac naukowych publikowanych w czasopismach międzynarodowych:

a) Recenzent 1 artykułu w czasopiśmie Journal of Materials Science Springer
b) Recenzent 3 artykułów w czasopiśmie Materials Letters Elsevier
c) Recenzent 2 artykułów w czasopiśmie Advanced Engineering Materials Wiley
d) Recenzent 1 artykułu w czasopiśmie Physica Status Solidi B Wiley
e) Recenzent 1 artykułu w czasopiśmie Journal of Applied Physics AIP Publishing
f) Recenzent 2 artykułów w czasopiśmie Metals MDPI
g) Recenzent 1 artykułu w czasopiśmie Coatings MDPI
h) Recenzent 1 artykułu w czasopiśmie Nanomaterials MDPI

14. Wykaz uczestnictwa w programach europejskich lub innych programach międzynarodowych.

14.1 Uczestnictwo w programie Unii Europejskiej Horyzont 2020 i Horyzont Europa w ramach pracy w projekcie Eurofusion

15. Wykaz udziału w zespołach badawczych, realizujących projekty inne niż określone w pkt. II.9.

15.1 GRANT Rady Naukowej Dyscypliny, Wydział Inżynierii Materiałowej Politechniki Warszawskiej „Kształtowanie nanostruktury stopu aluminium w procesie starzenia pod wysokim ciśnieniem hydrostatycznym" 2022-2023, kierownik
15.2 GRANT IDUB Technologie Materiałowe – 1, Wydział Inżynierii Materiałowej Politechniki Warszawskiej „Stabilność termiczna i mechanizmy odkształcania hybrydowych materiałów nanokrystalicznych wytwarzanych technikami skręcania pod wysokim ciśnieniem (HPT)" 2020-21, wykonawca

16. Wykaz uczestnictwa w zespołach oceniających wnioski o finansowanie badań, wnioski o przyznanie nagród naukowych, wnioski w innych konkursach mających charakter naukowy lub dydaktyczny.

16.1. Wykaz uczestnictwa w zespołach oceniających wnioski o finansowanie badań:
a) Recenzent i członek panelu ekspertów oceniający 2 wnioski projektowe złożonych w ramach Programu Operacyjnego Inteligentny Rozwój 2014-2020 (NCBiR)

b) Recenzent i członek panelu ekspertów oceniający 1 wniosek projektowy złożonych w ramach Programu Bekker (NAWA)

c) Recenzent i członek panelu ekspertów oceniający 1 wniosek projektowy złożonych w ramach konkursu Preludium (NCN)

2) WSPÓŁPRA Z OTOCZENIEM SPOŁECZNYM I GOSPODARCZYM

1. Wykaz dorobku technologicznego.

Brak

2. Współpraca z sektorem gospodarczym.

2.1 Współpraca w ramach pracy w projekcie Techmatsrateg III (NCBiR) z firmami Sanha i Albatros w celu opracowania cienkich powłok nowej generacji o bardzo wysokiej twardości, odporności na ścieranie oraz małej chropowatości. Powłoki te maja za zadanie przyczynić się do istotnej poprawy trwałości matryc stosowanych na szeroką skalę przez firmę Sanha Polska m.in. do kucia na gorąco bezołowiowego stopu miedzi CW 724R. oraz firmie Albratros Aluminium do wyciskania profili aluminiowych.

2.2 Współpraca w ramach pracy w projekcie INGA (NCBiR) z firmą Energodiagnostyka, która zajmuje się badaniami wad w rurociągach metodą bezkontaktowej diagnostyki magnetycznej. W wyniku współpracy udało się opracować technologię nieniszczącego diagnozowania gazociągów w oparciu o magnetyczną metodę bezkontaktową i sensory zintegrowane z wykorzystaniem algorytmów uczenia maszynowego.

3. Wykaz uzyskanych praw własności przemysłowej, w tym uzyskanych patentów krajowych lub międzynarodowych.

3.1 **Patent polski**, nr PL 238391, *Sposób wytwarzania elementów konstrukcyjnych z kompozytów na bazie szkieł metalicznych metodą selektywnego przetapiania*

proszków, współautorzy z jednostki: W. Święszkowski, **A.T. Krawczyńska**, R. Wróblewski, rok uzyskania praw: 2021

3.2 **Patent polski**, nr PL 229820, *Sposób obróbki prętów materiału dla nadania mu plastyczności w niskich temperaturach oraz zastosowanie materiału poddanego obróbce do wytwarzania elementów pracujących w ciekłym azocie*, współautorzy z jednostki: Z. Pakieła, M. Lewandowska, **A.T. Krawczyńska**, rok uzyskania praw: 2018

4. Wykaz wdrożonych technologii.

4.1 **Wdrożenie polskie**: nr PL 233190, *Sposób wytwarzania addytywnego trójwymiarowych obiektów,* współautorzy z jednostki **A. T. Krawczyńska**, W. Święszkowski, K. Kurzydłowski, rok wdrożenia 2018, nazwa podmiotu wdrażającego: 3D-Lab sp. z o.o.

5. Wykaz wykonanych ekspertyz lub innych opracowań wykonanych na zamówienie instytucji publicznych lub przedsiębiorców.

5.1 Udział jako wykonawca w pracach na zlecenie przemysłu:

a) Badania mikrostruktury pianek produkowanych przez firmę KFB w celu zobrazowania wielkości i rozmieszczenia porów w piankach do wygłuszania pomieszczeń

6. Wykaz udziału w zespołach eksperckich lub konkursowych.

6.1 Recenzent i członek panelu ekspertów oceniający 2 wnioski projektowe złożonych w ramach Programu Operacyjnego Inteligentny Rozwój 2014-2020 (NCBiR)

7. Wykaz projektów artystycznych realizowanych ze środowiskami pozaartystycznymi.

Brak

3) DANE NAUKOMETRYCZNE

1. Impact Factor (w dziedzinach i dyscyplinach, w których parametr ten jest powszechnie używany jako wskaźnik naukometryczny).

Sumaryczny Impact Factor: 135,895

2. Liczba cytowań publikacji wnioskodawcy, z oddzielnym uwzględnieniem autocytowań.

- **Web of Science Core Collection** (opcja Researchers i Cited Reference)

	sumarycznie	z wykluczeniem autocytowań
Liczba cytowań	556	487

- **Scopus** (opcja Basic Search i Secondary Documents)

	sumarycznie	z wykluczeniem autocytowań
Liczba cytowań	590	523

3. Indeks Hirscha.

- **Web of Science Core Collection** (opcja Researchers i Cited Reference)

	sumarycznie	z wykluczeniem autocytowań
Indeks Hirscha	14	13

- **Scopus** (opcja Basic Search i Secondary Documents)

	sumarycznie	z wykluczeniem autocytowań
Indeks Hirscha	15	13

Zestawienie tabelaryczne osiągnięć przedstawionych w wykazie

L.P.	L.P.	Kryterium wg Pkt II, III, IV	Tak(liczba)/Brak
II	1.	Wykaz opublikowanych monografii naukowych.	Brak
	2.	Wykaz opublikowanych rozdziałów w monografiach naukowych.	Brak
	3.	Wykaz członkostwa w redakcjach naukowych monografii.	Brak
	4.	Wykaz opublikowanych artykułów w czasopismach naukowych: - publikacje naukowe w czasopismach z bazy JCR, - publikacje naukowe w czasopismach spoza bazy JCR.	Tak 45 9
	5.	Wykaz osiągnięć projektowych, konstrukcyjnych, technologicznych.	Brak
	6.	Wykaz publicznych realizacji dzieł artystycznych.	Brak
	7.	Wykaz wystąpień na krajowych lub międzynarodowych konferencjach naukowych lub artystycznych, z wyszczególnieniem przedstawionych wykładów na zaproszenie i wykładów plenarnych. - poster - referat	Tak 16 12
	8.	Wykaz udziału w komitetach organizacyjnych i naukowych konferencji krajowych lub międzynarodowych, z podaniem pełnionej funkcji.	Tak 1
	9.	Wykaz uczestnictwa w pracach zespołów badawczych realizujących projekty finansowane w drodze konkursów krajowych lub zagranicznych, z podziałem na projekty zrealizowane i będące w toku realizacji, oraz z uwzględnieniem informacji o pełnionej funkcji w ramach prac zespołów.	Tak 14
	10.	Wykaz członkostwa w międzynarodowych lub krajowych organizacjach i towarzystwach naukowych wraz z informacją o pełnionych funkcjach.	Tak 1
	11.	Wykaz staży w instytucjach naukowych lub artystycznych, w tym zagranicznych, z podaniem miejsca, terminu, czasu trwania stażu i jego charakteru.	Tak 8
	12.	Wykaz członkostwa w komitetach redakcyjnych i radach naukowych czasopism wraz z informacją o pełnionych funkcjach (np. redaktora naczelnego, przewodniczącego rady naukowej, itp.).	Brak
	13.	Wykaz recenzowanych prac naukowych lub artystycznych, w szczególności publikowanych w czasopismach międzynarodowych.	Tak 12
	14.	Wykaz uczestnictwa w programach europejskich lub innych programach międzynarodowych.	Tak 1
	15.	Wykaz udziału w zespołach badawczych, realizujących projekty inne niż określone w pkt. II.9.	Tak 2
	16.	Wykaz uczestnictwa w zespołach oceniających wnioski o finansowanie badań, wnioski o przyznanie nagród naukowych, wnioski w innych konkursach mających charakter naukowy lub dydaktyczny.	Tak 4

III	1.	Wykaz dorobku technologicznego.	Brak
	2.	Współpraca z sektorem gospodarczym.	Tak 2
	3.	Wykaz uzyskanych praw własności przemysłowej, w tym uzyskanych patentów krajowych lub międzynarodowych.	Tak 2
	4.	Wykaz wdrożonych technologii	Tak 1
	5.	Wykaz wykonanych ekspertyz lub innych opracowań wykonanych na zamówienie instytucji publicznych lub przedsiębiorców.	Tak 1
	6.	Wykaz udziału w zespołach eksperckich lub konkursowych.	Tak 2
	7.	Wykaz projektów artystycznych realizowanych ze środowiskami pozaartystycznymi.	Brak
IV	1.	Impact Factor (w dziedzinach i dyscyplinach, w których parametr ten jest powszechnie używany jako wskaźnik naukometryczny).	135,895
	2.	Liczba cytowań publikacji wnioskodawcy, z oddzielnym uwzględnieniem autocytowań. - Web of Science bez autocytowań - Scopus bez autocytowań	 556 487 590 523
	3.	Indeks Hirscha. - Web of Science (bez autocytowań) - Scopus (bez autocytowań)	 13 13

A. Kwaczyńska

.....

(podpis wnioskodawcy)

Załącznik 5

Warszawa, 07.08.2023 r.

Biblioteka
Główna

Dotyczy:

informacji o cytowaniach publikacji, których autorem lub współautorem jest **dr inż. Agnieszka Krawczyńska**

- **Web of Science Core Collection** (opcja Researchers i Cited Reference)

	sumarycznie	z wykluczeniem autocytowań
Liczba cytowań	556	487
Indeks Hirscha	14	13
JIF	135,895	

- **Scopus** (opcja Basic Search i Secondary Documents)

	sumarycznie	z wykluczeniem autocytowań
Liczba cytowań	590	523
Indeks Hirscha	15	13

- **Punkty MNiSW**

Punkty MNiSW	3370

KIEROWNIK
Oddziału Informacji Naukowej
i Analiz Bibliometrycznych
Biblioteki Głównej PW
mgr Iwona Socik

Wykonała:
mgr inż. Joanna Gola
Oddział Informacji Naukowej
i Analiz Bibliometrycznych BG PW

Politechnika
Warszawska

Plac Politechniki 1
00-661 Warszawa
www.bg.pw.edu.pl

Załącznik 6

Statement

Publication title, journal, year, doi:

Impact of high pressure torsion processing on helium ion irradiation resistance of molybdenum, Mater. Charact. 191 (2022). https://doi.org/10.1016/j.matchar.2022.112151.

Imiona i nazwiska autorów publikacji:

***Agnieszka Teresa Krawczyńska**, Łukasz Ciupiński, Michał Gloc, Daria Setman, Maciej Spychalski, Bogusława Adamczyk-Cieślak, Przemysław Suchecki, Maciej Oskar Liedke, Maik Butterling, Andreas ~~Wanger~~ Wagner, Eric Hirschmann, Per Petersson*

Statement on the substantive contribution of the work to the above-mentioned publication and consent to submit it for habilitation

Lp.	Autor	Contribution	Signature
1	***Agnieszka Teresa Krawczynska***	In this article I was responsible for: - conceptualization of all performed research, - methodology selection, - performing HPT experiments, - performing microhardness experiments and analysing results, - analysing nanohardness, dislocation density, positron annihilation spectroscopy and reflectivity results in the context of the research subject, - performing all microstructure observations using scanning, transmission electron microscopes and a focused ion beam, analysis of obtained microstructures, - writing the original draft of the paper, reviewing and editing.	A. Krawczyńska
Co-authors' contribution:			
2	*Łukasz Ciupiński*	Analysing reflectivity measurements, results discussion and editing the final version of the article	Ł. Ciupiński
3	*Michał Gloc*	Preparing samples for scanning electron microscopy observations	M. Gloc
4	*Daria Setman*	Conceptualization of HPT experiments	
5	*Maciej Spychalski*	Performing nanohardness measurements and calculation of nanohardness values	
6	*Przemysław Suchecki*	Preparing samples for positron annihilation spectroscopy experiments	Suchecki
7	*Bogusława Adamczyk-Cieślak*	Performing X-ray diffraction experiments and calculating gathered data	

Statement

Publication title, journal, year, doi:

Impact of high pressure torsion processing on helium ion irradiation resistance of molybdenum, Mater. Charact. 191 (2022). https://doi.org/10.1016/j.matchar.2022.112151.

Imiona i nazwiska autorów publikacji:

Agnieszka Teresa Krawczyńska, Łukasz Ciupiński, Michal Gloc, Daria Setman, Maciej Spychalski, Bogusława Adamczyk-Cieślak, Przemysław Suchecki, Maciej Oskar Liedke, Maik Butterling, Andreas ~~Wanger~~ Wagner, Eric Hirschmann, Per Petersson

Statement on the substantive contribution of the work to the above-mentioned publication and consent to submit it for habilitation

Lp.	Autor	Contribution	Signature
1	***Agnieszka Teresa Krawczynska***	In this article I was responsible for: - conceptualization of all performed research, - methodology selection, - performing HPT experiments, - performing microhardness experiments and analysing results, - analysing nanohardness, dislocation density, positron annihilation spectroscopy and reflectivity results in the context of the research subject, - performing all microstructure observations using scanning, transmission electron microscopes and a focused ion beam, analysis of obtained microstructures, - writing the original draft of the paper, reviewing and editing.	A Krawczyńska
Co-authors' contribution:			
2	*Łukasz Ciupiński*	Analysing reflectivity measurements, results discussion and editing the final version of the article	Ł. Ciupiński
3	*Michal Gloc*	Preparing samples for scanning electron microscopy observations	M. Gloc
4	*Daria Setman*	Conceptualization of HPT experiments	
5	*Maciej Spychalski*	Performing nanohardness measurements and calculation of nanohardness values	
6	*Przemysław Suchecki*	Preparing samples for positron annihilation spectroscopy experiments	
7	*Bogusława Adamczyk-Cieślak*	Performing X-ray diffraction experiments and calculating gathered data	

8	*Maciej Oskar Liedke*	Performing positron annihilation spectroscopy experiments and analysing obtained results	
9	*Maik Butterling*	Performing positron annihilation spectroscopy experiments and analysing obtained results	
10	*Andreas ~~Wanger~~ Wagner*	Performing positron annihilation spectroscopy experiments and analysing obtained results	
11	*Eric Hirschmann*	Performing positron annihilation spectroscopy experiments and analysing obtained results	
12	*Per Petersson*	Preparing mirrors surface for irradiation experiments, irradiating mirrors with helium ions and reflectivity measurements and analysis	

Statement

Publication title, journal, year, doi:

Microstructural characterization and residual stress distribution in a nanostructured austenitic stainless steel, Int. J. Mater. Res. (2018). https://doi.org/10.3139/146.111672.

Names and surnames of publication authors:

Agnieszka Teresa Krawczynska, Małgorzata Lewandowska, Anthony Thomas Fry

Statement on the substantive contribution of the work to the above-mentioned publication and consent to submit it for habilitation

No.	Author	Contribution	Signature
1	***Agnieszka Teresa Krawczynska***	In this article I was responsible for: - conceptualization of all performed research, - methodology selection, - performing microhardness measurements and analysing results, - performing residual stress measurements and analysing residual stress results in the context of the research subject, - performing all microstructure observations using transmission electron microscopes, analysing obtained microstructures, - writing the original draft of the paper (including the discussion part), reviewing and editing.	A. Krawczyńska
Co-authors' contribution:			
2	*Małgorzata Lewandowska*	Editing the final version of the article	
3	*Antony Thomas Fry*	Verifying residual stress measurements results and analysis, editing the final version of the article	

Oświadczenie

Tytuł publikacji, czasopismo, rok wydania, strony:

Mechanical properties and corrosion resistance of ultrafine grained austenitic stainless steel processed by hydrostatic extrusion, Mater. Des. 136 (2017). https://doi.org/10.1016/j.matdes.2017.09.050.

Imiona i nazwiska autorów publikacji:

***Agnieszka Teresa Krawczyńska**, Witold Chromiński, Ewa Ura-Bińczyk, Mariusz Kulczyk, Małgorzata Lewandowska*

Oświadczenie o merytorycznym wkładzie pracy w wyżej wymienioną publikację i wyrażenie zgody na przedstawienie do habilitacji

Lp.	Autor	Zakres wkładu w pracę	Podpis
1	***Agnieszka Teresa Krawczyńska***	W tym artykule byłam odpowiedzialna za: - opracowanie całościowej koncepcji artykułu, - opracowanie metodyki badań mikrostruktury i właściwości mechanicznych, - wykonanie obserwacji mikrostruktury przy użyciu transmisyjnej mikroskopii elektronowej oraz analiza uzyskanych mikrostruktur, - analizę wyników badań wytrzymałościowych, - dyskusję wyników bez części dotyczącej korozji, - zredagowanie i przygotowanie publikacji.	A. Krawczyńska
Wkład pozostałych współautorów:			
2	*Witold Chromiński*	Wykonanie badań EBSD wraz z ich analizą, zredagowanie części artykułu poświęconej analizie EBSD	
3	*Ewa Ura-Bińczyk*	Opracowanie metodyki badań korozyjnych, wykonanie badań odporności korozyjnej i analizy wyników oraz części dyskusji dotyczącej odporności na korozję stali austenitycznych	
4	*Mariusz Kulczyk*	Opracowanie parametrów wyciskania hydrostatycznego i wytworzenie materiału do badań	
5	*Małgorzata Lewandowska*	Nadzór nad realizacją badań, kierowanie projektem, w ramach którego powstała praca, współudział w dyskusji wyników i współredagowanie manuskryptu	

Oświadczenie

Tytuł publikacji, czasopismo, rok wydania, strony:

Formation of the Nitrided Layers on an Austenitic Stainless Steel with Different Grain Structures, Adv. Eng. Mater. (2018). https://doi.org/10.1002/adem.201701049.

Imiona i nazwiska autorów publikacji:

***Agnieszka Teresa Krawczyńska**, Joanna Zdunek, Ryszard Sitek, Małgorzata Lewandowska,*

Oświadczenie o merytorycznym wkładzie pracy w wyżej wymienioną publikację i wyrażenie zgody na przedstawienie do habilitacji

Lp.	Autor	Zakres wkładu w pracę	Podpis
1	***Agnieszka Teresa Krawczyńska***	W tym artykule byłam odpowiedzialna za: - opracowanie całościowej koncepcji artykułu, - opracowanie metodyki badań, - wykonanie obserwacji mikrostruktury przy użyciu transmisyjnej i skaningowej mikroskopii elektronowej oraz mikroskopii jonowej, analizę uzyskanych mikrostruktur, - analizę wyników badań składu fazowego i składu chemicznego warstw w kontekście tematu badań, - zredagowanie i przygotowanie publikacji (włączając dyskusję wyników).	A. Krawczyńska
Wkład pozostałych współautorów:			
2	*Joanna Zdunek*	Przeprowadzenie badań składu fazowego oraz analiza uzyskanych wyników	
4	*Ryszard Sitek*	Przygotowanie zgładów metalograficznych i wykonanie ich obserwacji przy użyciu mikroskopu świetlnego, opracowanie parametrów niskotemperaturowego azotowania jarzeniowego	R. Sitek
5	*Małgorzata Lewandowska*	Nadzór nad realizacją badań, kierowanie projektem, w ramach którego powstała praca, współudział w dyskusji wyników i współredagowanie manuskryptu	

Statement

Publication title, journal, year, doi:

The impact of high hydrostatic pressure maintenance after high-pressure torsion on phenomena during high hydrostatic pressure annealing, Mater. Sci. Eng. A. 840 (2022) 142874. https://doi.org/10.1016/j.msea.2022.142874.

First and second names of co-authors:

***Agnieszka Teresa Krawczyńska**, Michael Kerber, Przemysław Suchecki, Barbara Romelczyk-Baishya, Maciej Oskar, Maik Butterling, Eric Hirschmann, Andreas Wagner, Małgorzata Lewandowska, Daria Setman*

Statement on the substantive contribution of the work to the above-mentioned publication and consent to submit it for habilitation

Lp.	Autor	Contribution	Signature
1	***Agnieszka Teresa Krawczyńska***	In this article I was responsible for: - conceptualization of all performed research, - methodology selection, - assisting in redevelopment of the HPT device into the HPT and HPA device, - performing HPT and HPA experiments, - performing microhardess measurements and analysis of results, - analysing tensile tests results in the context of the research subject, - analysing variable energy positron annihilation lifetime spectroscopy results in the context of the research subject, - performing all microstructure observations using scanning, transmission electron microscopes and a focused ion beam, analysis of obtained microstructures, - writing the original draft of the paper, reviewing and editing.	A. Krawczyńska
Co-authors' contribution:			
2	*Michael Kerber*	Redeveloping the HPT device into the HPT and HPA device	
3	*Przemysław Suchecki*	Preparing samples for scanning electron microscopy observations and positron annihilation spectroscopy experiments	Suchecki
4	*Barbara Romelczyk-Baishya*	Performing tensile tests and calculating obtained parameters	Romelczyk
5	*Maciej Oskar Liedke*	Performing the variable energy positron annihilation lifetime spectroscopy experiment and analysing obtained results	

6	*Maik Butterling*	Performing the variable energy positron annihilation lifetime spectroscopy experiment and analysing obtained results	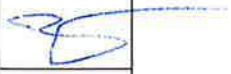
7	*Eric Hirschmann*	Performing the variable energy positron annihilation lifetime spectroscopy experiment and analysing obtained results	
8	*Andreas Wagner*	Performing the variable energy positron annihilation lifetime spectroscopy experiment and analysing obtained results	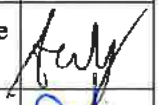
9	*Małgorzata Lewandowska*	Editing the final version of the article	
10	*Daria Setman*	Conceptualization of HPA experiments	

Statement

Publication title, journal, year, doi:

The impact of high hydrostatic pressure maintenance after high-pressure torsion on phenomena during high hydrostatic pressure annealing. Mater. Sci. Eng. A. 840 (2022) 142874. https://doi.org/10.1016/j.msea.2022.142874.

First and second names of co-authors:

***Agnieszka Teresa Krawczyńska**, Michael Kerber, Przemysław Suchecki, Barbara Romelczyk-Baishya, Maciej Oskar, Maik Butterling, Eric Hirschmann, Andreas Wagner, Małgorzata Lewandowska, Daria Setman*

Statement on the substantive contribution of the work to the above-mentioned publication and consent to submit it for habilitation

Lp.	Autor	Contribution	Signature
1	***Agnieszka Teresa Krawczyńska***	In this article I was responsible for: - conceptualization of all performed research, - methodology selection, - assisting in redevelopment of the HPT device into the HPT and HPA device, - performing HPT and HPA experiments, - performing microhardess measurements and analysis of results, - analysing tensile tests results in the context of the research subject, - analysing variable energy positron annihilation lifetime spectroscopy results in the context of the research subject, - performing all microstructure observations using scanning, transmission electron microscopes and a focused ion beam, analysis of obtained microstructures, - writing the original draft of the paper, reviewing and editing.	
Co-authors' contribution:			
2	*Michael Kerber*	Redeveloping the HPT device into the HPT and HPA device	
3	*Przemysław Suchecki*	Preparing samples for scanning electron microscopy observations and positron annihilation spectroscopy experiments	
4	*Barbara Romelczyk-Baishya*	Performing tensile tests and calculating obtained parameters	
5	*Maciej Oskar Liedke*	Performing the variable energy positron annihilation lifetime spectroscopy experiment and analysing obtained results	

6	*Maik Butterling*	Performing the variable energy positron annihilation lifetime spectroscopy experiment and analysing obtained results	
7	*Eric Hirschmann*	Performing the variable energy positron annihilation lifetime spectroscopy experiment and analysing obtained results	
8	*Andreas Wagner*	Performing the variable energy positron annihilation lifetime spectroscopy experiment and analysing obtained results	
9	*Malgorzata Lewandowska*	Editing the final version of the article	
10	*Daria Setman*	Conceptualization of HPA experiments	Setman

Statement

Publication title, journal, year, doi:

Recrystallization and grain growth of a nano/ultrafine structured austenitic stainless steel during annealing under high hydrostatic pressure, J. Mater. Sci. (2018). https://doi.org/10.1007/s10853-018-2459-1.

Names and surnames of publication authors:

***Agnieszka Teresa Krawczyńska**, Stanisław Gierlotka, Przemysław Suchecki, Daria Setman, Bogusława Adamczyk-Cieślak, Małgorzata Lewandowska, Michael Zehetbauer*

Statement on the substantive contribution of the work to the above-mentioned publication and consent to submit it for habilitation

No.	Author	Contribution	Signature
1	***Agnieszka Teresa Krawczyńska***	In this article I was responsible for: - conceptualization of all performed research, - methodology selection, - performing HPT experiments, - performing microhardness experiments and analysing results, - analysing X-ray diffraction results in the context of the research subject, - performing all microstructure observations using scanning and transmission electron microscopes, analysing obtained microstructures, - writing the original draft of the paper (including the discussion part), reviewing and editing. I was the leader of the project SONATA under which the research was carried out.	A. Krawczyńska
Co-authors' contribution:			
2	*Stanisław Gierlotka*	Performing HPA experiments	Gierlotka
3	*Przemysław Suchecki*	Preparing samples for scanning electron microscopy observations	Suchecki
4	*Daria Setman*	Conceptualization of HPT experiments	
5	*Bogusława Adamczyk-Cieślak*	Performing X-ray diffraction experiments and calculating gathered data	
6	*Małgorzata Lewandowska*	Editing the final version of the article	
7	*Michael Zehetbauer*	Editing the final version of the article	

Statement

Publication title, journal, year, doi:

Recrystallization and grain growth of a nano/ultrafine structured austenitic stainless steel during annealing under high hydrostatic pressure, J. Mater. Sci. (2018). https://doi.org/10.1007/s10853-018-2459-1.

Names and surnames of publication authors:

***Agnieszka Teresa Krawczynska**, Stanisław Gierlotka, Przemysław Suchecki, Daria Setman, Bogusława Adamczyk-Cieślak, Małgorzata Lewandowska, Michael Zehetbauer*

Statement on the substantive contribution of the work to the above-mentioned publication and consent to submit it for habilitation

No.	Author	Contribution	Signature
1	***Agnieszka Teresa Krawczynska***	In this article I was responsible for: - conceptualization of all performed research, - methodology selection, - performing HPT experiments, - performing microhardness experiments and analysing results, - analysing X-ray diffraction results in the context of the research subject, - performing all microstructure observations using scanning and transmission electron microscopes, analysing obtained microstructures, - writing the original draft of the paper (including the discussion part), reviewing and editing. I was the leader of the project SONATA under which the research was carried out.	
Co-authors' contribution:			
2	*Stanisław Gierlotka*	Performing HPA experiments	
3	*Przemysław Suchecki*	Preparing samples for scanning electron microscopy observations	
4	*Daria Setman*	Conceptualization of HPT experiments	
5	*Bogusława Adamczyk-Cieślak*	Performing X-ray diffraction experiments and calculating gathered data	
6	*Małgorzata Lewandowska*	Editing the final version of the article	

Statement

Publication title, journal, year, doi:

Recrystallization and grain growth of a nano/ultrafine structured austenitic stainless steel during annealing under high hydrostatic pressure, J. Mater. Sci. (2018). https://doi.org/10.1007/s10853-018-2459-1.

Names and surnames of publication authors:

***Agnieszka Teresa Krawczynska**, Stanisław Gierlotka, Przemysław Suchecki, Daria Setman, Bogusława Adamczyk-Cieślak, Małgorzata Lewandowska, Michael Zehetbauer*

Statement on the substantive contribution of the work to the above-mentioned publication and consent to submit it for habilitation

No.	Author	Contribution	Signature
1	***Agnieszka Teresa Krawczynska***	In this article I was responsible for: - conceptualization of all performed research, - methodology selection, - performing HPT experiments, - performing microhardness experiments and analysing results, - analysing X-ray diffraction results in the context of the research subject, - performing all microstructure observations using scanning and transmission electron microscopes, analysing obtained microstructures, - writing the original draft of the paper (including the discussion part), reviewing and editing. I was the leader of the project SONATA under which the research was carried out.	
Co-authors' contribution:			
2	*Stanisław Gierlotka*	Performing HPA experiments	
3	*Przemysław Suchecki*	Preparing samples for scanning electron microscopy observations	
4	*Daria Setman*	Conceptualization of HPT experiments	
5	*Bogusława Adamczyk-Cieślak*	Performing X-ray diffraction experiments and calculating gathered data	
6	*Małgorzata Lewandowska*	Editing the final version of the article	
7	*Michael Zehetbauer*	Editing the final version of the article	

Statement

Publication title, journal, year, doi:

Phenomena Occurring in Nanostructured Stainless Steel 316LVM during Annealing under High Hydrostatic Pressure, Adv. Eng. Mater. (2018). https://doi.org/10.1002/adem.201800101.

Names and surnames of publication authors:

Agnieszka Teresa Krawczyńska, *Stanisław Gierlotka, Przemysław Suchecki, Daria Setman, Bogusława Adamczyk-Cieślak, Michał Gloc, Witold Chromiński, Małgorzata Lewandowska, Michael Zehetbauer*

Statement on the substantive contribution of the work to the above-mentioned publication and consent to submit it for habilitation

No.	Author	Contribution	Signature
1	***Agnieszka Teresa Krawczyńska***	In this article I was responsible for: - conceptualization of all performed research, - methodology selection, - performing HPT experiments, - analysing X-ray diffraction results and corrosion results in the context of the research subject, - performing all microstructure observations and chemical analysis of precipitates using scanning and transmission electron microscopes, analysing obtained microstructures and EDS results, - writing the original draft of the paper (including the discussion part), reviewing and editing. I was the leader of the project SONATA under which the research was carried out.	A. Krawczyńska
Co-authors' contribution:			
2	*Stanisław Gierlotka*	Performing HPA experiments	Gierlotka
3	*Przemysław Suchecki*	Preparing samples for scanning electron microscopy observations	Suchecki
4	*Daria Setman*	Conceptualization of HPT experiments	
5	*Bogusława Adamczyk-Cieślak*	Performing X-ray diffraction experiments and analysis of the results	Adamczyk-Cieślak
6	*Michał Gloc*	Performing corrosion experiments	M. Gloc
7	*Witold Chromiński*	Performing EBSD research and results analysis, editing the part of the article devoted to EBSD analysis	

Statement

Publication title, journal, year, doi:

Phenomena Occurring in Nanostructured Stainless Steel 316LVM during Annealing under High Hydrostatic Pressure, Adv. Eng. Mater. (2018). https://doi.org/10.1002/adem.201800101.

Names and surnames of publication authors:

***Agnieszka Teresa Krawczynska**, Stanisław Gierlotka, Przemysław Suchecki, Daria Setman, Bogusława Adamczyk-Cieślak, Michał Gloc, Witold Chromiński, Małgorzata Lewandowska, Michael Zehetbauer*

Statement on the substantive contribution of the work to the above-mentioned publication and consent to submit it for habilitation

No.	Author	Contribution	Signature
1	***Agnieszka Teresa Krawczynska***	In this article I was responsible for: - conceptualization of all performed research, - methodology selection, - performing HPT experiments, - analysing X-ray diffraction results and corrosion results in the context of the research subject, - performing all microstructure observations and chemical analysis of precipitates using scanning and transmission electron microscopes, analysing obtained microstructures and EDS results, - writing the original draft of the paper (including the discussion part), reviewing and editing. I was the leader of the project SONATA under which the research was carried out.	
Co-authors' contribution:			
2	*Stanisław Gierlotka*	Performing HPA experiments	
3	*Przemysław Suchecki*	Preparing samples for scanning electron microscopy observations	
4	*Daria Setman*	Conceptualization of HPT experiments	Setman
5	*Bogusława Adamczyk-Cieślak*	Performing X-ray diffraction experiments and analysis of the results	
6	*Michał Gloc*	Performing corrosion experiments	
7	*Witold Chromiński*	Performing EBSD research and results analysis, editing the part of the article devoted to EBSD analysis	

8	*Małgorzata Lewandowska*	**Editing the final version of the article**	
9	*Michael Zehetbauer*	**Editing the final version of the article**	

8	*Małgorzata Lewandowska*	Editing the final version of the article	
9	*Michael Zehetbauer*	Editing the final version of the article	

Oświadczenie

Tytuł publikacji, czasopismo, rok wydania, doi:

Influence of high hydrostatic pressure annealing on the recrystallization of nanostructured austenitic stainless steel, Mater. Sci. Eng. A. (2019). https://doi.org/10.1016/j.msea.2019.138381.

Imiona i nazwiska autorów publikacji:

Agnieszka Teresa Krawczyńska, *Przemysław Suchecki, Bogusława Adamczyk-Cieślak, Barbara Romelczyk-Baishya, Małgorzata Lewandowska*

Oświadczenie o merytorycznym wkładzie pracy w wyżej wymienioną publikację i wyrażenie zgody na przedstawienie do habilitacji

Lp.	Autor	Zakres wkładu w pracę	Podpis
1	***Agnieszka Teresa Krawczyńska***	W tej pracy odpowiedzialna byłam za: - opracowanie całościowej koncepcji artykułu, - opracowanie metodyki badań, - wykonanie badań mikrotwardości wraz z analizą wyników, - analizę wyników tekstury oraz parametrów wytrzymałościowych w kontekście tematu badań, - przeprowadzenie obserwacji mikrostruktury przy użyciu elektronowej mikroskopii skaningowej i transmisyjnej oraz analizę uzyskanych mikrostruktur, - przygotowanie i zredagowanie publikacji (włączając dyskusję wyników). Byłam Kierownikiem projektu SONATA w ramach którego zostały zrealizowane badania.	A. Krawczyńska
Wkład pozostałych współautorów:			
2	*Przemysław Suchecki*	Przygotowanie próbek do obserwacji przy użyciu skaningowej mikroskopii elektronowej	
3	*Bogusława Adamczyk-Cieślak*	Przeprowadzenie badania i analizy tekstury próbek wraz z opracowaniem metodyki badań dotyczącej badania tekstury	
4	*Barbara Romelczyk-Baishya*	Wykonanie badań wytrzymałościowych oraz wyznaczenie odpowiednich parametrów	
5	*Małgorzata Lewandowska*	Edycja ostatecznej wersji artykułu	

Statement

Publication title, journal, year, doi:

The impact of the stacking fault energy of nanostructured metals on phenomena during annealing at the high hydrostatic pressure, Mater. Sci. Eng. A. 808 (2021) 140913. https://doi.org/10.1016/j.msea.2021.140913

Names and surnames of publication authors:

***Agnieszka Teresa Krawczynska**, Michael Kerber, Przemysław Suchecki, Barbara Romelczyk-Baishya, Małgorzata Lewandowska, Daria Setman,*

Statement on the substantive contribution of the work to the above-mentioned publication and consent to submit it for habilitation

No.	Author	Contribution	Signature
1	***Agnieszka Teresa Krawczynska***	In this article I was responsible for: - conceptualization of all performed research, - methodology selection, - assisting in redevelopment of the HPT device into the HPT and HPA device, - performing HPT and HPA experiments, - analysing tensile tests results and DSC results in the context of the research subject, - performing all microstructure observations using scanning, transmission electron microscopes as well as focused ion beam and analysing obtained microstructures, - writing the original draft of the paper (including the discussion part), reviewing and editing. I was the leader on the Polish Side of the project WTZ within which the research was carried out.	A. Krawczyńska
Co-authors' contribution:			
2	*Michael Kerber*	Redeveloping the HPT device into the HPT and HPA device	
3	*Przemysław Suchecki*	Preparing samples for scanning electron microscopy observations	Suchi
4	*Barbara Romelczyk-Baishya*	Performing tensile tests and calculating obtained parameters	Romelczyk
5	*Małgorzata Lewandowska*	Editing the final version of the article	
6	*Daria Setman*	Conceptualization of HPT and HPA experiments, performing DSC measurements	

Statement

Publication title, journal, year, doi:

The impact of the stacking fault energy of nanostructured metals on phenomena during annealing at the high hydrostatic pressure, Mater. Sci. Eng. A. 808 (2021) 140913. https://doi.org/10.1016/j.msea.2021.140913

Names and surnames of publication authors:

***Agnieszka Teresa Krawczynska**, Michael Kerber, Przemysław Suchecki, Barbara Romelczyk-Baishya, Małgorzata Lewandowska, Daria Setman,*

Statement on the substantive contribution of the work to the above-mentioned publication and consent to submit it for habilitation

No.	Author	Contribution	Signature
1	***Agnieszka Teresa Krawczynska***	In this article I was responsible for: - conceptualization of all performed research, - methodology selection, - assisting in redevelopment of the HPT device into the HPT and HPA device, - performing HPT and HPA experiments, - analysing tensile tests results and DSC results in the context of the research subject, - performing all microstructure observations using scanning and transmission electron microscopes as well as a focused ion beam and analysing obtained microstructures, - writing the original draft of the paper (including the discussion part), reviewing and editing. I was the leader on the Polish Side of the WTZ project within which the research was carried out.	
Co-authors' contribution:			
2	*Michael Kerber*	Redeveloping the HPT device into the HPT and HPA device	Kerber
3	*Przemysław Suchecki*	Preparing samples for scanning electron microscopy observations	
4	*Barbara Romelczyk-Baishya*	Performing tensile tests and calculating obtained parameters	
5	*Małgorzata Lewandowska*	Editing the final version of the article	
6	*Daria Setman*	Conceptualization of HPT and HPA experiments, performing DSC measurements	Setman

Załącznik 7

Materials Characterization 191 (2022) 112151

Contents lists available at ScienceDirect

Materials Characterization

journal homepage: www.elsevier.com/locate/matchar

Impact of high pressure torsion processing on helium ion irradiation resistance of molybdenum

A.T. Krawczyńska [a,*], Ł. Ciupiński [a], M. Gloc [a], D. Setman [b], M. Spychalski [a], P. Suchecki [a], B. Adamczyk-Cieślak [a], M.O. Liedke [c], M. Butterling [c], A. Wanger [c], E. Hirschmann [c], P. Petersson [d]

[a] Faculty of Materials Science and Engineering, Warsaw University of Technology, 02-507 Warsaw, Poland
[b] Faculty of Physics, University of Vienna Boltzmanngasse 5,1090 Vienna, Austria
[c] Institute of Radiation Physics, Helmholtz-Zentrum Dresden-Rossendorf, Bautzner Landstraße 400, 01328 Dresden, Germany
[d] Department of Fusion Plasma Physics, KTH Royal Institute of Technology, 100 44 Stockholm, Sweden

ARTICLE INFO

Keywords:
Nanomaterials
Ion irradiation
electron microscopy
Vacancy
Severe plastic deformation

ABSTRACT

The microstructure of Mo was significantly refined by high pressure torsion to verify its irradiation tolerance in comparison with its micrograined counterpart. After deformation microhardness increased from 231 Hv0.2 for a microgarined sample to 542 and 558 Hv0.2, respectively after one and five rotations. Concurrently, the grain refinement was observed, as the grain size decreased with the increase of the deformation degree down to 480 and 110 nm, respectively for one and five rotations. Subsequently, deformed Mo and a micrograined one were irradiated by He ions to the dose of 8×10^{16}/cm ^{2} to verify their potential application as fusion mirrors. Irradiations were followed by reflectivity measurements in the 300–2400 nm range with a dual beam spectrometer. The measurements revealed that the applied dose causes a decrease in total reflectivity of the micrograined sample, whereas the total reflectivity of deformed samples decreases by additional 2.5%. Nanohardness measurements, detailed microscopy observations using focused ion beam and scanning transmission electron microscope as well as positron annihilation spectroscopy investigations were performed to elucidate changes in the microstructure and understand the different mechanisms of bubble creation after irradiation in micrograined and high pressure torsion processed samples.

1. Introduction

In this paper, the radiation tolerance of bulk nanostructured Mo is verified before its potential application in fusion reactors.

(i) Firstly and most importantly, nanostructured Mo is proposed since grain refinement appear to be an efficient way to improve radiation resistance [1–3]. Irradiation by energetic particles firstly leads to atomic displacement defects followed by recombination of defects up to the formation of clusters, bubbles and voids. In the final phase macroscopic defects such as cracks, surface blistering and fuzz are observed also depending on irradiation conditions. Although various approaches have been proposed for reducing materials degradation due to irradiation such as metallic glass or high-entropy alloys production, nanostructurization shows the greatest potential. It is owed to presence of high density of grain boundaries in nanostructured materials. It has been proven that grain boundaries are sinks for the irradiation-induced defects and emit interstitials which can recombine with irradiation produced vacancies in grain interiors, which brings about the self-healing capacity of nanostructured materials [4]. Moreover, grain boundaries can trap He atoms [5] and their structure has an impact on the efficiency of He atoms accumulation [6]. Preferable are grain boundaries which contain grain boundary dislocations as well as high-energy grain boundaries of large He-to-vacancy ratio [7]. In this context interesting is the efficiency of He ion trapping in non-equilibrium grain boundaries created by severe plastic deformation (SPD) processes [8–13]. SPD methods produce bulk samples with nanostructured grains throughout the entire volume, resulting in

* Corresponding author.
E-mail address: agnieszka.krawczynska@pw.edu.pl (A.T. Krawczyńska).

https://doi.org/10.1016/j.matchar.2022.112151
Received 24 March 2022; Received in revised form 5 July 2022; Accepted 20 July 2022
Available online 23 July 2022

properties different to their coarse grained counterparts most notably superior mechanical properties such as exceptionally high strength with significant plasticity. Exceptionally high strength can be achieved since increased hydrostatic pressure during deformation suppresses fracture and influences the movement and interaction of the lattice defects which results in the creation of nanograins of high-angle grain boundaries with non-equilibrium structures. Non-equilibrium grain boundaries possess high density of dislocations and large residual microstrain, factors facilitating diffusion [14].Concerning nanostructured materials for fusion application, most of the research concentrates on tungsten as tungsten is considered as the best candidate for a plasma facing component (PFC) material. The studies have shown that there exists a critical grain size (60 nm) below which, in tungsten produced by orthogonal machining process, lower He bubble density has been detected [15]. Reducing grain size is also essential in the latest stage of irradiation when macroscopically observable damage is registered. Nanostructured tungsten produced by high pressure torsion (HPT) showed up to the He dose of $1.0x10^{23}m^{-2}$ no blisters contrary to coarse grained tungsten [16]. The scarce work on nanostructured ferritic steels reduced activation that are planned to be applied for the first wall in fusion reactors indicate that nanostructured steels produced by surface mechanical attrition treatment (SMAT) and irradiated by He ions are characterized by lower bubble density and smaller average bubble size in comparison with coarse grained counterparts [17]. Little is known about the radiation resistance of bulk nanostructured Mo apart from the work on magnetron sputtered nanocrystalline Mo of a columnar structure [18]. In that work it has been evidenced that in He irradiated grains smaller than 90 nm finer dislocation loops and He bubbles are created as well as lower defect density is observed.

(ii) Secondly, nanostructured molybdenum is proposed considering its potential application for diagnostic mirrors. Diagnostic mirrors guide plasma radiation to variety of control and diagnostic systems. Apart from the fact that their surface may degrade from sputtering by plasma particles, their reflectivity will be decreased by deposition of plasma impurities [19–24]. Actually, the main candidate is single crystal Mo [24]. However, nanostructured materials prove promising reflectivity after cleaning [25]. Deposition of plasma contaminants on mirrors is hard to avoid during reactor operation, thus in-service mirror cleaning seems indispensable. Therefore, the major sputtering will be produced by the in-situ cleaning. Hence, mirrors should not lose their reflectivity due to cleaning [25,26]. When the 10-cycle cleaning was performed with 60 MHz radiofrequency-simulated argon plasma capacitively coupled (CCRF) to the Mo coated mirrors, significant increase of roughness of up to 70% was detected for micrograined whereas nanocrystalline coatings stayed unchanged [25]. A microcrystalline variant in comparison with nanocrystalline while cleaned with H_2 and Ar at high energy exhibited doubled increase in diffuse reflectivity. These facts suggest that nanocrystalline Mo coatings should preserve better properties after cleaning than micrograined ones. However, the cleaning of coatings can lead to their sputtering by some 20 nm per a cleaning cycle with several hundreds of cycles envisaged for a mirror lifetime. For this reason, in the present study an SPD technique as HPT is proposed as an efficient technique to obtain nanostructured bulk Mo mirrors. HPT technique has been selected since it is the most efficient technique in grain refinement in comparison with other SPD techniques [27–29]. As recent publications showed, HPT can be successfully applied to refine the microstructure of Mo [30,31]. Relatively few reports are available on the HPT-processed Mo since this body-centered cubic metal has very high strength, which makes SPD-processing difficult at ambient temperature.

The objective of our work is to compare the radiation tolerance of bulk nanostructured Mo with micrograined Mo. There is scarce information about nanostructured mirrors in the literature especially about the investigation by microcopy techniques of the impact of the grain size on the radiation tolerance. It is well-known that single crystal mirrors are the best option. However, in order to verify the impact of grain refinement by microscopy studies on radiation tolerance, the fact that micrograins are observed, not single crystals, is meaningless since in the microscope provides too localized probe from single grains only. Accordingly, two types of materials were studied, namely micrograined polycrystalline samples and nanostructured ones obtained by microstructure refinement effected with HPT processing. Although in real reactor plasma conditions mirrors will be concurrently irradiated by neutrons, hydrogen isotopes and He, in the present study only irradiation by He ions is investigated. It is well-known that neutron irradiation induces displacement damage resulting in formation of vacancies and interstitial-type defects. Considering that there is a strong interaction of He with this kind of defects and that HPT can also lead to the creation of the high concentration of vacancies, any pre-damage simulating neutron irradiation effects has been discarded.

2. Methods

2.1. Material

The material used in the present study is sintered, high purity (99,97 wt%) Mo supplied by Plansee A.G in a form of a rod of 10 mm in diameter. The microstructure of Mo mirrors was refined by HPT. To this aim, the material was cut into disks of 10 mm in diameter and 0.8 mm in thickness. The disks were torsionally strained to 1 and 5 revolutions at a constant pressure of 6 GPa at the room temperature with speed of 0.2 rpm. The strain defined as simple shear, γ, was calculated according to the equation $\gamma = 2\pi \times r \times n/t$, where r, n and t are the distance from the torsion axes, the number of applied revolutions and the mean thickness of the sample, respectively. The equivalent strains $\varepsilon_{eq} = \gamma/\sqrt{3}$ calculated 5 mm from the central point of the sample after 5 rotations were equal to 113. After HPT the final thickness of samples was 0.5 mm. PT experiments were performed at the Faculty of Physics at the University of Vienna. Further in the text, for simplification, samples are marked AS-R, HPT_1 and HPT_5 for as-received, one rotation and five rotations, respectively.

2.2. Ion irradiation

Before irradiation samples were mechanically grounded and polished following the same procedure for AS-R, HPT_1 and HPT_5 using firstly increasingly smaller diamond grains (30, 15, 6, 3 and 1.5 μm) followed by (1, 0.3 and 0.05 μm) alumina suspension for the final surface finish. The irradiation of Mo samples was performed with 2 keV $^4He^+$ beams at the Ion Technology Centre (ITC) of the Uppsala University using a 350 kV Danfysik 1090 implanter with a beam current of up to 1 mA at room temperature. Irradiation conditions were based on the Stopping and Range of Ions in Matter by prof. Jonas F. Ziegler (SRIM) [32] predictive modelling to implant in the optically active layer: 15–20 nm. The irradiation dose was 8×10^{16} cm^{-2}. The conditions were selected based on previous unpublished results which enabled finding the threshold dose when the effects of irradiation are clearly visible in the microstructure by scanning transmission electron microscopy (STEM) since microscopy studies are necessary to understand and explain changes induced by radiation in grains interiors and at grain boundaries. At this irradiation dose, He nano bubbles were nucleated and resolvable in STEM studies of micrograined Mo polycrystalline samples.

2.3. Analytical methods

2.3.1. X-ray measurements

Measurements of the crystallite size (using the Williamson-Hall method) was performed by X-ray diffraction (XRD), at room temperature using a Bruker D8 Discover diffractometer with filtered Co Kα (λ = 0.17902 nm) radiation, operated at Warsaw University of Technology (WUT). X-ray patterns were collected from an area of approximately 1.5 mm in diameter, which centre was located 3.5 mm from the sample center. The conditions of analysis were as follows: voltage of 40 kV, current of 40 mA, angular range of 2θ from 35° to 120°, step Δ2θ =0.025°, and the counting time = 5 s. The XRD was also applied to quantify the dislocation densities in the investigated materials. The dislocations density, ρ, was calculated from XRD peak broadening using modified Williamson-Hall plot:

$$\rho = \frac{K\epsilon^2}{b^2} \tag{1}$$

where K for bcc materials equals 14.4 with the Burgers vector of dislocations, b, along ⟨111⟩, ε is the lattice strain evaluated from W-H plot, b is the Burgers vector for molybdenum- 0.272 nm.

2.3.2. Microhardness and nanohardness measurements

The micro- and nanohardness measurements were performed at WUT. The values of Vickers microhardness, Hv, were recorded along a diameter with a separation of 0.5 mm. These measurements were made using a Zwick microhardness tester under a load of 200 g and loading time of 10s. Nanohardness tests were performed using a Triboscope 950 HYSITRON equipped with a Berkovich indenter. The loading force was 3 mN, the loading, holding and unloading times were 10, 2 and 10s, respectively. The hardness values were calculated following the model of Oliver and Pharr [33]. The tip area function was determined by a series of indents at various depths (normal loads) in the sample of the known elastic modulus (silica standard). Approximately 50 measurements were performed in every sample before and after irradiation at the perimeters with radii of 2.5, 3 and 3.5 mm.

The mean value (MV) and standard deviation (SD) were calculated from microhardness and nanohardness measurements.

2.3.3. Doppler broadening variable energy positron annihilation spectroscopy and variable energy positron annihilation lifetime spectroscopy

Doppler broadening variable energy positron annihilation spectroscopy (DB-VEPAS) measurements have been conducted at the Helmholtz-Zentrum Dresden-Rossendorf using apparatus for in-situ defect analysis (AIDA) [34] of the slow positron beamline (SPONSOR) [35]. Positrons have been implanted into samples AS-R and HPT_5 with discrete kinetic energies E_p in the range between 0.05 and 35 keV, which allows for depth profiling from the surface down to couple of micrometers. A mean positron implantation depth $< z >$ can be approximated by a simple material density dependent formula: $<z \geq 36/\rho \cdot E_p^{1.62}$, where ρ = 10.28 g·cm^{-3}. The measurements enabled calculating of the so-called S-parameter representing a fraction of positrons annihilating with low momentum valence electrons and describes vacancy like defects concentration and/or size [36]. For the analysis of positron diffusion length, L_+, which is inverse proportional to defect concentration the VEPFit code [37] has been utilized, which permits to fit $S(E_p)$ curves for multilayered systems and to acquire thickness, L_+, and specific S-parameters for each layer within a stack.

Variable energy positron annihilation lifetime spectroscopy (VEPALS) measurements have been conducted at the Mono-energetic Positron Source (MePS) beamline at HZDR, Germany [38,39]. Typical lifetime spectrum N(t) is described by:

$$N(t) = \sum_i \left(\frac{1}{\tau_i}\right) e^{-\frac{t}{\tau_i}} \tag{2}$$

where t is the time scale, τ_i and I_i are the i-th positron lifetime component and the relative intensity of the i-th component, respectively ($\Sigma I_i = 1$) [40]. All the spectra were deconvoluted using a PALSfit fitting software [41] into 3 discrete lifetime components τ_i, which directly evidence 2 different defect types (sizes). The 3rd component (τ_3) was neglected as residual fingerprint of surface Positronium a bound state of electron and positron (<<0.5%) [42]. The corresponding relative intensities I_i reflect to a large extend concentration of each defect type (size). In general, positron lifetime is directly proportional to defects size, i.e., the larger is the open volume, the lower is the probability and longer it takes for positrons to be annihilated with electrons [40,43,44]. The positron lifetime and its intensity has been probed in function of positron implantation energy E_p or in the other words implantation depth (thickness) $< z >$.

2.3.4. Reflectivity measurements

The reflectivity was measured by Spectrophotometer Lambda 950 manufactured by PerkinElmer at Uppsala University Sweden with a step of 5 nm in the 300–2400 nm range. An additional collimator was used to handle the smaller size of the samples. As reference for the reflectivity an Al mirror with known reflectivity was used. The uncertainty of the measurement is largely limited by the amount of signal reaching the detector that varieties for different wavelengths and can be seen by the scatter of the data.

2.3.5. Microscopy observations

The microstructure of the samples has been studied at Microscopy Laboratory of WUT. Microstructures of samples were revealed using scanning electron microscope (SEM) SU8000 Hitachi in a back scattered electron (BSE) – mode at 5 kV and transmission electron microscopy (TEM) JEOL1200 at 120 kV. Surface observations of samples, both before and after irradiation, were performed using SEM in scanning secondary electron (SE) – mode at 15 kV electron accelerating voltage. Observations were performed 3.5 mm from the sample center. Secondly, cross-sectional lamellae before irradiation and of the ion irradiated region in the implanted samples were prepared by focused ion beam (FIB) Hitachi NB5000, parallel to the radius direction. Before FIB cutting, the surface of the sample was protected by thin carbon layer. Subsequently, their microstructure was studied using STEM Hitachi HD2700 in bright field (BF) – mode and *Z*-contrast (ZC) – mode operated at 200 kV and TEM. Quantitative investigation of grains was performed using stereological and image analysis methods [45,46]. To determine their size and shape parameters such as equivalent diameter, d_2, and elongation parameter, d_{max}/d_2, were used. The equivalent diameter is defined as the diameter of a circle having an area equal to the surface area of a given grain. The grain elongation factor is defined as the ratio of the maximum to the equivalent diameter d_{max}/d_2. Moreover, the grain boundary area in the unit volume, Sv, was determined by counting the intersection points of the test lines with the grain boundary network [47].

3. Results

3.1. Microhardness and nanohardness measurements after HPT

Microhardness of HPT-processed samples measured is presented in Fig. 1 and Table 1. It has been proven that even after one rotation microhardness significantly increased from 231 to 542 Hv0.2. The increase of number of rotations to five caused further slight increase of microhardness to 558 Hv0.2. The average values of nanohardness are presented in Table 2. Nanohardness, similarly as microhardness increases with the increase of the deformation degree from 4.7 to 7.8 and 8.7 GPa while measured at the perimeter of radius 3.5 mm for AS-R, HPT_1 and HPT_5 samples, respectively. Nanohardness measured at the perimeters of radii 2.5 and 3 mm showed comparable values. The

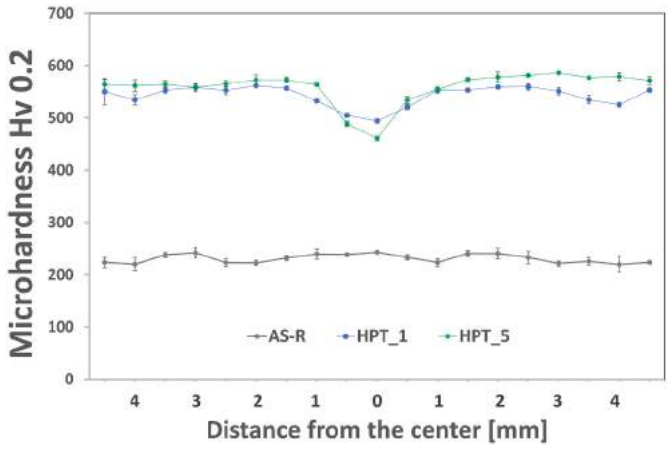

Fig. 1. Microhardness distribution on the diameter of AS-R and HPT-processed Mo samples.

Table 1
Mean Value (MV) and Standard Deviation (SD) of microhardness measured on the diameter of AS-R and HPT-processed Mo samples.

	MV (Hv0.2)	SD (Hv0.2)
AS-R	231	8
HPT_1	542	19
HPT_5	558	31

Table 2
Mean Value (MV) and Standard Deviation (SD) of nanohardness measured along various perimeters of AS-R and HPT-processed Mo samples.

	AS-R		HPT_1		HPT_5	
Radius [mm]	MV (NH3) [GPa]	SD (NH 3) [GPa]	MV (NH 3) [GPa]	SD (NH 3) [GPa]	MV (NH 3) [GPa]	SD (NH 3) [GPa]
2.5	4.5	0.3	7.3	0.4	8.6	0.6
3	4.7	0.3	7.6	0.3	8.7	0.7
3.5	4.7	0.3	7.8	0.4	8.7	0.6

increase in microhardness and nanohardness after HPT is the effect of defects creation and grain refinement which will be analyzed in detail in section 3.2.

3.2. Microstructure evolution after HPT

3.2.1. Microstructure observations

HPT-processing leads to a significant grain refinement of Mo samples even after one rotation as presented in Fig. 2. The average equivalent diameter decreases from 2.12 μm to 480 nm. It is accompanied by changes in the shape factors. In AS-R samples grains are elongated parallel to the rod direction with the elongation parameter of 1.7. After one rotation ultra-fined grains become elongated perpendicularly to the foreseen irradiation direction and elongation parameter increases to 2.4. After five rotations the average equivalent diameter is reduced to 110 nm and the elongation decreases to 1.2, meaning that grains become uniaxial. In microstructures after HPT-processing prevail high-angle grain boundaries as can be recognized from the well-contrasting grains. The decrease of the grain size is accompanied by the increase of Sv which increases from 1.6 in the AS-R sample to 3.4 and 16.5 $\mu m^2/\mu m^3$ after HPT-processing to 1 and 5 rotations, respectively.

3.3. X-ray measurements

The X-ray patterns are presented in Fig. 3 and the crystallite size, dislocation density and strains in Table 3. As already seen at the microstructure images, HPT processing refined the crystallite size from a value greater than measurable by X-ray technique to approximately 500 and 100 nm for HPT_1 and HPT_5, respectively. Which is in a good agreement with the grain size evaluated from the microstructural studies. HPT led to a considerable increase in the dislocation density. The dislocation density increased from 7.3×10^{14} to 8.3×10^{15} and 4.9×10^{15} m^{-2} after 1 and 5 rotations, respectively. The quite high density of dislocations in the AS-R sample is certainly due to mechanical grinding and polishing. The drop in the dislocation density between HPT_1 and HPT_5 samples shall be attributed to the rearrangement of dislocations after higher deformation, which contributed to the creation of greater grain boundary density. The lattice distortion, da/a, increases from 0.0019 for AS-R to 0.0065 for HPT_1 and afterwards slightly decreases to 0.0050 for HPT_5.

3.4. Reflectivity measurements

The results of reflectivity measurements are presented in Figs. 4 and 5. The total reflectivity of undeformed and deformed samples irradiated with a He ion dose of $8x10^{16}cm^{-2}$ decreased, as presented in Fig. 4. However, the total reflectivity of deformed samples decreased more profoundly by approximately 2.5%, which is clearly observable in the infrared range up to 2000 nm since above 2000 nm distortions start to appear. This difference in reflectivity is well-visible at the magnified part of the chart (Fig. 4 **b)**).

The diffuse and specular reflectivity is presented in Fig. 5. The diffuse reflectivity values are relatively low. Before irradiation diffuse reflectivity up to the wavelength of 2000 nm reaches maximally 8% for one of the AS-R samples and simultaneously for the second AS-R sample is below 2%. Before irradiation for HPT-processed samples the diffuse reflectivity is between the values for two AS-R ones. As the diffuse reflectivity is very sensitive to the quality of the samples surface finish, and the two extreme values are observed for the non-deformed

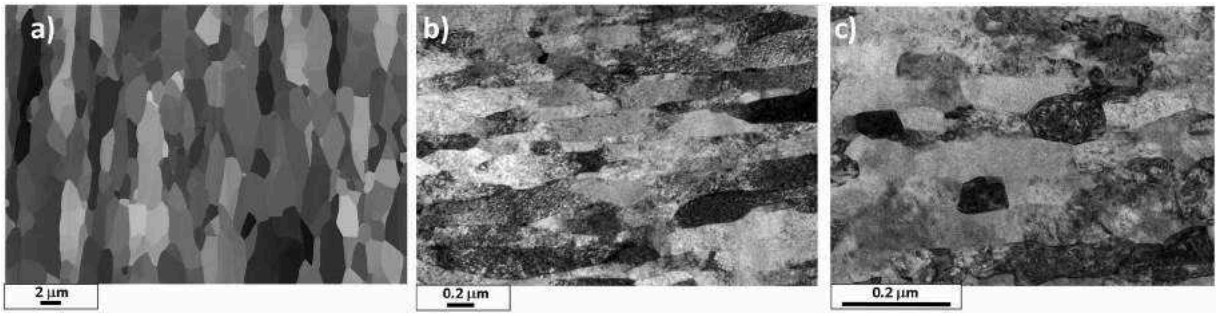

Fig. 2. Microstructures of a) AS-R, b) HPT_1, c) HPT_5 - cross sections; a) BSE -SEM (SU8000 Hitachi) b), c) TE-TEM direction of foreseen irradiation is parallel to the shorter edges of images.

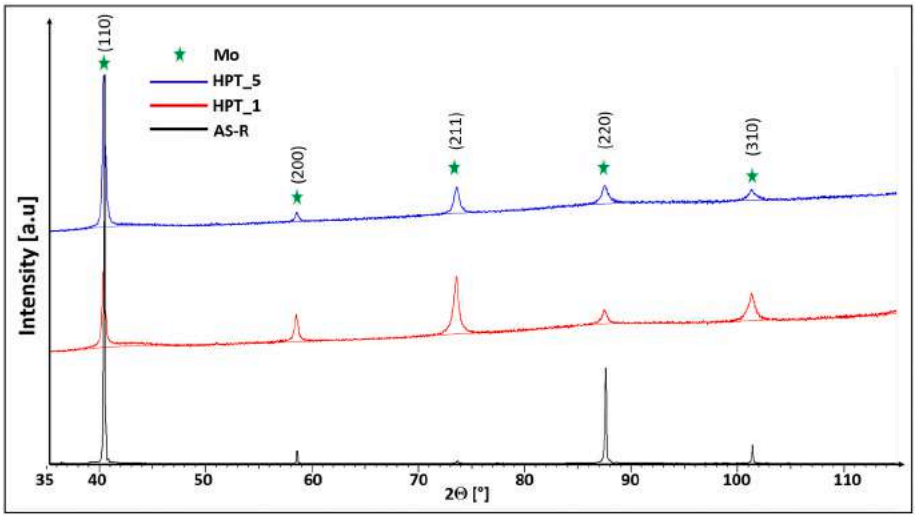

Fig. 3. X-ray patterns of AS-R and HPT-processed samples.

Table 3
The crystallite size, lattice distortions and density of dislocations of the AS-R and HPT-processed samples.

Sample indication	Crystallite size [nm]	$\frac{da}{a}$	Density of dislocations $\rho[m^{-2}]$
AS-R	>1000	0.0019	7.3×10^{14}
HPT_1	522	0.0065	8.3×10^{15}
HPT_5	106	0.0050	4.9×10^{15}

materials, it can be argued that the refinement of microstructures of samples does not influence this property, whereas obtaining consistently the same surface finish for all samples is challenging. After irradiation the diffuse reflectivity drops for all samples except the one non-deformed with the lowest values before irradiation. The most significant drop in diffuse reflectivity is observed for the samples with the highest values before irradiation, that is for the one of AS-R samples and the HPT_5 one. Based on the results, it can be argued that the applied irradiation induces "smoothening" of the samples surfaces and that this effect is more pronounced for non-deformed materials and those with worse initial surface finish.

Not surprisingly, before irradiation the specular reflectivity measurements yield revers results of those for diffuse reflectivity. Here again, the two deformed materials fall into the envelope of the undeformed ones but in reversed order, HPT_1 heaving higher specular reflectivity than HPT_5. After irradiation, before irradiation the best performing materials, that is AS-R and HPT_1, lose the most in the specular reflectivity values. It might be concluded the samples with the best surface finish before irradiation quality are affected the most by the He irradiation. The maximum difference in far infrared for non-irradiated samples was in range of 8% whereas after irradiation this spread of values diminishes to about 4%. As it was already mentioned when discussing the total reflectivity, the deformed samples perform worse than the non-deformed ones.

It is worth noticing, that in the range of some 700 nm to 1000 nm all the samples after irradiation exhibit higher specular reflectivity values than their non-irradiated counterparts.

3.5. Surface observations of irradiated samples

Exemplary images of samples surface after irradiation are presented in Fig. 6. Irradiation by He ions with a dose of $8x10^{16}cm^{-2}$ does not lead to the creation of blisters on the samples surface contrary to earlier observations of samples irradiated prior to He ions by Mo ions at 30 keV to 10 dpa [48]. The bright particles that appear at the surface are residues of polishing with Al_2O_3 slurry. The images look exactly the same as before irradiation.

3.6. Nanohardness measurements of irradiated samples

The penetration depth of the indenter, depending on the sample, ranged from 70 to 110 nm (Fig. 7). This is more than the depth of He ion

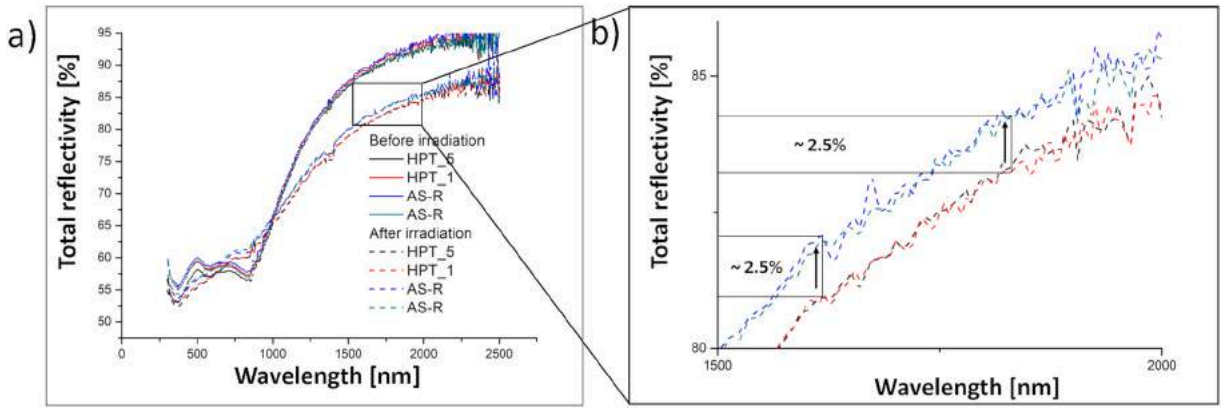

Fig. 4. a) Variation of total reflectivity in Mo samples irradiated with a He ion dose of $8x10^{16}cm^{-2}$; b) magnified part of a).

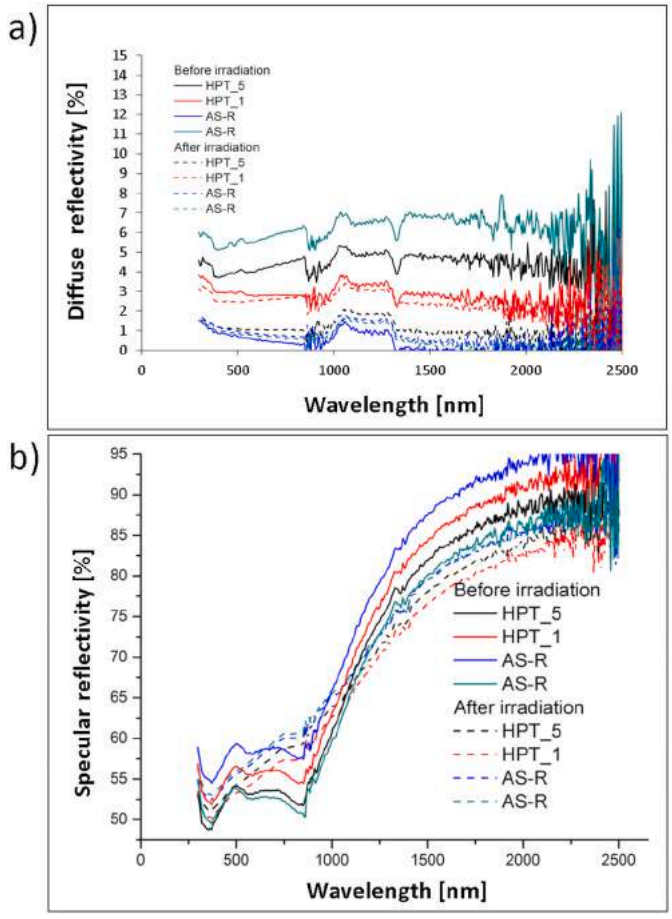

Fig. 5. Variation of a) diffuse and b) specular reflectivity in Mo samples irradiated with a He ion dose of $8x10^{16}cm^{-2}$.

implantation, which is about 20 nm. It is not possible to test the nanohardness of such a thin layer because it would require testing with a maximum indentation depth of about 2 nm, which is a value much lower than that at which we are able to determine nanohardness. This is due to the fact that the indenters for nanohardness measurements are not sharp enough and the useful measurement ranges start from about 30–40 nm. The aim of the nanohardness test on samples after He ion implantation was to investigate the influence of this implantation, which was obtained by comparing the hardness values before and after implantation. The obtained results indicate an increase in hardness after implantation, which implicates that the layer with structural changes as a result of this implantation has a higher hardness, although we were not able to measure the hardness of the layer itself.

The comparison of nanohardness values before and after irradiation is summarized in Fig. 8. HPT-processing of samples results in a less significant increase in nanohardness after irradiation approximately of 10% on average than measured in the undeformed sample approximately of 20%. Interestingly, in the case of AS-R and HPT_5 samples independently of the perimeter the nanohardness increases of a similar value in comparison with the non-irradiated state. However, in the case of HPT_1 sample with the increase of perimeter one observes the decrease in the difference between the nanohardness after HPT and nanohardness after irradiation by 15, 11 and 6% respectively for 2.5, 3 and 3.5 mm radii. This difference is caused by the various degree of deformation reached at the diameter of the sample during HPT and the higher the deformation degree the lower increase in nanohardness after irradiation. It also indicates that deformation after 5 rotations is more uniform.

3.7. Cross section observations of irradiated samples

The microstructure of sample cross-sections after irradiation is presented in Fig. 9. The detailed observation of cross sections enabled perceiving He bubbles down to 20 nm from the surface, both in undeformed and deformed samples. Moreover, nanocracks at some grain boundaries were noticed in the near-surface region. The creation of nanocracks by the mechanism of bubble accumulation at the grain boundary observed in irradiated HPT_5 sample is presented in Fig. 10.

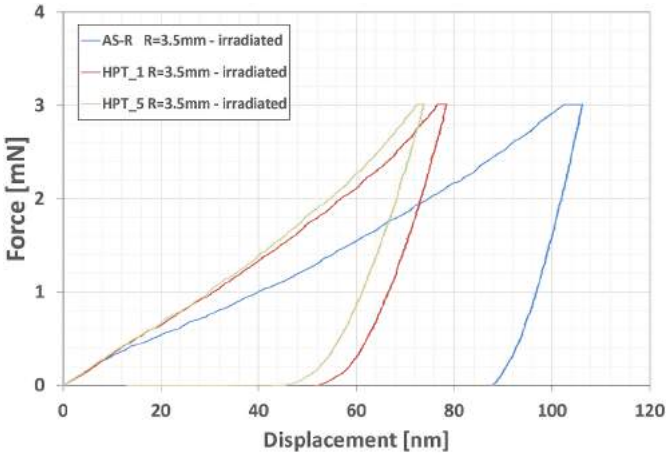

Fig. 7. Curves force-displacement of AS-R and HPT-processed Mo samples after irradiation for the radius of 3.5 mm.

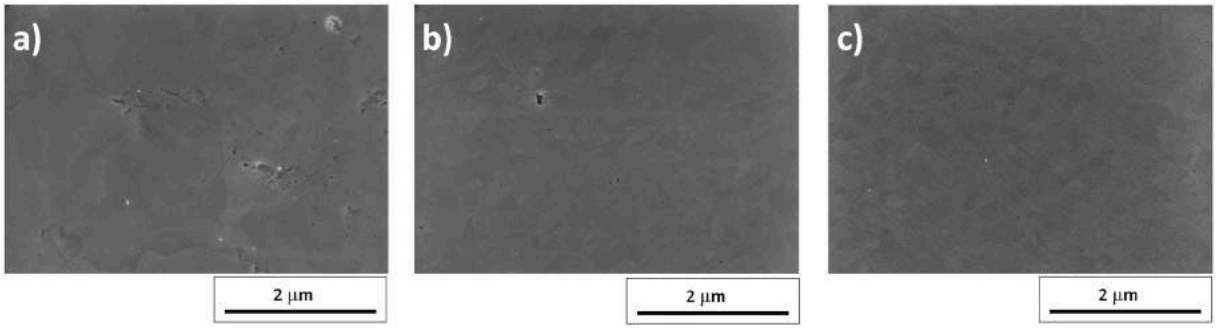

Fig. 6. Samples surface after irradiation a) AS-R, b) HPT_1, c) HPT_5,

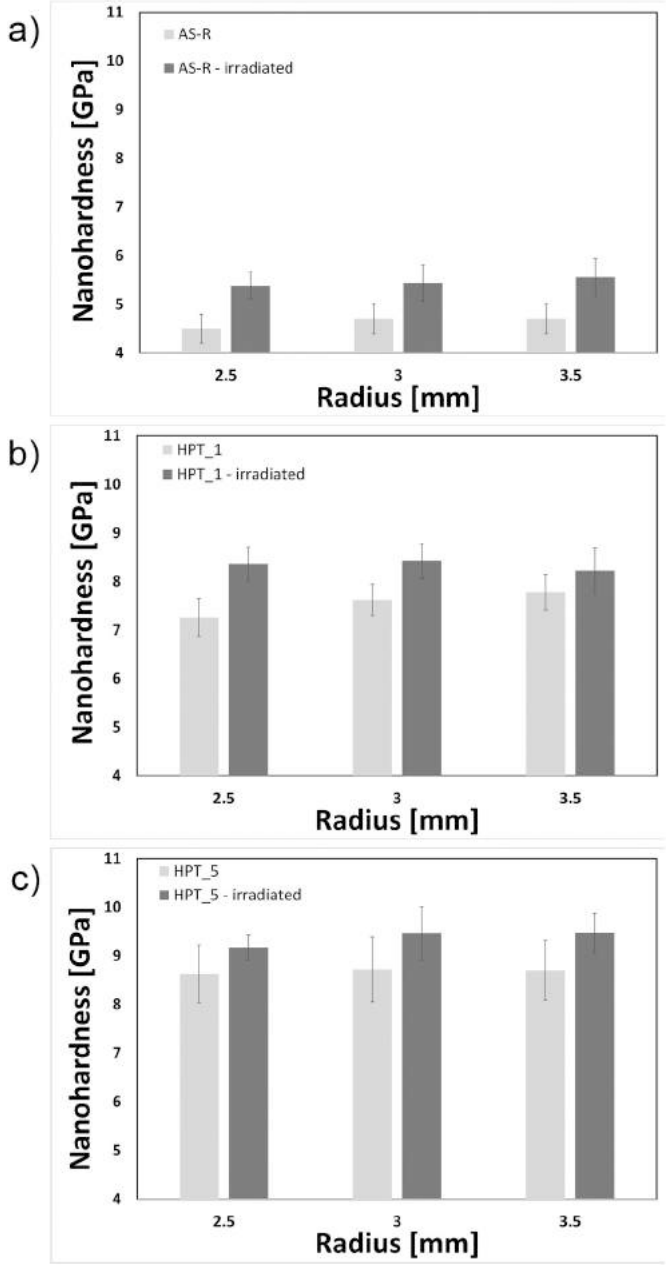

Fig. 8. Nanohardness measured on various perimeters of AS-R and HPT-processed Mo samples before and after irradiation.

4. Discussion

4.1. What is the reason for the variation in the magnitude of the increase in mechanical properties after irradiation between nanostructured and micrograined samples?

HPT leads to the microstructure refinement to approximately 500 and 100 nm after 1 and 5 rotations, respectively. The measurements show greater grain refinement than in Mo investigated in [49,47]. It might result from the choice of a different section for microscopy observations or difference in purity. The HPT does not only reduce the grain size but it also leads to the increase in the dislocation density as measured by X-rays. The dislocation density increases rapidly after 1 rotation and then slightly decreases after 5 rotations due to the annihilation of dislocations during the transformation of low angle grain boundaries into high angle grain boundaries. It is worth to notice that the initial density of dislocation is also at a considerable level. The density of dislocations for annealed Mo should be approximately 3×10^{12} m^{-2} [50]. In this study in the AS-R sample obtained by powder sintering the density of dislocations is much higher and equals $7.3x10^{14}m^{-2}$ as a result of conventional grinding and polishing applied to obtain mirror like surface finish of the samples. This may be the reason for the homogenous distribution of bubbles in the optically active layer in undeformed and deformed samples. The homogenous distribution stems from a trapping capacity of He ions by dislocations [5]. Since STEM observations enabled noticing that after irradiation by He^+ the depth where bubbles were created and distribution of bubbles is comparable for the micrograined and nanostructured variants it cannot, therefore, be the reason for the difference in reflectivity.

The reason for the differences in reflectivity between undeformed and deformed samples might originate from the difference in the grain boundary density. Because of the grain refinement the total grain boundary area in nanostructured Mo is far greater than that found in the micrograined Mo. During irradiation He ions are trapped at grain boundaries and since there is a large energy barrier for He diffusion back into the matrix, He remains at grain boundaries. The agglomeration of He ions gives the beginning to the bubble nucleation at grain boundaries with dimensions approaching the mean free path of migrating He and He-induced defects [51]. The bubbles agglomeration at grain boundaries leads to the creation of nanocracks in the optically active layer. These nanocracks can be responsible for the decrease of reflectivity of HPT-processed samples since the grain boundary density in HPT- processed samples is higher than in micrograined ones and therefore more sites for crack nucleation exists. Nanocracks appear only at some grain boundaries which may be a result of many factors among which are misorientation of grains, grain boundary character and local strains. Moreover, the differences observed in the radiation response of various grains depend on the grain orientation relative to the direction of the irradiation which in turn has an impact on the grain boundary plane. The importance of this fact has been proven in the work on Mo mirrors of orientations (001), (110) and (111) irradiated by 3 keV He ions to a fluence of $1x10^{22}He/m^2$ at room temperature where the reflectivity measurements of the single crystals showed smaller reduction in (100) mirrors than in (110) and (111) mirrors [52]. This phenomenon can be explained by channeling effects [53].

Apart from the impact of the grain refinement on the reflectivity, one observes the impact of the grain refinement on the change in nanohardness values between non-irradiated and irradiated samples. The magnitude of irradiation induced hardening is greater for micrograined than HPT-processed samples. In [18], the hardening effect observed in He ion irradiated samples was mainly attributed to He bubbles and dislocation loops formation. It was suggested that in the case of nanocrystalline magnetron sputtered Mo for grain below 90 nm the irradiation-hardening decreased significantly since the density and size of dislocation loops and He bubbles decreased. In our study no significant difference in the bubble size was noticed between micrograined and nanostructured samples. Furthermore, due to the high density of bubbles, dislocation loops were difficult to measure and compare. Thus, we believe more nanocracks of intragranular character in HPT-processed than in micrograined samples may result in more effective sinks for He ions by creating open porosity. Moreover, vacancies generated by HPT-processing may interact with self-interstitials formed during irradiation which in turn lead to the decrease of the density and size of dislocation loops [54].

4.2. Why the difference in the reflectivity of samples is minor in comparison with the difference in their microstructures?

The minor difference in reflectivity between samples varying in the deformation degree in comparison to the great difference in their deformation degree might result from technique of sample surface preparation for radiation experiments. Before irradiation samples were

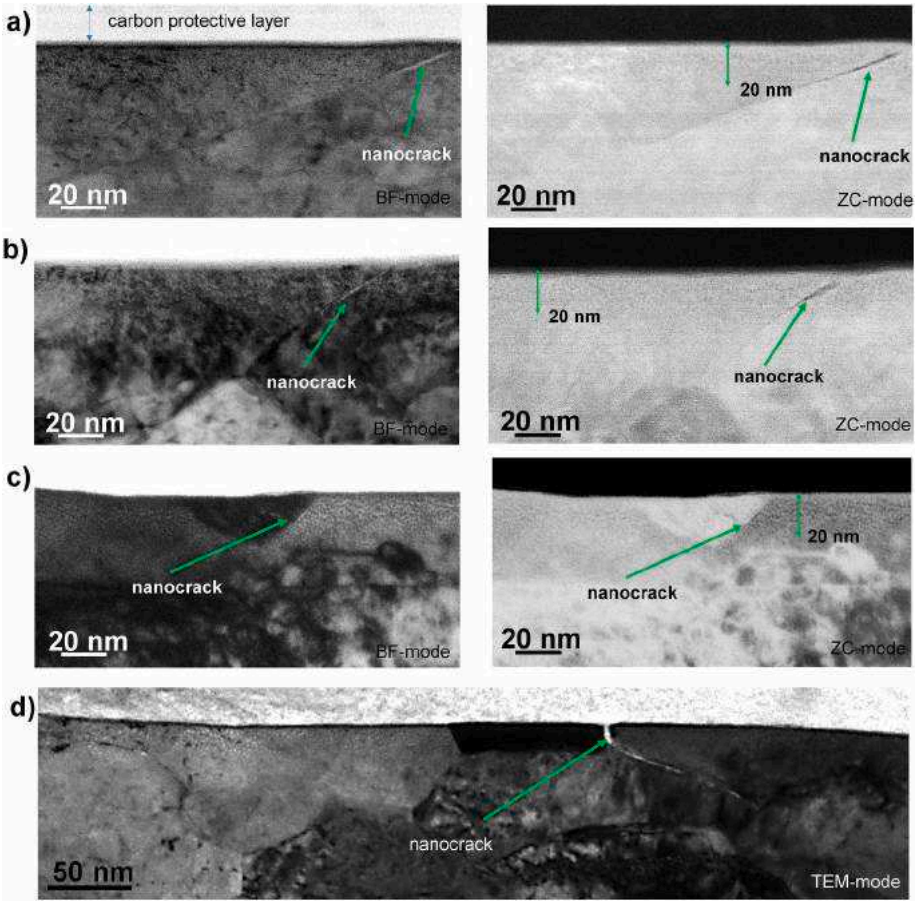

Fig. 9. Cross sections of Mo samples irradiated with He ions; a) AS-R, b) HPT_1, c) and d) HPT_5.

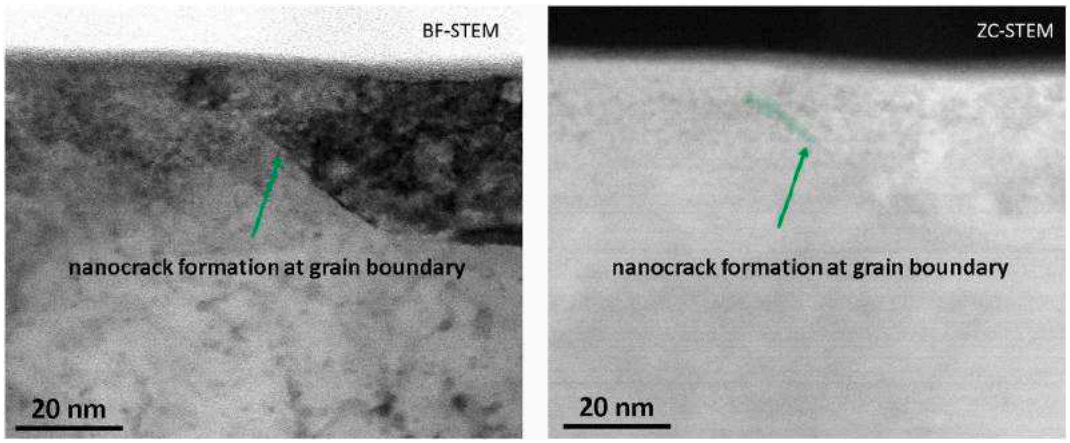

Fig. 10. The creation of nanocracks by the mechanism of bubble accumulation at the grain boundary (marked with the green arrow). (For interpretation of the references to colour in this figure legend, the reader is referred to the web version of this article.)

mechanically ground and polished. This method in comparison to e.g. electropolishing can introduce a high concentration of defects into the near-surface volume that is of interest in our studies. In the case of mechanically ground and polished tungsten, the depth up to which the effects of preparation were observed was 30 nm as obtained from DB-VEPAS [55]. To better explore the impact of the preparation technique on the optically active layer defects character, DB-VEPAS and PALS measurements were performed on samples varying the most noticeably in the deformation degree, namely AS-R and HPT_5. Fig. 11 shows the depth profile of the S parameter. It reaches the highest value approximately 20 nm below the samples surface. Below 20 nm it starts to decrease to reach a stable value at a depth of approximately 300 nm for HPT_5 and 1100 nm for As-R. In bulk samples contrary to the near surface layer it is visible that larger defect concentration is found in HPT_5 sample. The calculated positron diffusion length L_+ and corresponding defected layers thickness are presented in Table 4. The strongly defected sub-surface layer has been found having a thickness of about 18 and 37 nm for the AS-R and HPT_5, respectively. The defect concentration in the sub-layer is slightly higher for AS-R than HPT_5 sample. In the case of HPT_5 the same shape of S has been registered

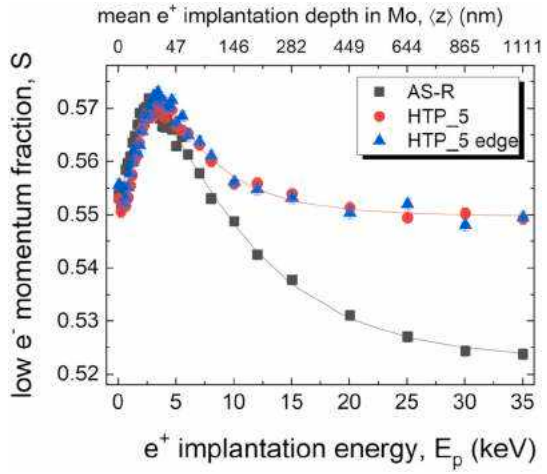

Fig. 11. Annihilation line parameter S (low electron momentum fraction) as a function of positron implantation energy E_p and mean positron implantation depth $< z >$.

Table 4
Sublayer thickness t_{surf} and positron diffusion lengths L_+.

Sample indication	Thickness, $t_{surf.}$ [nm]	$L_{+,surf.}$ [nm]	$L_{+,bulk}$ [nm]
AS-R	18	0.7	157
HPT_5	37	3	67

near the sample edge and in the middle of the sample suggesting that there are no changes in the defect concentration.

The analysis clearly shows that although the samples differ quite considerably in the deformation degree their optically active layers become quite comparable in terms of vacancy-type defect concentration due to the preparation technique. Defects like vacancies are necessary to create He-vacancy complexes and subsequently He bubbles or dislocation loops. The detailed characterization of defects in the optically active layer of AS-R and HPT_5 samples has been performed using PALS. The technique has been successfully employed to describe temperature dependent defect nanostructure in neutron [56–58] and α [59] irradiated Mo. More recently, recrystallization processes have been investigated by means of PALS in high temperature annealed [60] and subjected to a dry sliding [61] Mo as well. Positron lifetime components and their relative intensities measured down to the depth of about 50 nm in AS-R and HPT_5 samples are presented in Fig. 12. PALS analysis for the AS-R sample reveals mixture of dislocations (τ_1) and vacancy clusters (τ_2) as dominant positron trapping centres. The lifetime τ_1 is shorter compared to that for a monovacancy (blue dotted line in Fig. PALS) [62] and longer than for the value representing the delocalized bulk annihilation (at the crystal interstitial sites). The lifetime values which fall between these two specific states (single vacancy and bulk) are typical for dislocations. A dislocation line itself is only a shallow positron trap [63]. Once positrons reach a dislocation they will quickly diffuse along the dislocation line and will became trapped by a vacancy anchored in the compressive elastic field of dislocation [63]. Hence, positrons are finally annihilated in a monovacancy influenced by the elastic field of dislocations, which results in shorter lifetime [64]. Since τ_1 of the AS-R sample is shorter than of HPT_5 smaller concentration of vacancies connected to dislocations is expected. Hence, HPT_5 has larger density of monovacancies accordingly. The size of vacancy clusters can be estimated as agglomeration of about 8–9 [57] (and based on calculations for Nb having similar lattice parameter and bcc crystal structure [64]). While the low temperature HPT processing of Ti bcc produces vacancy clusters consisting on the average of three vacancies [65]. After HPT shorter lifetime τ_1 increases reaching nearly the value for monovacancy and the longer lifetime τ_2 became larger than 400 ps ($\geq$15 vacancies). At the same time the relative intensity I_1 (I_2) increases (decreases) suggesting generation of monovacancies due to HPT, which tend to agglomerate increasing the size of vacancy clusters. The concentration of vacancy clusters most probably drops with depth as indicated by smaller I_2. This drop is reflected in larger positron diffusion length L_+ of the sub-surface region after HPT processing, however, the overall defect concentration remains high. There is a high probability that vacancy clusters in AS-R and HPT_5 samples are located at grain boundaries. Since larger vacancy clusters are identified in HPT_5 sample than in AS-R, the more prone its grain boundaries may be to nanocrack formation.

Additionally, microstructure observation of the polished AS-R cross section directly after grinding and polishing has been done. Fig. 13 shows that the grinding and polishing can lead to the creation of subgrains even up to 1 μm.

This suggests that what differentiates the samples the most, is the density and character of grain boundaries rather than the density of vacancy-type defects. For this reason, with high probability grain boundaries play a decisive role in the observed reflectivity differences.

It should be pointed out that during in-situ cleaning not only will the deposited contaminants be removed but also approximately 20 nm of the mirror material in each cycle. Since hundreds of cycles are

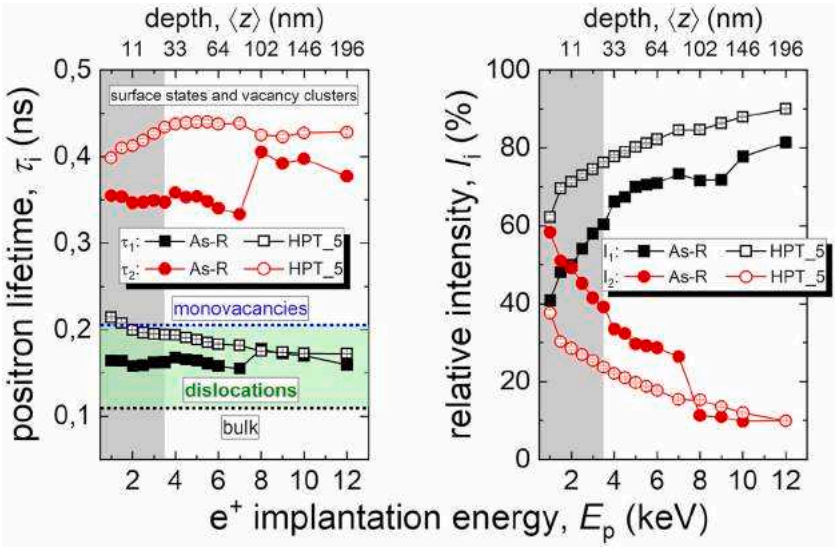

Fig. 12. Positron lifetime components and their relative intensities as a function of positron implantation energy and corresponding depth $< z >$ for AS-R and HPT_5 samples. Horizontal dotted lines mark literature lifetime values for bulk annihilation (black) and monovacancies (blue). At a green region, between bulk and monovacancies, dislocations are expected. The second lifetime component denotes surface states and vacancy clusters. (For interpretation of the references to colour in this figure legend, the reader is referred to the web version of this article.)

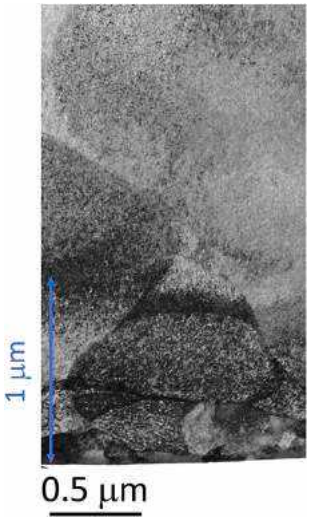

Fig. 13. Subgrains in the AS-R sample – cross section, BF-STEM.

envisaged, assuming 100, approximately 2 µm of the mirror will be removed (This by the way may be yet another limiting factor for using coatings for mirrors in fusion reactors). Analyzing the microstructure after standard grinding and polishing, one can notice the impact of this procedure to up to 1 µm. Of course, the impact of grinding and polishing decreases with depth. Another issue is the impact of the cleaning technique on the mirror defect concentration. Studies suggest that during sputtering also implantation occurs and leads to the creation of defects such as vacancies and dislocations beneath the surface [66,67] as well as argon deposition [68]. Taking these facts into consideration, the near surface area after cleaning will always contain more defects than the bulk material so the data presented in the present paper is highly relevant for the mirrors in fusion devices.

4.3. The perspective of application of nanostructured Mo as irradiation resistant materials

Although the present study shows that nanostructured Mo mirrors after irradiation with 8×10^{16} cm^{-2} He ions demonstrate lower reflectivity than micrograined ones, the trend might be reversed for higher doses. It may be due to the fact that nanocracks formed at some grain boundaries create open porosity which may facilitate an escape of He from mirrors and retard the formation of blisters, which will decrease the reflectivity drastically. This shall be further investigated in our future studies. The delay of blisters formation in nanostructured tungsten in comparison to micrograined one was observed during in situ He irradiation in a He ion microscope [16]. Moreover, it was found that the presence of nanochannels in tungsten film irradiated with 190 keV He ions accelerated the release of He and retarded the formation of large He bubbles [69].

5. Conclusions

1. High-pressure torsion-processing leads to a significant grain refinement up to 110 nm on the cross section.
2. The He-ion dose of $8x10^{16}cm^{-2}$ causes a decrease in total reflectivity of the micrograined sample, whereas the total reflectivity of deformed samples decreases by additional 2.5%.
3. Irradiation by He ions with a dose of $8x10^{16}cm^{-2}$ does not lead to the creation of blisters on the samples surface but causes He bubbles creation within the optically active layer and nanocracks at grain boundaries in all investigated samples. There is a higher density of grain boundaries in refined samples which leads to the higher density of nanocracks. It is highly probable that the nanocracks created at grain boundaries in the optically active layer during irradiation are responsible for lower after irradiation reflectivity of high-pressure torsion-processed samples.

Declaration of Competing Interest

The authors declare that they have no known competing financial interests or personal relationships that could have appeared to influence the work reported in this paper.

Data availability

Data will be made available on request.

Acknowledgements

'This work has been carried out within the framework of the EUROfusion Consortium and has received funding from the Euratom research and training programme 2014-2018 and 2019-2020 under grant agreement no. 633053. The views and opinions expressed herein do not necessarily reflect those of the European Commission'. Work was performed under EUROfusion WP PFC support from the Swedish Research Council (VR) under contracts 2017-00643 and 2015-04884. This research work is published as part of an international project co-financed by the program of the Minister and Science of Higher Education of Poland entitled "PMW" in the year 2020; agreement No. 5125/H2020-Euratom/2020/2.

Parts of this research were carried out at ELBE at the Helmholtz-Zentrum Dresden - Rossendorf e. V., a member of the Helmholtz Association. We would like to thank facility staff Ahmed G. Attallah for assistance. This work was partially supported by the Impulse-und Networking fund of the Helmholtz Association (FKZ VH-VI-442 Memriox), and the Helmholtz Energy Materials Characterization Platform (03ET7015).

The raw/processed data required to reproduce these findings cannot be shared at this time due to technical or time limitations.

References

[1] W. Liu, Y. Ji, P. Tan, H. Zang, C. He, D. Yun, C. Zhang, Z. Yang, Irradiation induced microstructure evolution in nanostructured materials: a review, Materials (Basel). (2016), https://doi.org/10.3390/ma9020105.
[2] N. Nita, R. Schaeublin, M. Victoria, Impact of irradiation on the microstructure of nanocrystalline materials, J. Nucl. Mater. (2004), https://doi.org/10.1016/j.jnucmat.2004.04.058.
[3] T.D. Shen, Radiation tolerance in a nanostructure: is smaller better? Nucl. Instruments Methods Phys. Res. Sect. B Beam Interact. with Mater. Atoms. (2008) https://doi.org/10.1016/j.nimb.2008.01.039.
[4] X.M. Bai, A.F. Voter, R.G. Hoagland, M. Nastasi, B.P. Uberuaga, Efficient annealing of radiation damage near grain boundaries via interstitial emission, Science (80-.) (2010), https://doi.org/10.1126/science.1183723.
[5] B.N. Singh, T. Leffers, W.V. Green, M. Victoria, Nucleation of helium bubbles on dislocations, dislocation networks and dislocations in grain boundaries during 600 MeV proton irradiation of aluminium, J. Nucl. Mater. (1984), https://doi.org/10.1016/0022-3115(84)90556-7.
[6] P.L. Lane, P.J. Goodhew, Helium bubble nucleation at grain boundaries, Philos. Mag. A Phys. Condens. Matter, Struct. Defects Mech. Prop. (1983), https://doi.org/10.1080/01418618308244330.
[7] W. Qin, A.K. Chauhan, J.A. Szpunar, Helium bubble nucleation at grain boundaries and its influence on intergranular fracture, Philos. Mag. (2019), https://doi.org/10.1080/14786435.2018.1551634.
[8] T.C. Lowe, R.Z. Valiev, The use of severe plastic deformation techniques in grain refinement, JOM. (2004), https://doi.org/10.1007/s11837-004-0295-z.
[9] R. Valiev, Y. Estrin, Z. Horita, T.G. Langdon, M.J. Zehetbauer, Y.T. Zhu, Producing Bulk Ultrafined Grained Materials by Severe Plastic Deformation, Jom, 2006.
[10] J. Zrnik, S. Dobatkin, I. Mamuzic, Processing of metals by severe plastic deformation (SPD)-structure and mechanical properties respond, Metal. 47 (2008) 211–216.
[11] R.Z. Valiev, Y. Estrin, Z. Horita, T.G. Langdon, M.J. Zehetbauer, Y. Zhu, Producing bulk ultrafine-grained materials by severe plastic deformation: ten years later, JOM. (2016), https://doi.org/10.1007/s11837-016-1820-6.
[12] Z. Zhang, D. Liu, Y. Wang, Y. Pang, F. Zhang, Y. Yang, J. Wang, A novel method for preparing bulk ultrafine-grained material: three dimensional severe plastic deformation, Mater. Lett. (2020), https://doi.org/10.1016/j.matlet.2020.128209.

[13] R. Pippan, S. Scheriau, A. Taylor, M. Hafok, A. Hohenwarter, A. Bachmaier, Saturation of fragmentation during severe plastic deformation, Annu. Rev. Mater. Res. (2010), https://doi.org/10.1146/annurev-matsci-070909-104445.
[14] X. Sauvage, G. Wilde, S.V. Divinski, Z. Horita, R.Z. Valiev, Grain boundaries in ultrafine grained materials processed by severe plastic deformation and related phenomena, Mater. Sci. Eng. A (2012), https://doi.org/10.1016/j.msea.2012.01.080.
[15] O. El-Atwani, J.A. Hinks, G. Greaves, S. Gonderman, T. Qiu, M. Efe, J.P. Allain, In-situ TEM observation of the response of ultrafine- and nanocrystalline-grained tungsten to extreme irradiation environments, Sci. Rep. (2014), https://doi.org/10.1038/srep04716.
[16] Z. Chen, L.L. Niu, Z. Wang, L. Tian, L. Kecskes, K. Zhu, Q. Wei, A comparative study on the in situ helium irradiation behavior of tungsten: coarse grain vs. nanocrystalline grain, Acta Mater. (2018), https://doi.org/10.1016/j.actamat.2018.01.015.
[17] W.B. Liu, J.H. Zhang, Y.Z. Ji, L.D. Xia, H.P. Liu, D. Yun, C.H. He, C. Zhang, Z. G. Yang, Comparative study of He bubble formation in nanostructured reduced activation steel and its coarsen-grained counterpart, J. Nucl. Mater. (2018), https://doi.org/10.1016/j.jnucmat.2017.12.041.
[18] G.M. Cheng, W.Z. Xu, Y.Q. Wang, A. Misra, Y.T. Zhu, Grain size effect on radiation tolerance of nanocrystalline Mo, Scr. Mater. (2016), https://doi.org/10.1016/j.scriptamat.2016.06.007.
[19] A. Litnovsky, V. Voitsenya, T. Sugie, G. De Temmerman, A.E. Costley, A.J. H. Donné, K.Y. Vukolov, I. Orlovskiy, J.N. Brooks, J.P. Allain, V. Kotov, A. Semerok, P.Y. Thro, T. Akiyama, N. Yoshida, T. Tokunaga, K. Kawahata, Progress in research and development of mirrors for ITER diagnostics, Nucl. Fusion. (2009), https://doi.org/10.1088/0029-5515/49/7/075014.
[20] M. Rubel, S. Moon, P. Petersson, A. Garcia-Carrasco, A. Hallen, A. Krawczynska, E. Fortuna-Zaleśna, M. Gilbert, T. Plocinski, A. Widdowson, J.E.T. Contributors, Metallic mirrors for plasma diagnosis in current and future reactors: tests for ITER and DEMO, Phys. Scr. T170 (2017), 014061.
[21] M. Rubel, S. Moon, P. Petersson, A. Widdowson, R.A. Pitts, S. Aleiferis, E. Fortuna-Zaleśna, G. De Temmerman, R. Reichle, First mirror erosion-deposition studies in JET using an ITER-like mirror test assembly, Nucl. Fusion. 61 (2021), https://doi.org/10.1088/1741-4326/abdb92.
[22] A. Garcia-Carrasco, P. Petersson, M. Rubel, A. Widdowson, E. Fortuna-Zalesna, S. Jachmich, M. Brix, L. Marot, Plasma impact on diagnostic mirrors in JET, Nucl. Mater. Energy. 12 (2017) 506–512.
[23] A. Garcia-Carrasco, P. Petersson, A. Hallén, J. Grzonka, M.R. Gilbert, E. Fortuna-Zalesna, M. Rubel, Impact of helium implantation and ion-induced damage on reflectivity of molybdenum mirrors, Nucl. Instruments Methods Phys. Res. Sect. B Beam Interact. with Mater. Atoms. 382 (2016) 91–95.
[24] A. Litnovsky, V.S. Voitsenya, R. Reichle, M. Walsh, A. Razdobarin, A. Dmitriev, N. Babinov, L. Marot, L. Moser, R. Yan, M. Rubel, A. Widdowson, S. Moon, S.G. Oh, Y. An, P. Shigin, I. Orlovskiy, K.Y. Vukolov, E. Andreenko, A. Krimmer, V. Kotov, P. Mertens, Diagnostic mirrors for ITER: research in the frame of international tokamak physics activity, Nucl. Fusion. (2019), https://doi.org/10.1088/1741-4326/ab1446.
[25] L. Moser, L. Marot, R. Steiner, R. Reichle, F. Leipold, C. Vorpahl, F. Le Guern, U. Walach, S. Alberti, I. Furno, R. Yan, J. Peng, M. Ben Yaala, E. Meyer, Plasma cleaning of ITER first mirrors, in, Phys. Scr. (2017), https://doi.org/10.1088/1402-4896/aa8f30.
[26] L. Moser, L. Marot, R. Steiner, M. Newman, A. Widdowson, D. Ivanova, J. Likonen, P. Petersson, G. Pintsuk, M. Rubel, E. Meyer, Plasma cleaning of beryllium coated mirrors, Phys. Scr. (2016), https://doi.org/10.1088/0031-8949/T167/1/014069.
[27] A.P. Zhilyaev, T.G. Langdon, Using high-pressure torsion for metal processing: fundamentals and applications, Prog. Mater. Sci. (2008), https://doi.org/10.1016/j.pmatsci.2008.03.002.
[28] K. Edalati, Z. Horita, A review on high-pressure torsion (HPT) from 1935 to 1988, Mater. Sci. Eng. A (2016), https://doi.org/10.1016/j.msea.2015.11.074.
[29] A. Vorhauer, R. Pippan, On the homogeneity of deformation by high pressure torsion, Scr. Mater. (2004), https://doi.org/10.1016/j.scriptamat.2004.04.025.
[30] P. Li, Q. Lin, X. Wang, Y. Tian, K. Xue, Recrystallization behavior of pure molybdenum powder processed by high-pressure torsion, Int. J. Refract. Met. Hard Mater. 72 (2018) 367–372, https://doi.org/10.1016/j.ijrmhm.2018.01.002.
[31] X. Wang, P. Li, Y. Huang, N. Gao, T.G. Langdon, Microstructure and microhardness evolution in pure molybdenum processed by high-pressure torsion, Adv. Eng. Mater. (2020), https://doi.org/10.1002/adem.201901022.
[32] J.F. Ziegler, The Stopping and Range of Ions in Solids, 2nd edn, Pergamon, New York, 1996.
[33] G.M. Pharr, An improved technique for determining hardness and elastic modulus using load and displacement sensing indentation experiments, J. Mater. Res. (1992), https://doi.org/10.1557/JMR.1992.1564.
[34] M.O. Liedke, W. Anwand, R. Bali, S. Cornelius, M. Butterling, T.T. Trinh, A. Wagner, S. Salamon, D. Walecki, A. Smekhova, H. Wende, K. Potzger, Open volume defects and magnetic phase transition in Fe 60 Al 40 transition metal aluminide, J. Appl. Phys. 117 (2015), 163908, https://doi.org/10.1063/1.4919014.
[35] W. Anwand, G. Brauer, M. Butterling, H.R. Kissener, A. Wagner, Design and construction of a slow positron beam for solid and surface investigations, Defect Diffus. Forum. 331 (2012) 25–40, https://doi.org/10.4028/www.scientific.net/DDF.331.25.
[36] M. Clement, J.M.M. de Nijs, P. Balk, H. Schut, A. van Veen, Analysis of positron beam data by the combined use of the shape- and wing-parameters, J. Appl. Phys. 79 (1996) 9029–9036, https://doi.org/10.1063/1.362635.
[37] A. van Veen, H. Schut, M. Clement, J.M.M. de Nijs, A. Kruseman, M.R., IJpma, VEPFIT applied to depth profiling problems, Appl. Surf. Sci. 85 (1995) 216–224, https://doi.org/10.1016/0169-4332(94)00334-3.
[38] A. Wagner, W. Anwand, A.G. Attallah, G. Dornberg, M. Elsayed, D. Enke, A.E. M. Hussein, R. Krause-Rehberg, M.O. Liedke, K. Potzger, T.T. Trinh, Positron annihilation lifetime spectroscopy at a superconducting electron accelerator, J. Phys. Conf. Ser. 791 (2017), 012004, https://doi.org/10.1088/1742-6596/791/1/012004.
[39] A. Wagner, M. Butterling, M.O. Liedke, K. Potzger, R. Krause-Rehberg, Positron annihilation lifetime and Doppler broadening spectroscopy at the ELBE facility, in: AIP Conf. Proc, 2018, 040003, https://doi.org/10.1063/1.5040215.
[40] R. Krause-Rehberg, H.S. Leipner, Positron Annihilation in Semiconductors: Defect Studies, 1999.
[41] J.V. Olsen, P. Kirkegaard, N.J. Pedersen, M. Eldrup, PALSfit: a new program for the evaluation of positron lifetime spectra, Phys. Status Solidi 4 (2007) 4004–4006, https://doi.org/10.1002/pssc.200675868.
[42] M.J. Puska, R.M. Nieminen, Theory of positrons in solids and on solid surfaces, Rev. Mod. Phys. 66 (1994) 841–897.
[43] F. Tuomisto, I. Makkonen, Defect identification in semiconductors with positron annihilation: experiment and theory, Rev. Mod. Phys. 85 (2013) 1583–1631, https://doi.org/10.1103/revmodphys.85.1583.
[44] E.H. Khan, M.H. Weber, M.D. McCluskey, Formation of isolated Zn vacancies in ZnO single crystals by absorption of ultraviolet radiation: a combined study using positron annihilation, photoluminescence, and mass spectroscopy, Phys. Rev. Lett. 111 (2013), 017401, https://doi.org/10.1103/PhysRevLett.111.017401.
[45] T. Wejrzanowski, W. Spychalski, K. Rozniatowski, K. Kurzydłowski, Image based analysis of complex microstructures of engineering materials, Int. J. Appl. Math. Comput. Sci. 18 (2008) 33–39, https://doi.org/10.2478/v10006-008-0003-1.
[46] T. Wejrzanowski, M. Lewandowska, K.J. Kurzydlowski, Stereology of nano-materials, Image Anal. Stereol. 29 (2010) 1–12, https://doi.org/10.5566/ias.v29.p1-12.
[47] K.M. Xue, Z. Wang, X. Wang, Y.F. Zhou, P. Li, Nano-indentation nanohardness and elastic modulus evolution of molybdenum processed by high-pressure torsion, Mater. Sci. Technol. (United Kingdom). (2020), https://doi.org/10.1080/02670836.2020.1740863.
[48] A.T. Krawczynska, Ł. Ciupiński, P. Petersson, Impact of material migration and radiation damage on the reflectivity of molybdenum mirrors: laboratory test for DEMO, Phys. Scr. (2020), https://doi.org/10.1088/1402-4896/ab3e81.
[49] S. Lee, K. Edalati, Z. Horita, Microstructures and mechanical properties of pure V and Mo processed by high-pressure torsion, Mater. Trans. (2010), https://doi.org/10.2320/matertrans.M2009375.
[50] G.K. Williamson, R.E. Smallman III, Dislocation densities in some annealed and cold-worked metals from measurements on the X-ray Debye-Scherrer spectrum, Philos. Mag. (1956), https://doi.org/10.1080/14786435608238074.
[51] O. El-Atwani, J.A. Hinks, G. Greaves, S. Gonderman, T. Qiu, M. Efe, J.P. Allain, In-situ TEM observation of the response of ultrafine- and nanocrystalline-grained tungsten to extreme irradiation environments, Sci. Rep. (2014), https://doi.org/10.1038/srep04716.
[52] M. Miyamoto, H. Takaoka, K. Ono, S. Morito, N. Yoshida, H. Watanabe, A. Sagara, Crystal orientation dependence of surface modification in molybdenum mirror irradiated with helium ions, J. Nucl. Mater. (2014), https://doi.org/10.1016/j.jnucmat.2014.06.030.
[53] B.W. Kempshall, S.M. Schwarz, B.I. Prenitzer, L.A. Giannuzzi, R.B. Irwin, F. A. Stevie, Ion channeling effects on the focused ion beam milling of Cu, J. Vac. Sci. Technol. B Microelectron. Nanom. Struct. (2001), https://doi.org/10.1116/1.1368670.
[54] H. Xie, N. Gao, K. Xu, G.H. Lu, T. Yu, F. Yin, A new loop-punching mechanism for helium bubble growth in tungsten, Acta Mater. (2017), https://doi.org/10.1016/j.actamat.2017.09.005.
[55] S. Wang, W. Guo, Y. Yuan, N. Gao, X. Zhu, L. Cheng, X. Cao, E. Fu, L. Shi, F. Gao, G. H. Lu, Evolution of vacancy defects in heavy ion irradiated tungsten exposed to helium plasma, J. Nucl. Mater. (2020), https://doi.org/10.1016/j.jnucmat.2020.152051.
[56] T. Hyodo, R.J. Douglas, R. Grynszpan, B.T.A. McKee, A.T. Stewart, Temperature dependence of positron trapping at small voids in neutron-irradiated Mo, J. Phys. F Met. Phys. 13 (1983) 573–579.
[57] M. Eldrup, M. Li, L.L. Snead, L.L.S.J. Zinkle, Characterization of defect accumulation in neutron-irradiated Mo by positron annihilation spectroscopy, Nucl. Instruments Methods Phys. Res. Sect. B Beam Interact. with Mater. Atoms 266 (2008) 3602–3606.
[58] M. Li, M. Eldrup, T.S. Byun, N. Hashimoto, L.L. Snead, S.J. Zinkle, Low temperature neutron irradiation effects on microstructure and tensile properties of molybdenum, J. Nucl. Mater. 376 (2008) 11–28, https://doi.org/10.1016/j.jnucmat.2007.12.001.
[59] S.V. Naidu, A. Gupta, R. Sen, P. Roy, R.K. Bhandari Sen, Positron annihilation study of post-irradiation annealing of defects in α-irradiated molybdenum, Philos. Mag. A 52 (1985) 255–266.
[60] J. Dryzek, M. Wróbel, Recovery and recrystallization in molybdenum studied by positron annihilation and X-ray methods, Int. J. Refract. Met. Hard Mater. 97 (2021), 105514.
[61] J. Dryzek, M. Wróbel, Detection of dynamical recrystallization in a tribolayer of pure molybdenum using positron annihilation and EBSD techniques, Wear 466–467 (2021), 203524.
[62] J.M.C. Robles, E. Ogando, F. Plazaola, Positron lifetime calculation for the elements of the periodic table, J. Phys. Condens. Matter 19 (2007), 176222, https://doi.org/10.1088/0953-8984/19/17/176222.

[63] L.C. Smedskjaer, B.W. Veal, D.G. Legnini, A.P. Paulikas, L.J. Nowicki, Positron trapping in the superconductor YBa2Cu3Ox: Ba2Cu3Ox, Phys. B+C. 150 (1988) 56–60, https://doi.org/10.1016/0378-4363(88)90106-4.
[64] J. Čížek, O. Melikhova, Z. Barnovská, I. Procházka, R.K. Islamgaliev, Vacancy clusters in ultra fine grained metals prepared by severe plastic deformation, J. Phys. Conf. Ser. 443 (2013), 012008, https://doi.org/10.1088/1742-6596/443/1/012008.
[65] F. Lukáč, J. Čižek, J. Knapp, I. Procházka, P. Zháňal, R.K. Islamgaliev, Ultra fine grained Ti prepared by severe plastic deformation, J. Phys. Conf. Series, Institute of Physics Publishing (2016), https://doi.org/10.1088/1742-6596/674/1/012007.
[66] D. Kiener, C. Motz, M. Rester, M. Jenko, G. Dehm, FIB damage of Cu and possible consequences for miniaturized mechanical tests, Mater. Sci. Eng. A 459 (1) (2007) 262.
[67] E.I. Preiß, B. Merle, Y. Xiao, F. Gannott, J.P. Liebig, J.M. Wheeler, M. Göken, Applicability of focused Ion beam (FIB) milling with gallium, neon, and xenon to the fracture toughness characterization of gold thin films, J. Mater. Res. 36 (2021) 2505–2514, https://doi.org/10.1557/s43578-020-00045-w.
[68] F. Granberg, A. Litnovsky, K. Nordlund, Low energy sputtering of Mo surfaces, J. Nucl. Mater. 539 (2020), 152274, https://doi.org/10.1016/j.jnucmat.2020.152274.
[69] W. Qin, S. Jin, X. Cao, Y. Wang, P. Peres, S.Y. Choi, C. Jiang, F. Ren, Influence of nanochannel structure on helium-vacancy cluster evolution and helium retention, J. Nucl. Mater. (2019), https://doi.org/10.1016/j.jnucmat.2019.151822.

Agnieszka T. Krawczynska[a], Malgorzata Lewandowska[a], Anthony T. Fry[b]
[a]Warsaw University of Technology, Faculty of Materials Science and Engineering, Warsaw, Poland
[b]National Physical Laboratory, Hampton Road, Teddington, England

Microstructural characterization and residual stress distribution in a nanostructured austenitic stainless steel

In this paper, residual stress distribution is investigated by a novel X-ray cosα diffraction technique in a nanostructured austenitic stainless steel after hydrostatic extrusion processes. Hydrostatic extrusion performed at 20 °C and with a total true strain of 2.3 leads to the creation of a nanostructure consisting of nanotwins and shear bands. The results reveal that the greatest compressive residual stresses of –1 GPa are found 3 mm from the surface of the nanostructured austenitic stainless steel. These compressive residual stresses restrict crack growth into the material, thereby preventing catastrophic failure.

Keywords: Residual stresses; X-ray diffraction (XRD); Nanostructured materials; Austenitic stainless steel

1. Introduction

Recently, much effort has been made to transform a conventional micrograined microstructure into an ultrafine grained and nanocrystalline one using the methods of severe plastic deformation (SPD). The most effective SPD techniques are: equal channel angular pressing (ECAP), accumulative roll-bonding (ARB), cyclic extrusion compression (CEC), high pressure torsion (HPT) and hydrostatic extrusion (HE) [1, 2]. Among them one can single out HE as this is a technique that leads to the creation of quite large volumes of materials in the form of rods compared with other techniques, which was described in [3] by Lewandowska and Kurzydlowski. SPD can be successfully applied to refine the microstructure of various materials including austenitic stainless steels. Austenitic stainless steels are especially interesting materials due to their excellent corrosion and thermomechanical properties. They can be applied as structural materials in biomedical, pharmaceutical, petrochemical and nuclear power related applications. One of their main disadvantages is a relatively low strength. This can be significantly improved using SPD. The improvement in strength of a nanostructured and ultrafine grained austenitic stainless steel compared with a microcrystalline one has been reported in many works. As a result of the grain refinement after HPT and HE the strength increases to 1 900 MPa and 1 750 MPa, respectively [4, 5]. Moreover, SPD of steels can lead to the improvement of wear and corrosion resistance [6–8]. All these properties of steels after various SPD processes are reported in the literature. However, it seems quite obvious that apart from these properties SPD has an impact on others such as residual stresses. Their presence can contribute to material failure by mechanisms such as creep, fatigue and stress corrosion cracking, with the majority of failures initiating at or close to the surface. For this reason, residual stresses in the near-surface region which are tensile are considered detrimental to material performance and those that are compressive are beneficial, as proved for example by Webster [9]. The issue of residual stress measurements to the best knowledge of the authors is neglected for nanomaterials and ultrafine grained materials obtained by SPD. Measurements which have been performed mainly refer to refined microstructures obtained by shot peening as proved Zhan et al. [10]. Shot peening is not an SPD technique, but is a mechanical surface treatment in which small spherical peening media with sufficient hardness are accelerated in peening devices of various kinds and impact with the surface of the treated work piece with a quantity of energy able to cause surface plastic deformation. Shot peening is capable of introducing high compressive stresses close to the surface and leads to the improvement of the fatigue resistance. It is certain that the SPD techniques create high residual stresses. Their magnitude is not well described since Alexandrov et al. [11] found that materials after SPD are highly textured and in the case of textured materials, the application of the conventional X-ray $\sin^2\psi$ technique is limited. However, a few reports can be found. For example, Mizera et al. [12] measured residual stresses using a $\sin^2\psi$ technique in Ti–Al and Ti–Al–Nb refined by HPT. They were found to be compressive of approximately 660 MPa and 420 MPa in Ti–Al and Ti–Al–Nb, respectively.

In this work, an attempt has been made to evaluate the residual stresses in a nanostructured austenitic stainless steel processed by HE using the cosα diffraction technique, which enables the measurement of stresses with a high precision and short time even for highly textured materials [13–19]. This technique has recently enjoyed widespread commercial application. It is still in the phase of optimization, with lately X-ray incident angle oscillation introduced by Miyazaki et al. and described in detail [15]. Moreover, Delbergue et al. [19] found that the cosα method showed better measurement repeatability than the $\sin^2\psi$ when applied on a martensitic steel.

2. Experimental procedure

Sandvik Bioline 316LVM austenitic stainless steel, supplied as annealed 50 mm diameter rods, possessing the chemical composition shown in Table 1, was used in this study.

Billets were cut from rods and subjected to an HE process [20, 21]. The HE process was performed under various conditions. Hot HE of the billet heated to a temperature of 1 000 °C was realized in one pass to achieve a final diameter of 25 mm, equating to a total true strain of 1.4. HE at 20 °C was realized in two passes to achieve a final diameter of 25 mm and in five passes to achieve a final diameter of 16 mm equating to total true strains of 1.4 and 2.3, respectively. In this article, these samples will be referred to as HOT_HE_1.4, HE_1.4 and HE_2.3.

The X-ray diffraction (XRD) profile of HOT_HE_1.4 was obtained using a Bruker D8 Advance diffractometer with Co-K_α irradiation. The microstructures were examined using a JEOL JEM 1200 EX transmission electron microscope (TEM) operated at 120 kV. High-resolution imaging was performed using a Hitachi-HD2700 scanning transmission electron microscope (STEM) equipped with a Cs corrector and operated at 200 kV. For the transmission electron microscopy examination, the samples were prepared by mechanical polishing to a disk thickness of about 100 µm. Further thinning to reach a thickness appropriate for electron transparency was carried out by electropolishing using Struers electrolyte A2. The thin foils were cut to observe the microstructure on longitudinal and cross section. The microhardness of the samples was measured using Vickers method under a load of 200 g.

For residual stress measurements, samples were polished according to a conventional mechanical polishing procedure (firstly with diamond suspension containing particles of 3 µm in diameter under a load of 15 N for 10 min and subsequently with diamond particles of 1µm in diameter under a load of 10 N for 10 min). Residual stresses were measured on cross-sections of samples using a Pulstec µ-x360 XRD system (Fig. 1). The residual stress measurement is based on the cosα analysis method. This method uses a single fixed angle of incident X-rays, in this case 30° inclined to the sample surface. All the 360°-omnidirectional diffracted X-rays are collected by a 2-dimensional detector plate in a single exposure, producing an image of the whole Debye–Scherrer ring, from which the residual stress is determined. The principle of this method was first developed by Taira et al. [13]. Hiratsuka et al. [14] showed good agreement between this technique and with measured stresses applied mechanically. The measurement was conducted using Cr-K_β (λ = 2.085 Å) with a 1 mm pinhole collimator. Additionally, oscillations were applied for measurements of the annealed samples – coarse grained in order to improve the measurement accuracy. Residual stresses were calculated by analysing the Debye ring from the {311} planes, assuming a Young's modulus of 193 GPa, a Poisson's ratio of 0.3 and a d_0 of 148.513° 2-theta as the reference value – a value for the austenitic steel free from stresses. The values of residual stresses presented are directly calculated by the software and corrected manually in the case of highly textured areas through the re-evaluation of the diffraction cone. The manual correction involved altering the range over which the software made the calculation, essentially reducing the portion of the diffraction cone being used. Once this was done the software performed the analysis as before but on a reduced dataset. For every value of residual stress there is an associated reliability value, which expresses the potential error band of a single measurement.

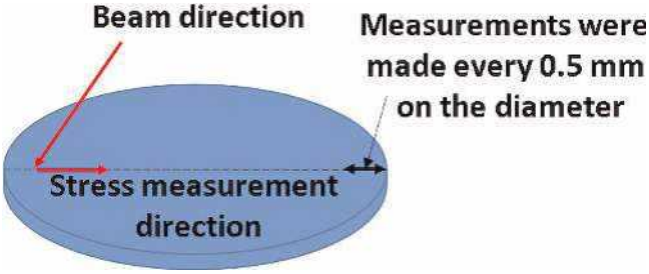

Fig. 1. A sketch of the specimen indicating the location and also the direction of residual stress measurement.

3. Results and discussion

The microstructures after HE to a strain of 1.4 carried out at room and elevated temperatures are presented in Fig. 2. For the HOT_HE_1.4 sample, there are two types of region visible on cross-sections. Type 1 features well developed subgrains with the average size of 300 nm in the orientation <001> (Fig. 1c). Type 2 possesses deformed microstructure with a high density of dislocations arranged in dislocation walls and cells with similar size of 300 nm. The orientation z of these regions is widely spread around <111> direction, as illustrated in Fig. 2d. On longitudinal sections, the subgrains in type 1 region are elongated, while dislocation cells in type 2 regions are more equiaxial. In the case of the HE_1.4 sample, the microstructure is highly inhomogeneous and areas deformed by dislocation slip and twinning are visible. On longitudinal sections microstructural elements are weakly oriented along the HE direction. Further deformation leads to the refinement of the microstructure to the nanoscale (Figs. 3 and 4). When observed on the cross-section (Fig. 3), the microstructure consists of deformation twins of 20 nm in width and 200 nm on average in length and shear bands. The presence of deformation twins is confirmed by observations in the dark field (Fig. 3b–d). On the longitudinal section, microstructural elements are arranged along the HE direction and one can distinguish deformation nanotwins of a few nanometers in width (Fig. 4b).

Table 1. Chemical composition (wt.%) of 316LVM austenitic stainless steel (Fe bal.).

C	Si	Mn	P	S	Cr	Ni	Mo	Cu	N
0.025	0.6	1.7	0.025	0.003	17.5	13.5	2.8	0.1	<0.1

The residual stress profile is of interest since it affects component fatigue performance. Initially, measurements were performed on a cross-section of an annealed sample in order to assess the impact of preparation technique on the measured stresses. One could expect that annealed samples will be stress-free. However, some stresses are introduced during polishing. In this experiment the average value of residual stress is –196 MPa in an annealed sample polished in a conventional way with a standard deviation of 58 MPa and the reliability of ±76 MPa. This is in line with the impact of standard polishing on residual stresses reported by Rocha et al. [22]. It must be pointed out that these compressive stresses introduced by polishing differ between samples as the samples differ in the degree of work hardening, which can be represented by changes in microhardness values. In the annealed sample the microhardness is on average 168 Hv0.2. After hot HE, it increases to 253 Hv0.2. HE at 20 °C to the true strain of 1.4 and 2.3 causes a considerable increase in microhardness to 424 and 435 Hv0.2, respectively. The residual stresses were then measured at the diameter of samples after various HE processes applying the cosα technique. As one can see from the X-ray diffraction profile of a HOT_HE_1.4 sample in Fig. 5, there is no signal from {220} or {311} planes which are commonly used in the $\sin^2\psi$ method. For this reason, this technique is not suitable in this case. Results of these

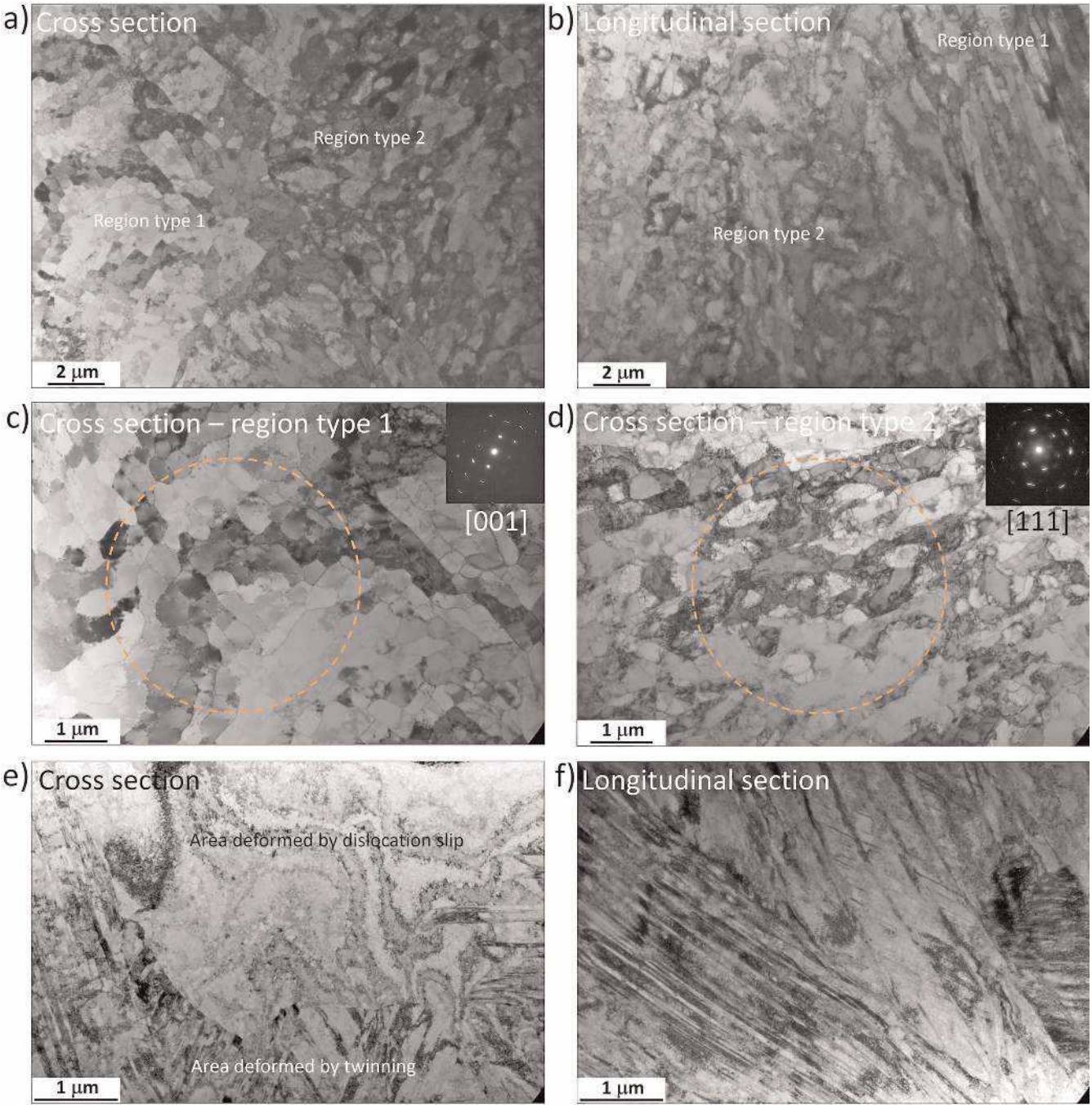

Fig. 2. Microstructures of (a–d) HOT_HE_1.4, and (e–f) HE_1.4 samples with selected area diffraction patterns (SAED) from areas indicated by a circle.

measurements are presented in Fig. 6. In the case of a HOT_HE_1.4 sample residual stresses are distributed quite homogeneously, with a tendency for them to be more tensile in the middle than at the edges. Their value is low and can be considered insignificant if one takes into consideration the possible impact of polishing procedure on the value of residual stresses. In the case of a HE_1.4 sample, residual stresses are tensile (200 MPa) at the centre, becoming highly compressive (–500 MPa) around 7 mm from the centre. Nearer to the edge they become less compressive (–100 MPa). In the case of the HE_2.3 sample, the distribution of stresses is similar to that observed for the HE_1.4 sample. However, the changes in stress values between tensile and compressive are substantial. In the former sample, the maximum residual stresses achieved were –500 MPa in compression and 200 MPa in tension. In the case of HE_2.3 the maximum compressive stress achieved was –1 000 MPa with tensile stresses of 600 MPa. It appears that the higher the compressive stresses the higher the tensile residual stresses required to balance them. In the literature there is little information about the effect of the reduction in area on the residual stress distribution in HE rods. Inoue et al. [23] found that it is dependent on the extrusion ratio, die angle and temperature. However, no exact values of residual stresses were given. It was noticed that after hydrostatic extrusion of copper, with an extrusion ratio of 2, that tensile residual stress is left near the surface in the tangential and longitudinal directions and compressive stresses should be expected in the centre. Others reported that the compressive residual stresses in the centre of the rods increase first, when the extrusion ratio increased from 1.25 to about 2.25. Mitha [24]. found that further increase in extrusion ratio to 3.7 makes these stresses less compressive. However, in this study the reduction in area was much higher reaching 4.1 (HE_1.4) and 9.7 (HE_2.3). As a result, high tensile stresses were created in the middle of the sample reaching almost 600 MPa for the most deformed sample changing into high compressive stresses of –1 000 MPa 3 mm from the edge and then becoming less compressive near the edge. These values are novel and original as they reveal how high residual stresses can be generated in nanostructured austenitic stainless steel after HE.

These results show that the creation of nanostructure by HE leads to the creation of high compressive stresses. It is worth mentioning that by applying HE to the reduction in area of 9.7 Ye et al. [25] introduced higher compressive stresses than in highly deformed austenitic stainless steel 304 after ultrasonic nanocrystal surface modification (–450 MPa). The value of compressive stresses introduced by HE to the nanostructured sample can be compared with those present after shot peening performed on an austenitic stainless steel sample in a traditional way (–637 MPa) or after dual and triple shot peening (–683 and –756 MPa, respectively) measured by Zhan et al. [10]. Nanostructures obtained by sintering nanopowders or nanostructures obtained by SPD and subjected to annealing even without grain growth will exhibit no or much lower residual stresses. Therefore, the magnitude of residual stresses does not depend on the grain size but on the magnitude of the degree of deformation. The grain refinement is an effect of the deformation, and HE as well as shot peening can lead to the creation of nanostructures [26, 27]. It should be emphasized that while one obtains a nanostructure by SPD, the sample will contain high residual stresses. The distribution of these stresses depends on the selected deformation techniques. In the case of shot peening the compressive residual stresses are near the surface; in the case of HE they are situated 2–3 mm below the surface.

During residual stress measurements by the cosα technique Debye rings from the {311} are collected. These rings illustrate qualitatively that there is texture present in the samples via the presence of the two intense regions. In the case of an annealed sample the Debye ring is similar to a perfect ring (Fig. 6a). The intensity, however, slightly changes on the diameter, which indicates that the signal comes from only a few grains. Debye rings collected 1 mm and 4 or 6 mm from the edge and from the centre of the sample are presented in Fig. 7. It can be noticed that a highly textured microstructure is obtained after Hot HE, uniformly at the diameter. However, after HE at 20 °C the texture alters considerably at the diameter and becomes the sharpest in the middle of the sample.

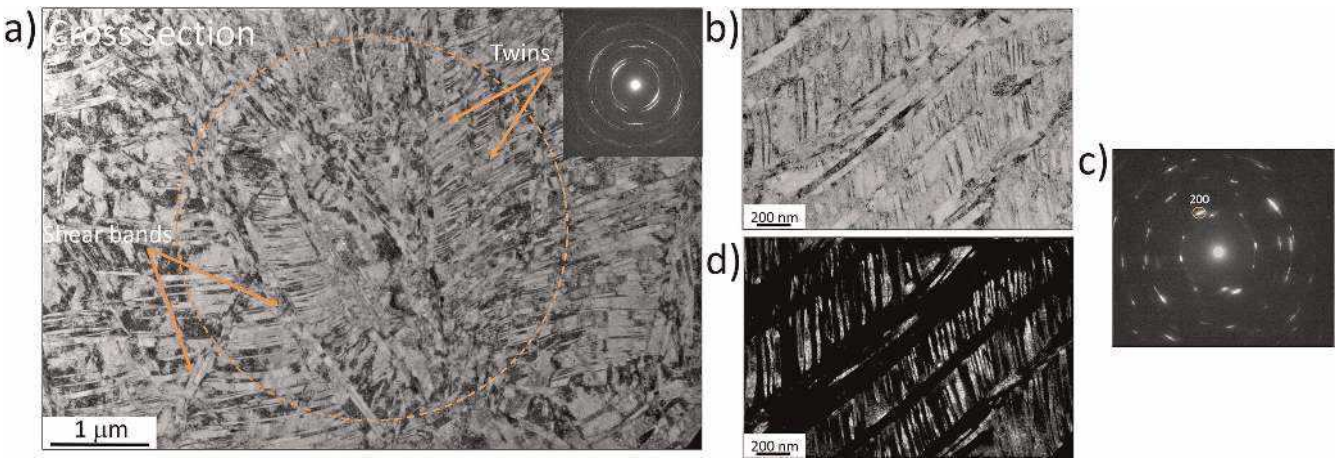

Fig. 3. Microstructures of an HE_2.3 sample – a cross-section: (a) a general view with SAED from an area indicated by a circle; (b–d) deformation twins on the cross-section in the bright and dark fields and the corresponding SAED with the circled spot used in the dark field imaging.

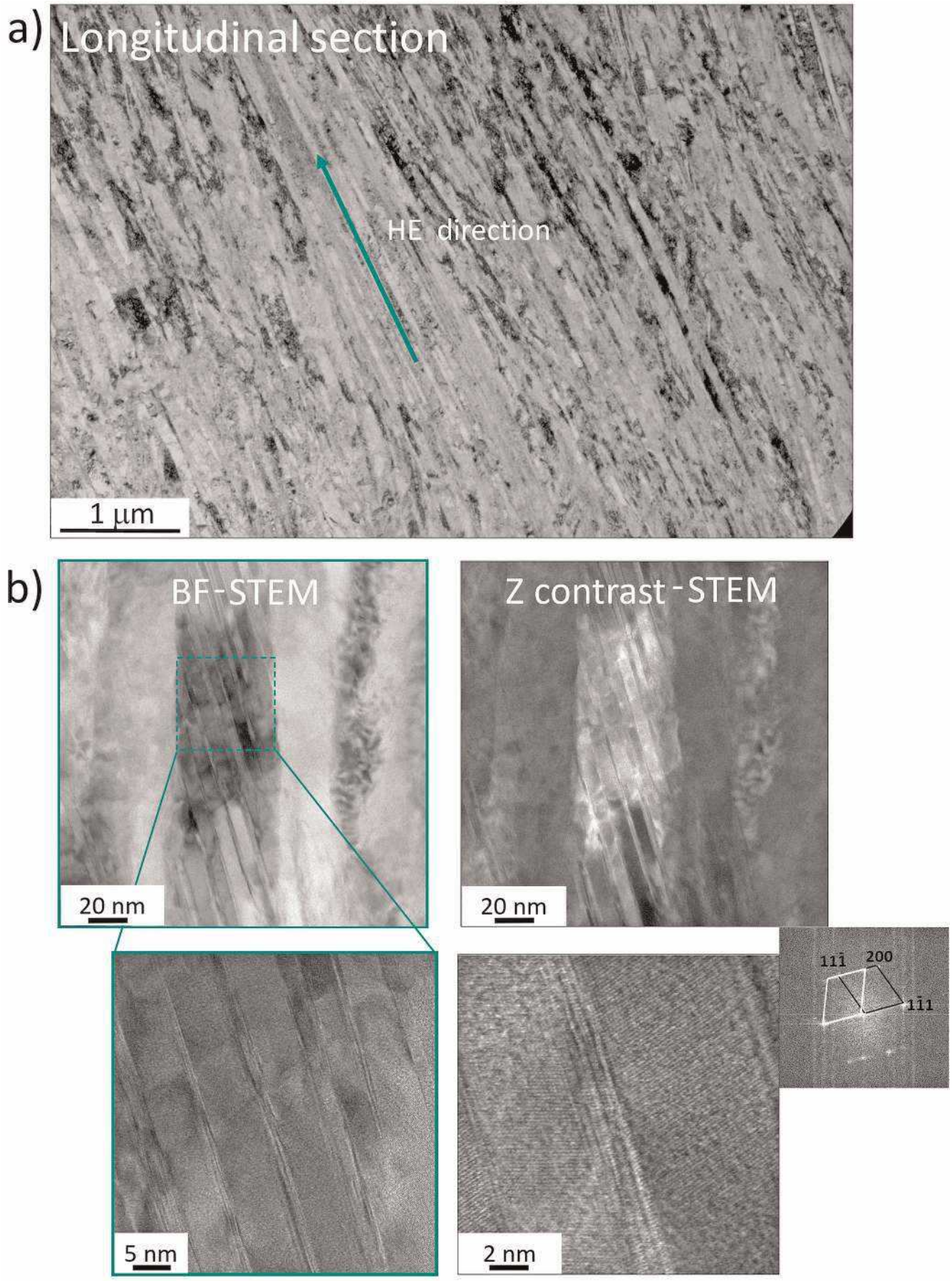

Fig. 4. Microstructures of a HE_2.3 sample – a longitudinal section: (a) a genaral view; (b) the nanotwins visible on the longitudinal section with the Fourier transform pattern in the orientation [011] of the matrix and [0$\bar{1}\bar{1}$] of nanotwins.

4. Conclusions

In summary, the novel X-ray cosα technique was successfully applied to measure the residual stresses in a nanostructured highly textured 316LVM austenitic stainless steel. HE performed at 1 000 °C led to the creation of almost stress-free samples. HE performed at 20 °C, $\varepsilon = 2.3$, introduced compressive residual stresses of the magnitude of –600 MPa and –1 000 MPa approximately 2 and 3 mm form the surface, respectively. These values are comparable with those measured for shot peened samples. The findings suggest that the compressive residual stresses restrict crack growth into the material, thereby preventing catastrophic failure.

This work was supported by Polish National Science Centre project OPUS No.UMO-2013/11/B ST8/03641. The HE was carried out at the Institute of High Pressure Physics of the Polish Academy of Sciences.

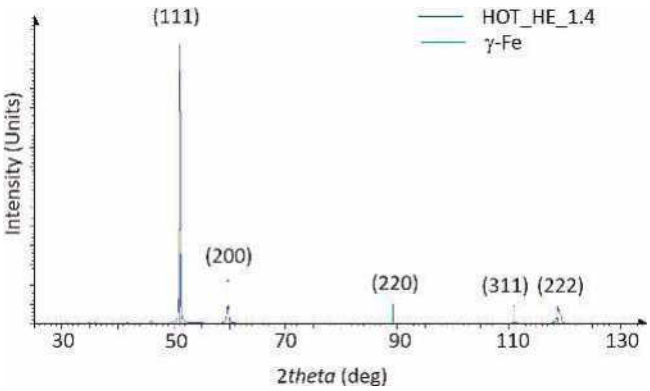

Fig. 5. The X-ray diffraction profile of a HOT_HE_1.4 sample.

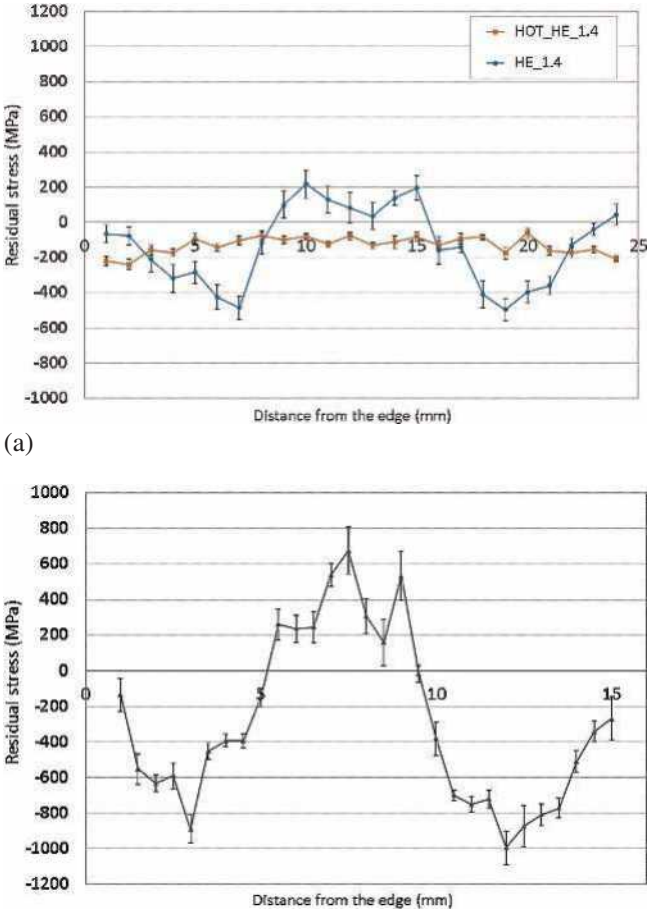

Fig. 6. Residual stress distribution along the diameter of samples: (a) HOT_HE_1.4 and HE_1.4; (b) HE_2.3 with error bars indicating the reliability value.

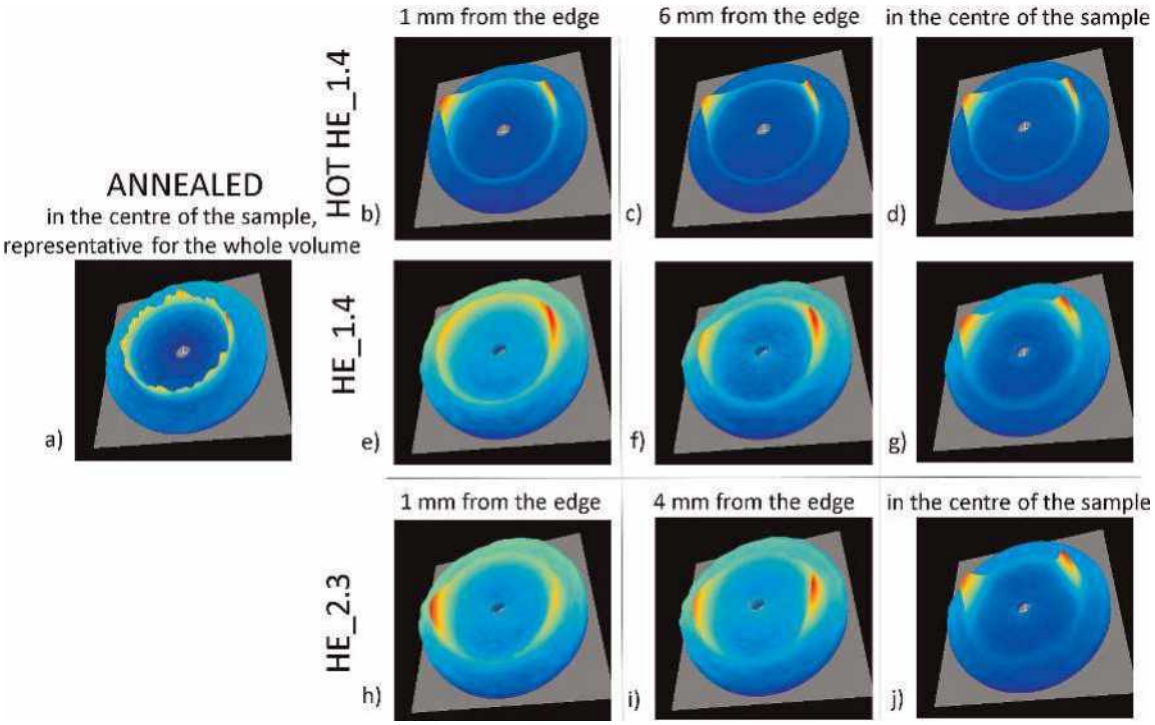

Fig. 7. 3D plots of Debye rings from the {311} planes for the (a) annealed, (b–d) HOT_HE_1.4, (e–g) HE_1.4 and (h–j) HE_2.3 samples; the intensity of the measurements increases with the change in color from blue (lowest intensity) through green to red (the highest intensity).

References

[1] R.Z. Valiev: Nat. Mater. 3 (2004) 511–516. PMid:15286754; DOI:10.1038/nmat1180
[2] R.Z. Valiev, Y. Estrin, Z. Horita, T. Langdon, M. Zehetbauer, Y.Zhu: JOM 68 (2016) 1216–1226. DOI:10.1007/s11837-016-1820-6
[3] M. Lewandowska, K. Kurzydlowski: J. Mater. Sci. 43 (2008) 72–99. DOI:10.1007/s10853-008-2810-z
[4] A. Vorhauer, S. Kleber, R. Pippan: Mater. Sci. Eng. A 410–411 (2005) 281–284. DOI:10.1016/j.msea.2005.08.119
[5] A.T. Krawczynska, T. Brynk, S. Gierlotka, E. Grzanka, S. Stelmakh, B. Pałosz, M. Lewandowska, K.J. Kurzydłowski: Mech. Mater. 67 (2013) 25–32. DOI:10.1016/j.mechmat.2013.07.017
[6] J. Budniak, M. Lewandowska, W. Pachla, M. Kulczyk, K.J. Kurzydłowski: Solid State Phenom. 114 (2006) 57–62. DOI:10.4028/www.scientific.net/SSP.114.57
[7] M. Pisarek, P. Kedzierzawski, T. Plocinski, M. Janik-Czachor, K.J.Kurzydlowski: Mater. Charact. 59 (2008) 1292–1300. DOI:10.1016/j.matchar.2007.11.002
[8] D. Klassek, T. Suter, P. Schmutz, W. Pachla, M. Lewandowska, K.J. Kurzydlowski, Olivier von Trzebiatowski: Solid State Phenom. 114 (2006) 189–195. DOI:10.4028/www.scientific.net/SSP.114.189
[9] G.A. Webster: Mater. Sci. Forum 347–349 (2000) 1–11. DOI:10.4028/www.scientific.net/MSF.347–349.1
[10] K. Zhan, C.H. Jiang, V. Ji: Mater, Lett, 99 (2013) 61–64. DOI:10.1016/j.matlet.2012.08.147
[11] I.V. Alexandrov, A.A. Dubravina, A.R. Kilmametov, V.U. Kazykhanov, R.Z. Valiev: Met. Mater.Int 9 (2003) 151–156. DOI:10.1007/BF03027271
[12] J. Mizera, Z.Pakiela, K.J. Kurzydlowski: Arch. Matall. Mater. 50 (2005) 395–402.
[13] S. Taira, K. Tanaka, T.J. Yamasaki: Soc. Mater. Sci. Japan 27 (1978) 251. DOI:10.2472/jsms.27.251
[14] K. Hiratsuka, T. Sasaki, K. Seki, Y. Hirose: International Centre for Diffraction Data. 46 (2003) 61–7.
[15] T. Miyazaki, Y. Maruyama, Y. Fujimoto, T. Sasaki: Powder Diffr. 30 (2015) 250–255. DOI:10.1017/S0885715615000433
[16] J. Ramirez-Rico, S.-Y. Lee, J.J. Ling, I.C. Noyan: J. Mater. Sci. 51 (2016) 5343–5355. DOI:10.1007/s10853-016-9837-3
[17] T. Miyazaki, T. Sasaki: Int. J. Mater. Res. 106 (2015) 1002–1004. DOI:10.3139/146.111268
[18] T. Miyazaki, T. Sasaki: Int. J. Mater. Res. 106 (2015) 237–241. DOI:10.3139/146.111179
[19] D. Delbergue, D. Texier, M. Lévesque, P. Bocher: Intern. Conf. Residual Stress 2016 2 (2016) 55–60. DOI:10.21741/9781945291173-10
[20] W. Pachla, J. Skiba, M. Kulczyk, S. Przybysz, M. Przybysz: Mater. Sci. Eng. 615 (2014) 116–127. DOI:10.1016/j.msea.2014.07.069
[21] A.T. Krawczynska, W. Chrominski, E. Ura-Binczyk, M. Kulczyk, M. Lewandowska: Mater. Des. 136 (2017) 34–44. DOI:10.1016/j.matdes.2017.09.050
[22] A.S. Rocha, T. Strohaecker, T. Hirsch: Surf. Coat. Tech. 165 (2003) 176–185. DOI:10.1016/S0257-8972(02)00768-5
[23] N. Inoue, M. Nishihara: Hydrostatic Extrusion: Theory and Applications, Elsevier Applied Science Publishers LTD, New York (1985). DOI:10.1007/978-94-009-4954-6
[24] S. Midha: PhD thesis, Cold extruded rods: residual stresses and mechanical properties, Loughborough University, UK (1976).
[25] Ch. Ye, A. Telang, A.S. Gill, S. Suslov, Y. Idell, K. Zweiacker, J.Wiezorek, Z. Zhou, D. Qian, S. Mannava, V. Vasudevan: Mat. Sci. Eng. 613 (2014) 274–288. DOI:10.1016/j.msea.2014.06.114
[26] P.K. Rai, V. Pandey, K. Chattopadhyay, L.K. Singhal, V. Singh: J. Mater. Eng. Perform 23 (2014) 4055–4064. DOI:10.1007/s11665-014-1180-8
[27] A.T. Krawczynska, M. Lewandowska, K.J. Kurzydlowski: Solid State Phenom. 140 (2008) 173–8. DOI:10.4028/www.scientific.net/SSP.140.173

(Received December 28, 2017; accepted March 26, 2018)

Correspondence address

Agnieszka Krawczyńska
PhD Faculty of Materials Science and Engineering
Warsaw University of Technology
Woloska 141
Warsaw 02-507
Poland
Tel.: +48222348455
Fax:+48222348514
E-mail: akrawczy@inmat.pw.edu.pl
Web: www.inmat.pw.edu.pl

Bibliography
DOI 10.3139/146.111672
Int. J. Mater. Res. (formerly Z. Metallkd.)
109 (2018) E; page 1–7

ISSN 1862-5282

Materials and Design 136 (2017) 34–44

Contents lists available at ScienceDirect

Materials and Design

journal homepage: www.elsevier.com/locate/matdes

Mechanical properties and corrosion resistance of ultrafine grained austenitic stainless steel processed by hydrostatic extrusion

Agnieszka Teresa Krawczynska [a,*], Witold Chrominski [a], Ewa Ura-Binczyk [a], Mariusz Kulczyk [b], Malgorzata Lewandowska [a]

[a] Warsaw University of Technology, Faculty of Materials Science and Engineering, Woloska 141, 02-507 Warsaw, Poland
[b] Institute of High Pressure Physics, Sokolowska 29/37, 01-142 Warsaw, Poland

HIGHLIGHTS

- After HE performed at RT strength reaches 1468 MPa and total elongation 8.4%.
- After HE at 1000 °C, strength reaches 911 MPa and total elongation 23.0%.
- HE at RT and at 1000 °C assures resistance to uniform corrosion in 0.1 M H_2SO_4.
- HE at 1000 °C assures resistance to corrosion in a 0.1 M H_2SO_4 + 0.5 M NaCl solution.

GRAPHICAL ABSTRACT

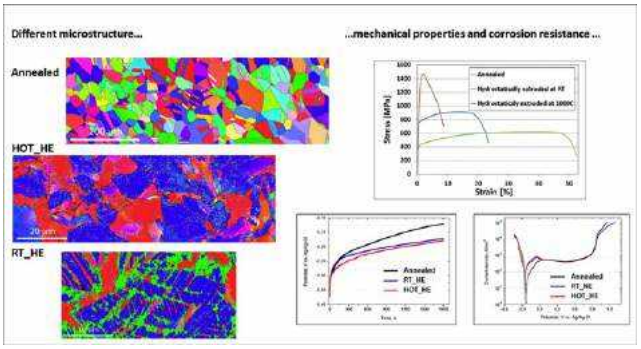

ARTICLE INFO

Article history:
Received 29 May 2017
Received in revised form 30 August 2017
Accepted 20 September 2017
Available online 21 September 2017

Keywords:
Austenitic stainless steel
Hydrostatic extrusion
Severe plastic deformation
Dynamic recrystallization
Corrosion resistance

ABSTRACT

The material studied is a commercially available 316LVM stainless steel with an initial grain size of 30 μm. To refine the microstructure down to the nanoscale, hot (at 1000 °C) and room temperature hydrostatic extrusion were applied with a total true strain of 1.4. An annealed sample with coarse grains of 35 μm in diameter was used as a reference sample. The results indicate that after hot hydrostatic extrusion, the microstructure consisted mainly of cells with tangled dislocation walls, while after room temperature hydrostatic extrusion, twins of various width and shear bands could be distinguished. Hydrostatic extrusion is also an efficient way to tailor the corrosion resistance and mechanical properties of 316LVM stainless steel. Performed at room temperature, hydrostatic extrusion resulted in an ultra-high-strength material with limited but sufficient ductility. Performed at high temperature, hydrostatic extrusion resulted in a material with a very good combination of strength (approximately 900 MPa) and ductility (elongation to failure higher than 20%). Both hydrostatically extruded steels maintained good passivation behavior in 0.1 M H_2SO_4. In the presence of chloride ions, susceptibility to localized attack increased for the steel extruded at room temperature, but did not change for the hot-extruded steel.

1. Introduction

Austenitic stainless steels are widely used in many industrial sectors, including chemical and bioengineering, due to their good corrosion resistance. However, conventional microcrystalline austenitic stainless steels exhibit relatively low hardness and mechanical strength. These

* Corresponding author.
E-mail address: akrawczy@inmat.pw.edu.pl (A.T. Krawczynska).

https://doi.org/10.1016/j.matdes.2017.09.050
0264-1275/

drawbacks restrict their wider use in other industrial branches. The mechanical properties (strength and fatigue behavior) of such steels can be significantly improved by refining their structure to the nanoscale regime, as has already been proved in a number of studies [1–9]. Microstructural refinement is an effective approach for strengthening; it can be induced by extremely high plastic deformation using such methods as equal channel angular pressing (ECAP) [2,3], high-pressure torsion (HPT) [4–5], dynamic plastic deformation (DPD) [7], and hydrostatic extrusion (HE) [8,9].

In general, grain size refinement results in improved resistance to corrosion, but that improvement is strongly dependent on the processing route used to obtain the refined structure [10–13]. The complex interplay between a material and the method of processing affects several characteristics, such as grain size distribution, chemical homogeneity, internal stresses, dislocation density, and the volume fraction of grain boundaries and texture, all of which affect corrosion resistance [14,15]. It has been demonstrated that the passive films formed on ultrafine-grained (UFG) and/or nanostructured (NS) stainless steel have better barrier properties. A study by Zheng et al. [16] showed that NS 304 stainless steel obtained by ECAP exhibits higher corrosion resistance in 0.5 M H_2SO_4. The improved barrier properties of the passive oxide were attributed to its greater compactness and stability. Similarly, Zhang et al. [17] found that the improved passivity properties of mild steel are due to the formation of a more continuous and denser passive film. In contrast, the improved corrosion resistance of an Fe-20Cr alloy obtained by a high-energy ball mill was attributed to the Cr enrichment of the passive film [18].

In solutions containing Cl^- ions, UFG and NS stainless steels generally show improved resistance against pitting corrosion [18–21]. A study by Pisarek [22,23] revealed that a 316 stainless steel obtained by hydrostatic extrusion exhibited an extended stable passivity region, by about 0.4 V in a borate buffer + 0.1 M NaCl. A comprehensive review of the pitting corrosion of NS stainless steel was presented by Liu et al. [24]; it was demonstrated that a nanocrystalline structure leads to a faster repassivation rate and lower probability of stable pit growth. Hamada et al. revealed that cold-rolling deteriorates the corrosion resistance while the annealing of the cold-rolled austenitic steels improves their resistance to localized attack [25]. However, there is a lack of detailed studies on the influence of grain structure and grain boundary characteristics on the corrosion behavior of UFG materials.

An improvement in strength is often accompanied by a decrease in ductility, due to the inability to accumulate dislocations. This feature is one of the major drawbacks of UFG/NS materials produced by severe plastic deformation (SPD) and has restricted their practical application. However, it should be emphasized that some research groups have demonstrated UFG or NS materials with improved ductility [26–28]. To improve the ductility of UFG/NS materials produced by SPD, several strategies have been employed [29,30]. In this context, the key issue is to provide stabilizing mechanisms to avoid the instabilities that occur during straining. One strategy that seems promising is to create a bimodal or multimodal grain size distribution. In such a microstructure, large grains are responsible for great elongation, and the nanostructure for enhanced strength. The idea is simple and can be induced through unconventional as well as conventional thermomechanical treatment. In the case of Cu, after ECAP cryo-rolling to >2000% and recrystallization at 200 °C for 3 min, a bimodal grain size distribution was obtained [29]. Approximately 25% of the material was composed of micron-sized grains, while the rest of the grains had sizes ranging from nanocrystalline up to a few hundred nanometers. This sample displayed high uniform strain and high overall ductility, while its strength was five to six times higher than that of coarse-grained Cu. By changing the volume fraction and distribution of the coarse grains, one can tailor the material to have certain desired properties.

In the case of austenitic stainless steels, a spectacular result has been obtained for a DPD-processed and annealed material, where a combination of 1 GPa tensile strength with an elongation-to-failure of 27% was achieved [7,31,32]. Such extraordinary properties were attributed to the material's specific microstructure, consisting of coarse grains surrounded by nanotwins. The nanotwin bundles acted as a crucial strengthening component, while statically recrystallized grains in the shear banding regions were responsible for the high ductility. Also, cold rolling and reversion annealing may lead to high strength (ranging from 600 to 1000 MPa) combined with the elongation varying from 27 to 52%, depending on the annealing temperature [26]. However, for other techniques of producing UFG and NS materials, mostly based on SPD, a general trend has been observed: the higher the strength, the lower the ductility. Therefore, there is still a need to develop a technology capable of obtaining better ductility without compromising strength and corrosion resistance.

In this context, the present study was initiated to evaluate the applicability of HE as a method of producing high strength corrosion resistant austenitic stainless steel with improved ductility. The major advantage of HE includes its capability to produce relatively large volumes of products. In addition, it can be conducted at either room or elevated temperature, making it possible to obtain various microstructures that differ in terms of grain size and grain boundary characteristics. Both factors are known to play an important role in controlling the properties of materials. Therefore, the specific aim of the present study is to evaluate the influence of various microstructures (that differ in terms of grain size and grain boundary characteristics) on the mechanical properties and corrosion resistance of an austenitic stainless steel.

2. Material and methods

Sandvik Bioline 316LVM, a low carbon, vacuum-melted 316L grade stainless steel, UNS S31673 certified to ASTM F138, supplied as annealed 50 mm-diameter rods, of the chemical composition shown in Table 1, was used in this study.

Billets were cut from the rods and subjected to an HE process according to the procedure described in Ref. [33]. The HE process was performed under two conditions. Hot HE of a billet pre-heated to a temperature of 1000 °C was performed in one pass to achieve a final diameter of 25 mm (which corresponds to a cross-section reduction ratio of 2). HE at 20 °C was carried out in three passes to achieve the same final diameter, equivalent to a total true strain of 1.4. The strain rate during the hot HE was 3.05 s^{-1} and the room temperature HE 0.94, 2.39 and 3.66 s^{-1}, respectively in each pass. In the further text, these samples will be referred to as HOT_HE and RT_HE, respectively. The as-received annealed sample was used as a reference.

The samples for transmission electron microscopy (TEM) examination and electron backscatter diffraction (EBSD) orientation mapping were mechanically polished to a disk thickness of about 100 μm. Further thinning to reach a thickness appropriate for electron transparency was carried out by electropolishing using Struers electrolyte A2. The microstructures of the cross-sections perpendicular to the extrusion axis were examined using a JEOL 1200 TEM at 120 kV. In order to better display the substructure, weak beam observations were applied. The EBSD orientation mapping was performed on a Hitachi SU70 analytical scanning electron microscope (acceleration voltage of 20 kV) equipped with a Schottky emitter.

Depending on the degree of deformation, various step sizes were used to capture the details of the microstructure, i.e. 500, 80 and 40 nm for the annealed, HOT_HE and RT_HE samples, respectively. Because of the high level of deformation applied to the material investigated, high density of microstructural defects and significant grain refinement reduced the index rate of the Kikuchi maps during the

Table 1
Chemical composition (wt%) of austenitic stainless steel 316LVM.

C	Si	Mn	P	S	Cr	Ni	Mo	Cu	N
0.025	0.6	1.7	0.025	0.003	17.5	13.5	2.8	0.1	<0.1

EBSD scans. However, for the HOT_HE sample, this was still close to 80%, and so these maps were treated as reliable. In the case of the RT_HE sample, the index rate was at a level of 56%. The orientation map obtained for this condition is presented in the Results section, but no detailed analysis was performed due to its poor quality. The index rate of the annealed sample was close to 99%. Data analysis and orientation maps were prepared with dedicated HKL Channel5 software. On the orientation maps, the boundaries with a misorientation angle >3° are indicated by white lines, and boundaries with misorientation angle >15° by black lines. The grains for grain size calculations from the orientation maps were recognized as regions surrounded with boundaries with a misorientation angle >15°. Qualitative and quantitative studies of the subgrains visible in TEM pictures were carried out using stereological and image analysis methods [34,35]. The grain and subgrain sizes were determined as the equivalent diameter, d_2, defined as the diameter of a circle having an area equal to the surface area of a given grain. To establish the variation of the size of individual grains, a variation coefficient, $CV(d_2)$, defined as the ratio of the standard deviation to the mean value, was determined. The tensile tests were carried out on an MTS Q Test/10 machine at a strain rate of 10^{-3} 1/s. The samples for the tensile tests had the following dimensions: a diameter of 2 mm and a gauge length of 18 mm. For each condition three samples were tested.

The electrochemical measurements were performed in 0.1 M H_2SO_4 and 0.1 M H_2SO_4 + 0.5 M NaCl solutions made from analytical grade reagents and distilled water and deaerated using argon prior and during the measurements. Before electrochemical testing, the surface of the samples was successively ground with 2500# SiC papers, and then polished using polishing cloths with a diamond suspension of from 3 to 1 μm until a mirror-bright surface finish was obtained. Finally, the surfaces were cleaned ultrasonically in ethanol.

The measurements were performed using an AutoLab PGSTAT302N potentiostat/galvanostat from Methrom in a conventional three-electrode electrochemical cell, with the sample as a working electrode (the exposed surface was 0.79 cm^2), a platinum plate as auxiliary electrode, and a silver chloride electrode as a reference electrode. Before polarizing, the samples were cleaned cathodically at a current of −5 mA for 180 s to remove any pre-existing oxides. The open circuit potential was measured for 30 min before the measurement. The potentiodynamic scanning was initiated 150 mV below the open circuit potential (OCP) at a scan rate of 1 mV/s, and the scan was stopped (0.1 M H_2SO_4) or reversed (0.1 M H_2SO_4 + 0.5 M NaCl) when the current density reached 1 mA/cm^2.

3. Results

3.1. EBSD observations

EBSD orientation maps for annealed (as-received) and HE processed samples are presented in Fig. 1. The annealed sample has a microstructure typical of a recrystallized, low stacking fault energy material. It consists of coarse grains having a privileged orientation of ⟨100⟩ parallel to the extrusion direction (Fig. 1a). There is also a high density of annealing twins present in this sample, as can be seen in both the orientation map in Fig. 1a and the misorientation angle distribution chart (Fig. 2a) – a dominate misorientation angle of 60° is typical of the twin boundaries.

In the case of the HOT_HE sample, primary grain boundaries are no longer evident, and the microstructure has undergone an advanced transformation. According to the EBSD maps, areas of orientation of ⟨111⟩ and ⟨100⟩ parallel to the extrusion direction are formed (Fig. 1b) during hot HE. These two orientations are typical of fcc materials after HE. However, the intensity of the former is much stronger. It is important to note that, in the case of the HOT_HE sample, there is a high density of low-angle grain boundaries with a misorientation of <15 degrees (Fig. 2b). They are arranged in the substructure within bigger larger areas having a particular orientation (see the white lines in Fig. 2b). It should be noted that only grain boundaries with a misorientation angle higher >3° are presented in this map. More detailed observations of the substructure were performed with TEM, as discussed in the next subsection.

The EBSD orientation map of the RT_HE sample is presented in Fig. 1c. The typical orientations of ⟨100⟩ and ⟨111⟩ parallel to the extrusion direction are accompanied by unresolved areas marked in green. This indicates that this sample contains a high density of defects or microstructure elements of sizes below the resolution of the EBSD technique. However, one can recognize regions with a low index rate, which most likely contain deformation twins and shear bands.

The average equivalent diameter of grains in the annealed and HOT_HE samples are presented in Table 2. It should be noted that for the calculation of the grain size, only high angle grain boundaries were taken into account. In the annealed sample, the microstructure is homogenous and the average grain equivalent diameter is 35 μm. In the case of HOT_HE sample, it is inhomogeneous and one can distinguish larger grains (with the average diameter of 6.4 μm) which have specific orientations of either ⟨100⟩ and ⟨111⟩ parallel to the extrusion direction and smaller ones whose average equivalent diameter is 1.2 μm and are randomly oriented. The larger grains are divided into subgrains, which are analyzed in detail in Section 3.2.

3.2. TEM observations

In the case of the HOT_HE sample, the TEM observations revealed that the ⟨111⟩ oriented regions consist of a high density of dislocations arranged in dislocation walls, while some randomly distributed dislocations are also visible (Fig. 3a–b). The ⟨100⟩ regions consist of square-shaped subgrains with a low density of dislocations in their interiors (Fig. 3c–d). The smearing of diffraction spots in the diffraction pattern in the ⟨111⟩ orientated regions is more profound than in the ⟨100⟩ regions, suggesting that the number of misorientations in the former regions is higher. Moreover, new completely recrystallized grains with an orientation of ⟨100⟩ of approximately 3 μm in size were formed (Fig. 3e).

The presence of dislocation substructures in ⟨100⟩ oriented regions indicates that dynamic recrystallization (DRX) occurs during hot HE [36]. The ⟨100⟩ orientation is typical of recrystallized grains. The Schmid factor for resolved shear stress shows eight active slip systems in a grain with ⟨100⟩ orientation parallel to the HE axis. This favors the formation of cells and subgrains within grains so oriented (Fig. 3c–d). In addition, the rare existence of dislocation-free recrystallized grains suggests static recrystallization (Fig. 3e) [36]. Static recrystallization could have taken place after the hot working, while the workpiece remaining at a high temperature. Another possibility is that new dislocation-free grains might form during hot deformation, with their number increasing during the cooling stage of the sample after deformation [37]. The average equivalent diameters of subgrains in the HOT_HE sample are presented in Table 3. In the ⟨111⟩ oriented regions, subgrains of 560 nm in size are present. Smaller subgrains of 359 nm are visible in the ⟨100⟩ oriented regions.

In the case of the RT_HE sample, the microstructure consists of nanotwins and shear bands, visible in Fig. 4. Austenitic stainless steels are low stacking fault energy materials, and so their plastic deformation at relatively low temperatures occurs through a number of mechanisms present simultaneously. Firstly, mobility of dislocations is significantly lower than that of high stacking fault energy materials. Secondly, perfect dislocations are prone to dissociate into partials that can glide on only one plane. Due to this phenomenon, deformation twins are created, such as those visible in Fig. 4. On the other hand, when the ability to increase the density of dislocations and nanotwins has been reduced, plastic deformation can be accommodated by the formation of shear bands.

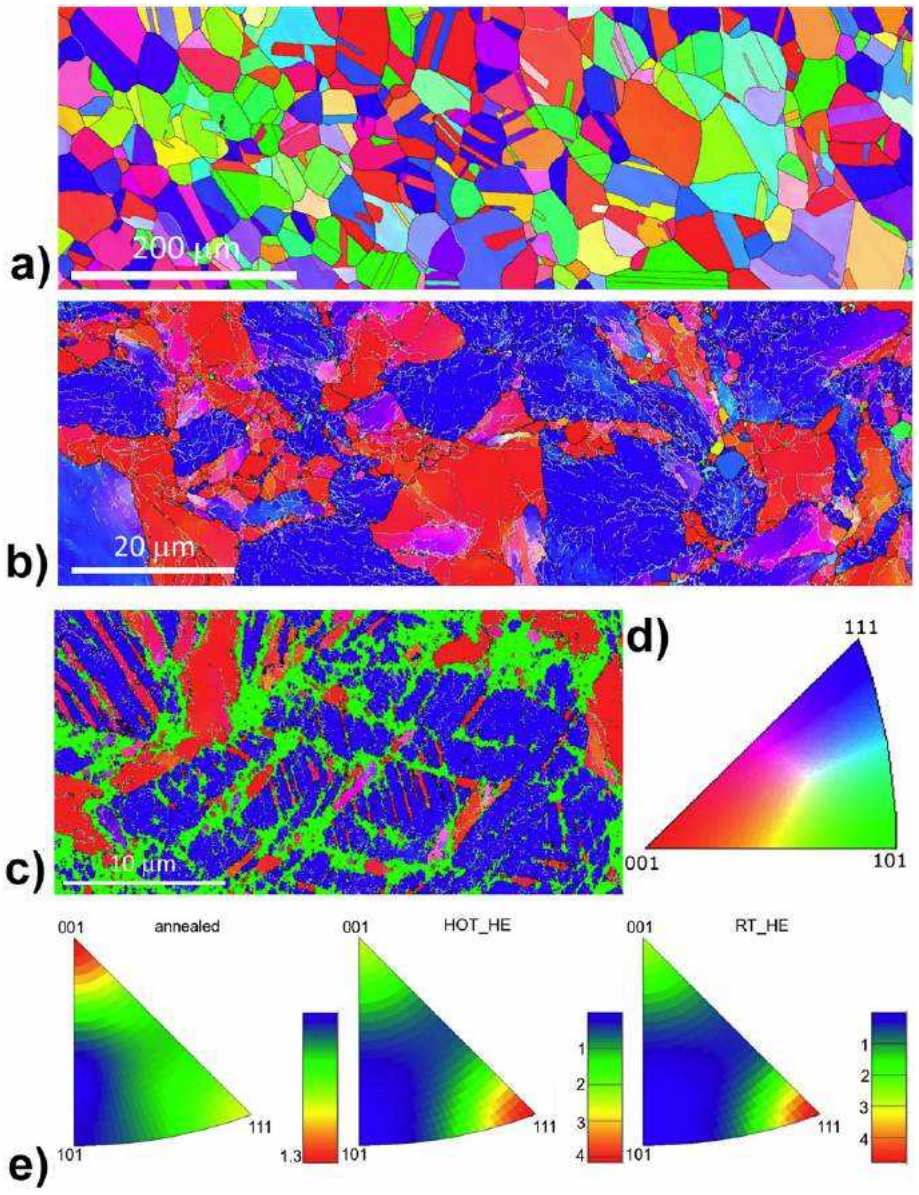

Fig. 1. EBSD orientation maps of a) annealed, b) HOT_HE, c) RT_HE samples, d) grain orientation colour code and e) corresponding inverse pole figures.

3.3. Tensile tests

The stress–strain curves obtained during the room temperature tensile tests for the annealed, HOT_HE and RT_HE samples are shown in Fig. 5. The mean values and standard deviation of ultimate tensile strength, yield stress, uniform elongation, and total elongation are summarized in Table 4. The fracture surfaces of samples are presented in Fig. 6.

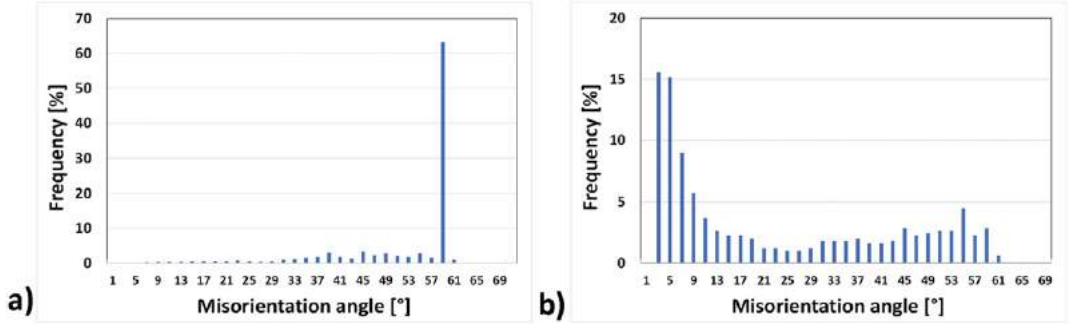

Fig. 2. Misorientation angle distribution from EBSD measurements of a) annealed, and b) HOT_HE samples.

Table 2
Average equivalent diameter d_2 of grains with standard deviation SD (d_2) and coefficient of variation CV(d_2) for annealed and HOT_HE samples.

Sample	Avg (d_2) [μm]	SD (d_2) [μm]	CV(d_2)
Annealed	35	27	0.76
HOT_HE (grains in orientations ⟨111⟩ and ⟨100⟩)	6.4	4.0	0.62
HOT_HE (grains in orientations other than ⟨111⟩ and ⟨100⟩)	1.2	0.6	0.54

Table 3
Average equivalent diameter d_2, standard deviation SD (d_2), and coefficient of variation CV(d_2) of subgrains in the HOT_HE sample in ⟨111⟩ and ⟨100⟩ oriented regions.

Subgrains in HOT_HE sample	Avg (d_2) [nm]	SD (d_2) [nm]	CV(d_2)
⟨111⟩ oriented regions	560	239	0.42
⟨100⟩ oriented regions	359	74	0.21

After RT_HE, the ultimate tensile strength increased to a value of 1468 MPa, and the uniform and total elongation were 1.3% and 8.4%, respectively. After HOT_HE, the ultimate tensile strength increased to a value of 911 MPa, and the uniform and total elongation were 13.8% and 23.0%, respectively. It can be stated, then, that the process of HE conducted at different temperatures is an efficient tool for tailoring the mechanical properties of stainless steels. RT_HE leads to a material having high strength accompanied by acceptable ductility. HOT_HE provides lower strength but significantly enhanced ductility in comparison to the RT process.

Observations of the fracture surface reveal dimples in all samples, which are typical of a plastic fracture. This indicates that although the samples differ significantly in ductility represented by elongations (uniform and total), the HE processed samples still have capacity to plastic deformation before failure.

3.4. Corrosion tests

The polarization curves for the annealed, RT_HE and HOT_HE samples in the testing solutions are shown in Figs. 7 and 8. The electrochemical parameters obtained from the polarization curves are listed in Table 5.

In the 0.1 M H_2SO_4 solution, both hydrostatically extruded samples show similar electrochemical behavior that differs slightly from that of the annealed sample. After 30 min, the highest OCP was observed for the annealed sample, while for both extruded samples it was lower by ~50–60 mV (Fig. 7a). The major differences in the scan are lower current density in the cathodic branch and in the active-passive domain for the annealed sample (Fig. 7b). This may suggest that the air-formed passive films are more easily reduced on the extruded samples

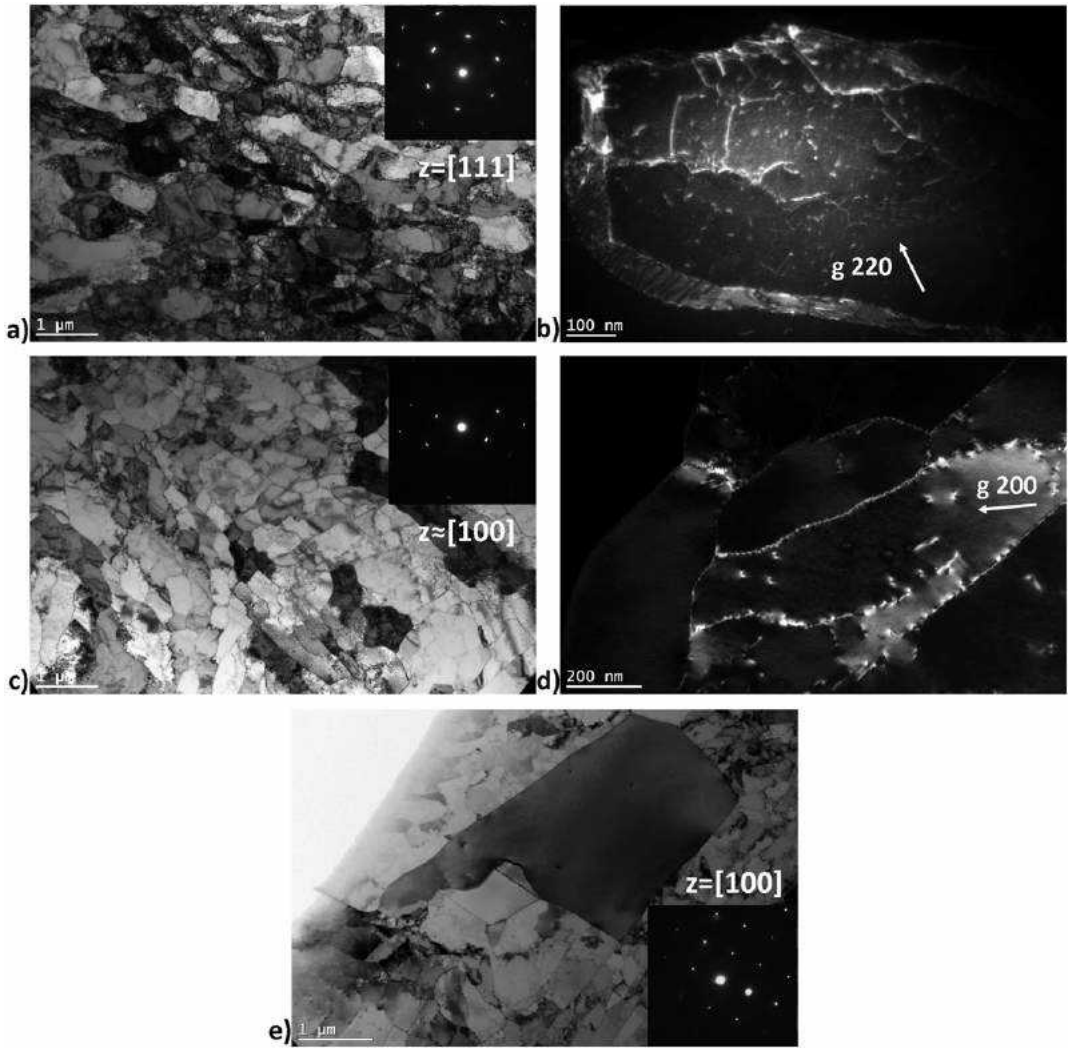

Fig. 3. Microstructure of HOT_HE sample showing areas in orientation ⟨111⟩ (a, b) and ⟨100⟩ (c, d, e); observations of substructures using the weak beam technique b) and d).

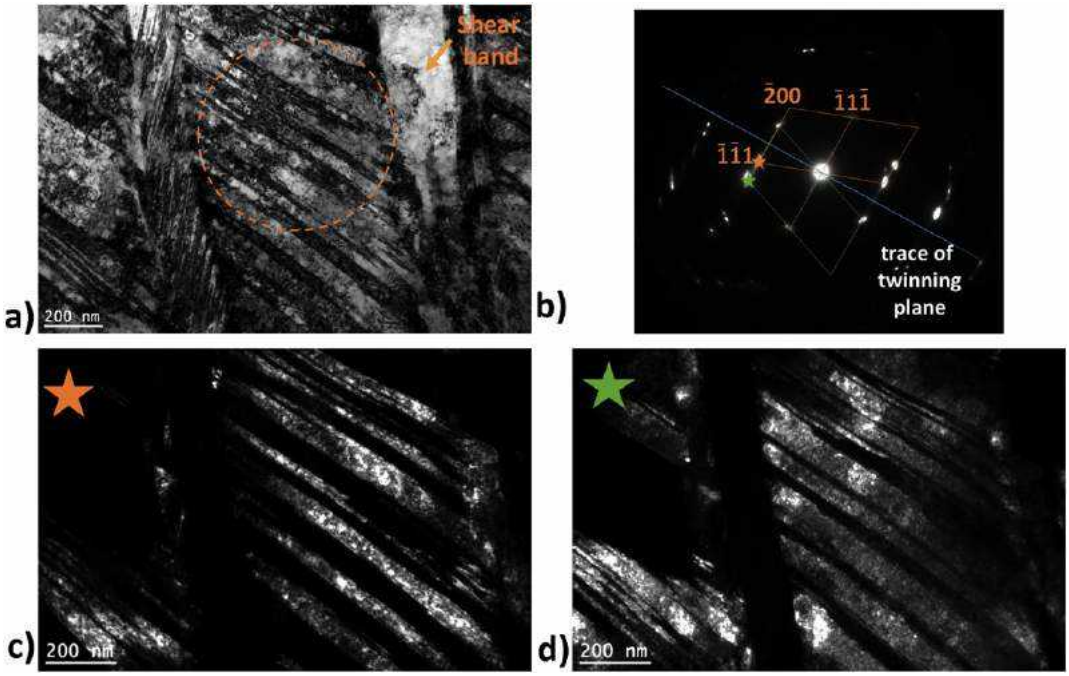

Fig. 4. Nanotwins in RT_HE samples a) with a corresponding diffraction pattern, b) dark field images in the orientation [011] of nanotwins, c) and [0-1-1] of matrix d); the circle in a) indicates the position of the SAED aperture.

than on the annealed sample. This resulted in a smaller current in the active-passive domain for the annealed sample. In the passive region, the current densities are slightly lower for the extruded samples, and up to 0.9 $V_{Ag/AgCl}$ all three samples exhibit very similar behavior. Above 0.9 V, the current density in the transpassive region is slightly lower for the RT_HE sample.

Susceptibility to localized corrosion attack was studied by means of cyclic polarization tests in a 0.1 M H_2SO_4 + 0.5 M NaCl solution (Fig. 8). The breakdown potential (E_b) is the potential at which the current density increases abruptly, while the intersection of the reverse scan with anodic curve gives the repassivation potential (E_{rep}). Higher values of E_b and E_{rep}, and a smaller area enclosed by the loop indicate improved corrosion resistance to localized attack. After cathodic prepolarization, the OCP quickly increased during the first 200 s and reached a similar value of about ~ −0.29 $V_{Ag/AgCl}$ after 30 min exposure, for all samples (Fig. 8a). The corrosion potentials and currents calculated from the Tafel plots from the potentiodynamic scan (Fig. 8b) are very similar for all the samples; slightly lower currents and potentials were observed for the extruded samples. All the samples show a small active-passive transition peak after which the current density slowly decreases in the passive region. The breakdown potential is the lowest for the RT_HE sample, and an increase in current is already observed at a potential of about 0.5 $V_{Ag/AgCl}$. In the reverse scan, the RT_HE sample has the largest area enclosed by a loop, indicating its high susceptibility to crevice corrosion, whereas the annealed and HOT_HE samples repassivate more readily.

These results are consistent with the SEM examination of the surface, which revealed a severe corrosion attack under the rubber ring (Fig. 9c). The annealed and HOT_HE sample repassivates more readily, and showed only a few, individual corrosion pits on the surface (Fig. 8a–b).

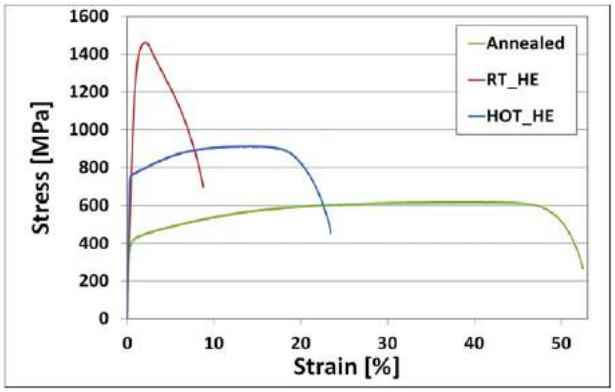

Fig. 5. Stress–strain curves of austenitic stainless steel: annealed, RT_HE, HOT_HE samples.

4. Discussion

4.1. Effect of processing parameters on the microstructure refinement

As presented in the microstructure section, various microstructures can be formed in 316LVM austenitic stainless steel, depending on the processing conditions. The most important processing parameters that affect microstructure evolution include strain, strain rate and temperature. The applied strains were identical in both HOT_HE and RT_HE samples. The combined effect of strain rate and deformation temperature are often represented by a single parameter called the Zener-Hollomon parameter, Z, which can be calculated from the following formula:

$$Z = \dot{\varepsilon} \exp(Q/RT) \quad (1)$$

Table 4
Room temperature mean values and standard deviation of ultimate tensile strength, UTS; yield stress, YS; total elongation, A_t; uniform elongation A_u of austenitic stainless steel samples annealed, RT_HE, HOT_HE.

Sample	UTS		YS		A_u		A_t	
	Average [MPa]	SD [MPa]	Average [MPa]	SD [MPa]	Average [%]	SD [%]	Average [%]	SD [%]
Annealed	614	3	374	26	34.1	6.4	51.6	0.5
RT_HE	1468	11	1212	14	1.3	0.1	8.4	0.2
HOT_HE	911	3	752	6	13.8	0.1	23.0	0.5

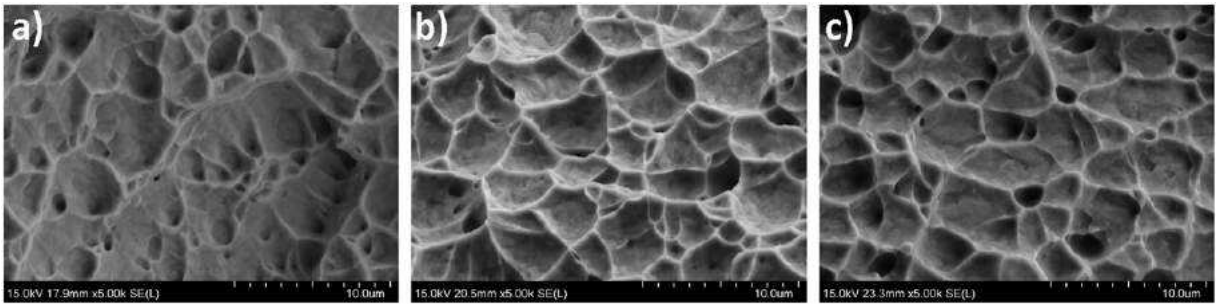

Fig. 6. Fracture surfaces of a) annealed, b) HOT_HE and c) RT_HE samples.

where, $\dot{\varepsilon}$ is the strain rate, R is the gas constant, Q is an activation energy for deformation, T is the deformation temperature. The Z parameter was calculated, assuming that $\dot{\varepsilon} = 3\ s^{-1}$, $Q = 400$ kJ/mol [38] for both HOT_HE and RT_HE samples and $T = 1273$ K and 273 K, respectively. Z equals $7.78 * 10^{16}$ and $1.1 * 10^{77}$ 1/s, respectively, which corresponds to lnZ of 39 and 177.

During hot deformation, one could expect DRX to occur and the value of Z (or lnZ) can be used to evaluate the ability of materials to this process under analyzed conditions. It was demonstrated that DRX tends to take place under low Z, i.e. high temperature and slow strain rate [39–41]. For high Z parameter, the strain required to complete DRX is higher and may not be achieved during deformation. In the HOT_HE sample, only partial DRX took place with several recrystallized grains formed at the very specific places, i.e. along the grain boundaries between the ⟨001⟩ and ⟨111⟩ oriented regions, as presented in Fig. 10. This resembles the necklace mechanism - the typical mechanism of DRX observed during the hot deformation of 316LVM stainless steel. The necklace mechanism was previously observed in the literature at a similar Z value $2.1 * 10^{16}$ 1/s [37]. The initiation of DRX is preceded by growing fluctuations in grain boundary shape. The pre-existing grain boundaries become serrated and some bugling occurs at parts of the grain boundary [37,42–44]. The appearance of nuclei in regions so oriented has been noticed previously, during the dynamic recrystallization of copper [45].

The occurrence of partial DRX in the HOT_HE sample might be due to the fact that the strain imposed (of 1.6) was too low to achieve a critical strain required for total DRX for such a high value of Z parameter. Furthermore, the initial grain size was quite large (above 30 μm), and it is well known that the rate of DRX is augmented by diminished initial grain size.

For room temperature deformation, Z parameter can be rather used to estimate the deformation mechanisms, as discussed in [46]. The very high Z value of $1.1 * 10^{77}$ 1/s ($\ln Z = 177$) favors deformation twinning, which is in agreement with microstructural observations of the RT_HE sample. The room temperature deformation does not allow so many phenomena to happen at the same time, and therefore the resulting microstructure is less heterogeneous. TEM images reveal a microstructure typical of cold-deformed low SFE metals, with a significant amount of nanotwins and shear bands filled with dislocations.

4.2. Effect of microstructural features on tensile properties

Microstructural features have a direct influence on the response of a material when external stresses are imposed. The stress-strain curves presented in Fig. 5 show different behavior, depending on the processing conditions and microstructure. The RT_HE sample shows almost no susceptibility to accumulate strain after the value of yield strength is exceeded. Plastic deformation basically occurs through the nucleation and motion of new dislocations. This is possible when active sources are present as well, as there is room for gliding. In a defected microstructure such as that of the RT_HE sample, where the dislocation free path is significantly reduced by the presence of nanotwin grain boundaries and dislocations stored inside nanotwins, the emission of new dislocations is not likely to occur. This results in a high value of yield strength, but limits the material's ability to deform uniformly.

The HOT_HE sample behaves differently. Its yield strength value is lower than that measured for the RT_HE, but work hardening occurs during tensile tests. The subgrain structure observed in these samples promotes further plastic deformation. Additionally, recrystallized grains that are free from defects provide additional ductility. They can deform easily, since no deformation substructure is present within them. The dislocations can then be nucleated at a lower stress and glide unhindered. The value of the yield stress of the HOT_HE sample (752 MPa) can be compared with the literature data for austenitic steels of refined microstructures. In the case of steels with the average grain size of 1 μm, the yield stress is 520 MPa for a 301 LN austenitic stainless steel [47], 618 MPa for an Nb-alloyed low-Ni high-Mn austenitic steel [48] and 700 MPa for a 304 austenitic steel [49]. The higher value obtained in the present study for 316LVM steel can be attributed to higher content of alloying elements, which effectively strengthen the material as well as to the substructure present in the microstructure, which provides additional strengthening effect.

The results show that the best method for maintaining quite a high total elongation and improving ultimate tensile strength compared

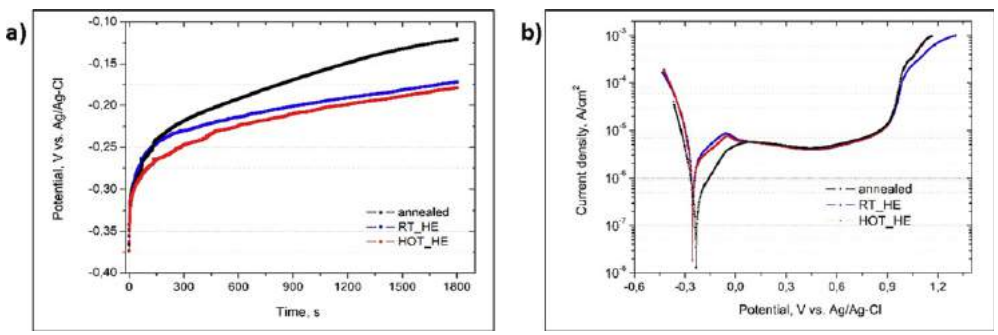

Fig. 7. OCP observations (a) and potentiodynamic polarization curves (b) obtained for annealed, RT_HE, HOT_HE samples in 0.1 M H_2SO_4 solution.

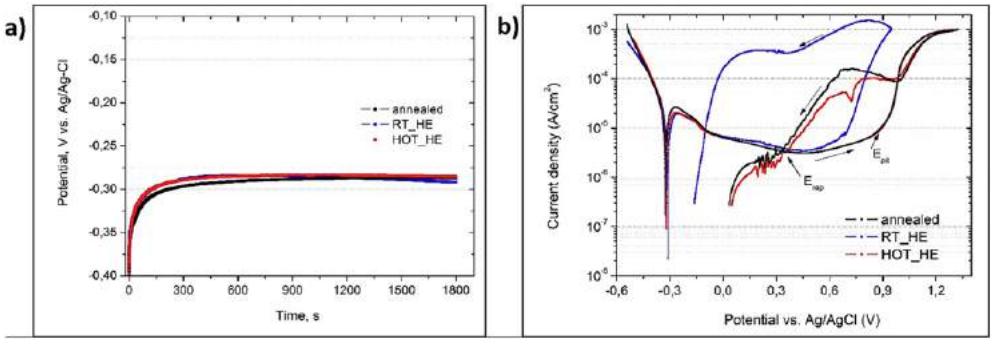

Fig. 8. OCP observations (a) and potentiodynamic polarization curves (b) obtained for annealed, RT_HE, HOT_HE samples in a 0.1 M H_2SO_4 + 0.5 M NaCl solution.

with the annealed sample is to apply hot HE. HOT_HE at 1000 °C led to a 150% increase in strength while total elongation decreased to only 45% of the initial value. Meanwhile, RT_HE led to a 240% increase in strength while total elongation fell to just 16% of the initial value. In this case, the value of the total elongation is comparable to the value obtained for the RT_HE sample extruded to a true strain of 1.8, as reported in [50] (total elongation of 8.4 for a true strain of 1.4 - initial diameter of 50 mm; total elongation of 7.8% for a true strain of 1.8 - initial diameter of 10 mm). I t must be pointed out that, in these two cases, the elongation is nearly the same, while the ultimate tensile strength is greater in the sample with the greater true strain (1470 MPa for 1.4 true strain, and 1800 MPa for 1.8 true strain). This suggests that, during RT_HE, a high density of dislocations is created for these true strains. This reaches a saturation level so that new dislocations cannot be accumulated. For this reason, it would seem sensible to apply a higher true strain to gain strength without losing plasticity.

It should be underlined that a value of elongation of 8% with an ultimate tensile strength of 1470 MPa is a satisfactory result if one considers the dimensions of the processed billet, which were 25 mm in diameter and nearly one meter in length. (If the true strain is 1.5 and the final diameter reaches 5 mm, one can achieve an ultimate tensile strength of 1320 MPa and total elongation of 14.5% [33]). Such a volume of material provides opportunities for manufacturing construction elements - in contrast to DPD, where the samples are 15 mm in diameter and 25 mm in length [7], or HPT, where typical samples are 8 mm in diameter and 0.8 mm in height [4,51]. This quite high total elongation compared with the elongation after HPT of approximately 4% [51] can be attributed to the presence of nano-scale twins. Nanotwin boundaries are effective in blocking dislocation motion, and at the same time they act as slip planes that accommodate dislocations. Whereas in the HPT samples deformed to high strains, nanograins are present as a result of further fragmentation of submicron shear bands and the profuse intersection of twins.

Fig. 11 shows a comparison of the mechanical properties of austenitic stainless steels after selected plastic deformation processes, including our HOT_HE sample, whose quite high elongation and strength can be attributed to the presence of substructures. It must be emphasized that its elongation is higher than in commercial grade 316LVM, yet its ultimate tensile strength is at the same level. This fact makes this treatment interesting in terms of practical applications. The prospective applications of a nanostructured stainless steel obtained by HE was previously demonstrated in [33], where the first batch of medical implants and instruments made of 316LVM steel manufactured by Unipress in cooperation with Clavmed was presented. However, one must remember that, to be used in aggressive environments, austenitic stainless steels must also have high corrosion resistance.

Table 5
Corrosion parameters of annealed, RT_HE, HOT_HE samples obtained from cyclic polarization curves: E_{corr} – corrosion potential calculated from Tafel plots, i_{corr} – corrosion current calculated from Tafel plots, i_{pass} – current density in the passive domain at 0.45 V vs. Ag/AgCl, E_b – breakdown potential, E_{rep} – repassivation potential.

Solution	Sample	E_{corr}, V vs Ag/AgCl	i_{corr}, μA/cm²	i_{pass}, μA/cm²	E_b, V vs. Ag/AgCl	E_{rep}, V vs. Ag/AgCl
0.1 M H_2SO_4	Annealed	−0.24	0.3	4.3	–	–
	RT_HE	−0.24	2.0	3.9	–	–
	HOT_HE	−0.25	1.4	4.0	–	–
0.1 M H_2SO_4 + 0.5 M NaCl	Annealed	−0.30	15.1	4.0	0.96	0.34
	RT_HE	−0.31	14.6	4.3	0.59	−0.10
	HOT_HE	−0.32	11.6	3.9	0.96	0.38

4.3. Effect of microstructural features on corrosion resistance

It has been reported that a high density of active sites such as defects, dislocations and grain boundaries in a nanomaterial where the passive film can nucleate leads to a higher formation rate [21,55–57] and a more compact, non-porous structure. Nanotwins and nanograins can also enhance the passivation ability of 316L steel obtained by DPD [55]. Another factor that can affect passivation behavior is texture. Both HE-processed samples had a texture typical of fcc metals subjected to extrusion processes. The strongest ⟨111⟩ texture was found in the RT_HE sample. Also, in the HOT_HE sample, the majority of grains have ⟨111⟩ orientation and the rest have ⟨100⟩ parallel to the extrusion direction. The annealed sample has ⟨100⟩ as its dominant orientation. Lindell and Peterson [58] investigated the influence of crystallographic anisotropy of 316L steel on the corrosion rate of 316L stainless steel in 30 vol% H_2SO_4, and found that the corrosion rate increases in the order ⟨111⟩ / ⟨110⟩ / ⟨100⟩ .

Despite the large differences in the microstructures of both extruded samples, their electrochemical behavior in 0.1 M H_2SO_4 is almost the same, and not very different from that of the annealed sample. The only differences are evident in the larger current densities in the cathodic domain and in the active-passive transition region, which may suggest that the passive film in the HE processed samples can be more easily reduced during pre-polarization at −5 mA/cm². This suggests that the passive film on the HE-processed steels is probably more defected and can therefore be more easily reduced during cathodic polarization, while the material can dissolve more easily in the active-passive potential region. Despite the completely different microstructures of the RT_HE and HOT_HE, those differences do not influence the electrochemical behavior in 0.1 M H_2SO_4.

In the presence of aggressive chloride ions (Cl^-), it is generally assumed that all microstructural defects (grain boundaries, dislocations, MnS inclusions) cause increased susceptibility to localized attack in austenitic steels. The density of defects that can deteriorate corrosion resistance is much higher in a refined material. A higher density of defects might lead to a lower concentration of chloride ions on each defect, and so a greater driving force is needed for a stable pit to grow [59,60]. In the 0.1 M H_2SO_4 + 0.5 M NaCl solution, a drop of resistance to localized attack was observed only in RT_HE sample, while the

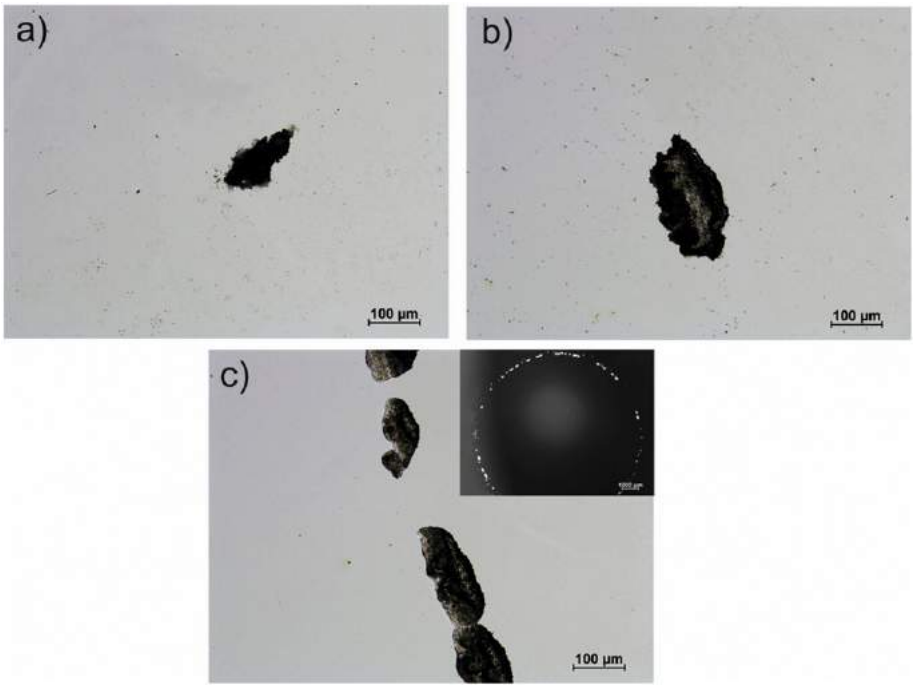

Fig. 9. Light micrographs of morphology of localized attacks of a) annealed, b) HOT_HE and c) RT_HE samples after a potentiodynamic scan in a 0.1 M H_2SO_4 + 0.5 M NaCl (in the upper right corner, light micrograph from the stereoscopic microscope).

HOT_HE sample maintained high corrosion resistance in the presence of chloride ions. The morphology of corrosion attack reveals that the RT_HE sample is very prone to crevice corrosion, while on the HOT_HE sample only pitting corrosion occurred. Undoubtedly, the effect of the microstructure of the RT_HE and HOT_HE samples on corrosion resistance is much more pronounced in the presence of aggressive ions, and has a large impact on the type of corrosion that occurs. However, this is a very complex phenomenon that depends on a large number of factors, and needs further research. Generally, the chemical reactivity of cold-worked steels is higher than that of annealed steels, as their internal energy is high. The morphology of corrosion attack reveals that the RT_HE sample is very prone to crevice corrosion and a severe localized attack is observed under the O-ring. The shape of the potentiodynamic curves is almost identical despite the differences in the microstructure of these two samples. It seems that the grain refinement of the microstructure of HOT_HE sample, and its different texture and misorientation angle, do not affect its susceptibility to localized attack in the solution tested.

5. Conclusions

1. The study proved that it is possible to improve the strength-plasticity balance in an austenitic stainless steel 316LVM produced by SPD without a loss in corrosion resistance.
2. Hydrostatic extrusion results in various microstructures, depending on processing conditions: (1) performed HE at 1000 °C leads to the an equiaxial microstructure observed on a cross section, which that differs for various orientations; (2) HE at RT results in a nanotwinned microstructure and regions having a high density of dislocations.
3. Hydrostatic extrusion is an efficient way to tailor the mechanical properties of 316LVM stainless steel. After HE performed at ambient temperature, ultimate tensile strength increased to a value of 1468 MPa, while uniform and total elongation were 1.3% and 8.4%, respectively. After HE at 1000 °C, ultimate tensile strength increased to a value of 911 MPa, while uniform and total elongation were 13.8% and 23%, respectively.

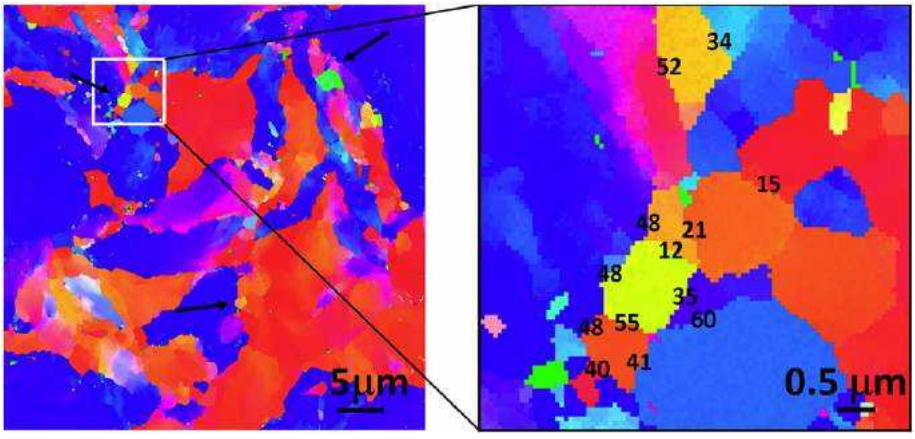

Fig. 10. Magnified detail of EBSD orientation map for the HOT_HE from Fig. 1; areas where the necklace mechanism is observed are indicated by arrows; misorientation angles between newly recrystallized grains are placed at grain boundaries.

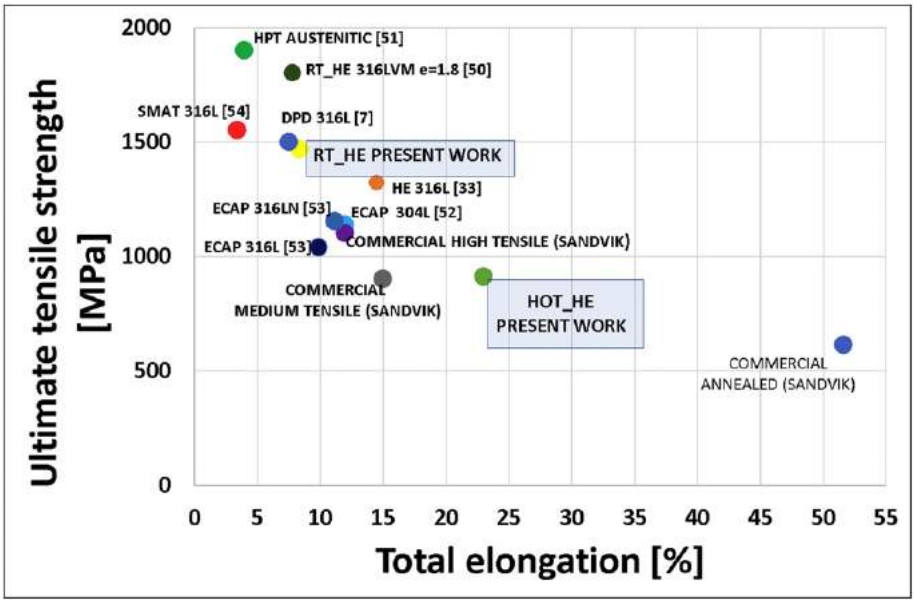

Fig. 11. Comparison of mechanical properties of various austenitic stainless steels after plastic deformation [52–54].

4. The very promising combination of elongation and strength observed for the HOT_HE sample was attributed to the substructure created during hot extrusion.
5. Hydrostatic extrusion at RT and at an elevated temperature makes it possible to maintain resistance to uniform corrosion in 0.1 M H_2SO_4. Moreover, hydrostatic extrusion at an elevated temperature makes it possible to maintain corrosion resistance in a 0.1 M H_2SO_4 + 0.5 M NaCl solution, whereas the grain refinement at RT leads to a decrease in corrosion resistance.

The various microstructures created during hydrostatic extrusion have an impact not only on strength, elongation and corrosion resistance, but also on other properties such as wear resistance and the diffusion processes that occur during surface modification (e.g. nitriding). This is the subject of ongoing research.

Acknowledgements

This work was supported by Polish National Science Centre (NCN) project No. UMO-2013/11/B ST8/03641.

References

[1] A.T. Krawczynska, T. Brynk, S. Gierlotka, E. Grzanka, S. Stelmakh, B. Pałosz, M. Lewandowska, K.J. Kurzydłowski, Mechanical properties of nanostructured stainless steel 316LVM annealed under pressure, Mech. Mater. 67 (2013) 25–32.
[2] N.S. De Vincentis, A. Kliauga, M. Ferrante, M. Avalos, H.-G. Brokmeier, R.E. Bolmaro, Evaluation of microstructure anisotropy on room and medium temperature ECAP deformed F138 steel, Mater. Charact. 107 (2015) 98–111.
[3] Z.J. Zheng, J.W. Liu, Y. Gao, Achieving high strength and high ductility in 304 stainless steel through bi-modal microstructure prepared by post-ECAP annealing, Mater. Sci. Eng. A 680 (2017) 426–432.
[4] Y. Mine, K. Koga, K. Takashima, Z. Horita, Mechanical characterisation of microstructural evolution in 304 stainless steel subjected to high-pressure torsion with and without hydrogen pre-charging, Mater. Sci. Eng. A 661 (2016) 87–95.
[5] M. El-Tahawy, Y. Huang, T. Um, H. Choe, J.L. Lábár, T.G. Langdon, J. Gubicza, Stored energy in ultrafine-grained 316L stainless steel processed by high-pressure torsion, J. Mater. Res. Technol. (2017) (in press, corrected proof).
[6] S.V. Dobatkin, O.V. Rybalchenko, N.A. Enikeev, A.A. Tokar, M.M. Abramova, Formation of fully austenitic ultrafine-grained high strength state in metastable Cr–Ni–Ti stainless steel by severe plastic deformation, Mater. Lett. 166 (2016) 276–279.
[7] F.K. Yan, G.Z. Liu, N.R. Tao, K. Lu, Strength and ductility of 316L austenitic stainless steel strengthened by nano-scale twin bundles, Acta Mater. 60 (2012) 1059–1071.
[8] P. Czarkowski, A.T. Krawczyńska, R. Slesinski, T. Brynk, J. Budniak, M. Lewandowska, K.J. Kurzydłowski, Low temperature mechanical properties of 316L type stainless steel after hydrostatic extrusion, Fusion Eng. Des. 9–11 (2011) 2517–2521.
[9] P. Czarkowski, A.T. Krawczynska, T. Brynk, M. Nowacki, M. Lewandowska, K.J. Kurzydłowski, Cryogenic strength and microstructure of a hydrostatically extruded austenitic steel 1.4429 (AISI 316LN), Cryogenics 64 (2014) 1–4.
[10] R.K. Gupta, N. Birbilis, The influence of nanocrystalline structure and processing route on corrosion of stainless steel: a review, Corr. Sci. 92 (2015) 1–15.
[11] K.D. Ralston, N. Birbils, C.H.J. Davies, Revealing the relationship between grain size and corrosion rate of metals, Scr. Mater. 63 (2010) 1201–1204.
[12] P. Bazarnik, M. Lewandowska., M. Andrzejczuk, K.J. Kurzydlowski, The strength and thermal stability of Al-5Mg alloys nano-engineered using methods of metal forming, Mater. Sci. Eng. A 556 (2012) 134–139.
[13] P. Bazarnik, Y. Huang, M. Lewandowska, T.G. Langdon, Structural impact on the Hall–Petch relationship in an Al–5Mg alloy processed by high-pressure torsion, Mater. Sci. Eng. A 626 (2015) 9–15.
[14] S. Gollapudi, Grain size distribution effects on the corrosion behaviour of materials, Corros. Sci. 62 (2012) 90–94.
[15] B. Ravi Kumar, R. Singh, B. Mahato, P.K. De, N.R. Bandyopadhyay, D.K. Bhattacharya, Effect of texture on corrosion behavior of AISI 304L stainless steel, Mater. Charact. 54 (2005) 141–147.
[16] Z.J. Zheng, Y. Gao, Y. Gui, M. Zhu, Corrosion behaviour of nanocrystalline 304 stainless steel prepared by equal channel angular pressing, Corros. Sci. 54 (2012) 60–67.
[17] L. Zhang, A. Ma, J. Jiang, D. Yang, D. Song, J. Chen, Sulphuric acid corrosion of ultrafine-grained mild steel, processed by equal-channel angular pressing, Corr. Sci. 75 (2013) 434–442.
[18] R.K. Gupta, R.K. Singh Raman, C.C. Koch, Electrochemical characteristics of nano and microcrystalline Fe–Cr alloys, J. Mater. Sci. 47 (2012) 6118–6124.
[19] S.G. Wang, M. Sun, K. Long, The enhanced even and pitting corrosion resistances of bulk nanocrystalline steel in HCl solution, Steel Res. Int. 83 (2012) 800–807.
[20] M. Eskandari, M. Yeganeh, M. Motamedi, Investigation in the corrosion behaviour of bulk nanocrystalline 316L austenitic stainless steel in NaCl solution, Micro Nano Lett. 7 (2012) 380–383.
[21] 3 C. Pan, L. Liu, Y. Li, S. Wang, F. Wang, Passive film growth mechanism of nanocrystalline 304 stainless steel prepared by magnetron sputtering and deep rolling techniques, Electrochim. Acta 56 (2011) 7740–7748.
[22] M. Pisarek, P. Kędzierzawski, M. Janik-Czachor, K.J. Kurzydłowski, The effect of hydrostatic extrusion on resistance of 316 austenitic stainless steel to pit nucleation, Electrochemi. Comm. 9 (2007) 2463–2466.
[23] M. Pisarek, P. Kedzierzawski, T. Płociński, M. Janik-Czachor, K.J. Kurzydłowski, Characterization of the effects of hydrostatic extrusion on grain size, surface composition and the corrosion resistance of austenitic stainless steels, Mater. Charact. 59 (2008) 1292–1300.
[24] L. Liu, Y. Li, F. Wang, Electrochemical corrosion behavior of nanocrystalline materials – a review, J. Mater. Sci. Technol. 26 (2010) 1–14.
[25] A.S. Hamada, L.P. Karjalainen, M.C. Somani, Electrochemical corrosion behaviour of a novel submicron-grained austenitic stainless steel in an acidic NaCl solution, Mater. Sci, Eng. A 431 (2006) 211–217.
[26] M.C. Somani, P. Juntunen, L.P. Karjalainen, R.D.K. Misra, A. Kyrolainen, Enhanced mechanical properties through reversion in metastable austenitic stainless steels, Metall. Mater. Trans. 40A (2009) 729–744.
[27] R.Z. Valiev, I.V. Alexandrov, Y. Zhu, T.C. Lowe, Paradox of strength and ductility in metals produced by severe plastic deformation, J. Mater. Res. 17 (2002) 5–8.
[28] Y. Wang, M. Chen, F. Zhou, E. Ma, High tensile ductility in a nanostructured metal, Nature 419 (2002) 912–915.
[29] Y.M. Wang, E. Ma, Three strategies to achieve uniform tensile deformation in a nanostructured metal, Acta Mater. 52 (2004) 1699–1709.
[30] E. Ma, Eight routes to improve the tensile ductility of bulk nanostructured metals and alloys, J. Microsc. (2006) 49–53.

[31] F. Sansoz, K. Lu, T. Zhu, A. Misra, Strengthening and plasticity in nanotwinned metals, MRSBulletin (2016) 292–297.
[32] F.K. Yan, N.R. Tao, K. Lu, Tensile ductility of nanotwinned austenitic grains in an austenitic steel, Scripta Mater. 84–85 (2014) 31–34.
[33] W. Pachla, J. Skiba, M. Kulczyk, S. Przybysz, M. Przybysz, Nanostructurization of 316L type austenitic stainless steels by hydrostatic extrusion, Mater. Sci. Eng. 615 (2014) 116–127.
[34] T. Wejrzanowski, W.L. Spychalski, K. Rozniatowski, K.J. Kurzydlowski, Image based analysis of complex microstructures of engineering materials, Int. J. App. Math. Comput. Sci. 18 (2008) 33–39.
[35] T. Wejrzanowski, M. Lewandowska, K.J. Kurzydlowski, Stereology of nano-materials, IAS 29 (2010) 1–12.
[36] M.C. Mataya, E.L. Brown, M.P. Reindeau, Effect of hot working on structure and strength of type 304L austenitic stainless steel, Metal Trans. A (1990) 1969–1987.
[37] M. Jafari, A. Najafizadeh, Dynamic recrystallization by neckless mechanism during hot deformation of 316 stainless steel, Metal (2008) 13–15.
[38] D.K. Suker, T.A. Elbenawy, A.H. Backar, H.A. Ghulman, M.W. Al-Hazmi, Hot deformation characterization of AISI316 and AISI304 stainless steels, IJMME 17 (2017) 1–14.
[39] L. Sun, K. Muszka, B.P. Wynne, E.J. Pamiere, On the interactions between strain path reversal and dynamic recrystallization in 316L stainless steel studied by hot torsion, Mater. Sci. Eng. A 568 (2013) 160–170.
[40] M. Shaban, B. Eghbali, Characterization of austenite dynamic recrystallization under Z parameters in a microalloyed steel, J. Mater. Sci. Technol. 27 (2011) 359–363.
[41] A.D. Samantaray, S. Mandal, M. Jayalakshmi, C.N. Athreya, A.K. Bhaduri, V. Subramanya Sarma, New insights into the relationship between dynamic softening phenomena and efficiency of hot working domains of a nitrogen enhanced 316L(N) stainless steel, Mater.Sci. Eng. A 598 (2014) 368–375.
[42] S. Wang, M. Zhang, H. Wu, B. Yang, Study on the dynamic recrystallization model and mechanism of nuclear grade 316LN austenitic stainless steel, Mater. Charact. 118 (2016) 92–101.
[43] K. Huang, R.E. Loge, A review of dynamic recrystallization phenomena in metallic materials, Mater. Design. 111 (2016) 548–574.
[44] T. Sakai, A. Beyakov, R. Kaibyshev, H. Miura, J.J. Jonas, Dynamic and post-dynamic recrystallization under hot, cold and severe plastic deformation conditions, Prog. Mater. Sci. 60 (2014) 130–207.
[45] N. Mortazavi, N. Bonora, A. Ruggiero, M.H. Colliander, Dynamic recrystallization during high-strain-rate tension of copper, Metal Trans. A 47A (2016) 2555–2557.
[46] Y.S. Li, Y. Zhang, N.R. Tao, K. Lu, Effect of the Zener-Hollomon parameter on the microstructures and mechanical properties of Cu subjected to plastic deformation, Acta Mater. 57 (2009) 761–772.
[47] S. Rajasekhara, P.J. Ferreira, L.P. Karjalainen, A. Kyrolainen, Hall-Petch behavior in ultra-fine grained AISI 301LN stainless steel, Metall. Mater. Trans. A 38A (2007) 1202–1209.
[48] A. Kisko, A.S. Hamada, J. Talonen, D. Porter, L.P. Karjalainen, Effects of reversion and recrystallization on microstructure and mechanical properties of Nb-alloyed low-Ni high-Mn austenitic stainless steels, Mater. Sci. Eng. A 657 (2016) 359–370.
[49] A. Di Schino, I. Salvatori, J.M. Kenny, Effects of martensite formation and austenite reversion on grain refining of AISI 304 stainless steel, J. Mater. Sci. 37 (2002) 4561–4565.
[50] A.T. Krawczynska, M. Lewandowska, K.J. Kurzydlowski, Fabrication of nanostructured stainless steel via hydrostatic extrusion, Conference Proceedings 6th European Stainless Steel Conference Science and Market Helsinki 2008, pp. 239–243.
[51] A. Vorhauer, S. Kleber, R. Pippan, Influence of processing temperature on microstructural and mechanical properties of high-alloyed single-phase steels subjected to severe plastic deformation, Mater. Sci. Eng. A 410–411 (2005) 281–284.
[52] S. Qu, C.X. Huang, Y.L. Gao, G. Yang, S.D. Wu, Q.S. Zang, Z.F. Zhang, Tensile and compressive properties of AISI 304L stainless steel subjected to equal channel angular pressing, Mater. Sci. Eng. A 475 (2008) 207–216.
[53] F.Y. Dong, P. Zhang, J.C. Pang, D.M. Chen, K. Yang, Z.F. Zhang, Optimizing strength and ductility of austenitic stainless steels through equal-channel angular pressing and adding nitrogen element, Mater. Sci. Eng. A 587 (2013) 185–191.
[54] X.H. Qu, J. Lu, L. Lu, K. Lu, Tensile properties of a nanocrystalline 316L austenitic stainless steel, Scripta Mater. 52 (2005) 1039–1044.
[55] T. Li, L. Liu, B. Zhang, Y. Li, F. Yan, N. Tao, F. Wang, Passive behavior of a bulk nanostructured 316L austenitic stainless steel consisting of nanometer-sized grains with embedded nano-twin bundles, Corros. Sci. 85 (2014) 331–342.
[56] C. Pan, L. Liu, Y. Li, F.H. Wang, Pitting corrosion of 304ss nanocrystalline thin film, Corros. Sci. 73 (2013) 32.
[57] F. Yan, N. Tao, C. Pan, L. Liu, Microstructures and corrosion behaviors of an austenitic stainless steel strengthened by nanotwinned austenitic grains, Adv. Eng. Mater. 18 (2016) 650.
[58] D. Lindell, R. Pettersson, Crystallographic effects in corrosion of austenitic, Mate. Corros. 16 (2015) 727.
[59] R.B. Intruri, Z. Szklarska-Smialowska, Localized corrosion of nanocrystalline 304 type stainless steel films, Corrosion 48 (1992) 398.
[60] L. Liu, Y. Li, F. Wang, Influence of nanocrystallization on pitting corrosion behavior of an austenitic stainless steel by stochastic approach and in situ AFM analysis, Electrochimi. Acta 55 (2010) 2430.

ADVANCED ENGINEERING MATERIALS
www.aem-journal.com

Formation of the Nitrided Layers on an Austenitic Stainless Steel with Different Grain Structures

Agnieszka T. Krawczyńska, Joanna Zdunek, Ryszard Sitek, and Małgorzata Lewandowska*

In this work, the formation of nitrided layers on an austenitic stainless steel with very different grain structures is analyzed. Two different grain structures, that is, 1) nanotwined and 2) consisted of dislocation low-angle grain boundaries are produced by hydrostatic extrusion either hot (with preheating at 1000 °C) or room temperature with a total true strain of 1.4. The coarse-grained sample is used as a reference one. These three types of samples are nitrided using low-temperature plasma-assisted nitriding at 430 °C for 5 h. Nitrided layers consisting of S-phase are produced on all the samples. However, only minor differences in their thickness are observed. The analysis reveals that the formation of nitrided layers is controlled by volume diffusion disregarding the grain structure of the substrates. This is attributed to very specific grain boundaries (twin and dislocation grain boundaries) dominating in hydrostatically extruded samples. Such special grain boundaries do not provide fast diffusion channel but act as trapping sites for diffusing atoms. As a consequence, much more nitrogen is stored in the layers formed on the samples previously subjected to hydrostatic extrusion but the layer thickness does not differ significantly.

1. Introduction

Nitriding is a thermo-chemical treatment widely used to improve surface properties such as the resistance of various materials to wear and corrosion. It has been successfully applied with a number of materials, including Ti alloys and steels.[1–6] In its conventional version, nitriding is carried out within a temperature range of 450–600 °C. Nitriding can also effectively improve properties of austenitic stainless steels, which feature excellent corrosion resistance but suffer from low mechanical strength and wear resistance. It should be noted however, that austenitic stainless steels undergo sensitization upon annealing at 480–815 °C due to the grain boundary precipitation of chromium carbides. As a result, areas in the vicinity of grain boundaries become depleted in chromium and lose their corrosion resistance. Therefore, in the case of austenitic stainless steels, a lower processing temperature is required to avoid this phenomenon.

Modern low-temperature nitriding methods have been developed and make it possible to produce nitriding layers within a temperature range of 300–450 °C, which is significantly lower than that of carbide precipitation. There are a large number of reports on the low-temperature nitriding of conventional coarse-grained austenitic stainless steel.[7–15] In general, they describe the formation of expanded austenite γ_N (the S phase) on the surface layers and a resulting enhancement in wear and corrosion resistance. One of the advantages of modern nitriding is a cathodic sputtering process, which is applied prior to nitriding in the same working chamber, enabling the effective removal of oxides and contaminants from the treated surfaces. Controlling the nitriding potential in the nitrogen-hydrogen atmosphere of the furnace is also possible, and makes it possible to obtain the desired physico-chemical properties of the nitrided layers.

The nitriding process is well established and well understood for conventional coarse-grained materials. However, with the recent rapid development of ultrafine-grained (UFG) and nanocrystalline (NC) materials, the question arises as to how grain refinement will affect nitriding. UFG and NC materials feature a large number of grain boundaries which, on the one hand, strengthen the material and ensure that it has very high mechanical strength, but on the other hand, may act as potential fast atomic diffusion channels. Enhanced atomic diffusivity in UFG and NC materials compared with their coarse-grained counterparts has been experimentally proven.[16–19] It is due to the fact that in conventional materials the lattice diffusion of nitrogen dominates, while in ultrafine-grained materials nitrogen diffuses along the grain boundaries because the activation energy is much lower than that for lattice diffusion. Moreover, from a thermodynamic point of view, the driving force for nitride formation is also enhanced in the case of materials having a refined grain structure. This phenomenon was noticed in α-Fe nitrided at 300 °C for 9 h.[20] After nitriding, a continuous dark gray surface layer about 10 μm thick was observed on the surface of an UFG Fe sample where two types of iron nitrides were

Dr. A. T. Krawczyńska, Dr. J. Zdunek, Dr. R. Sitek, Prof. M. Lewandowska
Faculty of Materials Science and Engineering
Warsaw University of Technology
Woloska 141, Warsaw 02-507, Poland
E-mail: akrawczy@inmat.pw.edu.pl

The ORCID identification number(s) for the author(s) of this article can be found under https://doi.org/10.1002/adem.201701049.

DOI: 10.1002/adem.201701049

found. In the coarse-grained sample, the nitrogen concentration was negligible from the top surface to the substrate. Similar conclusions were drawn from an experiment of nitriding nanostructured and coarse-grained Ti Grade 2 at 500 °C.[21] In the nanostructured sample, a thicker layer was observed that consisted of a more complex phase composition.

The effect of grain refinement on the nitriding process in austenitic stainless steels was mostly studied in combination with SMAT processing.[22–27] The idea was that SMAT improved the subsequent nitrogen diffusion so that a thicker nitride layer was formed, which enhanced the material's mechanical properties. The results revealed that nitriding a nanostructured austenitic steel previously subjected to SMAT at 425 °C for 20 h leads to the creation of a layer twice as thick as in the original sample only if the nitriding is performed after prior polishing.[28] These nitriding conditions did not affect the nanostructure, which was composed of nanograins smaller than 50 nm. The process of polishing was necessary to remove the barrier oxide. In some cases, it was observed that the severe surface deformation applied on austenitic steel samples can cause a phase transformation from an austenitic to a martensitic phase.[29] As a consequence, a nitrided layer two times thicker was noticed on the samples with a martensitic phase. The increase in thickness in this example may represent not a contribution to microstructure refinement, but rather to a higher value of the nitrogen diffusion coefficient in the martensite than in the austenite.[30]

UFG and NC materials are frequently produced by employing methods of severe plastic deformation (SPD). In these methods, unusually high strain is applied, which brings about grain refinement. However, it should be noted that the microstructure of austenitic stainless steels subjected to SPD may differ substantially depending on the processing conditions, and consists of either ultrafine/nano grains (as in[31–34]) or nanotwins.[35–37] In this context, one may ask: does grain refinement always make diffusion occur faster? In this work, we study the formation of a nitrided layer during low temperature plasma-assisted nitriding of different grain structures in austenitic stainless steel. Various microstructures were obtained by hydrostatic extrusion (HE) at elevated temperatures and at room temperature. HE was proven to be an efficient method of refining grain and enhancing the properties of austenitic stainless steel.[33]

2. Experimental Section

The material used was Sandvic Bioline 316LVM (LVM stands for low-carbonated vacuum melted) austenitic stainless steel with the chemical composition as follows 0.023C–0.6Si–1.7Mn–17.5Cr–13.5Ni–2.8Mo. It was delivered in the form of annealed rods with a diameter of 50 mm.

To refine the microstructure, hot (with pre-heating at 1000 °C) and room temperature (RT) HE was applied with a total true strain of 1.4 (the diameter was reduced to 25 mm). The samples were named annealed, RT_HE and HOT_HE. To reveal the microstructure, the samples were cut, ground, polished and etched using 50 cm^3 $HCl + 25\ cm^3$ $HNO_3 + 25\ cm^3$ H_2O reagent to reveal their microstructure using a light microscope (LM) – a NIKON EPHIPHOT 200. Next, thin foils were prepared for examination using transmission electron microscopy by mechanical polishing to a disk thickness of about 100 μm. Further thinning to reach a thickness appropriate for electron transparency was carried out by electropolishing. The microstructures were examined using a JEOL 1200 transmission electron microscope (TEM) working at 120 kV.

The samples for plasma-assisted nitriding were in the form of discs 15 mm in diameter and 4 mm in height, with disc plane perpendicular to the rod axis. They were polished and placed in a special form to avoid "the edge effect." Nitriding process of the steel was carried out in a device by Sulzer Metaplas Gmbh in the Aviation Industry Testing Laboratory-Rzeszow University of Technology at 430 °C in a nitrogen-hydrogen mixture (N2–25%, H2–75% vol.) under a reduced pressure of 3 hPa for 5 h. The samples were placed directly on the cathode in a special grip protecting against the edge effect. Next, the nitriding samples were ground and polished according to the standard procedures and then etched with 50 cm^3 $HCl + 25\ cm^3$ $HNO_3 + 25\ cm^3$ H_2O for 30 s. The nitriding layers were observed using an SU-8000 scanning electron microscope (SEM) in the SE (at 30 kV) and BSE (5 kV) modes, a JEOL 1200 TEM transmission electron microscope (at 120 kV), and a dedicated Hitachi HD2700 scanning electron microscope (at 200 kV). The lamellae were prepared using a Hitachi NB5000focused ion beam. A high resolution Scanning Auger Microprobe-Microlab 350 (Thermo Electron) equipped with a FEG-tip (Field-Emission Electron Gun)) was used for the Auger electron spectroscopy (AES) analysis. The Microlab 350 was used to monitor local chemical composition utilizing the Auger line scan function of the spectrometer with a lateral resolution of about 20 nm. The all Auger spectra were excited at a primary energy of $E = 10$ kV and recorded after sputtering process (ion energy 3 keV, beam current 1.3 μA, crater size 9 mm^2, time 20 min) to remove the surface contamination. For a better visualization of the received AES data, the results presented on the line profiles were normalized only to Fe (LM2) and N (KL1) signals. The X-ray diffraction study was carried out to determine the phase composition after nitriding. Phase composition was investigated in samples cut perpendicularly to the rod axis, oriented with the surface prepared for nitriding and nitrided surface perpendicular to the X-ray direction. For this study, a D8 DISCOVER Bruker diffractometer was used with a Co Kα irradiation.

3. Results

3.1. Microstructure Observation Prior to Nitriding

The microstructure of 316LVM stainless steel after annealing consists of recrystallized equiaxed grains of 35 μm in the equivalent diameter (**Figure 1**a). In the case of the RT_HE sample, the microstructure was highly refined and no microstructure elements were observed using a light microscope (Figure 1b). In the case of the HOT_HE sample, one can distinguish two types of areas with no microstructural features, as seen in the micrograph (Figure 1c). More detailed information on these two HE processed samples is revealed by transmission electron microscopy. In the case of the RT_HE sample, the microstructure consists of nanotwins and shear bands, as illustrated in **Figure 2**b and e. The sizes of the nanotwins are

Figure 1. LM microstructures of austenitic stainless steel – cross-sections a) annealed, b) RT_HE, c) HOT_HE.

diverse – one can distinguish first-order twins of an average length of about 400 nm and second-order twins (inside the previous ones) of an average length of about 40 nm. The average distance between the twin boundaries is about 30 nm. Hot HE makes it possible to obtain a more equiaxial microstructure when observed in cross-section, with subgrains of 300 nm in diameter varying in shape and in the structure of their sub-boundaries (Figure 2a, c, d). It can be thus concluded that the samples differ significantly in terms of their grain boundaries, that is, twin boundaries (TB) are dominant in the RT_HE sample, while low-angle grain boundaries (LAGB) and high-angle grain boundaries (HAGB) are characteristic for the HOT_HE and annealed samples, respectively. A detailed analysis of microstructures in the austenitic stainless steel 316LVM produced by HE at RT and elevated temperature can be found elsewhere.[38]

It should also be noted that the samples differ not only in their grain boundary characteristics, but also in their specific surface area (area per unit volume), which can be estimated using the following simple formula:

$$Sv = 2P_L, \tag{1}$$

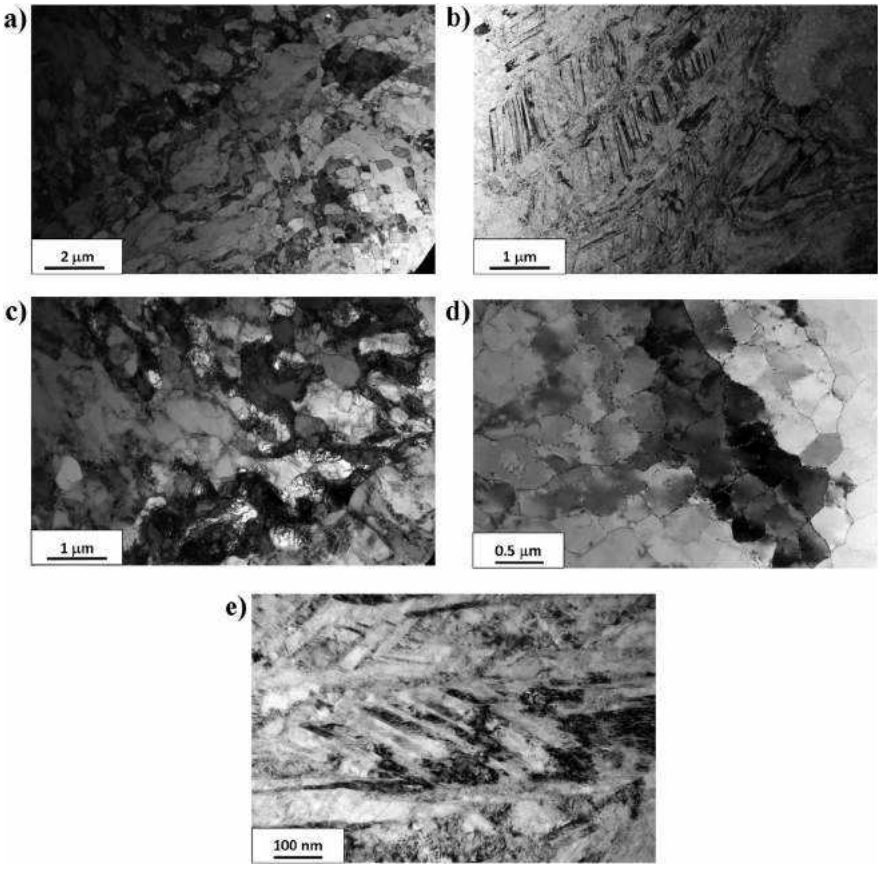

Figure 2. TEM microstructures of austenitic stainless steel – cross-sections. a) HOT_HE-general view, b) RT_HE- general view, c) and d) subgrains of various shapes in HOT_HE, e) nanotwins in RT_ HE.

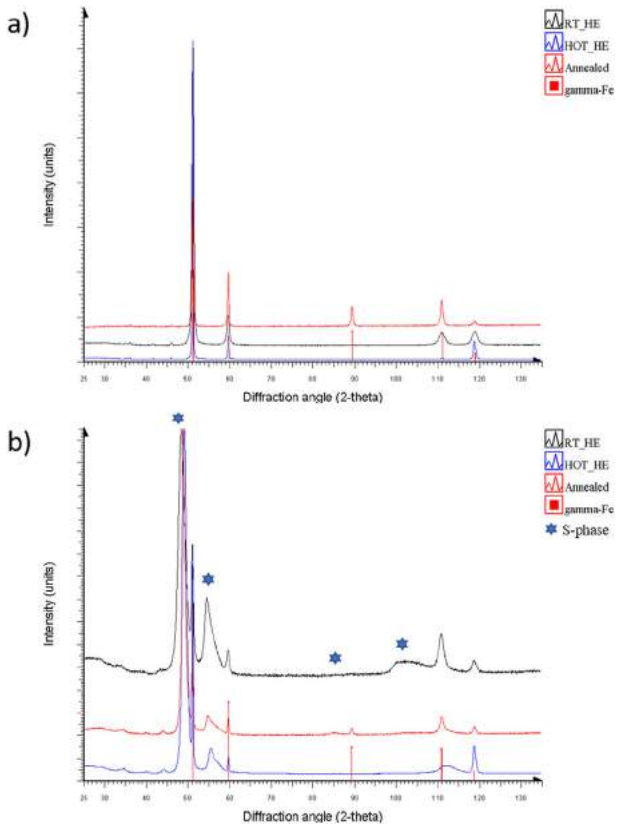

Figure 3. Phase composition of substrates a) and nitrided layers b) in annealed, RT_HE and HOT_HE samples.

where P_L is the density of intersection points of the grain boundaries with lines randomly piercing the surface of the grain boundaries in the volume of a polycrystal.[39] The specific surface area can be calculated as 67, 6.7×10^3, and 6.67×10^4 mm^{-1} for the annealed, HOT_HE and RT_HE samples, respectively.

3.2. X-Ray Analysis

Before nitriding, the investigated steel consisted only of an austenitic (γ) phase as visible in **Figure 3**a). One should also notice that as a result of HE samples are highly textured with the privileged orientations <111> and <100> parallel to extrusion direction. This indicates that no phase transformation occurs during hydrostatic extrusion, neither at room nor elevated temperatures. It is well-known that nitriding leads to the formation of a new phase called S-phase or expanded austenite (γ_N), which is a solid solution of nitrogen in austenite. Apart from this phase, other phases such as iron nitrides γ'-Fe_4N or ε-$Fe_{2,3}N$, chromium nitrides CrN and Cr_2N can be created.[40] The precipitation of chromium nitrides increases hardness but severely reduces corrosion resistance.

XRD analysis revealed that a γ_N-phase formed in all samples (Figure 3b). All of the γ_N-phase peaks were shifted to lower angles compared the austenite phase peaks, which indicates lattice expansion in the nitrided layer. In the literature, the γ_N-phase is best described by a special triclinic (t) crystalline structure with a distortion ε of the lattice angles due to the presence of nitrogen in solid solution.[17] The location of the γ_N-phase peaks is almost the same in the annealed and HOT_HE samples, but is significantly shifted to lower diffraction angles for the RT_HE sample, which suggests that this sample stores a higher number of nitrogen atoms. In the XRD diffraction patterns, one can also notice peaks corresponding to the γ-phase, which come from the substrate and indicate the relatively low thickness of the nitrided layers (the signal is gathered from a thickness much greater than the thickness of the layer). It should also be underlined that there are no other peaks beside γ and γ_N – particularly, there is no evidence of either CrN or α' martensitic phases.

3.3. Thickness of the Layers

Layer thickness can be evaluated in two ways: 1) by measuring the thickness of the γ_N-phase on the cross-sections observed in SEM, or 2) by determining the nitrogen depth profiles by AES. SEM images of nitrided layers formed on the three types of substrates during nitriding for 5 h are shown in **Figure 4**. In these figures, good quality continuous γ_N-phase layers are clearly visible. Surprisingly, only minor differences in the layer thickness can be seen. The thinnest layer was formed on the annealed sample, and does not exceed 5 μm. The thickness of the nitrided layers on the HE processed samples is slightly above 5 μm.

To further investigate the layers, nitrogen depth profiles were determined using AES; these are presented in **Figure 5**. An inspection of the figures shows that nitrogen diffuses a bit deeper than throughout the γ_N-phase. The nitrogen-enriched

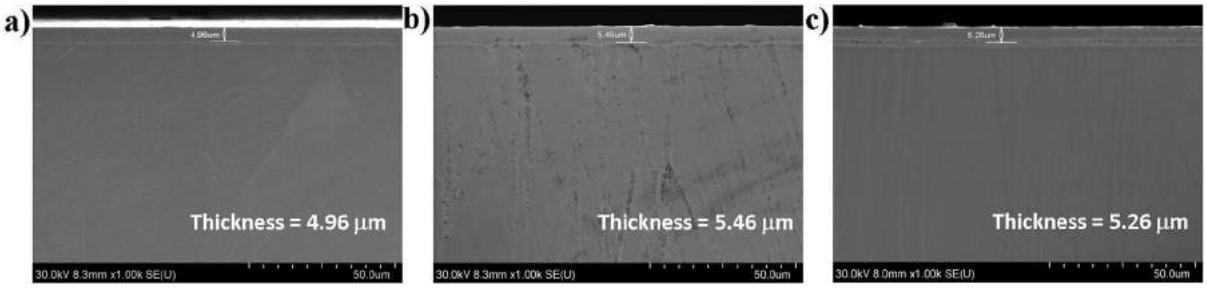

Figure 4. Cross-sections of nitrided layers formed in a) annealed, b) HOT_HE, c) RT_HE samples; SEM-SE mode.

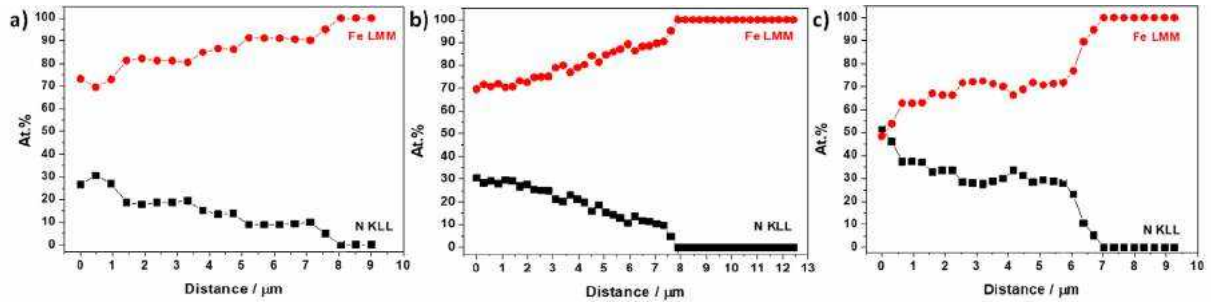

Figure 5. Nitrogen depth profiles formed in a) annealed, b) HOT_HE, c) RT_HE samples.

layer has a depth of 8 μm for the annealed and HOT_HE samples, and 7 μm for the RT_HE sample. The surface concentration of nitrogen is the highest (about 50 at%) for the RT_HE sample, and the lowest for the annealed sample (about 25 at%). The HOT_HE sample possesses about 30 at% of nitrogen close to the surface. The concentration of nitrogen decreases with increasing distance from the surface, but the shape of the profiles differs significantly. For the annealed sample, the nitrogen concentration decreases gradually and the curve slope is the highest. On the other hand, in the RT_HE sample the curve of nitrogen concentration is more flat until a depth of 6 μm, and thereafter decreases rapidly.

The areas below the concentration curves correspond to the amount of nitrogen diffused into the materials. It can be thus concluded that, although the thicknesses of the layers are similar, the amount of nitrogen introduced into the layers differs significantly, and is the highest for the RT_HE sample and the lowest for the annealed sample.

3.4. Microstructure Observations After Nitriding

Microstructures of nitrided layers and substrates in a BSE-mode are presented in **Figure 6**a–c. Additionally, thin lamellae were cut by means of a focused ion beam to reveal the microstructure of the S-phase. During this procedure defects, are introduced in the microstructure, and for this reason the density of dislocations created in the nitrided layers was not analyzed. The microstructures revealed are shown in Figure 6d–f). Firstly, it should be underlined that there is no change in the microstructure of the substrates, which indicates that nitriding at 430 °C preserves the UFG and NC grain structure produced during HE processing. Secondly, during nitriding of the annealed and HOT_HE, twins were formed in the S-phase. In the RT_HE sample, twins were induced during deformation, so it is difficult to confirm whether they were also introduced by nitriding. Furthermore, the diffraction patterns collected for all the samples reveal the presence of an austenitic phase. No

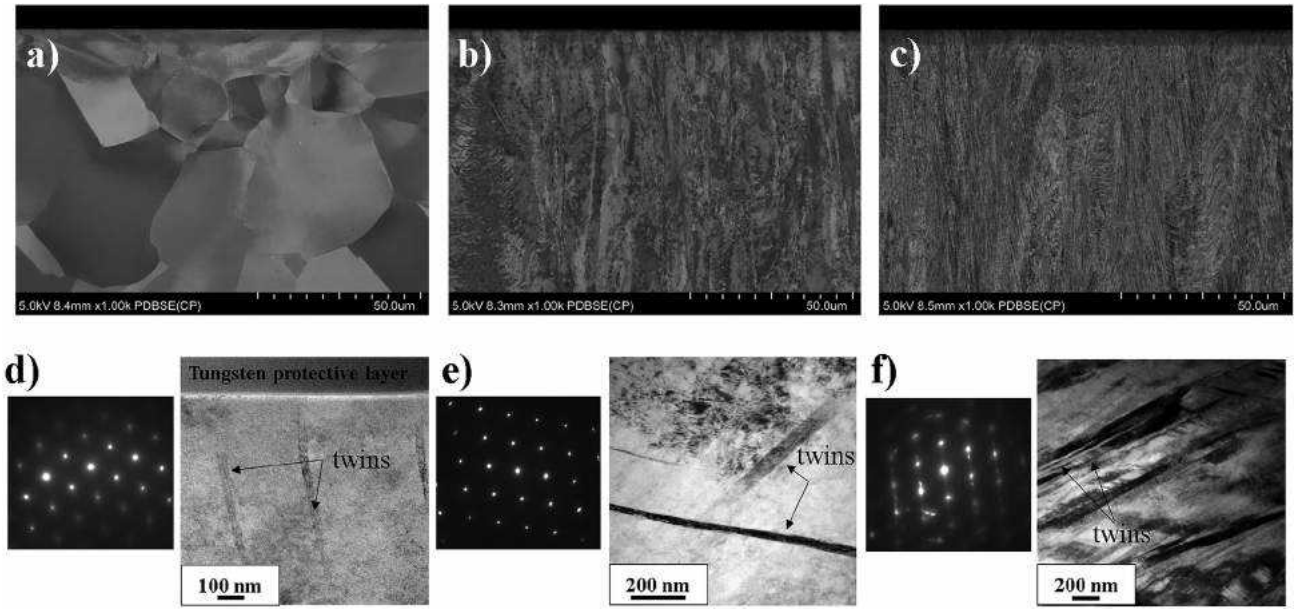

Figure 6. Global view of microstructures of nitrided layers and substrates in a) annealed, b) HOT_HE, c) RT_HE samples (SEM-BSE mode); microstructures of S-phase formed in a) annealed, b) HOT_HE, c) RT_HE samples with corresponding selected area diffraction patterns (SAED) in the orientation [110] (TEM).

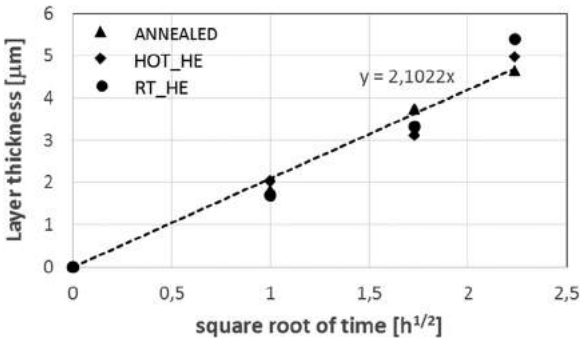

Figure 7. Time dependence of S-phase layer thickness.

kinematically forbidden {100} type spots were detected, contrary to.[41] Additionally, the diffraction pattern for the RT_HE sample reveals spots confirming the presence of twins.

An analysis of the layer growth kinetics revealed that the parabolic growth law typical of diffusion processes is obeyed by all the samples, as illustrated in **Figure 7**, which describes the time dependence of the thickness of the expanded austenite. In addition, the growth constant is the same for all the samples, which indicates that the same diffusional mechanism controls the nitrided layer growth. The growth law determined from the plots is similar for all samples, and can be given by Equation 2:

$$u = 2,1\ \sqrt{t} \tag{2}$$

where: u – layer thickness, t – nitriding time. Assuming that the nitrogen diffusion proceeds through the layer of expanded austenite, the effective diffusion coefficient of nitrogen in the expanded austenite can be determined by combining Equations 1 and 2[42]:

$$u = 2\sqrt{D_{\text{eff}} * t} \tag{3}$$

Thus, the value of D_{eff} obtained equals $2.8 \times 10^{-12}\,\text{cm}^2\,\text{s}^{-1}$, which is in agreement with other works on the nitriding of coarse-grained austenitic stainless steels. For instance, Keddam et al.[43] reported a value of $1.95 \times 10^{-12}\,\text{cm}^2\,\text{s}^{-1}$ for nitriding at 380 °C using a gas mixture of $85\%N_2 + 15\%H_2$ and 11.1×10^{-12} $\text{cm}^2\,\text{s}^{-1}$ for nitriding at 420 °C using a gas mixture of 90% $N_2 + 10\%H_2$. Moskalioviene et al.[44] evaluated the nitrogen diffusion coefficient in AISI 316 L stainless steel at 400 °C treated by the plasma nitriding process using a gas mixture of (60% $N_2 + 40\%H_2$), and obtained a value of $4.8 \times 10^{-12}\,\text{cm}^2\,\text{s}^{-1}$. It seems, therefore, that although the microstructure of the substrates are substantially different in our case, the layer growth is controlled by the volume diffusion. However, substantial differences in depth profiles suggest different diffusion paths.

4. Discussion

The nitrided layers obtained in the present study look very dense and uniform, with a thickness of up to 5 µm for 5 h of nitriding at 430 °C. In **Table 1**, the thicknesses of the plasma nitrided layers formed on austenitic stainless steels taken from literature data and the present study are summarized, depending on processing conditions, that is, temperature, time, and gas mixture. It is generally accepted that a higher nitriding temperature facilitates diffusion processes and that a thicker layer is formed. Also, diffusion processes are time-controlled, and the longer processing time the thicker the layer. However, one should also note the role of the gas mixture. Negm investigated the effect of (H_2/N_2) pressure ratios on the plasma nitriding of 304 steel, and found that the addition of hydrogen up to 50% might improve the efficiency of plasma nitriding.[45] It has also been shown that the addition of hydrogen gas to nitrogen gas provides a more effective cleaning of the treated samples.[46] Regarding the results obtained in the present study, it can be concluded that they are very similar to other nitriding experiments performed at similar process parameters.

In the literature, it is suggested that the nitrided layer formed on materials having a refined microstructure is thicker that that formed on microcrystallined materials.[20–30] This is due to the fact that non-equilibrium grain boundaries, triple junctions, and high density of dislocations at grain boundaries as well as within grains promote the diffusion of nitrogen. Moreover, in many cases a martensite phase is created during deformation, which was not the case here. It is reported that the diffusion of nitrogen in martensite is much faster than in austenite. In the present

Table 1. Thicknesses of the plasma nitrided layers formed on austenitic stainless steels depending on processing conditions, that is, temperature, time, and gas mixture

Steel	Nitriding temperature [°C]	Nitriding time [h]	Gas mixture	Layer thickness [µm]	Ref.
316LM	380	0.5	$85\%N_2 + 15\%H_2$	1.9	[47]
		8		4.3	
316 L	420	8	$90\%N_2 + 10\%H_2$	9.7	[43]
304 L	420	0.5	NH_3	2.3	[48]
316L	400	0.5	$25\%N + 75\%H_2$	5	[49]
316L	440	6	$50\%N_2 + 50\%H_2$	4	[50]
316L	400	5	$80\%N_2 + 20\%H_2$	5.7	[7]
321	500	5	$20\%N_2 + 80\%H_2$	12	[51]
316 LVM	430	5	$25\%N_2 + 75\%H_2$	5	This study

experiment, it was noticed that slightly thicker S-phase are present in the HE-processed samples than in the annealed ones. However, one can notice that the differences in the thickness of the layers between the annealed sample and the RT_HE sample were not as profound as in the literature. In addition, an analysis of the layer growth kinetics revealed that the parabolic growth law typical of diffusion processes is obeyed by all the samples as presented in Section 3.4.The growth controlled by the volume diffusion is typical of coarse-grained materials (the annealed sample in our case) since the amount of grain boundaries is insignificant and their role can be neglected. In the case of the HE-processed samples, the specific surface area of the grain boundaries increased enormously, as calculated in Section 3.1. Normally, such an increase results in faster diffusion and a much thicker layer. However, the grain structures induced by HE are very specific. For the HOT_HE sample, an array of sub-boundaries with a low misorientation angle was observed, while for the RT_HE sample, the microstructure consists mostly of nanotwins. In terms of diffusion processes, high-angle random boundaries are considered as a disordered phase where the diffusion is accelerated, while the special boundaries constitute a potential zone for trapping due to the high density of trapping sites. When an nitrogen atom reaches a special boundary (twin or dislocation type) is trapped in specific sites and as a result further diffusion does not proceed along boundary but inside grains, which explains higher nitrogen concentration in the layers formed on HE processed samples and similar layer thickness. It has also been reported that the diffusivity of highly defected twin boundaries is much lower than the diffusivity of high-angle grain boundaries, and higher than for low-angle grain boundaries.[52] In our study, the nitriding process was performed at 450 °C. At this temperature, one could expect that a process of relaxation of the twin boundaries occurred. It is well-known that diffusion along relaxed twin boundaries is hardly measurable. For this reason, twin boundaries do not accelerate the diffusion of nitrogen. Therefore, during the nitriding of the HE-processed samples, nitrogen atoms are trapped at the grain boundaries (either low-angle or twin) and do not migrate along them. The major diffusion stream is across grain interiors, and thus we cannot detect differences in layer thickness, although the substrate microstructure is much more defective. It can thus be concluded that grain refinement does not always result in faster diffusion, which depends on specific defect types and their arrangements.

It should be noted that texture may also play a role. Some publications show anisotropic diffusion for differently oriented grains in Ni and steel alloys.[53,54] Nitrogen prefers to move along the {200} planes. The HE processed samples are highly textured, with the main texture component being a <111> fiber. For such an orientation, all of the {200} planes are inclined by 55° to the direction of layer growth.

5. Conclusions

1) Low-temperature plasma-assisted nitriding was successfully applied to UFG and NC austenitic stainless steel with no major changes in the substrate's microstructure.
2) Uniform S phase layers were formed on CG, UFG, and NC samples, with only minor differences in their thickness.
3) Profound differences were observed in the nitrogen depth profiles, suggesting that although the growth kinetics is controlled by the same mechanism (i.e., volume diffusion), diffusion proceeds along different paths in materials differing in their microstructure.
4) The lack of differences in the thickness of the nitrided layers was attributed to the specific microstructures of the HE-processed samples, that is, the presence of nanotwins and dislocation boundaries instead of general grain boundaries.

Acknowledgement

This work was supported by Polish National Science Center project OPUS No. UMO-2013/11/B ST8/03641. The authors are grateful to Professor Marcin Pisarek from the Institute of Physical Chemistry Polish Academy of Sciences in Warsaw for his help in AES analysis and interpretation.

Conflict of Interest

The authors declare no conflict of interest.

Keywords

Austenitic stainless steel, hydrostatic extrusion, low temperature plasma-assisted nitriding

Received: November 27, 2017
Revised: January 28, 2018
Published online:

[1] M. Olejnik, T. Fraczek, *Inz. Mat.* **2008**, *6*, 997.
[2] M. A. Fontes, R. G. Pereira, F. A. P. Fernandes, L. C. Casteletti, P. A. de Paula Nascente, *J. Mater. Res. Technol.* **2014**, *3*, 210.
[3] Y. Li, L. Wang, J. Xu, D. Zhang, *Surf. Coat. Tech.* **2012**, *206*, 2430.
[4] Y. Hoshiyama, R. Mizobata, H. Miyake, *Surf. Coat. Tech.* **2016**, *307*, 1041.
[5] G. Y. Li, M. K. Lei, *J.M.P.T.* **2017**, *26*, 418.
[6] V. Singh, K Marchev, C. V Cooper, E. I Meletis, *Surf .Coat. Tech.* **2002**, *160*, 249.
[7] F. Borgioli, E. Galvanetto, T. Bacci, *Vacuum*, **2016**, *127*, 51.
[8] E. Menthe, A. Bulak, J. Olfe, A. Zimmermann, K. T. Rie, *Surf. Coat. Tech.* **2000**, *133–134*, 259.
[9] M. Yu. Smolyakova, D. S. Vershinin, Y. R. Kolobov, S. V. Chernikov, O. V. Stognei, I. M. Tregubov, *I norg. Mater.* **2012**, *3*, 440.
[10] Y. Sun, T. Bell, *Wear.* **1998**, *218*, 34.
[11] E. Menthe, K. Rie, *Surf. Coat. Tech.* **1999**, *119*, 199.
[12] X. Qin, X. Guo, J. Lu, L. Chen, J. Qin, W. Lu, *J. Alloys Compd.* **2017**, *698*, 1094.
[13] R. Djellal, A. Saker, B. Bouzabata, D. E. Mekki, *Surf. Coat. Tech.* **2017**, *325*, 533.
[14] W. J. Yang, M. Zhang, Y. H. Zhao, M. L. Shen, H. Lei, L. Xu. J. Q. Xiao, J. Gong, B. H. Yu. C. Sun, *Surf. Coat. Tech.* **2016**, *298*, 64.
[15] T. Czerwiec, N. Renevier, H. Michel, *Surf. Coat. Tech.* **2000**, *131*, 267.
[16] H. Ferkel, Y. Estrin, C. Blawert, R. Z. Valiev, *Surf. Coat. Tech.* **2003**, *174*, 1164.

[17] D. Manova, S. Mandl, H. Neumann, B. Rauschenbach, *Surf. Coat. Tech.* **2007**, *201*, 6686.
[18] H. Ferkel, M. Glatzer, Y. Estrin, R. Z. Valiev, C. Blawert, B. L. Mordike, *Mater. Sci. Eng.* **2003**, *348*, 100.
[19] H. Ferkel, M. Glatzer, Y. Estrin, R. Z. Valiev, *Scr. Mater.* **2002**, *46*, 623.
[20] W. P. Tong, N. R. Tao, Z. B. Wang, J. Lu, K. Lu, *Science* **2003**, *299*, 686.
[21] R. Sitek, H. Matysiak, Z. Pakieła, K. J. Kurzydłowski, *Inz. Mat.* **2012**, *3*, 169.
[22] T. Balusamy, T. S. N. S. Narayanan, K. Ravichandran, I. S. Park, M. H. Lee, *Mater. Charact.* **2013**, *85*, 38.
[23] J. Biehler, H. Hoche, M. Oechsner. *Surf. Coat. Tech.* **2017**, *313*, 40.
[24] Y. Lin, J. Lu, L. Wang, T. Xu, Q. Xue, *Acta Mater.* **2006**, *54*, 5599.
[25] M. Jayalakshmi, P. Huilgol, B. R. Bhat, K. U. Bhat, *Mater. Des.* **2016**, *108*, 448.
[26] M. Chemkhi, D. Retraint, A. Roos, C. Garnier, L. Waltz, C. Demangel, G. Proust, *Surf. Coat. Tech.* **2013**, *221*, 191.
[27] A. M. Gatey, S. S. Hosmani, C. A. Figueroa, S. B. Arya, R. P. Singh, *Surf. Coat. Tech.* **2016**, *304*, 413.
[28] M. Chemikhi, D. Retraint, A. Roos, C. Garnier, L. Waltz, C. Demangel, G. Proust, *Surf. Coat. Tech.* **2013**, *221*, 191.
[29] M. Golzar Shahri, M. Salehi, S. R. Hosseini, M. Naderi, *Surf. Coat. Tech.* **2017**, *310*, 231.
[30] S. J. Li, L. Wang, J. C. Sun, Z. K. Hei, *Surf. Coat. Tech.* **2005**, *195*, 81.
[31] A. Etienne, B. Radiguet, C. Genevois, J.-M. le Breton, R. Valiev, P. Pareige, *Mater. Sci. Eng. A* **2010**, *527*, 5805.
[32] S. Scheriau, Z. Zhang, S. Kleber, R. Pippan, *Mater. Sci. Eng.* **2011**, *528*, 2776.
[33] W. Pachla, J. Skiba, M. Kulczyk, S. Przybysz, M. Przybysz, *Mater. Sci. Eng.* **2014**, *615*, 116.
[34] A. Vorhauer, S. Kleber, R. Pippan, *Mater. Sci. Eng.* **2005**, *410*, 281.
[35] A. T. Krawczyńska, T. Brynk, S. Gierlotka, E. Grzanka, S. Stelmakh, B. Pałosz, M. Lewandowska, K. J. Kurzydłowski, *Mech. Mater.* **2013**, *67*, 25.
[36] F. K. Yan, G. Z. Liu, N. R. Tao, K. Lu, *Acta Mater.* **2012**, *60*, 1059.
[37] K. Lu, F. K. Yan, H. T. Wang, N. R. Tao, *Scripta Mater.* **2012**, *66*, 878.
[38] A. T. Krawczynska, W. Chrominski, E. Ura-Binczyk, M. Kulczyk, M. Lewandowska, *Mater. Des.* **2017**, *136*, 34.
[39] K. Kurzydlowski, B. Ralph, *The Quantitative Description of the Microstructure of Materials*, CRC Press, Boston **1995** p. 122.
[40] E. De Las Heras, G. Ybarra, D. Lamas, A. Cabo, E. L. Dalibon, S. P. Brühl, *Surf. Coat. Tech.* **2017**, *313*, 47.
[41] D. Stroz, M. Psoda, *J. Microsc.* **2010**, *237*, 227.
[42] P. Shewmon, *Diffusion in Solids*, Minerals, Metals and Materials Society, USA, **1999**.
[43] M. Keddam, G. Marcos, T. Thiriet, T. Czerwiec, H. Michel, *Matériaux Tech.* **2013**, *101*, 204.
[44] T. Moskalioviene, A. Galdikas, J. P. Rivière, L. Pichon, *Surf. Coat. Technol.* **2011**, *205*, 3301.
[45] N. Z. Negm, *Mater. Sci. Eng. B Solid-State Mater. Adv. Technol.* **2006**, *129*, 207.
[46] M. Hudis, *J. Appl. Phys.* **1973**, *44*, 1489.
[47] M. Keddam, T. Thiriet, G. Marcos, T. Czerwiec. *J. Min. Metall.* **2017**, *53*, 47.
[48] L. Wang, S. Ji, J. Sun, *Surf. Coat. Technol.* **2006**, *200*, 5067.
[49] L. Nosei, M. Avalos, B. J. Gómez, L. Nachez, J. Feugeas, *Thin Solid Films.* **2004**, *468*, 134.
[50] E. Skolek-Stefaniszyn, J. Kaminski, J. Sobczak, T. Wierzchon, *Vacuum.* **2010**, *85*, 164.
[51] M. Golzar Shahri, S. R. Hosseini, M. Salehi, M. Naderi, *Surf. Coat. Technol.* **2016**, *296*, 40.
[52] X. Sauvage, G. Wilde, S. V. Divinski, Z. Horita, R. Z. Valiev, *Mater. Sci. Eng.* **2012**, *540*, 1.
[53] H. He, J. Zou, C. Dong, T. Czerwiec, H. Michel, *Mater Sci. Forum* **2005**, *475*, 3669.
[54] H. Dong, *Int. Mater. Rev.* **2010**, *55*, 65.

Materials Science & Engineering A 840 (2022) 142874

Contents lists available at ScienceDirect

Materials Science & Engineering A

journal homepage: www.elsevier.com/locate/msea

The impact of high hydrostatic pressure maintenance after high-pressure torsion on phenomena during high hydrostatic pressure annealing

Agnieszka Teresa Krawczynska [a,*], Michael Kerber [b], Przemyslaw Suchecki [a], Barbara Romelczyk-Baishya [a], Maciej Oskar Liedke [c], Maik Butterling [c], Eric Hirschmann [c], Andreas Wagner [c], Malgorzata Lewandowska [a], Daria Setman [b]

[a] Warsaw University of Technology, Faculty of Materials Science and Engineering, Woloska 141, 02-507, Warsaw, Poland
[b] University of Vienna, Faculty of Physics, Boltzmanngasse 5, A-1090, Vienna, Austria
[c] Institute of Radiation Physics, Helmholtz-Zentrum Dresden – Rossendorf, Bautzner Landstraße 400, 01328, Dresden, Germany

ARTICLE INFO

Keywords:
Nanomaterials
High pressure torsion
Annealing
Positron annihilation
Defects

ABSTRACT

The impact of high hydrostatic pressure release after high-pressure torsion on subsequent high hydrostatic pressure annealing was analyzed by performing experiments on nanostructured Ni. Ni was deformed by high-pressure torsion at a pressure of 6 GPa in 5 turns. Directly after deformation, the pressure was reduced to 2 GPa, and under 2 GPa annealing at 400 °C was conducted for 5 min. For comparison, samples were also annealed under 2 GPa after deformation without loading between processes. Microhardness measurements, detailed microscopy observations and positron annihilation spectroscopy investigations were performed to elucidate the changes in the microstructures obtained after different processing routes. It is demonstrated that the pressure applied between deformation and high hydrostatic pressure annealing caused an increase in microhardness by 20% in comparison with pressure realize. Moreover, the pressure applied had an impact on the vacancy concentration, and consequently on the microstructure, leading to a smaller average grain size and a more heterogenous microstructure in terms of grain size, leaving space for optimizing the strength-ductility balance.

1. Introduction

Severe plastic deformation (SPD) processing contributes to the generation and storage of lattice defects such as vacancies and dislocations [1–3]. For relatively low strains, dislocation cell structures are created, and with increasing strain dislocations rearrange to form grain boundaries, including those of a non-equilibrium character [4]. The increase in dislocation density is accompanied with an increase in vacancy concentration. The defects introduced by SPD are essential, since they are responsible for unique mechanical and physical properties of SPD-processed materials.

The density of dislocations, which may reach an order of 10^{15} m^{-2} with an increasing applied strain in SPD, has been studied extensively using transmission electron microscopy [5,6]. However, the investigation of vacancies demands a more complex approach. For instance, a combined evaluation using X-ray line profile analyses, differential scanning calorimetry and residual electrical densitometry was used to reveal that, in the case of equal channel angular processed (ECAP) Cu - route B_c, a strongly enhanced concentration of vacancies is achieved in comparison with conventional deformation performed to a similar degree of deformation [7]. Similar investigations were performed on high-pressure torsion (HPT) processed Ni and Cu. They proved that, in HPT-processed Ni, in comparison with Cu the total maximum concentration of vacancies considering both agglomerates and single/double vacancies is higher. Moreover, single/double vacancies were observed in Ni, whereas in Cu only vacancy agglomerates were present [8]. It is highly probable that materials having a lower stacking fault energy (SFE) may be prone to form vacancy agglomerates. Moreover, the generation of a high density of vacancies during SPD processing was also proved by positron annihilation spectroscopy [9,10]. Vacancy

* Corresponding author.
E-mail addresses: agnieszka.krawczynska@pw.edu.pl (A.T. Krawczynska), michael.kerber@univie.ac.at (M. Kerber), przemyslaw.suchecki@pw.edu.pl (P. Suchecki), Barbara.Romelczyk-Baishya@pw.edu.pl (B. Romelczyk-Baishya), m.liedke@hzdr.de (M.O. Liedke), m.butterling@hzdr.de (M. Butterling), e.hirschmann@hzdr.de (E. Hirschmann), a.wagner@hzdr.de (A. Wagner), malgorzata.lewandowska@pw.edu.pl (M. Lewandowska), daria.setman@univie.ac.at (D. Setman).

https://doi.org/10.1016/j.msea.2022.142874
Received 9 December 2021; Received in revised form 19 February 2022; Accepted 21 February 2022
Available online 23 February 2022

agglomerates of 4–5 vacancies were found in the center of the HPT-processed Cu disc, while of 7–9 at the periphery. Generated vacancies are essential during the annealing of SPD-processed materials, as the rapid release of excess vacancies at the beginning of annealing is responsible for accelerated atomic mobility. Vacancies also govern the annihilation of edge dislocations by climbing. Moreover, the hardening by annealing effect arises from an agglomeration of deformation-induced vacancies [11].

Under the increased pressure during SPD processes, extra work must be applied to enable vacancies to migrate through the lattice. Consequently, the effective vacancy migration enthalpy increases, leading to a lower diffusion coefficient [12]. It was revealed by in situ X-ray diffraction experiments with the application of cooling of the anvils confining the sample after stopping deformation [13–15] that the size of the coherently scattering domains is not greatly influenced by the pressure release, whereas the dislocation density decreases significantly in the case of HPT-processed Cu. This phenomenon is observed to a lesser extent in HPT-processed Ni due to its higher activation enthalpy [14,15]. Moreover, in situ X-ray line profile analysis using synchrotron radiation proved for HPT-processed Ni that the higher the pressure applied during HPT, the higher the dislocation density and the earlier and more profound the annihilation of dislocations during pressure release [13].

Such changes in defect characteristics during high hydrostatic pressure release may have a major impact on the processes taking place during annealing, especially if the annealing is conducted under high hydrostatic pressure (HPA). During HPA, the movement of vacancies is made difficult, as are diffusion-govern processes. The annihilation of vacancies is impeded, because high hydrostatic pressure inhibits vacancy migration. Therefore, vacancy migration has an impact on the annihilation of edge dislocations by climbing and the microstructure transformation, as has been proved in previous HPA experiments [16–27]. These have shown that HPA hindered grain growth. However, the greater the deformation degree, the faster the grain growth under high hydrostatic pressure, as observed in conventionally deformed and HPT-processed austenitic stainless steel, which differed in the equivalent strain applied during deformation, after annealing at 900 °C for 10 min at 2 and 6 GPa [22]. Moreover, grain growth strongly depends on SFE [27]. It has been proved that factors such as higher vacancy concentration and lower deformation twins density were responsible for faster grain growth during HPA in Ni than in Ag of 125 and 16 mJ/m^{-2} SFE, respectively [28]. Additionally, the volume fraction of high-angle grain boundaries was influenced by HPA since HPA contributed to hindering the movement/creation of low-angle grain boundaries in HPT-processed austenitic stainless steel. Such boundaries are well-ordered and as a result their migration is only possible by the vacancy migration mechanism [20]. This mechanism is made difficult during HPA.

Therefore, this work was initiated in order to determine the impact of the pressure maintained between HPT and HPA on the microstructure and mechanical properties after HPA in comparison with the pressure release. It is important to underline that these modifications - pressure presence and release between deformation and HPA - have been applied for the first time in high hydrostatic pressure annealing experiments. It was only possible thanks to the application of high hydrostatic pressure device. A second goal was to evaluate the possibility of controlling grain size to achieve a better strength-plasticity balance, which is one of the most fundamental issues and long-standing conflicts in materials science and engineering.

2. Experimental

2.1. Materials and experiments

In this work, Ni of 99.99% purity was investigated. Spark erosion was used to cut disks of 0.8 mm in thickness and 10 mm in perimeter from Ni bars. Subsequently, the disks were annealed at 600 °C for 2 h to obtain a micro-grained microstructure, free from defects. The sample after conventional annealing has served as a reference sample.

The HPT experiments were performed at the Faculty of Physics at the University of Vienna. The disks were HPT-processed at a pressure of 6 GPa and a speed of 0.2 rpm up to 5 revolutions. The torsional shear strain was well defined as simple shear, γ, and was calculated according to the equation $\gamma = 2\pi \times r \times n/t$, where r, n and t are the distance from the torsion axes, the number of applied revolutions and the mean thickness of the sample, respectively. The equivalent strains $\epsilon_{eq} = \gamma/\sqrt{3}$, calculated at 0.5 and 3.5 mm from the torsion axis after 5 revolutions, were equal to 11 and 79, respectively. After HPT, the pressure was either decreased to 2 GPa or released completely and next the samples were annealed at 400 °C for 10 min under a pressure of 2 GPa in an HPT device. The heating and cooling rates during HPA were 1200 and 50 °C/min, respectively. The selection of experimental conditions was based on previous experiments [27]. Schematically the experiment is presented in Fig. 1.

Further on in this article, abbreviations will be applied for samples after various deformation and heat treatments as: Ni_HPT – after HPT; Ni_HPT_L_HPA – after HPT, loading under 2 GPa and HPA; Ni_HPT_U_HPA – after HPT unloading and HPA; Ni_A - after conventional annealing at 600 °C for 2h.

2.2. Analysis methods

a) Microhardness measurements

Microhardness measurements were performed on samples after conventional annealing, HPT and HPT combined with HPA using an MHT-4 microhardness tester manufactured by Paar equipped with a Zeiss microscope. The parameters of indentation were as follows: indentation force of 1 N, the indentation rate of 0.1 N/s and the holding time of 10 s. The indentations were done on the diameter of samples. The distance between indentations was 0.5 mm.

b) Variable energy positron annihilation lifetime spectroscopy

For variable energy positron annihilation lifetime spectroscopy (VEPALS) measurements, the samples after HPT, combined HPT and

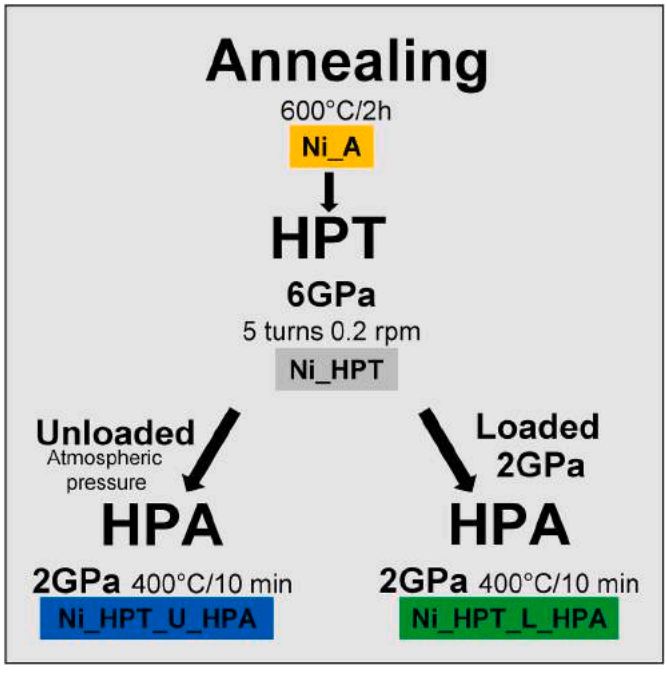

Fig. 1. Scheme of the experimental procedure.

HPA were polished under a conventional mechanical polishing procedure (firstly −10 min, under a load of 15 N, a diamond suspension: particles of 3 μm in diameter and subsequently - 10 min, under a load of 10 N, a diamond suspension: particles of 1 μm). Afterwards, polishing by vibrating polishing using a Buehler Vibromet in an amorphous colloidal silica suspension for 3 h was performed to remove defects introduced by conventional polishing. The VEPALS measurements were conducted at the Mono-energetic Positron Source (MePS) beamline at HZDR, Germany [29,30]. The beam size was approximately 5 mm in diameter. The measurements were performed in such a way that the beam center was located 2.5 mm from the sample center. There a positron lifetime was obtained as the time between positron generation and its annihilation with an electron inside the sample. Mono-energetic positrons were accelerated to discrete energies (Ep) and implanted in the sub-micrometer region below the sample surface. After a short diffusion, positrons annihilate in delocalized states between atoms and/or localize in vacancy like defects and their agglomerations, which serve as a very attractive trap for positrons. For the data acquisition a digital lifetime $CrBr_3$ scintillator detector was utilized, coupled to a Hamamatsu R13089-100 PMT. An in-house software employing a SPDevices ADQ14DC-2X digitizer with 14 bit vertical resolution and 2 GS/s horizontal resolution [31] was used. The overall time resolution was better than about 0.240 ns. The resolution function required for spectrum analysis uses two Gaussian functions with distinct intensities depending on the positron implantation energy, E_p, and appropriate relative shifts. The typical lifetime spectrum N(t) is described by $N(t) = \Sigma\ (1/\tau_i)\ I_i \exp(-t/\tau_i)$, where τ_i and I_i are the positron lifetime and relative intensity of the i-th component, respectively ($\Sigma I_i = 1$). All the spectra were deconvoluted, using PALSfit fitting software [32], into 3 discrete lifetime components, which directly evidence 2 different defect types (sizes). The 3rd component was neglected as a residual fingerprint of the surface ortho-Positronium (<0.5%). The corresponding relative intensities show the differences in concentration of each defect type (size). In general, the larger the open volume, the lower the probability and the longer it takes for positrons to be annihilated with electrons [33,34].

c) Microstructure observations

Microstructure observations in the plan view, 0.5 and 3.5 from the sample center on samples prepared by conventional grinding, polishing and vibrating polishing, as described in the VEPALS analysis and methods section, were performed using a SU8000 Hitachi scanning electron microscope (SEM) at 5 kV in the backscattered electron (BSE) mode. From the samples after HPT and combined HPT and HPA, lamellae were prepared approximately 3.5 mm from the sample center, parallel to the radius beneath the sample surface, by a NB5000 Hitachi focused ion beam (FIB). The lamellae were then observed in bright field (BF) mode by transmission electron microscopy (TEM) using a JEOL 1200 at 120 kV. The gathered microstructures were analyzed by stereological and image analysis methods that are elaborated at the Warsaw University of Technology, Faculty of Materials Science and Engineering [35,36]. Parameters such as the average grain size (calculated as the equivalent diameter Avg (d_2)), the standard deviation of the equivalent diameter SD(d_2), and the variation coefficient of the equivalent diameter CV(d_2) (calculated as the ratio of the standard deviation to the mean value) were determined.

d) Tensile tests

After conventional annealing, HPT and HPT combined with conventional annealing and HPA, uniaxial tensile tests were conducted at RT using a Zwick/Roell Z005 machine under the displacement control mode. An initial strain rate was $10^{-3}\ s^{-1}$. The digital image correlation method (DIC) was applied to measure strain. After each tensile test, parameters such as ultimate tensile strength (UTS), yield stress (YS), uniform elongation (Au), and total elongation (At) were determined. The minisamples of dimensions: a gauge section length of 2 mm and a cross section of 0.3 mm × 0.4 mm were cut.

3. Results

3.1. Microhardness measurements

The microhardness measurements after various deformations and annealing treatment are presented in Fig. 2. After HPT, the microhardness increased from 97 to 324 Hv0.1. Subsequent annealing under pressure decreased the microhardness to an average value of 160 Hv0.1. However, when the pressure was maintained between the HPT and annealing, the average microhardness reached a slightly higher value of 189 Hv0.1. It is important to underline that the SD of the microhardness of the loaded sample was two times greater. Additionally, the microhardness was measured for HPA samples at 0.5 and 3.5 mm from the center in order to verify what the impact of pressure was on a specific deformation degree. Similarly to the changes in the average microhardness values, the microhardness of the Ni_HPT_L_HPA was higher than for the Ni_HPT_U_HPA, at 178 and 149 Hv0.1, respectively, for 0.5 mm from the center and 205 and 175 Hv0.1, respectively, at 3.5 mm from the center.

3.2. Microstructure observations before HPA

Before the HPT experiments, Ni was annealed at 600 °C for 2 h to homogenize its microstructure, as presented in Fig. 3 a). After annealing, the average equivalent diameter was 31 μm. Subsequently, the HPT process was performed; it led to a refinement of grain size down to 140 nm on average (Fig. 3 b)). In the case of Ni_HPT microstructures are presented in the plan view and the cross section to enable the comparison in microstructures obtained by HPA.

3.3. Defects characterisation after HPT

Fig. 4 shows a depth profile of positron lifetime components and their relative intensities of the Ni_HPT sample surface from the depth of ~220 nm. Due to the relatively large density of Ni and the depth probing limitations of the PALS setup, only a depth of <400 nm could be investigated (the maximum penetration by positrons is about 2 × <z>). No reduced lifetime (no indication of positron annihilation at interatomic positions) was detected, which suggests a relatively large defect concentration. Spectra deconvolution leads to a positron lifetime τ_1 close to the literature value for Ni vacancy [37], but slightly lower, indicating mixed defect states with dislocations (mono-vacancy-dislocation complexes) [38,39]. The second lifetime

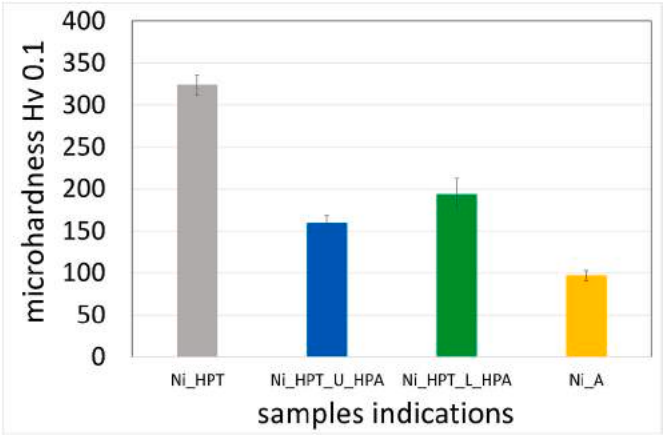

Fig. 2. Microhardness changes on the diameter of samples after various deformation and annealing treatments.

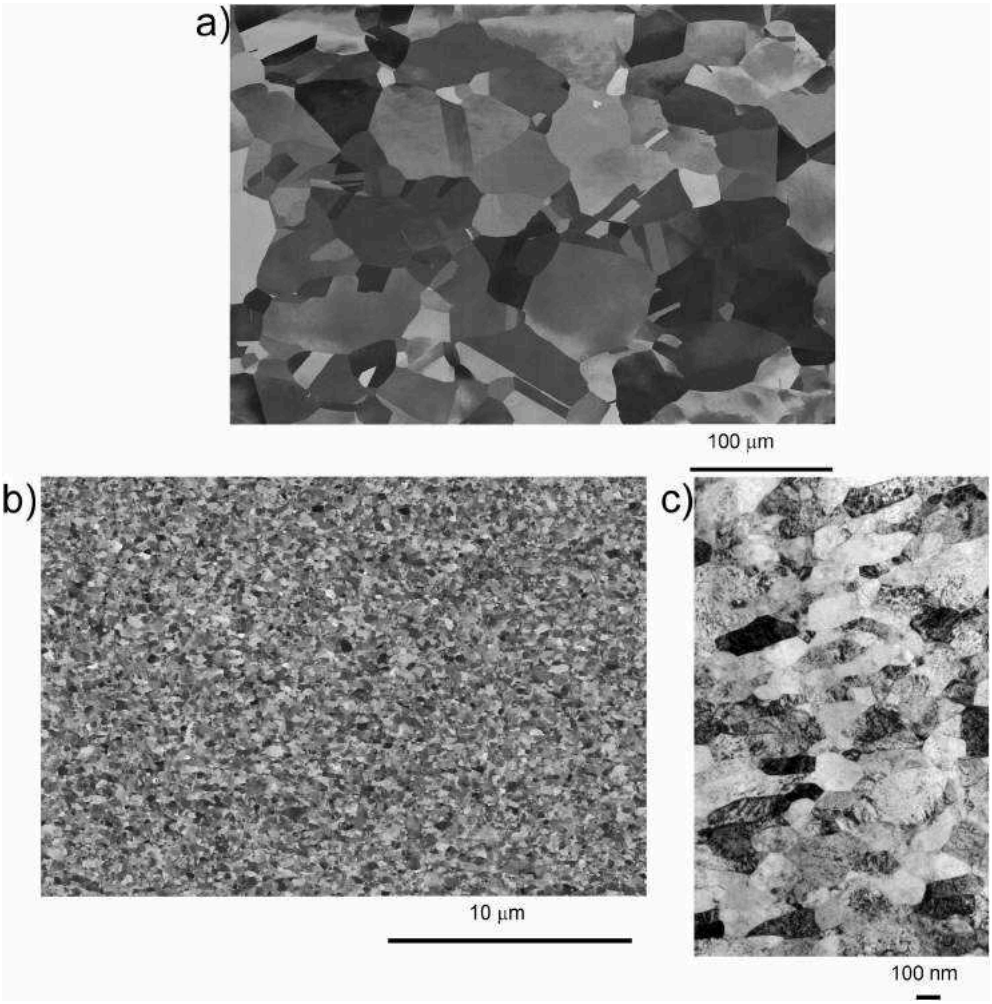

Fig. 3. Microstructures a) Ni_ A - plan view, b) Ni_HPT - plan view and c) Ni_HPT - cross section; a) and b) in BSE-mode, c) in BF-mode TEM.

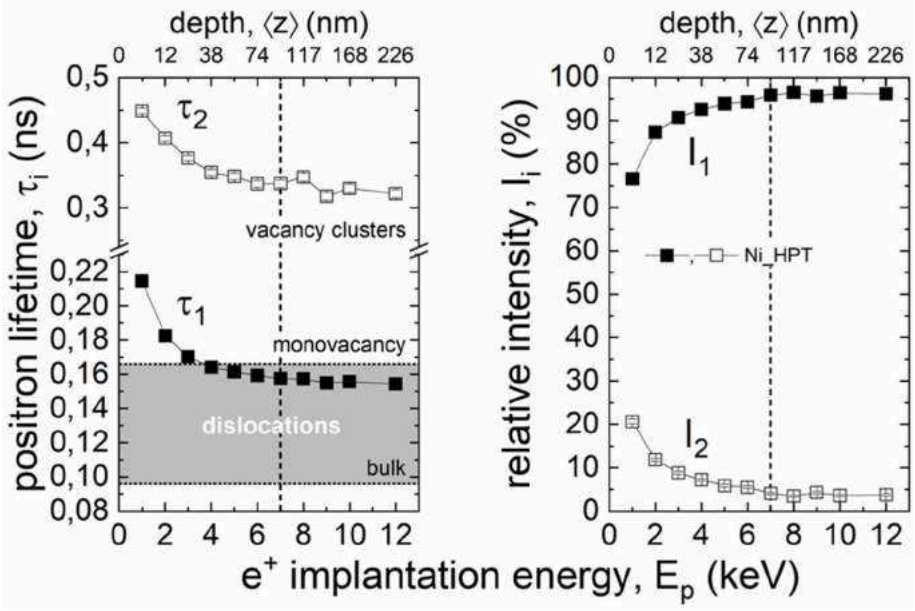

Fig. 4. Positron lifetime components τ_i and their relative intensities, I_i, as a function of positron implantation energy, E_p, and mean positron implantation depth, $\langle z \rangle$ for Ni_HPT. As a vertical line at $E_p = 7$ keV the sub-surface border is given. The vertical lines and grey area show the lifetime ranges for bulk, dislocations and monovacancies [31].

component τ_2 represents the superposition of surface states ($E_p < 7$ keV) and vacancy clusters [40,41]. One may expect to find vacancy clusters at grain boundaries, and the low intensity I_2 reflects their low density (a large overall size of crystallites). I_1 shows the tendency to increase with depth up to 95%, which reflects the decreasing signature of the surface and suggests that in the bulk material the main role is played by mono-vacancies associated with dislocations. These results are comparable with those obtained for HPT-processed Ni [41]. The large intensity of τ_1 suggests a large defect concentration, close to positron saturation trapping. The intensity of the component related to grain boundaries τ_2 is relatively low, which is in line with the general grain dimensions much larger than the positron diffusion length (estimated as not more than 20 nm for pristine sample). The fact that dislocations serve as positron traps in HPT-processed materials of relatively high melting temperature has been proved in the past [41].

3.4. Microstructure observations after HPT and subsequent HPA

The microstructures of the Ni samples after HPT and subsequent HPA with and without loading, observed 0.5 and 3.5 mm from the sample center, are presented in Fig. 5. The corresponding histograms of grain size distribution are shown in Fig. 6. The parameters characterising grain size and distribution are presented in Table 1. The results clearly show that the loading between HPT and HPA had an impact on the microstructure transformation. Firstly, in the case of Ni_HPT_U_HPA, the average equivalent diameter was greater than for Ni_HPT_L_HPA. It equalled 1.3 and 0.88 μm at 0.5 mm, and 0.85 and 0.51 μm at 3.5 mm from the center, respectively. Moreover, loading led to a more heterogeneous microstructure in terms of grain size. This was well reflected by CV(d_2), which was higher for Ni_HPT_L_HPA than Ni_HPT_U_HPA by 100 and 20% at 0.5 mm and 3.5 mm from the center, respectively. It seems that when in-between loading is applied nearer the center, the number of grains of an equivalent diameter below 500 nm drops at the expense of grains greater than 2 μm.

3.5. Defects characterisation after HPA

Up to 100 nm below the surface, Ni_HPT, Ni_HPT_U_HPA and Ni_HPT_L_HPA are characterised by comparable defect types and concentrations, as presented in Fig. 7 a). This phenomenon results from the surface preparation technique. However, approximately 100 nm below the surface one can clearly notice a difference between three samples. τ_1, representing monovacancy-dislocations complexes, has the highest intensity I_1 for Ni_HPT and the lowest for Ni_HPT_U_HPA. After HPA, τ_1 and I_1 slightly decreased, which indicates a reduction in the mono-vacancies associated with dislocations. For example, isolated

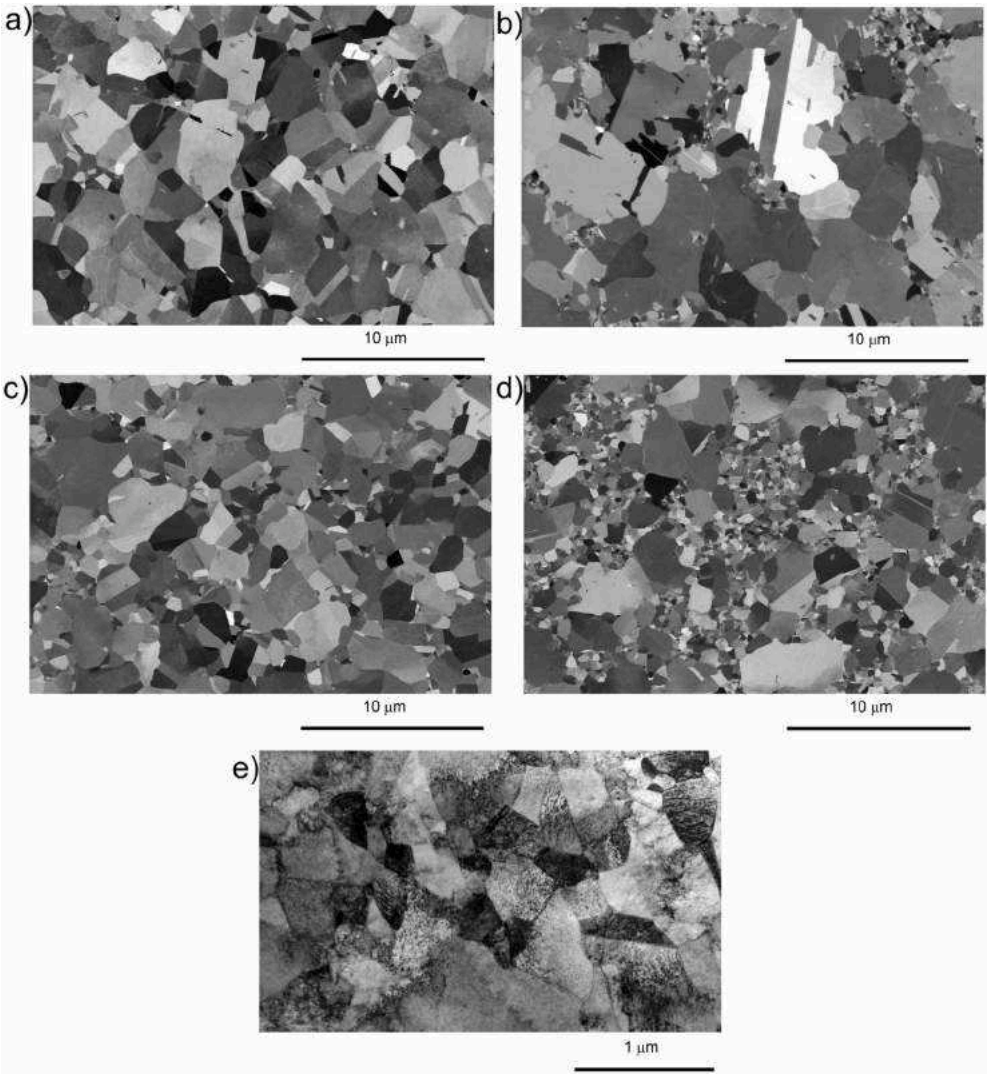

Fig. 5. Microstructures of Ni after HPT and subsequent HPA without a), c) and with b), d), e) loading after HPT; a)-D)-BSE-mode SEM, e) BF-mode TEM; a) and b) – 0.5 mm from the sample center ($\epsilon_{eq} = 11$), b), d, and e) – 3.5 mm from the sample center ($\epsilon_{eq} = 79$); a)-d) – plan view, e) cross section.

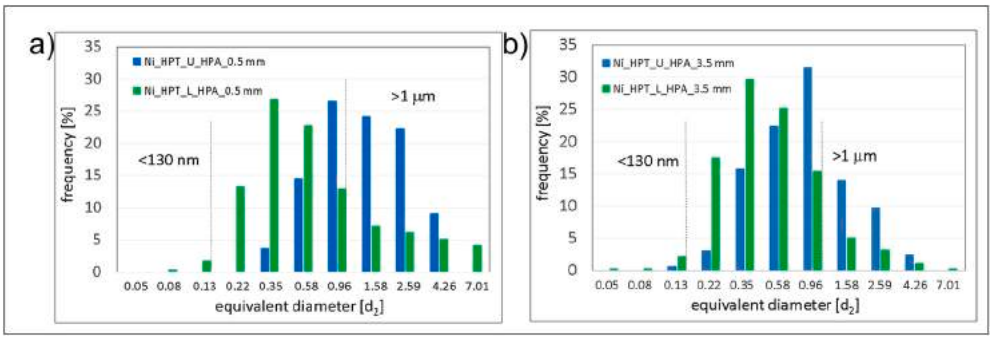

Fig. 6. Histograms of grain size distribution in Ni_HPT_L_HPA and Ni_HPT_U_HPA a) 0.5 mm ($\epsilon_{eq} = 11$) and b) 3.5 mm ($\epsilon_{eq} = 79$) from the sample center.

Table 1
Average equivalent diameter d_2, standard deviation SD (d_2), and coefficient of variation CV(d_2) of grains in the Ni_HPT_U_HPA and Ni_HPT_L_HPA samples.

Sample indication	Avg (d_2) [µm]	SD (d_2) [µm]	CV (d_2)
Ni_HPT_U_HPA – 0.5 mm from the center ($\epsilon_{eq} = 11$)	1.30	0.82	0.63
Ni_HPT_L_HPA– 0.5 mm from the center ($\epsilon_{eq} = 11$)	0.88	1.14	1.30
Ni_HPT_U_HPA– 3.5 mm from the center ($\epsilon_{eq} = 79$)	0.85	0.67	0.79
Ni_HPT_L_HPA– 3.5 mm from the center ($\epsilon_{eq} = 79$)	0.51	0.52	1.02

threading dislocations are normally shallow positron traps [42] and require a complex with a monovacancy to be detectable at room temperature. After HPA, a change in vacancy cluster size is detected as well. In Ni_HPT_L_HPA, larger vacancy agglomerations are found than in Ni_HPT_U_HPA.

3.6. Tensile tests

The stress–strain curves collected during RT tensile tests for Ni_HPT, Ni_HPT_L_HPA, Ni_HPT_U_HPA and Ni_A samples are shown in Fig. 8. The mean values (MV) and standard deviation (SD) of ultimate tensile strength (UTS), yield stress (YS), uniform elongation (Au), and total elongation (At) are presented in Table 2.

The results reveal that HPT increased the UTS from 349 after annealing to 1146 MPa. This value is in between the values reported in the literature, i.e. 1270 MPa [27] and 1015 MPa [43]. The results show that the loading applied between the HPT and HPA led to an increase in strength with a slight decrease in plasticity in comparison with Ni_HPT_U_HPA. This phenomenon can be explained by the greater volume of ultrafine grains in Ni_HPT_L_HPA than in Ni_HPT_U_HPA, which are responsible for higher strength.

It seems that by the proper selection of temperature and annealing pressure and with the application of loading between deformation and annealing, microstructures consisting of nanograins and micrograins of high strength (nanograins) and satisfactory ductility (micrograins) can be obtained. Creating such microstructures is one of the approaches that have been successfully applied to increase the plasticity of nanostructured and ultrafine grained materials [44].

The Hall-Petch plot summarizing the gathered data is presented in Fig. 9. It can be noticed that points representing Ni_HPT, Ni_HPT_U_HPA and Ni_A samples lie on the same trend line. However, the point representing the sample Ni_HPT_L_HPA is located slightly on the right side of the trend line. It shows that additional loading between HPT and HPA leads to the formation of unique microstructures.

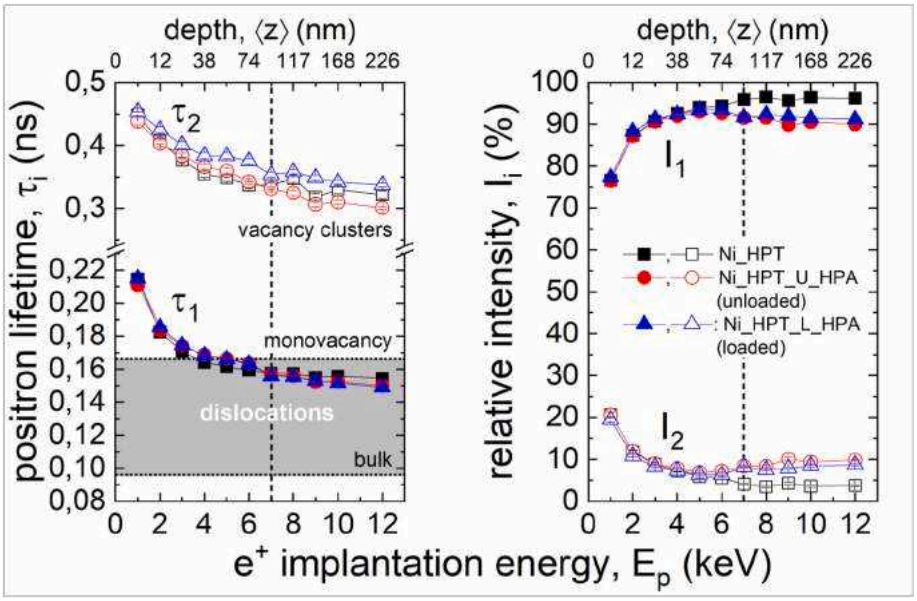

Fig. 7. Positron lifetime components τ_i and relative intensity, I_i, (a) as a function of positron implantation energy, E_p, and mean positron implantation depth, <z>, for Ni_HPT, Ni_HPT_U_HPA and Ni_HPT_L_HPA. The vertical line at $E_p = 7$ keV represents a sub-surface border. The vertical lines and grey area show lifetime ranges for the bulk, dislocations and monovacancies [31].

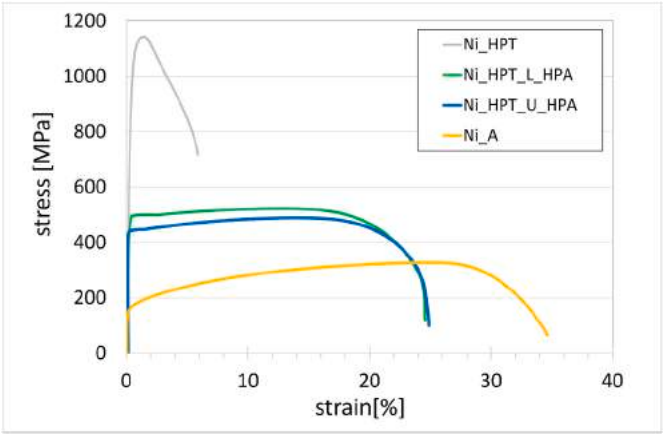

Fig. 8. Stress–strain curves collected during RT tensile tests for Ni_HPT, Ni_HPT_L_HPA, Ni_HPT_U_HPA and Ni_A samples.

Table 2
MV and SD of UTS, YS, Au, and At for Ni_HPT, Ni_HPT_L_HPA, Ni_HPT_U_HPA and Ni_A samples.

Parameter Sample indication	YS [MPa]		UTS [MPa]		Au [%]		At [%]	
	MV	SD	MV	SD	MV	SD	MV	SD
Ni_HPT	1049	6	1146	4	1.03	0.03	6.0	0.3
Ni_HPT_L_HPA	497	9	544	21	12.54	0.40	24.5	1.2
Ni_HPT_U_HPA	455	14	510	20	14.35	0.27	26.1	1.3
Ni_A	171	15	349	21	26.0	0.6	35.2	0.6

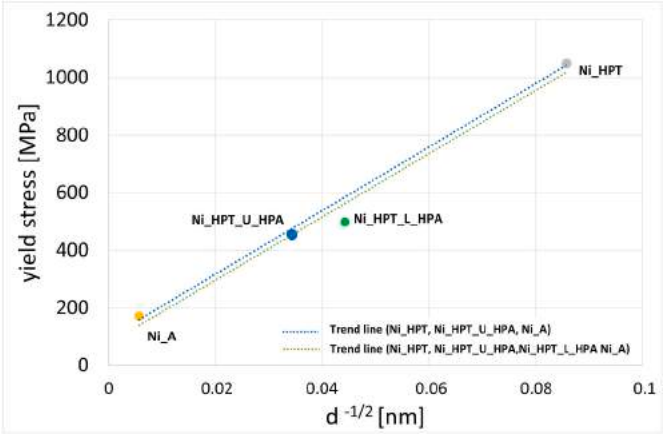

Fig. 9. Hall-Petch plot for Ni_HPT, Ni_ HPT_U_HPA, Ni_HPT_L_HPA and Ni_A samples.

4. Discussion

4.1. The impact of loading after HPT on microstructure transformation during HPA

Materials produced by SPD are usually less thermally stable than conventionally deformed materials because they have a higher stored energy in the form of lattice defects. The high hydrostatic pressure typical of HPT can increase the concentration of vacancies due to the limited atomic mobility that exists under such conditions. Therefore, during annealing after HPT, the atomic diffusion is enhanced significantly, since it is directly proportional to the concentration of vacancies [45]. Some SPD-processed materials can even exhibit self-annealing due to their stored energy and to their low melting temperature, which can accelerate recrystallization and grain growth [46,47].

Moreover, it is important to add that in SPD-processed materials some grain boundaries are what is known as 'non-equilibrium' grain boundaries. Non-equilibrium grain boundaries are specific grain boundaries that are described as those possessing an increased free energy that is the result of a high density of defects such as dislocations and vacancies, and consequently high residual microstrains [48]. These boundaries are characterised by enhanced diffusivity, which in turn can enhance grain growth. In SPD-processed pure fcc metals, the activation energy of recovery/recrystallization is approximately 0.5 ± 0.1 of self-diffusion, which well-corresponds with the value of activation energy of diffusion along grain boundaries and dislocations [49–51].

As expected, the thermal stability of the SPD-processed Ni was lower than that of the conventionally deformed material [52]. Previous experiments have shown that additional pressure during annealing - 2 GPa at 400 °C for 1 h - slowed down grain growth in HPT-processed Ni in comparison with atmospheric pressure annealing, so that the grain size after HPA reached approximately 70% of the grain size after conventional annealing [27]. Moreover, the process also affected the homogeneity of the microstructures by significantly increasing CV(d_2) [27]. This study proved that additional loading between deformation and annealing made it possible to preserve some of the vacancies generated during HPT - some, not all, since the HPT was performed at a pressure of 6 GPa and the HPA at a pressure of 2 GPa. The fact that in Ni_HPT_L_HPA the concentration of representing monovacancy-dislocations complexes was slightly higher than in Ni_HPT_U_HPA was confirmed by the VEPALS measurements. Moreover, the applied loading made the migration of released vacancies to grain boundaries difficult, so some of them might have agglomerated, creating larger vacancy clusters than those in Ni_HPT_U_HPA, as proved by the VEPALS, too. This means that, even though the vacancy concentration was higher in the loaded sample during HPA than in the unloaded sample, their migration to defect sinks, which in the case of HPT-processed materials are mainly grain boundaries and dislocations, was limited [53]. Consequently, the migration of grain boundaries was hindered, and Ni_HPT_L_HPA was characterised by a smaller average equivalent diameter than Ni_HPT_U_HPA.

It is also interesting that a more heterogeneous microstructure was created in Ni_HPT_L_HPA than in Ni_HPT_U_HPA. The fact that abnormal grain growth occurred in Ni_HPT_L_HPA can be deduced from the microstructure images, since abnormal grains demonstrate a high twin density, probably due to an increased grain boundary migration rate [54]. It might be that the distribution of vacancies within boundaries is orientation-dependent, combined with the presence of orientation gradients that promote selective grain growth [55]. Moreover, it may also result from the presence of some percentage of low-angle grain boundaries in the HPT-processed Ni [4]. Low-angle grain boundaries migrate only by the vacancy migration mechanism [20], which is strongly constarined during HPA. For this reason, in such areas grain growth can be restricted.

4.2. The impact of torsional shear strain on the microstructure transformation during HPA

This study made it possible to observe that the greater the torsional shear strain, and the further from the sample center, in the case of Ni_HPT_U_HPA and Ni_HPT_L_HPA the smaller the average grain size after annealing. The significantly enhanced thermal stability for higher strains is an interesting phenomenon, since during annealing under atmospheric pressure the inverse behaviour is usually observed. In Ag, Au and Cu after HPT being hold at RT for a long time, the softening turns out to be more distinct the nearer the sample edge [46]. However, the significantly enhanced thermal stability for higher strains in this study may be justified by the faster recovery of non-equilibrium grain boundaries under pressure for higher strains due to their enhanced diffusivity, as mentioned in Ref. [56]. The fact that materials deformed to higher strains show greater thermal stability than materials deformed to lower strains was also revealed on the example of profile-rolled (PR)

and HPT-processed austenitic stainless steel. In the former case, after conventional annealing for 10 min at 900 °C, grain growth was enhanced. This was due to the fact that the microstructure of PR-processed steel was heterogeneous. Areas with high local misorientations became the favoured sites for nuclei formation. In the case of HPT-processed austenitic stainless steel, normal grain growth was observed [22]. A similar phenomenon can also be observed in this study. After HPT, the higher the strains, the more refined and homogenous the microstructure [57], while homogeneity promotes slower grain growth under pressure. This is achieved because there is limited atomic mobility of vacancies under high pressure.

5. Conclusions

1. Additional loading under 2 GPa between deformations by HPT under 6 GPa and HPA under 6 GPa at 400 °C for 5min causes an increase in microhardness by 20% in comparison with no loading applied.
2. Additional loading under 2 GPa between deformation by HPT under 6 GPa and HPA under 6 GPa at 400 °C leads to a smaller average equivalent diameter and a more heterogenous microstructure in terms of grain size in comparison with no loading applied. Moreover, it leads to a higher concentration of representing monovacancy-dislocations complexes and larger vacancy clusters in comparison with no loading applied.
3. The greater the torsional shear strain, the smaller the grain size after HPA since there is limited atomic mobility under pressure in the homogeneous areas of samples.
4. Additional pressure between HPT and HPA may be successfully applied to modify the microstructure and obtain an optimised strength-plasticity balance.

CRediT authorship contribution statement

Agnieszka Teresa Krawczynska: Conceptualization, Methodology, Investigation, Writing – original draft, Writing – review & editing. **Michael Kerber:** Investigation, Conceptualization. **Przemyslaw Suchecki:** Investigation. **Barbara Romelczyk-Baishya:** Investigation. **Maciej Oskar Liedke:** Investigation, Visualization, Writing – original draft. **Maik Butterling:** Investigation. **Eric Hirschmann:** Investigation. **Andreas Wagner:** Investigation. **Malgorzata Lewandowska:** Supervision. **Daria Setman:** Conceptualization, Supervision.

Declaration of competing interest

The authors declare that they have no known competing financial interests or personal relationships that could have appeared to influence the work reported in this paper.

Acknowledgements

Parts of this research were carried out at ELBE at the Helmholtz-Zentrum Dresden - Rossendorf e. V., a member of the Helmholtz Association. We would like to thank the facility staff for assistance, especially Ahmed G. Attallah.

The raw/processed data required to reproduce these findings cannot be shared at this time due to technical or time limitations.

References

[1] R.Z. Valiev, R.K. Islamgaliev, I.V. Alexandrov, Bulk nanostructured materials from severe plastic deformation, Prog. Mater. Sci. (2000), https://doi.org/10.1016/S0079-6425(99)00007-9.
[2] Y.T. Zhu, T.G. Langdon, The fundamentals of nanostructured materials processed by severe plastic deformation, J. Occup. Med. (2004), https://doi.org/10.1007/s11837-004-0294-0.
[3] R.Z. Valiev, Y. Estrin, Z. Horita, T.G. Langdon, M.J. Zehetbauer, Y.T. Zhu, Producing bulk ultrafine-grained materials by severe plastic deformation, J. Occup. Med. (2006), https://doi.org/10.1007/s11837-006-0213-7.
[4] X. Sauvage, G. Wilde, S.V. Divinski, Z. Horita, R.Z. Valiev, Grain boundaries in ultrafine grained materials processed by severe plastic deformation and related phenomena, Mater. Sci. Eng. 540 (2012) 1–12, https://doi.org/10.1016/j.msea.2012.01.080.
[5] X.H. An, S.D. Wu, Z.G. Wang, Z.F. Zhang, Significance of stacking fault energy in bulk nanostructured materials: insights from Cu and its binary alloys as model systems, Prog. Mater. Sci. (2019), https://doi.org/10.1016/j.pmatsci.2018.11.001.
[6] Y.B. Wang, J.C. Ho, Y. Cao, X.Z. Liao, H.Q. Li, Y.H. Zhao, E.J. Lavernia, S.P. Ringer, Y.T. Zhu, Dislocation density evolution during high pressure torsion of a nanocrystalline Ni-Fe alloy, Appl. Phys. Lett. (2009), https://doi.org/10.1063/1.3095852.
[7] E. Schafler, G. Steiner, E. Korznikova, M. Kerber, M.J. Zehetbauer, Lattice defect investigation of ECAP-Cu by means of X-ray line profile analysis, calorimetry and electrical resistometry, Mater. Sci. Eng. (2005), https://doi.org/10.1016/j.msea.2005.08.070.
[8] D. Setman, E. Schafler, E. Korznikova, M.J. Zehetbauer, The presence and nature of vacancy type defects in nanometals detained by severe plastic deformation, Mater. Sci. Eng. 493 (2008) 116–122, https://doi.org/10.1016/j.msea.2007.06.093.
[9] J. Čížek, M. Janeček, O. Srba, R. Kužel, Z. Barnovská, I. Procházka, S. Dobatkin, Evolution of defects in copper deformed by high-pressure torsion, Acta Mater. (2011), https://doi.org/10.1016/j.actamat.2010.12.028.
[10] J. Čížek, O. Melikhova, M. Janeček, O. Srba, Z. Barnovská, I. Procházka, S. Dobatkin, Homogeneity of ultrafine-grained copper deformed by high-pressure torsion characterized by positron annihilation and microhardness, Scripta Mater. (2011), https://doi.org/10.1016/j.scriptamat.2011.04.006.
[11] P. Cengeri, M.B. Kerber, E. Schafler, M.J. Zehetbauer, D. Setman, Strengthening during heat treatment of HPT processed copper and nickel, Mater. Sci. Eng. (2019), https://doi.org/10.1016/j.msea.2018.11.010.
[12] M.J. Zehetbauer, H.P. Stüwe, A. Vorhauer, E. Schafler, J. Kohout, The role of hydrostatic pressure in severe plastic deformation, Adv. Eng. Mater. (2003), https://doi.org/10.1002/adem.200310090.
[13] M. Kerber, F. Spieckermann, R. Schuster, B. Joni, N. Schell, E. Schafler, In-situ synchrotron profile analysis after high-pressure torsion deformation, Crystals (2019), https://doi.org/10.3390/cryst9050232.
[14] E. Schafler, Strength response upon pressure release after high pressure torsion deformation, Scripta Mater. (2011), https://doi.org/10.1016/j.scriptamat.2010.09.026.
[15] E. Schafler, Effects of releasing the hydrostatic pressure on the nanostructure after severe plastic deformation of Cu, Scripta Mater. (2010), https://doi.org/10.1016/j.scriptamat.2009.12.004.
[16] W. Lojkowski, D.A. Molodov, G. Gottstein, L.S. Shvidlerman, The mechanism of grain boundary migration in aluminium bicrystals, Mater. Sci. Forum 207–209 (1996) 537–540.
[17] L.S. Shvindlerman, U. Czubayko, G. Gottstein, D.A. Molodov, High pressure effect on grain boundary migration and mechanism of grain boundary migration, Mater. Sci. Forum 204–206 (1996) 45–54.
[18] A.F. Syrenko, G.P. Klinishev, V.T. Khoi, Recrystallization of copper under hydrostatic pressure up to 15kbar, J. Mater. Sci. 8 (1973) 765–769.
[19] L.E. Tanner, S.V. Radcliffe, Effect of hydrostatic pressure on the kinetics of recrystallization in high-purity copper, Acta Metall. Mater. 10 (1962) 1161–1169.
[20] V. Sursaeva, S. Protasova, W. Lojkowski, J. Jun, Microstructure evolution during normal grain growth under high pressure in 2-D aluminium foils, Textures Microstruct. (2008), https://doi.org/10.1155/tsm.32.175.
[21] A.T. Krawczynska, T. Brynk, S. Gierlotka, E. Grzanka, S. Stelmakh, B. Palosz, M. Lewandowska, K.J. Kurzydlowski, Mechanical properties of nanostructured 316LVM stainless steel annealed under pressure, Mech. Mater. (2013), https://doi.org/10.1016/j.mechmat.2013.07.017.
[22] A.T. Krawczynska, S. Gierlotka, P. Suchecki, D. Setman, B. Adamczyk-Cieslak, M. Lewandowska, M. Zehetbauer, Recrystallization and grain growth of a nano/ultrafine structured austenitic stainless steel during annealing under high hydrostatic pressure, J. Mater. Sci. (2018), https://doi.org/10.1007/s10853-018-2459-1.
[23] A.T. Krawczynska, S. Gierlotka, P. Suchecki, D. Setman, B. Adamczyk-Cieslak, M. Gloc, W. Chrominski, M. Lewandowska, M. Zehetbauer, Phenomena occurring in nanostructured stainless steel 316LVM during annealing under high hydrostatic pressure, Adv. Eng. Mater. (2018), https://doi.org/10.1002/adem.201800101.
[24] A.T. Krawczynska, P. Suchecki, B. Adamczyk-Cieslak, B. Romelczyk-Baishya, M. Lewandowska, Influence of high hydrostatic pressure annealing on the recrystallization of nanostructured austenitic stainless steel, Mater. Sci. Eng. (2019), https://doi.org/10.1016/j.msea.2019.138381.
[25] A.T. Krawczynska, M. Lewandowska, R. Kuziak, K.J. Kurzydłowski, Recrystallization and grain growth in nano-structured austenitic stainless steel under electric current heating, Phys. Status Solidi (2010), https://doi.org/10.1002/pssc.200983377.
[26] A.T. Krawczynska, T. Brynk, M. Rosioski, A. Michalski, S. Gierlotka, E. Grzanka, S. Stelmakh, B. Pałosz, M. Lewandowska, K.J. Kurzydłowski, Improving mechanical properties of nanometals by annealing, in: Proceedings of the 33rd Risoe International Symposium on Materials Science:Nanometals - Status and Perspective, 2012, pp. 279–286.
[27] A.T. Krawczynska, M. Kerber, P. Suchecki, B. Romelczyk-Baishya, M. Lewandowska, D. Setman, The impact of the stacking fault energy of nanostructured metals on phenomena during annealing at the high hydrostatic pressure, Mater. Sci. Eng. (2021), https://doi.org/10.1016/j.msea.2021.140913.
[28] P.C.J. Gallagher, The influence of alloying, temperature and related effects on the stacking fault energy, Metall. Trans. A 1 (1970) 2429–2461.

[29] A. Wagner, W. Anwand, A.G. Attallah, G. Dornberg, M. Elsayed, D. Enke, A.E. M. Hussein, R. Krause-Rehberg, M.O. Liedke, K. Potzger, T.T. Trinh, Positron annihilation lifetime spectroscopy at a superconducting electron accelerator, J. Phys. Conf. Ser. 791 (2017) 12004, https://doi.org/10.1088/1742-6596/791/1/012004.
[30] A. Wagner, M. Butterling, M.O. Liedke, K. Potzger, R. Krause-Rehberg, Positron annihilation lifetime and Doppler broadening spectroscopy at the ELBE facility, in: AIP Conf. Proc, 2018, p. 40003, https://doi.org/10.1063/1.5040215.
[31] E. Hirschmann, M. Butterling, U. Hernandez Acosta, M.O. Liedke, A.G. Attallah, P. Petring, M. Görler, R. Krause-Rehberg, A. Wagner, A new system for real-time data acquisition and pulse parameterization for digital positron annihilation lifetime spectrometers with high repetition rates, J. Instrum. 16 (2021) P08001, https://doi.org/10.1088/1748-0221/16/08/P08001.
[32] J.V. Olsen, P. Kirkegaard, N.J. Pedersen, M. Eldrup, PALSfit: a new program for the evaluation of positron lifetime spectra, Phys. Status Solidi 4 (2007) 4004–4006, https://doi.org/10.1002/pssc.200675868.
[33] R. Krause-Rehberg, H.S. Leipner, Positron Annihilation in Semiconductors: Defect Studies, 1999.
[34] F. Tuomisto, I. Makkonen, Defect identification in semiconductors with positron annihilation: experiment and theory, Rev. Mod. Phys. 85 (2013) 1583–1631, https://doi.org/10.1103/revmodphys.85.1583.
[35] T. Wejrzanowski, W.L. Spychalski, K. Rózniatowski, K.J. Kurzydłowski, Image based analysis of complex microstructures of engineering materials, Int. J. Appl. Math. Comput. Sci. (2008), https://doi.org/10.2478/v10006-008-0003-1.
[36] T. Wejrzanowski, K.J. Kurzydlowski, Stereology of grains in nano-crystals, Solid State Phenom. 94 (2003) 221–228.
[37] J.M.C. Robles, E. Ogando, F. Plazaola, Positron lifetime calculation for the elements of the periodic table, J. Phys. Condens. Matter 19 (2007) 176222, https://doi.org/10.1088/0953-8984/19/17/176222.
[38] J. Čížek, O. Melikhova, Z. Barnovská, I. Procházka, R.K. Islamgaliev, Vacancy clusters in ultra fine grained metals prepared by severe plastic deformation, J. Phys. Conf. Ser. 443 (2013) 12008, https://doi.org/10.1088/1742-6596/443/1/012008.
[39] L.C. Smedskjaer, M. Manninen, M.J. Fluss, An alternative interpretation of positron annihilation in dislocations, J. Phys. F Met. Phys. 10 (1980) 2237–2249, https://doi.org/10.1088/0305-4608/10/10/019.
[40] T. Yoshiie, M. Hasegawa, S. Kojima, K. Sato, Y. Saitoh, S. Yamaguchi, M. Kiritani, Positron lifetime measurement and latent vacancy clusters in 14 MeV neutron irradiated nickel, J. Nucl. Mater. 179–181 (1991) 931–934, https://doi.org/10.1016/0022-3115(91)90242-Y.
[41] J. Čížek, M. Janeček, T. Vlasák, B. Smola, O. Melikhova, R.K. Islamgaliev, S. V. Dobatkin, The development of vacancies during severe plastic deformation, Mater. Trans. (2019), https://doi.org/10.2320/matertrans.MF201937.
[42] S. Assali, M. Elsayed, J. Nicolas, M.O. Liedke, A. Wagner, M. Butterling, R. Krause-Rehberg, O. Moutanabbir, Vacancy complexes in nonequilibrium germanium-tin semiconductors, Appl. Phys. Lett. 114 (2019) 112–117, https://doi.org/10.1063/1.5108878.
[43] A.P. Zhilyaev, S. Lee, G.V. Nurislamova, R.Z. Valiev, T.G. Langdon, Microhardness and microstructural evolution in pure nickel during high-pressure torsion, Scripta Mater. (2001), https://doi.org/10.1016/S1359-6462(01)00955-1.
[44] Y.M. Wang, E. Ma, Three strategies to achieve uniform tensile deformation in a nanostructured metal, Acta Mater. 52 (2004) 1699–1709, https://doi.org/10.1016/j.actamat.2003.12.022.
[45] H. Mehrer, Numerical Data and Functional Relationship in Science and TechnologyVol. 26 Diffusion in Solid Metals and Alloys, Springer, Berlin, 1990.
[46] K. Edalati, Y. Hashiguchi, H. Iwaoka, H. Matsunaga, R.Z. Valiev, Z. Horita, Long-time stability of metals after severe plastic deformation: softening and hardening by self-annealing versus thermal stability, Mater. Sci. Eng. 729 (2018) 340–348, https://doi.org/10.1016/j.msea.2018.05.079.
[47] Z. Hegedus, J. Gubicza, P. Szommer, N.Q. Chinh, Y. Huang, T.G. Langdon, Inhomogeneous softening during annealing of ultrafine-grained silver processed by HPT, J. Mater. Sci. 48 (2013) 7384–7391, https://doi.org/10.1007/s10853-013-7553-9.
[48] X. Sauvage, G. Wilde, S.V. Divinski, Z. Horita, R.Z. Valiev, Grain boundaries in ultrafine grained materials processed by severe plastic deformation and related phenomena, Mater. Sci. Eng. 540 (2012) 1–12, https://doi.org/10.1016/j.msea.2012.01.080.
[49] C.M. Kuo, C.S. Lin, Static recovery activation energy of pure copper at room temperature, Scripta Mater. 57 (2007) 667–670, https://doi.org/10.1016/j.scriptamat.2007.06.054.
[50] J. Lian, R.Z. Valiev, B. Baudelet, On the enhanced grain growth in ultrafine grained metals, Acta Metall. Mater. 43 (1995) 4165–4170, https://doi.org/10.1016/0956-7151(95)00087-C.
[51] G. Kapoor, Y. Huang, V. Subramanya Sarma, T.G. Langdon, J. Gubicza, Evolution of the microstructure during annealing of ultrafine-grained Ni with different Mo contents, Mater. Char. 130 (2017) 56–63, https://doi.org/10.1016/j.matchar.2017.05.034.
[52] A.P. Zhilyaev, G.V. Nurislamova, R.Z. Valiev, et al., Thermal stability and microstructural evolution in ultrafine-grained nickel after equal-channel angular pressing (ECAP), Metall. Mater. Trans. 33 (2002) 1865–1868, https://doi.org/10.1007/s11661-002-0197-z.
[53] R. Enzinger, C. Neubauer, J. Kotzurek, W. Sprengel, R. Würschum, Kinetics of vacancy annealing upon time-linear heating applied to dilatometry, J. Mater. Sci. (2018), https://doi.org/10.1007/s10853-017-1780-4.
[54] C.S. Pande, M.A. Imam, B.B. Rath, Study of annealing twins in FCC metals and alloys, Metall. Trans. A, Phys. Metall. Mater. Sci. 21 A (1990) 2891–2896, https://doi.org/10.1007/BF02647209.
[55] S. Bunkholt, E. Nes, K. Marthinsen, Orientation independent and dependent subgrain growth during iso-thermal annealing of high- purity and commercial purity aluminium, Metals 9 (2019) 1–19, https://doi.org/10.3390/met9101032.
[56] R.Z. Valiev, Paradoxes of Severe Plastic DeformationAdvanced Engineering Materials, 5, 2003, 1org-10000abe6014d.eczyt.bg.pw.edu.pl/10.1002/adem.200310089.
[57] A. Vorhauer, R. Pippan, On the homogeneity of deformation by high pressure torsion, Scripta Mater. 51 (2004) 921–925, https://doi.org/10.1016/j.scriptamat.2004.04.025.

J Mater Sci (2018) 53:11823–11836

Metals

Recrystallization and grain growth of a nano/ultrafine structured austenitic stainless steel during annealing under high hydrostatic pressure

Agnieszka Teresa Krawczynska[1,*], Stanislaw Gierlotka[2], Przemyslaw Suchecki[1], Daria Setman[3], Boguslawa Adamczyk-Cieslak[1], Malgorzata Lewandowska[1], and Michael Zehetbauer[3]

[1] Faculty of Materials Science and Engineering, Warsaw University of Technology, Woloska 141, 02-507 Warsaw, Poland
[2] Institute of High Pressure Physics UNIPRESS, Polish Academy of Sciences, Sokolowska 29/37, 01-142 Warsaw, Poland
[3] Faculty of Physics, University of Vienna, Boltzmanngasse 5, 1090 Vienna, Austria

Received: 20 December 2017
Accepted: 14 May 2018
Published online: 21 May 2018

ABSTRACT

The aim of this study was to investigate the effect of high hydrostatic pressure applied during annealing on the processes of recrystallization and grain growth in nanostructured austenitic stainless steel 316LVM. The nanostructures were obtained by profile rolling to a total strain of 3.4 and by high-pressure torsion to a total strain of 79. These processes resulted in microstructures consisting of nanotwins and nanograins, respectively. The deformed samples were annealed at 900 °C for 10 min under atmospheric or hydrostatic pressures of 2 and 6 GPa. The resulting microstructures were examined using transmission and scanning electron microscopy techniques. The mechanical properties were evaluated in microhardness measurements. It was established that annealing under high hydrostatic pressure retards recrystallization and grain growth, both in profile-rolled and high-pressure torsion-processed samples. The magnitude of retardation depends on the character of the grain boundaries. The non-equilibrium high-angle grain boundaries present in the high-pressure torsion-processed sample show higher mobility under pressure than the nanotwinned and low-angle boundaries in the profile-rolled sample.

Introduction

Recovery, recrystallization and grain growth are some of the most important processes that affect the properties of crystalline materials. For this reason, many papers have been devoted to understanding these phenomena in microcrystalline [1, 2], and recently in nanocrystalline, materials [3–5]. During the annealing of nanocrystalline materials produced by severe plastic deformation (SPD) techniques, one can observe typical processes of recovery, recrystallization and grain growth, but they follow a different course than in materials deformed by conventional techniques [6–8]. In general, nanomaterials are less

Address correspondence to E-mail: akrawczynska@wp.pl; agnieszka.krawczynska@pw.edu.pl

https://doi.org/10.1007/s10853-018-2459-1

thermally stable than their microcrystalline counterparts, and recrystallization begins below their usual recrystallization temperatures. However, it has also been shown that, by creating uniform nanostructures having a uniform grain size distribution and a high content of high-angle grain boundaries, thermal stability can be significantly improved [9–11]. The enhanced thermal stability of a nanostructured austenitic stainless steel can be obtained by adding yttrium powders during mechanical milling [12]. The addition of 1.5 wt% stabilizes the microstructure around 116 nm grain size after 3 h annealing at 1100 °C. Moreover, the creation of deformation-induced nanotwins makes the microstructure stable up to 800 °C [13]. The processes of recrystallization and grain growth in nanostructured, and especially single-phased, materials have been quite well described. Nevertheless, one issue which remains almost completely neglected is how such materials behave during annealing under high hydrostatic pressure. This subject has been raised only in the author's previous work [14, 15]. In those studies, annealing under high hydrostatic pressure was applied to a hydrostatically extruded (HE) austenitic stainless steel to optimize its mechanical properties, particularly its strength to ductility balance. It was possible to achieve a controlled slowing of recrystallization processes to produce a nanostructured austenitic stainless steel possessing a good combination of strength and ductility (an ultimate tensile strength of 1247 MPa and a total elongation of 24.4%). The only experiments that have been performed under high pressure recently refer to the Ge precipitation rate in Ge+ ion-implanted SiO_2 films [16], a study on the effect of annealing under pressure on the material properties of Cu2ZnSn(S,Se)4 thin films [17] and an enhancement of magnetic refrigeration performance in metamagnetic MnCoSi alloy by high-pressure annealing [18].

However, several authors have studied the effect of hydrostatic pressure on diffusion, dislocation climb and glide, recrystallization and grain growth mobility in microcrystalline materials [19–27]. It is well known that high hydrostatic pressure has an impact on diffusion processes that are correlated with the motion of vacancies, as it affects the activation volume V^* of the crystal related to atomic rearrangements during thermally activated processes. The influence of pressure on V^* can be expressed by the equation:

$$V* = -RT\ln(v)/p \quad (1)$$

where R is the gas constant, v is the rate of the processes investigated and p is the pressure.

Furthermore, it was found during annealing of cold-rolled copper under a pressure of 4.2 GPa that the pressure retarded recrystallization [20]. The general conclusion that can be drawn from this work regarding grain growth is that the higher the hydrostatic pressure applied, the more significant the decrease in grain boundary mobility. Moreover, the impact of high pressure on the <100>, <110> and <111> tilt boundaries was analyzed [18, 22]. The results showed that the movement of <110> tilt boundaries depends on the activation energy, as this movement is effected by the cooperative motion of several atoms. The movement of the <100> and <111> tilt boundaries is not related to the activation energy and is effected by a single atom mechanism. It was also noticed during experiments on normal grain growth in aluminum under high hydrostatic pressure that the migration of low-angle grain boundaries was slowed down even more, nearly frozen in comparison with the case of general grain boundaries [26]. This is because low-angle grain boundaries can migrate by vacancy grain boundary migration, which is highly limited under high pressure.

In the view of published work within the subject of annealing under the high hydrostatic pressure, it seems that annealing under high hydrostatic pressure can be an effective way to control the grain growth in nanostructured materials and produce fine grain materials which could not be obtained under atmospheric pressure due to fast and uncontrollable grain growth. However, this requires full understanding of processes taking place during annealing under high hydrostatic pressure. Therefore, the aim of the current study was to investigate the influence of high pressure on the recrystallization and grain growth of a nanostructured stainless steel 316LVM. To this end, specimens of an austenitic stainless steel were deformed by profile rolling (PR)—a conventional deformation technique, and by high-pressure torsion (HPT)—an SPD technique; the samples were then annealed under a pressure of 2 and 6 GPa and, for comparison, under atmospheric pressure. The HPT process was chosen because it is one of the most efficient SPD processes for grain refinement [28–33].

Materials and methods

Sandvik Bioline 316LVM austenitic stainless steel was used; this is a low-carbon, vacuum-melted 316L grade stainless steel, UNS S31673 certified to ASTM F138, supplied as annealed in the form of 50-mm-diameter rods, possessing the chemical composition shown in Table 1.

The samples were conventionally deformed using profile rolling (PR) with a reduction in cross section of 23.8, which corresponds to a strain value of approximately 3.4. In this case, the strain was calculated according to the equation $\varepsilon = 2\ln(d_1/d_2)$, where d_1 (ϕ = 12 mm) is the initial diameter and d_2 (ϕ = 2.2 mm) the final diameter. It must be pointed out that this calculation is only an approximation, since the cross section is not actually a circle. Additionally, the material was cut into disks with a diameter of 10 mm and a thickness of 0.8 mm. The disks were processed at room temperature using an HPT device at a constant pressure of 6.0 GPa. The disks were torsionally strained to 5 revolutions. The strain was well defined as simple shear, γ, and was calculated according to the equation $\gamma = 2\pi \times r \times n/t$, where r, n and t are the distance from the torsion axes, the number of applied revolutions and the mean thickness of the sample, respectively. The equivalent strains $\varepsilon eq = \gamma/\sqrt{3}$ calculated 3.5 mm from the central point of the sample after 5 revolutions were equal to 79. A phase analysis of the as-received, HPT- and PR-processed samples was performed on a Bruker D8 Advance diffractometer with nickel-filtered copper radiation (λ = 0.154056 nm). The data were collected in a range between 10° and 120° 2Θ, with a step width of $\Delta 2\Theta = 0.02°$ and a counting time 5 s. The energy of the emitter beam was 40 kV, and the current was 40 mA.

After PR, samples of 3 mm in height were cut from a 500 mm rod. After the HPT experiments, disks of 5 mm in diameter were cut in such a way that the radius of the sample after HPT became the diameter of the sample for the annealing experiments. The dimensions of the samples were limited by the dimensions of the toroidal high-pressure cell. The samples were annealed at 900 °C for 10 min, either at atmospheric pressure (0.1 MPa) or at a hydrostatic pressure of 2 or 6 GPa and. To verify whether annealing under high hydrostatic pressure leads to the creation of similar microstructures as conventional annealing for a shorter time, additional experiments of annealing under 0.1 MPa for 4 min were performed. A toroidal high-pressure cell [34, 35] was used for the high-pressure annealing, and a conventional furnace for annealing at atmospheric pressure. Further on in this text, these samples will be referred to as PR_10_0.1 MPa, PR_10_2GPa, PR_10_6GPa, PR_4_0.1 MPa, HPT_10_0.1 MPa, HPT_10_2GPa, HPT_10_6GPa and HPT_4_0.1 MPa.

Table 1 Chemical composition (wt%) of austenitic stainless steel 316LVM

C	Si	Mn	P	S	Cr	Ni	Mo	Cu	N
0.025	0.6	1.7	0.025	0.003	17.5	13.5	2.8	0.1	<0.1

The microstructure of the samples was investigated using a Hitachi SU 8000 scanning electron microscope working at 5 kV in the BSE mode and a JEOL JEM 1200 EX transmission electron microscope working at 120 kV. For the scanning electron microscopy examination, the samples were prepared by electropolishing using Struers electrolyte A3. The parameters for electropolishing were as follows: voltage − 15 V, time − 15 s. For the transmission electron microscopy examination, the samples were prepared by mechanical polishing to a disk thickness of about 100 μm. Further thinning to reach a thickness appropriate for electron transparency was carried out by electropolishing using Struers electrolyte A2. In the case of the PR samples, the microstructure was analyzed in the center of the samples. In the case of the HPT samples, for microstructure analysis of the cross sections, disks with a diameter of 3 mm were cut from the edge regions of each disk so that the areas of observation were 3.5 mm from the central point. Further thinning was carried out by means of a conventional procedure. Qualitative and quantitative studies as well as the percentage share of the recrystallized areas of the microstructures were conducted using stereological and image analysis methods [36, 37]. The grain size was determined as the equivalent diameter, d_2, defined as the diameter of a circle having an area equal to the surface area of a given grain. The grain shape was described by grain elongation factor, defined as the ratio of the maximum to the equivalent diameter d_{max}/d_2. To establish the variation of the size of individual grains, a variation coefficient, CV(d_2), defined as the ratio of the

standard deviation SD (d_2) to the mean value, was determined.

Microhardness measurements were conducted on polished cross sections of the PR and HPT samples. These measurements were made using a Zwick microhardness tester under a load of 200 g. The values of the Vickers microhardness, Hv, were recorded along a diameter of the PR and HPT samples with a separation of 0.1 mm.

Results

X-ray diffraction analysis

Figure 1 shows X-ray diffraction profiles of the as-received, PR- and HPT-processed samples. The X-ray diffraction profiles reveal a γ-austenite phase (fcc) without any evidence of ε-martensite (hcp) or α′-martensite (bcc). The greatest broadening of peaks is observed for the HPT sample and is a result of microstructure refinement and microstrains.

Microhardness measurements

Microhardness measurements on cross sections of the PR- and HPT-processed samples after annealing at 900 °C under various pressures for 4 and 10 min are presented in Fig. 2. After HPT, the microhardness reaches an average value of 471 Hv0.2, which is higher by 46 units than after PR. Moreover, the HPT causes a more homogeneous distribution of microhardness on the diameter since the standard deviation equals 14 Hv0.2, whereas after PR it is twice as high (it must be pointed out that the diameter of the HPT sample is two times greater than that after PR). Annealing under high hydrostatic pressure has a considerable impact on the microhardness values of HPT- and PR-processed samples. There is a tendency for both samples that the higher the pressure during annealing, the higher the microhardness value retained. However, the PR samples showed greater microhardness values for annealing under a pressure of 2 and 6 GPa (301 and 390 Hv0.2, respectively) than the HPT samples (254 and 282 Hv0.2, respectively). Additionally, annealing was performed for 4 min at 0.1 MPa. In the case of the PR samples, the microhardness value after annealing for 4 min can be compared with that obtained for annealing under 2 GPa for 10 min (287 and 301 Hv0.2, respectively). In the case of the HPT samples, annealing for 4 min at 0.1 MPa causes changes in the microhardness similar to annealing under 6 GPa (282 and 284 Hv0.2, respectively).

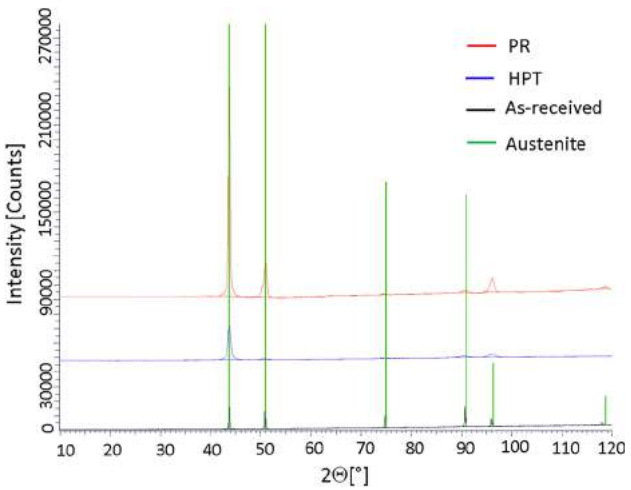

Figure 1 X-ray diffraction profiles of as-received, PR-, and HPT-processed samples.

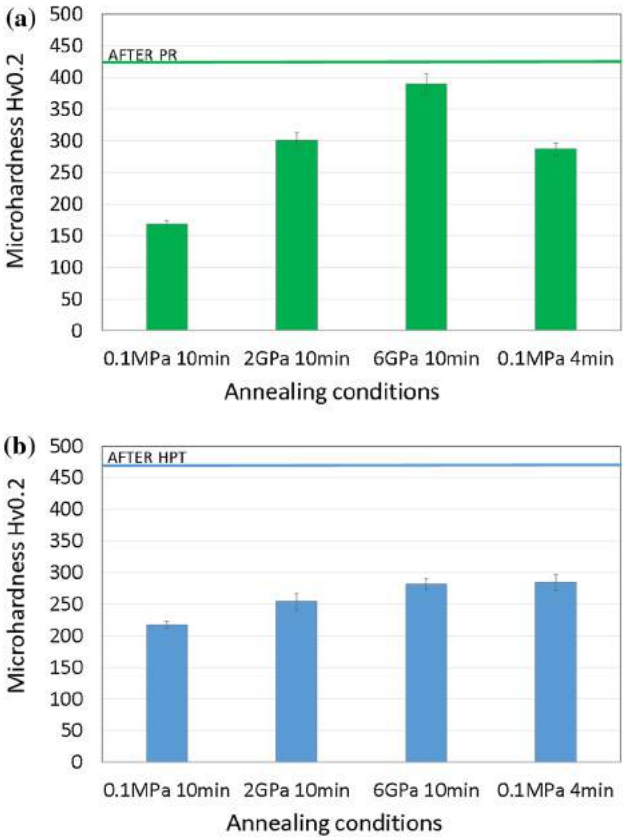

Figure 2 Microhardness Hv0.2 of PR- **a** and HPT-processed **b** austenitic stainless steel annealed under 0.1 MPa and 2 and 6 GPa at 900 °C for 10 min and additionally for 4 min under 0.1 MPa.

Microstructure observation

Microstructure observation after plastic deformation

The microstructure of the cross sections is severely refined in both the PR- and HPT-processed samples, as presented in Fig. 3. The microstructure observations are supported by the selected area diffraction (SAED) patterns from an area having a diameter of approximately 4 μm. The presence of diffraction rings in the SAED confirms that the microstructure has been refined. However, the non-uniform intensity of the rings in the SAED of the PR sample indicates that the microstructure is more textured after PR than after HPT. Moreover, the SAED patterns indicate that the PR- and HPT-processed samples consist of an γ-austenite phase. In the case of the HPT-processed sample, one can notice, apart from the γ-austenite phase (fcc), a weak ring from ε-martensite phase (hcp). Some authors suggest that ε-martensite is not a perfect hcp structure, but consider it as a heavily faulted fcc γ-austenite structure with a special arrangement of stacking faults [38]. The presence of an ε-martensite phase was not revealed in the X-ray analysis, probably due to the small volume of this phase beyond the detection threshold.

Microscopy observations at greater magnifications reveal that the microstructures of the PR and HPT samples differ considerably. The microstructure of the PR sample in cross section is non-homogeneous. It consists of elongated deformation bands divided into subgrains of thickness in the range of 50–100 nm and length of 100–300 nm, and deformation nanotwins of thickness of 5–10 nm, as shown in detail in Fig. 4. In the case of the HPT sample, in cross section the microstructure has been transformed into small fragments forming nanocrystallites. The average grain size is below 100 nm. Inside some grains, one can notice a high density of dislocations (Fig. 5). It was also observed that the longest grain axis is oriented parallel to the HPT shear plane. However, as this has been the subject of previous research, this issue will not be further explored here [39, 40].

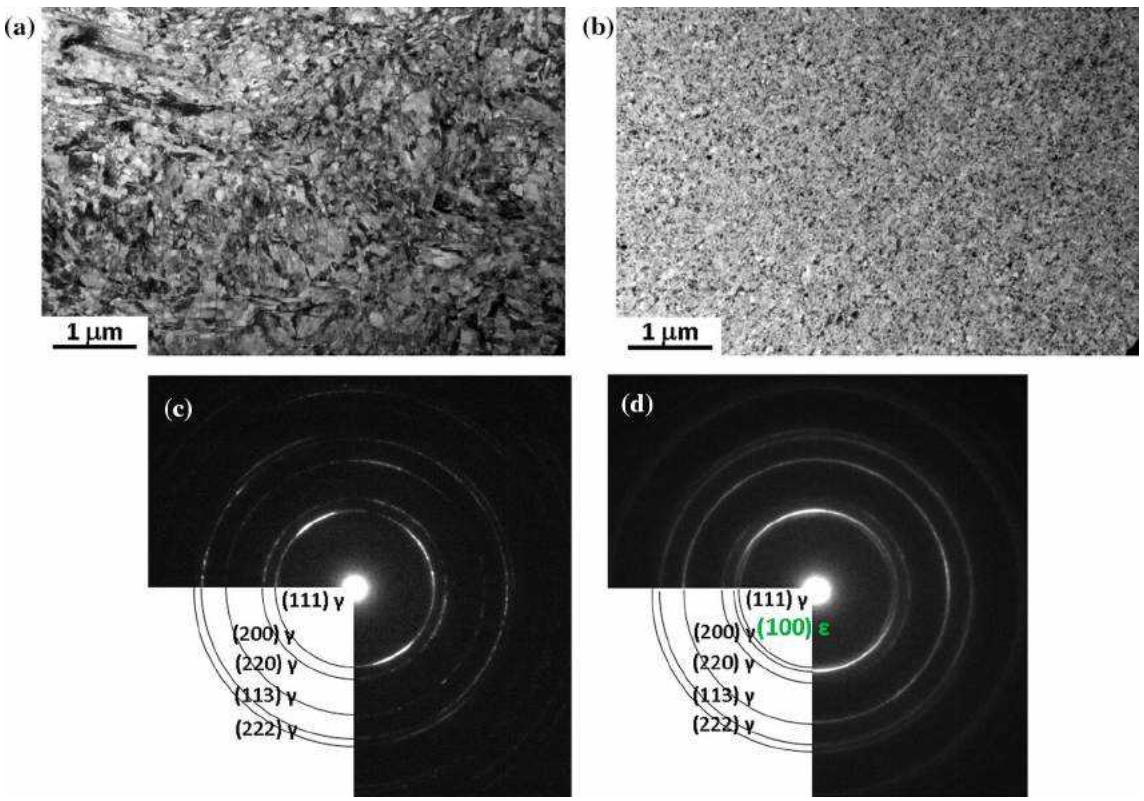

Figure 3 Microstructures of the **a** PR- and **b** HPT-processed samples—cross sections, SAED patterns of **c** PR- and **d** HPT-processed samples.

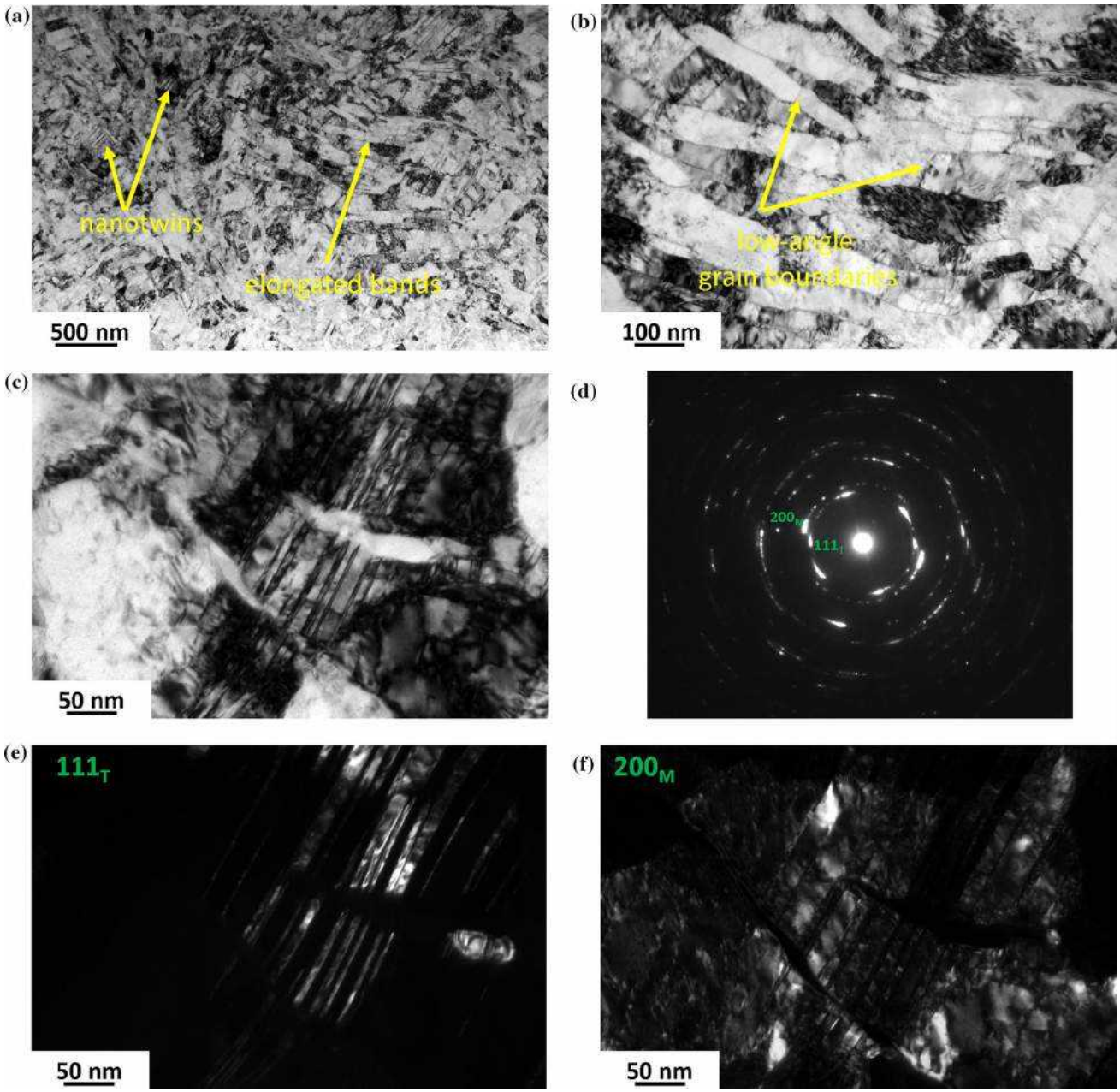

Figure 4 Microstructures of the PR-processed sample—cross section: **a** global view, **b** deformation bands, **c** deformation nanotwins in the bright field, **d** SAED pattern from nanotwinned area of 0.6 μm in diameter, **e** deformation nanotwins in the dark field, **f** matrix in the dark field.

Microstructure observations after annealing

The microstructures of the PR samples and HPT samples after annealing at 900 °C under 0.1 MPa, 2 and 6 GPa for 10 min are shown in Fig. 6 (in BSE mode SEM) and Fig. 7 (TEM). The average equivalent diameter d_2, standard deviation SD (d_2) and coefficient of variation CV(d_2) of grains are presented in the form of charts in Fig. 7. An analysis of the microstructures of HPT_10_0.1 MPa and PR_10_0.1 MPa leads to the conclusion that the samples are fully recrystallized. The average equivalent diameter is greater for the PR_10_0.1 MPa than for the HPT_10_0.1 MPa (4.3 and 2.0 μm, respectively). Furthermore, the microstructure elongation factor values are comparable (1.35 and 1.28, respectively, for PR_10_0.1 MPa and HPT_10_0.1 MPa), which indicates fully equiaxial grain structure.

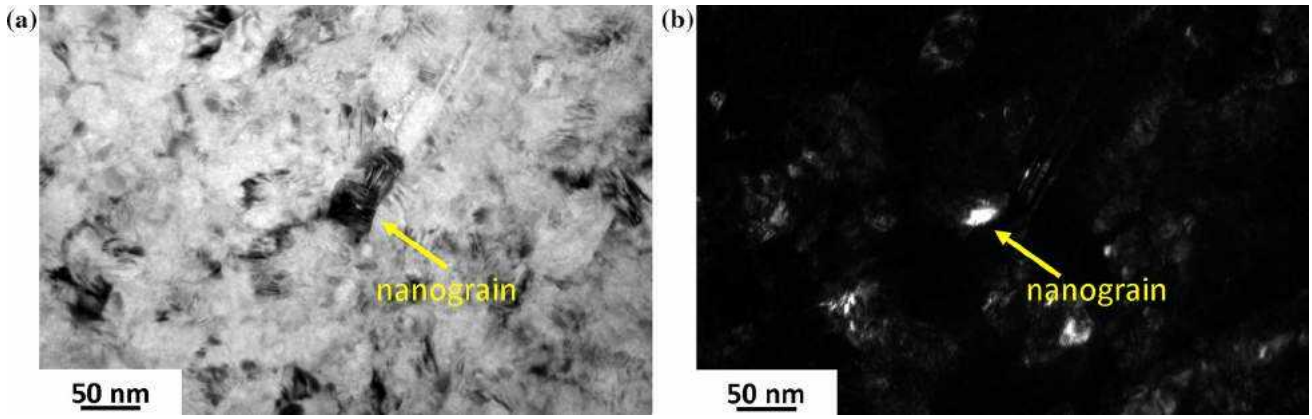

Figure 5 Microstructures of the HPT-processed sample—**a** in the bright field, **b** in the dark field, obtained by selecting a part of a diffraction ring from the (111) planes.

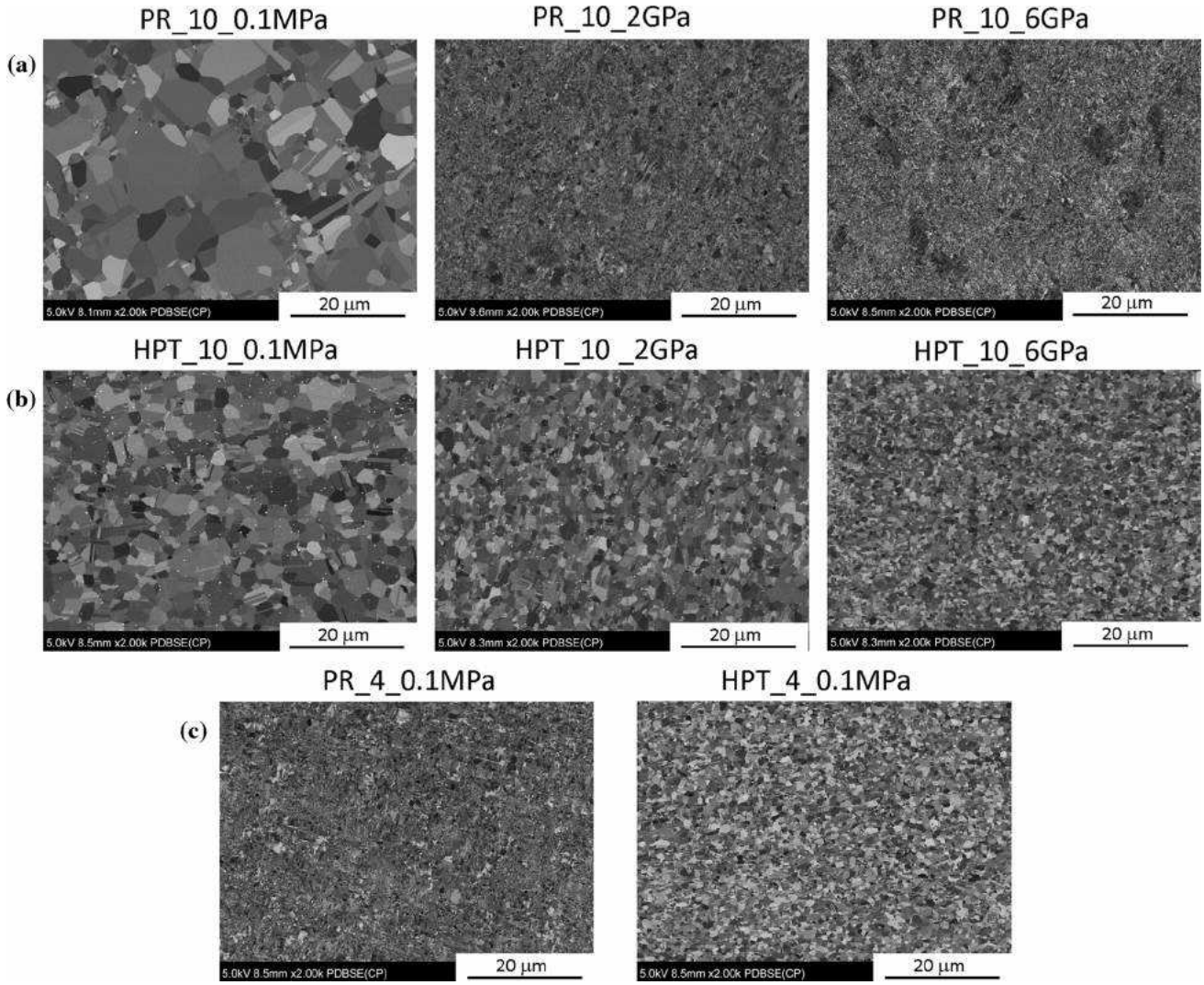

Figure 6 **a** Microstructures of PR-processed samples after annealing at 900 °C for 10 min under 0.1 MPa, 2 GPa and 6 GPa; **b** microstructures of HPT-processed samples after annealing at 900 °C for 10 min under 0.1 MPa, 2 and 6 GPa; **c** microstructures of PR- and HPT-processed samples after annealing at 900 °C for 4 min under 0.1 MPa; SEM in BSE mode.

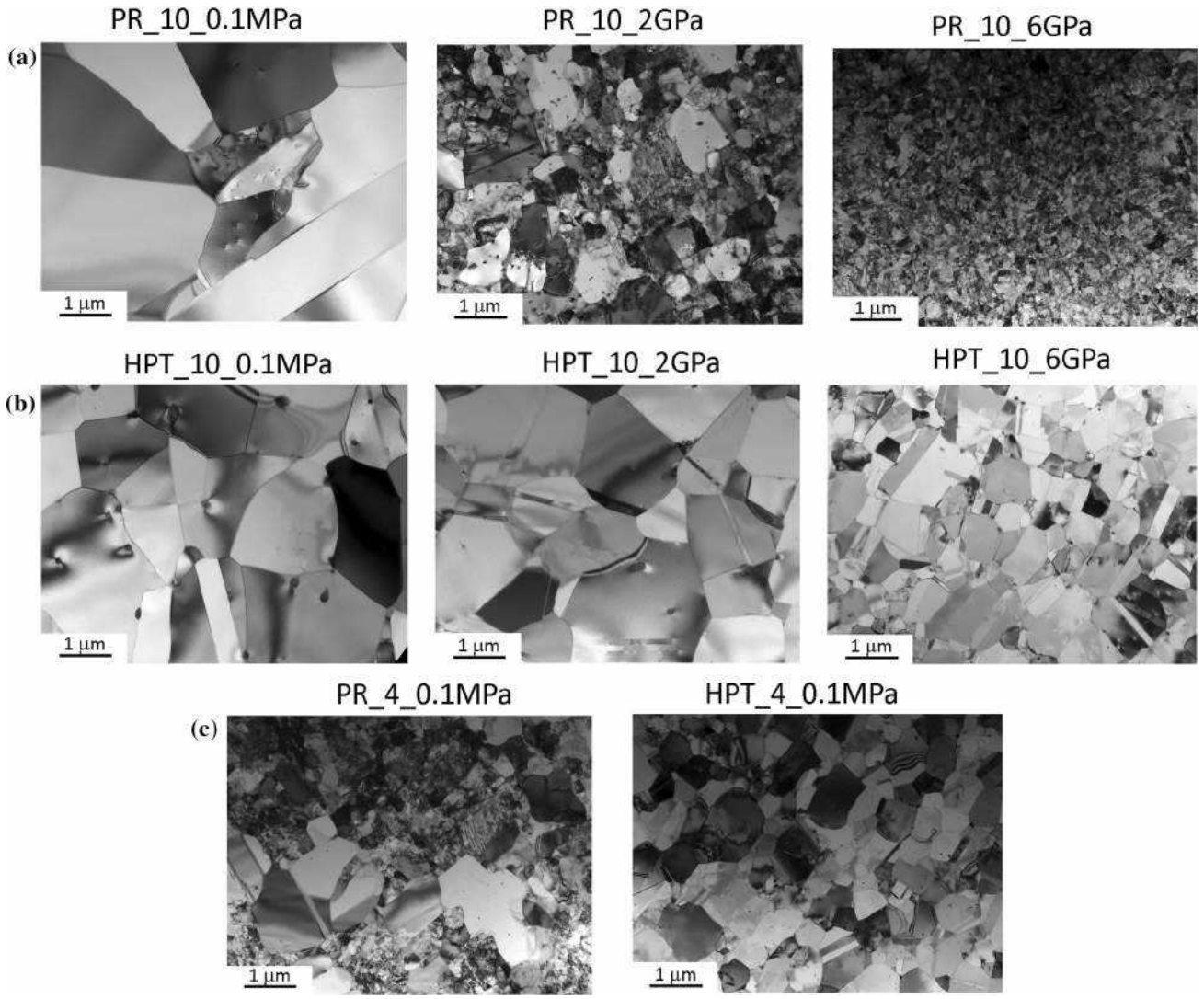

Figure 7 **a** Microstructures of PR-processed samples after annealing at 900 °C for 10 min under 0.1 MPa, 2 and 6 GPa; **b** microstructures of HPT-processed samples after annealing at 900 °C for 10 min under 0.1 MPa, 2 and 6 GPa; **c** microstructures of PR- and HPT-processed samples after annealing at 900 °C for 4 min under 0.1 MPa; TEM.

Nevertheless, they differ in the value of the coefficient of variation, which is significantly higher for the PR_10_0.1 MPa (0.79) than for the HPT_10_0.1 MPa (0.47). This implies that the distribution of the equivalent diameter in the PR_10_0.1 MPa is wider than in the HPT_10_0.1 MPa. The smaller grains in the PR_10_0.1 MPa contain some dislocations, whereas the HPT_10_0.1 MPa contains grains free from dislocations.

Applied annealing pressure at 900 °C hinders recrystallization and grain growth in the PR-processed samples and grain growth in the HPT-processed samples. In the case of the PR samples, the equivalent diameter reaches 0.42 μm under 2 GPa and only 0.087 μm under 6 GPa. Between the recrystallized areas, one can notice areas where there has been no recrystallization. In the case of the HPT samples, the equivalent diameter reaches 1.35 μm under 2 GPa and 0.58 μm under 6 GPa, which is greater than in the PR samples. Moreover, in contrast to the PR samples, there are no non-recrystallized areas between the recrystallized grains. As well as investigating the effect of high hydrostatic pressure on the equivalent diameter of the PR and HPT samples, attention was paid to the impact of high hydrostatic pressure on the elongation parameter and coefficient of variation. It seems that the high hydrostatic pressure applied had no impact on the

elongation parameter, which was approximately 1.3 for all annealing conditions for both the PR and HPT samples. Nevertheless, the pressure applied during annealing had a significant impact on the coefficient of variation. There are two tendencies visible. In the case of the PR samples, the coefficient of variation decreases with an increase of pressure from 0.79 under 0.1 MPa to 0.46 under 6 GPa, whereas in the case of the HPT samples it increases from 0.47 under 0.1 MPa to 0.64 under 6 GPa. It means that the abnormal grain growth, represented by a high coefficient of variation, is favorized in the PR sample under the atmospheric pressure and in the HPT sample under the increased pressure.

To verify whether annealing under high hydrostatic pressure leads to the creation of similar microstructures as does conventional annealing, but over a shorter time, additional experiments of annealing under 0.1 MPa were performed. The microstructures obtained are presented in Figs. 6 and 7. The average equivalent diameter d_2, standard deviation SD (d_2) and coefficient of variation CV(d_2) of the grains are presented in Fig. 8. This experiment makes it possible to observe that the retardation of annealing induced by annealing at 2 GPa for 10 min in the case of the PR samples can be compared with annealing for 4 min under 0.1 MPa (d_2 = 0.42, d_{max}/d_2 = 1.31, CV(d_2) = 0.78—for PR_10_2 GPa, d_2 = 0.44, d_{max}/d_2 = 1.39, CV(d_2) = 0.74—for PR_4_0.1 MPa). In the case of the HPT samples, 4-min annealing at 0.1 MPa causes similar changes in the microstructure as annealing at 6 GPa for 10 min (d_2 = 0.58, d_{max}/d_2 = 1.31, CV(d_2) = 0.64—for HPT_10_6 GPa, d_2 = 0.55, d_{max}/d_2 = 1.33, CV(d_2) = 0.54—for HPT_4_0.1 MPa). One difference in the microstructure between HPT_10_6GPa and HPT_4_0.1 MPa lies in the value of the coefficient of variation, which is significantly higher for annealing at 6 GPa than at 0.1 MPa.

Discussion

Comparison of the thermal stability of HPT- and PR-processed samples under 0.1 MPa

Even though the TEM observations confirmed the refinement of the microstructures of the HPT- and PR-processed samples, their behavior during annealing under 0.1 MPa was different. The differences are visible after annealing for 4 and 10 min. After 4 min of annealing, it can be noticed that in the PR-processed samples discontinuous recrystallization occurred, whereas in the HPT-processed samples the recrystallization was continuous. This discontinuous recrystallization (frequently called primary recrystallization) is the result of an inhomogeneous microstructure produced during deformation. If the microstructure after deformation is inhomogeneous, which is true for low-to-moderate strains (in the case of the PR-processed samples $-\varepsilon = 3.4$) during deformation, it means that there are preferred sites for the formation of nuclei having high local misorientations, e.g., highly misoriented regions within deformation bands [41]. The process of heterogeneous nucleation leads, over a longer annealing time, to a microstructure that is fully recrystallized but of diversified grain size. In the case of the austenitic stainless steel, continuous recrystallization was reported for a total strain of 6.4 reached during multi-axial compression [42]. During annealing of the HPT-processed sample that was deformed to a high strain of 79, the strain-induced high-angle grain boundaries change to conventional ones. As a result, homogeneous nucleation and, for longer times, normal grain growth were perceived. This kind of behavior has been previously observed in austenitic stainless steels deformed by HPT and subsequently annealed [43].

Moreover, after 10 min of annealing, the HPT-processed samples showed smaller grain size than the PR-processed samples. The visibly enhanced thermal stability here may be explained by the fact that, during heating, the recovery of the non-equilibrium grain boundary structure (definitely present in a higher volume in the HPT-processed samples than in the PR-processed samples) proceeds quite rapidly due to their high diffusivity [44]. Non-equilibrium grain boundaries are specific grain boundaries that possess an increased free energy density, increased width, a high density of dislocations associated with the near-boundary region, and correspondingly large residual microstrains [8]. This leads to a rapid decrease in the driving force of the grain growth. Another important factor explaining the enhanced thermal stability of a HPT sample is the more uniform microstructure after deformation in the case of HPT than in a PR-processed sample. The impact of the uniform microstructure on the thermal stability was proven in the experiment on

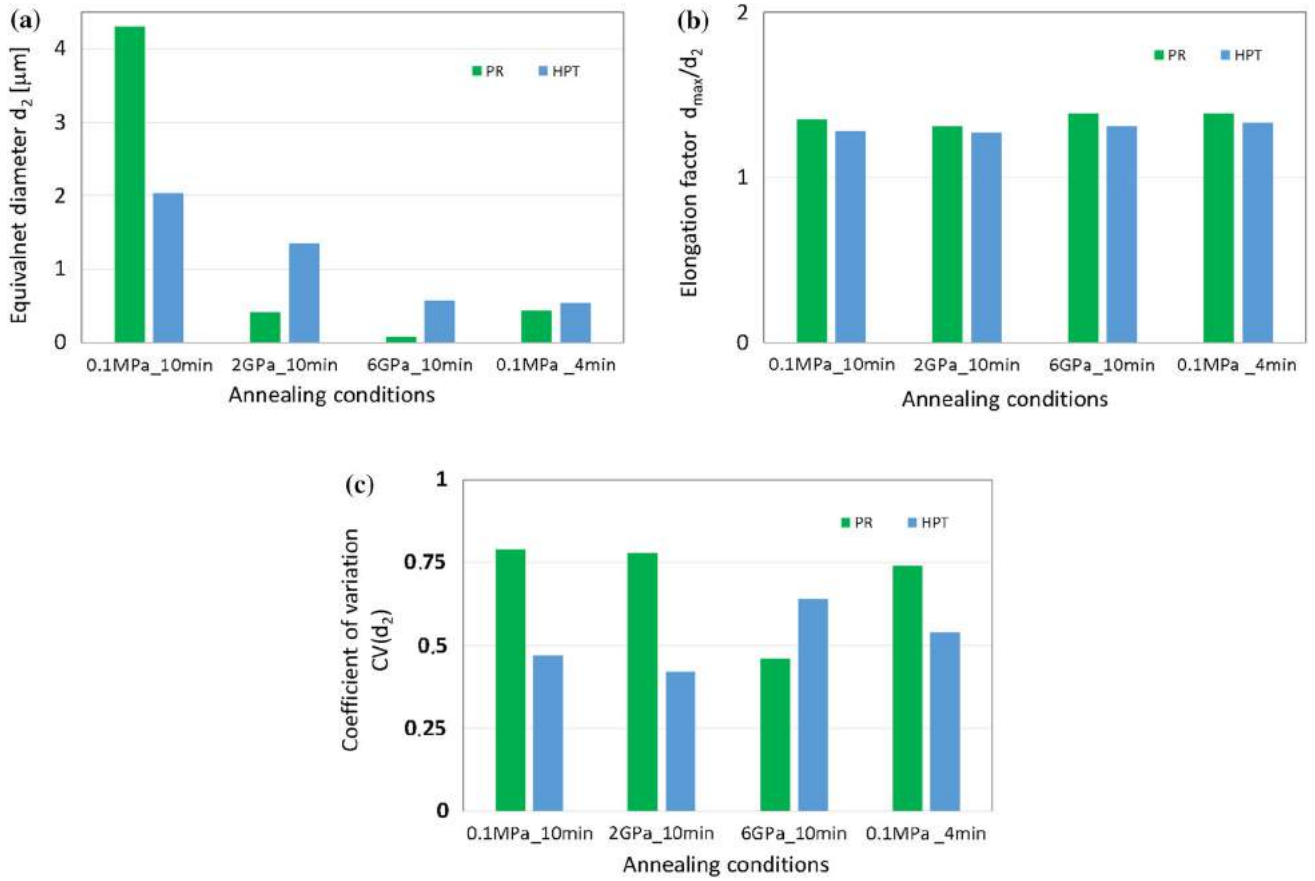

Figure 8 **a** Average equivalent diameter d_2, **b** elongation factor d_{max}/d_2, and **c** coefficient of variation CV(d_2) of grains in PR- and HPT-processed samples after annealing at 900 °C for 10 min under 0.1 MPa, 2 and 6 GPa and for 4 min under 0.1 MPa.

molybdenum [9]. The thermal stability of molybdenum processed by HPT exceeded significantly the respective one for multi-step forging despite the lower deformation degree in the latter case, which was related to the more homogeneous grain size distribution in the former case. As a result, the mobility of grain boundaries decreases, which results in their enhanced thermostability.

Impact of high hydrostatic pressure on recrystallization and grain growth in nanostructured austenitic steel 316LVM

The above results indicate that hydrostatic pressures of 2 and 6 GPa have a considerable impact on the process of recrystallization and grain growth in the PR samples and mainly on grain growth in the HPT samples. The fact that increasing the annealing pressure retards recrystallization and grain growth has been investigated in the past in numerous studies [20–27]. For example, in one such early study, it was found that a pressure of 4.2 GPa applied while annealing polycrystalline copper cold-rolled to 98% retarded both the initiation and the rate of recrystallization [20]. In another work, it was proved that that grain growth decreased by a factor of 1.3 under a high pressure of 1.2 GPa in aluminum rolled to a 90% reduction [26]. A similar effect of recrystallization retardation was observed during annealing at 300 °C of an Al-2%Mg alloy under an applied stress of 10 MPa [45].

In the present study, one fact that requires some explanation is the considerable difference in the retardation of the rate of recrystallization and grain growth between the PR- and HPT-processed samples. Such an explanation must take into consideration the different nature of the grain boundaries in the PR- and HPT-processed samples, despite the fact that both samples possess highly refined microstructures.

1. Firstly, in the PR-processed samples, most of the microstructure is occupied by nanotwins and

elongated deformation bands consisting of subgrains, whereas in the HPT-processed samples there is a preponderance of nanograins. In previous studies on micrograined materials, it was explained that low-angle grain boundaries, present in the PR samples, move by the vacancy diffusion mechanism [26]. However, the vacancy concentration in the material decreases with increasing pressure during annealing [26]. For this reason, the movement of low-angle grain boundaries is strongly slowed down during annealing under high hydrostatic pressure. This explains the fact that there are non-recrystallized areas in the PR-processed samples after annealing under high hydrostatic pressure. Moreover, in the PR samples there is a high density of nanotwin boundaries viewed as 60° <111> twist boundaries or 70.5° <110> tilt boundaries. It is known that <110> tilt boundaries move by some cooperative motion of several atoms, while <100> and <111> tilt boundaries move by a single atom mechanism, which can be achieved more easily under high hydrostatic pressure [21, 22]. This fact also explains the retardation of recrystallization under high hydrostatic pressure in the PR-processed samples. A strong retardation of grain growth was also observed in a nanotwinned austenitic stainless steel refined by HE after annealing for 10 min under a pressure of 6 GPa (d_2 = 133 nm). The behavior of HE-processed and PR-processed samples during annealing under high hydrostatic pressure confirms that the migration of twins boundaries is hampered under high pressure.

2. Secondly, these samples differ in the equivalent strain applied during deformation, which was 3.4 and 79 for the PR- and HPT-processed samples, respectively. According to previous studies, the higher the plastic deformation and hydrostatic pressure applied during deformation, the higher the density of vacancies in the material [46, 47]. The excess vacancy concentration in pure Cu and Ni samples processed by HPT can achieve values of (0.9–20)*10^(−4) [46, 47], whereas in α′-martensite processed by HPT the equivalent value are (5.2 ± 3.6)*10^(−4) [48]. Since austenitic stainless steel is a material having a low stacking fault energy and a high melting temperature, one can predict that a high density of agglomerated vacancies will appear in the HPT-processed samples, as opposed to the PR-processed samples. This means that even though the vacancy concentration decreases with increasing pressure during annealing, in the HPT-processed samples it must be much higher than in the PR-processed samples during annealing under high hydrostatic pressure, enabling dislocation climbing and the migration of grain boundaries even under a pressure of 6 GPa.
3. Thirdly, in the HPT-processed samples one can expect to find a high density of non-equilibrium grain boundaries. The specific structure of grain boundaries affects diffusivity, which is much higher than in the case of general high-angle grain boundaries and highly defected twin boundaries. It is also possible that there is a certain fraction of non-equilibrium grain boundaries present in the PR-processed samples, as it is highly deformed. Nevertheless, that value is much lower than in the HPT-processed samples. During annealing under 0.1 MPa, the rapid recovery of such boundaries may decrease their mobility. In contrast, under high pressure, such a rapid recovery may be suppressed, and the enhanced diffusivity and excess energy of the non-equilibrium boundaries may act as a driving force for grain growth.

Does annealing under high hydrostatic pressure result in the same microstructure as under atmospheric pressure?

In order to answer this question, experiments in which PR- and HPT-processed samples were annealed for 4 min under 0.1 MPa were performed. The results were compared with the microstructures obtained for annealing under 2 and 6 GPa for 10 min. It was discovered that, in the case of the PR-processed samples, the microhardness and microstructure after 4 min of annealing under 0.1 MPa are comparable to the values obtained after 10 min under 2GPa. However, they differ slightly in the percentage of the recrystallized area, which is greater for the PR_10_2GPa—approximately 80% than the PR_4_0.1 MPa—approximately 70%. The HPT-processed samples annealed for 4 min under 0.1 MPa were fully recrystallized and can be compared with the samples annealed for 10 min under 6 GPa. However, they differ slightly in the value of the coefficient of variation, which is greater for the

samples annealed under high hydrostatic pressure. This might result from the fact that under high pressure applied during annealing the migration of vacancies is highly reduced and various grain boundaries tend to migrate by various mechanisms and consequently at various rates [49].

Conclusions

1. HPT processing allows obtaining the nano-grained austenitic stainless steel 316LVM, while ultrafine grained one (with a mixture of nan-otwins and elongated deformation bands) can be obtained by a more conventional processing of PR.
2. Annealing under atmospheric pressure revealed that HPT-processed samples are more thermally stable when compared to PR-processed one. This was attributed to the more uniform microstruc-ture of a HPT samples and their higher content of non-equilibrium grain boundaries, which have the tendency to a rapid recovery during heating drastically reducing the driving force for grain growth.
3. Annealing under high hydrostatic pressures of 2 and 6 GPa retards the processes of recrystalliza-tion and grain growth in samples processed by both methods; however, the retardation is much more pronounced for a PR-processed samples. This was related to such microstructural features of HPT samples as a higher vacancy concentra-tion, lower frequency of low-angle grain bound-aries and higher fraction of non-equilibrium grain boundaries, which all enhance the mobility of grain boundaries under high pressure.
4. The microstructure reorganization during anneal-ing under high pressure proceeds in the same way as during annealing under atmospheric pressure; however, for the latter the same grain size is obtained after shorter annealing time.

Acknowledgements

This work was supported by Polish NSC project SONATA No. UMO-2014/15/D/ST8/00532.

References

[1] Doherty RD, Hughes DA, Humphreys FJ et al (1997) Current issues in recrystallization: a review. Mater Sci Eng A 238:219–274

[2] Rios PR, Siciliano FS, Sandim HRZ et al (2005) Nucleation and growth during recrystallization. Mater Res 8:225–238

[3] El-Tahawy M, Huang Y, Choi H et al (2017) High temperature thermal stability of nanocrystalline 316L stainless steel processed by high-pressure torsion. Mater Sci Eng A 682:323–331

[4] Novikov VY (2015) Grain growth in nanocrystalline materials. Mater Lett 159:510–513

[5] Tang L, Zhao Y, Islamgaliev RK et al (2017) Microstructure and thermal stability of nanocrystalline Mg–Gd–Y–Zr alloy processed by high pressure torsion. J Alloys Compd 721:577–585

[6] Valiev RZ, Islamgaliev RK, Alexandrov IV (2000) Bulk nanostructured materials from severe plastic deformation. Prog Mater Sci 45:103–189

[7] Lian J, Valiev RZ, Baudelet B (1995) On the enhanced grain growth in ultrafine grained metals. Acta Metall Mater 43:4165–4170

[8] Sauvage X, Wilde G, Divinski SV et al (2012) Grain boundaries in ultrafine grained materials processed by severe plastic deformation and related phenomena. Mater Sci Eng A 540:1–12

[9] Ivanov KV (2008) Characteristic features and thermal stability of molybdenum processed by different ways of severe plastic deformation. Mater Sci Forum 584–586:917–922

[10] Zhang Y, Ganeev AV, Gao X et al (2008) Influence of HPT deformation temperature on microstructure and thermal stability of ultrafine-grained tungsten. Mater Sci Forum 584–586:1000–1005

[11] Bazarnik P, Lewandowska M, Andrzejczuk M, Kurzydlowski KJ (2012) The strength and thermal stability of Al-5 Mg alloys nano-engineered using methods of metal forming. Mater Sci Eng A 556:134–139

[12] Kotan H (2015) Microstructural evolution of 316L stainless steels with yttrium addition after mechanical milling and heat treatment. Mater Sci Eng A 647:136–143

[13] Wang SJ, Jozaghi T, Karaman I et al (2017) Hierarchical evolution and thermal stability of microstructure with deformation twins in 316 stainless steel. Mater Sci Eng A 694:121–131

[14] Krawczynska AT, Brynk T, Gierlotka S et al (2013) Mechanical properties of nanostructured 316LVM stainless steel annealed under pressure. Mech Mater 67:25–32

[15] Gierlotka S, Grzanka E, Krawczynska A et al (2011) Strain relaxation and grain growth in 316LVM stainless steel annealed under pressure. Zeitschrift für Krist Proc 1:281–286

[16] Tyschenko IE, Volodin VA, Cherkov AG (2016) Enhanced germanium precipitation and nanocrystal growth in the Ge+ ion-implanted SiO2 films during high-pressure annealing. Solid State Commun 247:53–57

[17] Ranjbar S, Menon MRR, Fernandes PA, Da Cunha AF (2015) Effect of selenization conditions on the growth and properties of Cu2ZnSn(S,Se)4thin films. In: Thin solid films. pp 188–192

[18] Liu J, Si Y, Gong Y et al (2017) Enhanced magnetic refrigeration performance in metamagnetic MnCoSi alloy by high-pressure annealing. J Alloys Compd 701:858–863

[19] Hillard JE, Lommel JM, Hudson JB, Stein DF, Livingston JD (1960) Effect of annealing under high pressure on dislocations in lithum fluoride, aluminium, copper and iron. Acta Metall 9:787–794

[20] Tanner LE, Radcliffe SV (1962) Effect of hydrostatic pressure on the kinetics of recrystallization in high-purity copper. Acta Metall 10:1161–1169

[21] Lojkowski W, Molodov DA, Gottstein G, Shvidlerman LS (1996) The mechanism of grain boundary migration in aluminium bicrystals. Mater Sci Forum 207–209:537–540

[22] Shvindlerman LS, Czubayko U, Gottstein G, Molodov DA (1996) High pressure effect on grain boundary migration and mechanism of grain boundary migration. Mater Sci Forum 204–206:45–54

[23] Syrenko AF, Klinishev GP, Khôi VT (1973) Recrystallization of copper under hydrostatic pressure up to 15 kbar. J Mater Sci 8:765–769. https://doi.org/10.1007/BF00553726

[24] Kühlein W, Stüwe HP (1988) The influence of high hydrostatic pressure on recrystallization of α-brass. Acta Metall 36:3055–3059

[25] Lojkowski W (1988) On the effect of high pressures on the mobility of atoms in grain boundaries. J Phys-Paris 49:545–549

[26] Sursaeva V, Protasova S, Lojkowski W et al (1999) Microstructure evolution during normal grain growth under high pressure in 2-D aluminium foils. Texture Mictrostruct 32:175–185

[27] Hilliard JE, Lommel JM, Hudson JB, Stein DF, Livingston JD (1962) Effect of annealing under high pressures on dislocations in lithium fluoride, aluminum, copper and iron. Acta Metall Mater 9:787–794

[28] Dobatkin SV, Rybalchenko OV, Enikeev NA et al (2016) Formation of fully austenitic ultrafine-grained high strength state in metastable Cr–Ni–Ti stainless steel by severe plastic deformation. Mater Lett 166:276–279

[29] Edalati K, Horita Z (2016) A review on high-pressure torsion (HPT) from 1935 to 1988. Mater Sci Eng A 652:325–352

[30] Dong FY, Zhang P, Pang JC et al (2015) Strength, damage and fracture behaviors of high-nitrogen austenitic stainless steel processed by high-pressure torsion. Scr Mater 96:5–8

[31] Valiev RZ, Estrin Y, Horita Z et al (2006) Producing bulk ultrafine-grained materials by severe plastic deformation. J Microsc 58:33–39

[32] Vorhauer A, Pippan R (2004) On the homogeneity of deformation by high pressure torsion. Scr Mater 51:921–925

[33] Valiev RZ, Estrin Y, Horita Z et al (2016) Producing bulk ultrafine-grained materials by severe plastic deformation: 10 years later. JOM 68:1216–1226

[34] Khvostantsev LG, Vereshchagin LF, Novikov AP (1997) A verkh-niz (up-down) toroid device for generation of high pressure. High Temp-High Press 9:637

[35] Khvostantsev LG, Slesarev VN, Brazhkin VV (2004) Toroid type high-pressure device: history and prospects. High Press Res 24:371–383

[36] Wejrzanowski T, Spychalski W, Różniatowski K, Kurzydłowski K (2008) Image based analysis of complex microstructures of engineering materials. Int J Appl Math Comput Sci 18:33–39

[37] Wejrzanowski T, Lewandowska M, Kurzydłowski KJ (2010) Stereology of nano-materials. Image Anal Stereol 29:1–12

[38] Guy K, Butler EP, West DRF (1982) ε and α′ martensite formation and reversion in austenitic stainless steels. J Phys Colloq 43:575–580

[39] Rathmayr GB, Hohenwarter A, Pippan R (2013) Influence of grain shape and orientation on the mechanical properties of high pressure torsion deformed nickel. Mater Sci Eng A 560:224–231

[40] Pippan R, Scheriau S, Taylor A et al (2010) Saturation of fragmentation during severe plastic deformation. Annu Rev Mater Res 40:319–343

[41] Humphreys FJ, Hatherly M (1996) Recrystallization and related annealing phenomena. Pergamon Press, Oxford

[42] Belyakov A, Sakai T, Miura H et al (2002) Continuous recrystallization in austenitic stainless steel after large strain deformation. Acta Mater 50:1547–1557

[43] Renk O, Hohenwarter A, Eder K et al (2015) Increasing the strength of nanocrystalline steels by annealing: is segregation necessary? Scr Mater 95:27–30

[44] Valiev RZ (2003) Paradoxes of severe plastic deformation. Adv Eng Mater 5:296–300

[45] Winning M, Schäfer C (2006) Influencing recrystallization behaviour by mechanical loads. Mater Sci Eng A 419:18–24

[46] Setman D, Schafler E, Korznikova E, Zehetbauer MJ (2008) The presence and nature of vacancy type defects in nanometals detained by severe plastic deformation. Mater Sci Eng A 493:116–122

[47] Zehetbauer MJ, Steiner G, Schafler E, Korznikov A, Korznikova E. In Horita Z (ed) Proceedings of the 3rd international conference on nanomaterials by severe plastic deformation, Fukuoka, Japan (2005) Mater Sci Forum 503–504: 57–64

[48] El-Tahawy M, Huang Y, Um T et al (2017) Stored energy in ultrafine-grained 316L stainless steel processed by high-pressure torsion. J Mater Res Technol 6:336–347

[49] Winning M, Gottstein G, Shvindlerman LS (2002) On the mechanisms of grain boundary migration. Acta Mater 50:353–363

Phenomena Occurring in Nanostructured Stainless Steel 316LVM during Annealing under High Hydrostatic Pressure

Agnieszka T. Krawczynska, Stanislaw Gierlotka, Przemyslaw Suchecki, Daria Setman, Boguslawa Adamczyk-Cieslak, Michal Gloc, Witold Chrominski, Malgorzata Lewandowska, and Michael Zehetbauer*

The aim of the study is to demonstrate the impact of high hydrostatic pressure annealing on the grain boundary character, precipitation rate, and susceptibility to intergranular corrosion of nanostructured austenitic stainless steel 316LVM. To this end, samples of an austenitic stainless steel are deformed by high pressure torsion and subsequently annealed at 900 °C for 10 min under a pressure of 2, 6 GPa and, for comparison, under atmospheric pressure. The resulting microstructures are examined using electron beam scattering diffraction, and transmission and scanning electron microscopy. It is shown that the pressure applied during annealing leads to a higher percentage of high-angle grain boundaries than does atmospheric pressure. Moreover, it promotes the coexistence of two orientations, <111> and <100>, whereas atmospheric supports mainly <111>. High pressure hinders the growth of carbides, but drastically increases their number compared with atmospheric pressure annealing. As a consequence, the highest number of $Cr_{23}C_6$ carbides are present in the sample annealed under 6 GPa, making this sample susceptible to intergranular corrosion.

1. Introduction

Heat treatment has a significant impact on the properties of metals after plastic deformation, especially when it is applied to materials after severe plastic deformation (SPD). Thus produced nanostructured materials show excellent strength, often accompanied by reduced ductility compared to coarse-grained materials.[1–3] For example, in austenitic stainless steel deformed by high pressure torsion (HPT), which is one of the SPD techniques, the ultimate tensile strength reached 2250 MPa, but the elongation to failure was far below 5%.[4] Therefore, annealing may be an effective method for controlling microstructure, for example, to improve ductility at little cost to strength and good corrosion resistance. Moreover, a well-selected annealing treatment and conditions may enable enhanced material performance to be achieved through the engineering of grain boundaries.[5]

Various heat treatment methods have been studied and proposed as effective methods for controlling the microstructure of different materials. Most articles focus on conventional heat treatment.[4,6–8] This can be successful in improving the mechanical properties obtained in ultrafine-grained steel deformed by HPT and subsequently annealed at 723 °C. A remarkably good combination of yield strength (1330 MPa) and elongation to failure (43%) obtained in such a process has been attributed to the almost full reversion of martensite into austenite at a grain size of approximately 200 nm.[4] However, it seems that, by applying unconventional annealing techniques, new possibilities arise of producing microstructures unachievable by conventional annealing. One such approach is electropulsing treatment (EPT) – applying a high-density electric current to a deformed material.[9,10] It has been suggested that microstructural changes occur due to the thermal effect caused by Joule heating,[11,12] although the exact mechanisms have not been yet completely elaborated. It has been reported that after such heating the recrystallization kinetics of copper were accelerated, as was the recrystallization and grain growth of cold-rolled α-Ti.[13–15] Moreover, EPT can enhance the precipitation rate, as has been observed during electric-current-assisted aging in AA6061 alloy.[16] Summing up the research on EPT, it must be underlined that this treatment

Dr. A. T. Krawczynska, P. Suchecki, Dr. B. Adamczyk-Cieslak, Dr. M. Gloc, Dr. W. Chrominski, Prof. M. Lewandowska
Faculty of Materials Science and Engineering
Warsaw University of Technology
Woloska 141, Warsaw 02-507, Poland
E-mail: agnieszka.krawczynska@pw.edu.pl

Dr. S. Gierlotka
Polish Academy of Sciences
Institute of High Pressure Physics UNIPRESS
Sokolowska 29/37, Warsaw 01-142, Poland

Dr. D. Setman, Prof. M. Zehetbauer
University of Vienna
Faculty of Physics
Boltzmanngasse 5, Vienna A-1090, Austria

The ORCID identification number(s) for the author(s) of this article can be found under https://doi.org/10.1002/adem.201800101.

DOI: 10.1002/adem.201800101

enables new microstructures to be created by the acceleration of diffusion processes. However, when recrystallization and grain growth are accelerated, it is difficult to control microstructural changes.

More promising, then, is a technique that reduces the rate of recrystallization, grain growth, and precipitation. In this context, the authors propose high hydrostatic pressure annealing. Their previous work on annealing an austenitic stainless steel under high hydrostatic pressure showed that this annealing technique can lead to an unprecedented strength-plasticity balance, meaning an ultimate tensile strength of almost 1250 MPa combined with a uniform elongation of 7.7% and a total elongation of 24% (sample geometry: a cross-section of 0.4×0.3 mm and a gauge length of 1 mm) when compared to the results obtained for an austenitic stainless steel after HPT and conventional annealing at 450 °C, meaning an ultimate tensile strength of 1500 MPa with a uniform elongation of 2% and total elongation of 10% (sample geometry: a cross-section of 0.7×0.4 mm and a gauge length of 2.5 mm).[17,18] Earlier studies explained that high hydrostatic pressure slows down diffusion processes, which depend on the motion of vacancies.[19] As a result, the higher the pressure applied the more retarded the grain boundary mobility. This behavior of materials has been confirmed in aluminum bicrystals, copper, α-brass, and austenitic steel.[17–22] However, the question of the impact of high hydrostatic pressure during annealing on the precipitation rate has never been raised before. It is predictable that the precipitation rate will be reduced, since this phenomenon, as well as grain growth, is diffusion-driven. However, the extent to which it will be reduced should be investigated experimentally. It must be emphasized that, in austenitic stainless steel, the presence of precipitates of the $M_{23}C_6$ type (where M is Cr) at grain boundaries during annealing in a temperature range from 480 to 815 °C is the cause of their susceptibility to intergranular corrosion.[23,24] On the one hand, therefore, precipitates may be disadvantageous; on the other hand, they can lead to hardening when they appear in the form of nanostructure clusters in a ultrafine-grained austenitic steel.[25,26]

In the present study, the influence of high hydrostatic pressure annealing on the grain boundary character, precipitation rate, and susceptibility to intergranular corrosion was investigated for an austenitic stainless steel 316LVM deformed by HPT. Additionally, a conventional heat treatment using a furnace was performed for the sake of comparison.

2. Experimental Section

Sandvik Bioline 316LVM austenitic stainless steel was used; this is a low-carbon, vacuum-melted 316L grade stainless steel, UNS S31673 certified to ASTM F138, supplied as annealed in the form of 50 mm diameter rods, with a chemical composition in wt% as follows: 0.023C–0.6Si–1.7Mn–17.5Cr–13.5Ni–2.8Mo.

The material was cut into disks with a diameter of 10 mm and a thickness of 0.8 mm. The disks were processed at room temperature using an HPT device, at a constant pressure of 6 GPa. The disks were torsionally strained to five revolutions. The strain was well defined as simple shear, γ, and was calculated according to the equation $\gamma = 2\pi \times r \times n/t$, where r, n, and t are the distance from the torsion axes, the number of applied revolutions, and the mean thickness of the sample, respectively. All of the microstructure observations and analyses were performed 1.5 mm from the sample edge. For this reason, the equivalent strain $\varepsilon_{eq} = \gamma/\sqrt{3}$, which is 79, was calculated 3.5 mm from the central point of the sample after five revolutions.

After the HPT experiments, disks of 5 mm in diameter were cut in such a way that the radius of the sample after HPT became the diameter of the sample for the annealing experiments. The dimensions of the samples were limited by the dimensions of the toroidal high-pressure cell. The samples were annealed at 900 °C for 10 min, under either atmospheric pressure (0.1 MPa) or a hydrostatic pressure of 2 or 6 GPa. A toroidal high-pressure cell was used for the high pressure annealing, and a conventional furnace for the atmospheric pressure annealing. Further on in this text, these samples will be referred to as HPT_0.1 MPa, HPT_2 GPa, HPT_6 GPa.[17,27]

A texture analysis of the HPT-processed samples was performed on a Bruker D8 Advance diffractometer with nickel-filtered copper radiation ($\lambda = 0.154\ 056$ nm). The texture was measured over an area of approximately 1.5 mm^2 (the beam diameter was 1 mm), 1.5 mm from the sample edge. The <1 1 1>, <2 0 0>, <2 2 0>, and <3 1 1> pole figures were measured. The pole figures are characterized by the two angles: α and β. The α is a tilt angle from sample surface normal direction and the β is rotation angle around sample surface normal direction. The obtained diffracted intensity data is plotted as a function of α and β angles. During experiment the reflection technique was used and the pole figures were measurements from 0° at the center to 70° at the edge (α angle) and from 0° to 360° (β angle). The complete pole figures were calculated using the LaboTex v 3.0 program.

Taking into account that the texture changes on the radius of the sample, the EBSD technique seems to be more accurate than X-ray texture measurement where the signal comes from a much larger area. Therefore, for samples after annealing, the texture was analyzed using the EBSD technique. EBSD cannot be applied for the HPT-processed sample as the microstructure contains a high density of defects and microstructure elements of sizes below the resolution of the EBSD technique. The EBSD orientation mapping was performed on a Hitachi SU70 analytical scanning electron microscope (acceleration voltage of 20 kV) equipped with a Schottky emitter. For the scanning electron microscopy examination, the samples were prepared by electropolishing using Struers electrolyte A3. The parameters for electropolishing were as follows: voltage −15 V, time −15 s. Depending on the degree of deformation, various step sizes for the EBSD analysis were used to capture the details of the microstructure, that is, 200, 150, and 40 nm for the HPT_0.1 MPa, HPT_2 GPa, and HPT_6 GPa samples, respectively. The index rate of the Kikuchi maps during the EBSD scans was close to 90%. Data analysis and orientation maps were prepared with dedicated HKL Channel5 software. On the orientation maps, those boundaries having a misorientation angle between 5° and 15° are indicated by white lines, and boundaries with a misorientation angle greater than 15° by black lines.

The microstructure of the samples was investigated using a Hitachi SU8000 scanning electron microscope working at 5 kV

in the back-scattered electrons (BSE) mode, a JEOL JEM 1200 EX transmission electron microscope working at 120 kV and a Hitachi HD2700 scanning electron microscope working at 200 kV in the Z-contrast (ZC) mode. An EDS analysis of the precipitates was performed using a Hitachi HD2700 scanning electron microscope. For the transmission electron microscopy examination, the samples were prepared by mechanical polishing to a disk thickness of about 100 μm. Further thinning to reach a thickness appropriate for electron transparency was carried out by electropolishing using Struers electrolyte A2.

For the corrosion tests, the samples were ground and polished. The corrosion tests were performed in an aqueous solution consisting of 450 mL concentrated HNO_3 and 9 g NaF dm^{-3} (according to ASTM A262-77a). The corrosion resistance was evaluated based on microstructural observations.

Qualitative and quantitative studies of the precipitates and dimples were conducted using stereological and image analysis methods.[28,29] Their size was determined as the equivalent diameter, d_2, defined as the diameter of a circle having an area equal to the surface area of a given precipitate/dimple. The precipitate/dimple shape was described by the elongation factor, defined as the ratio of the maximum to the equivalent diameter d_{max}/d_2. To determine the variation of the size of individual precipitates/dimples, a variation coefficient, CV(d_2), defined as the ratio of the standard deviation SD to the mean value, was established. The spatial distribution of the precipitates and dimples was described by SKlZZ tessellation.[28,29] In this method, Voronoi (Av) cells surrounding each particle are generated. The variation coefficient of the Voronoi cells area, CV (Av), describes the uniformity of the spatial distribution of elements.

3. Results

3.1. Microstructure Observation and Texture Analysis after HPT

The microstructure visible on the cross-section is severely refined in the HPT-processed samples, as presented in **Figure 1**. The microstructure was transformed into small fragments forming nanocrystallites. The average grain size is below 100 nm, as is clearly evident in the dark field image (Figure 1b). Inside the grains there is a high density of dislocations and deformation twins. There are no shear bands visible. In a selected area diffraction pattern (SAED) one can notice rings, which confirm the microstructure refinement and high misorientation angles between individual grains. Moreover, there were no precipitates present. However, since the microstructure characterization of the HPT-processed sample has been the subject of previous research, this issue will not be further explored here.[30,31] In addition to the microstructure characterization, a texture analysis was performed, as shown in **Figure 2**. The measured texture is averaged over an area of approximately 1.5 mm^2. Results indicate that crystallites took a random orientation, the volume fraction of each of the orientations: <111> and <100>, analyzed farther for annealed under high hydrostatic pressure samples, is below 5%. One may expect that the results of measurements depend on the distance from the rotation axis, number of rotations and pressure.

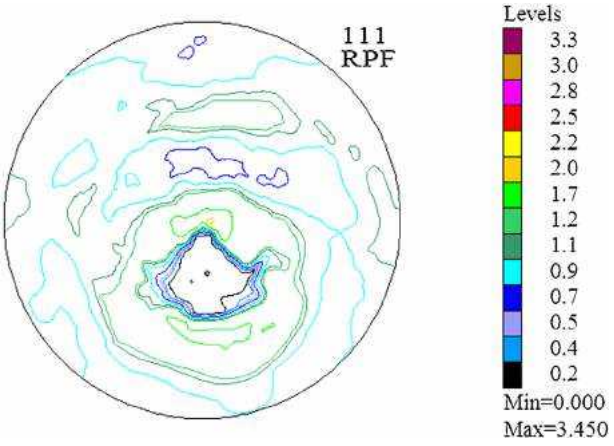

Figure 2. <111>recalculated pole figure of a HPT-processed sample, data collected parallel to the surface of the HPT disk.

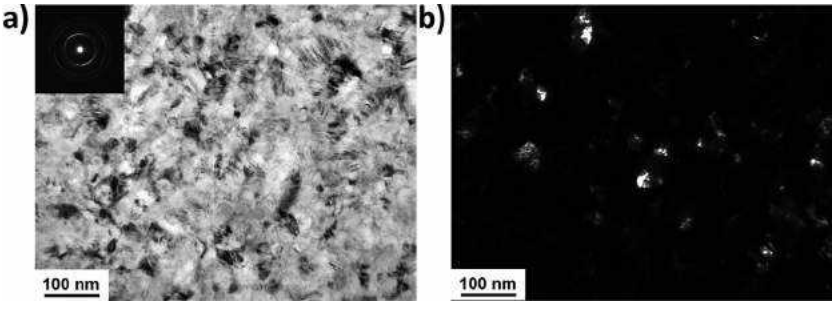

Figure 1. Microstructures of a HPT-processed sample parallel to the surface of the HPT disk a) in the bright field, b) in the dark field from planes (220); TEM images; SAED from an area of 4 μm in diameter in the left top corner of the bright field image.

3.2. The Impact of High Hydrostatic Pressure Annealing on the Misorientation of Grain Boundaries and Twinning Frequency using EBSD Technique

EBSD orientation maps of samples annealed under a pressure of 0.1 MPa, 2 and 6 GPa are presented in **Figure 3**. The samples have a microstructure typical of a recrystallized, low stacking fault energy material. It consists of coarse grains having a privileged orientation of <111> parallel to the HPT rotation axis. However, it must be noticed that in the HPT_2 GPa and HPT_6 GPa, apart from the privileged orientation of <111>, some grains are at an orientation of <100> (marked by red on the maps), approximately 6.4% and 4.2% for the HPT_2 GPa and HPT_6 GPa, respectively. (To calculate the fraction of <100> grains, the grains whose orientation varied by 10 degrees from the ideal orientation were taken into account). It seems that high hydrostatic pressure promotes the appearance of the orientation <100>, which in a conventionally annealed sample constitutes only 0.9%.

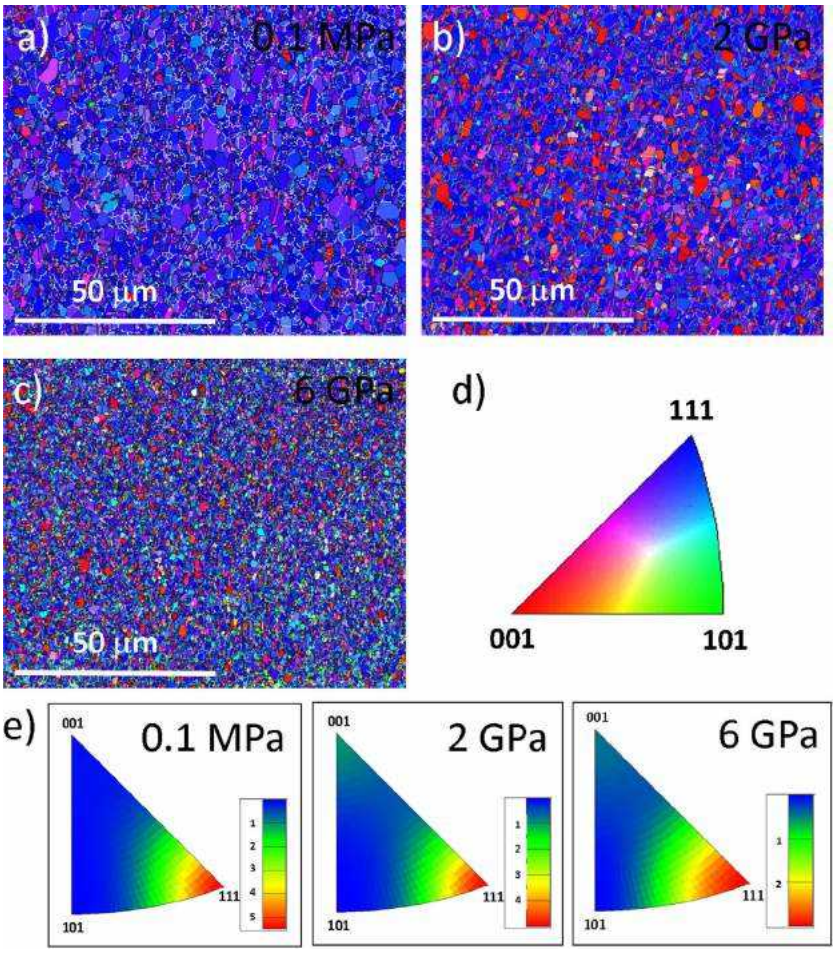

Figure 3. EBSD orientation maps of samples annealed under a) 0.1 MPa, b) 2 GPa, c) 6 GPa parallel to the surface of the HPT disk and with a shorter side of a map parallel to a sample radius; d) grain orientation colour code; e) corresponding inverse pole figures.

The misorientation angle distribution from the EBSD measurements is presented in **Figure 4**. In all samples, there is a prevalence of high-angle grain boundaries, understood as boundaries of an angle greater than 15 degrees. It is important to point out that the samples differ in their percentage of low-angle grain boundaries, which is 27% for the HPT_0.1 MPa and 12% for the HPT_2 GPa and HPT_6 GPa samples. This might suggest that the pressure somehow stimulates the creation of high-angle grain boundaries.

Moreover, in all samples, annealing twins appeared, which is indicated in Figure 4 as boundaries of the misorientation angle of 60°. The annealing twin frequency was 23%, 29%, and 21% for HPT_0.1 MPa, HPT_2 GPa, and HPT_6 GPa, respectively. The differences in the annealing twin frequency are negligible among the samples annealed under various hydrostatic pressures.

The impact of annealing under a pressure of 0.1 MPa, 2 GPa, and 6 GPa at 900 °C for 10 min on grain size and shape has been previously described and analyzed and will not be discussed in detail in this paper.[32] The main conclusion can be drawn that the pressure retards the grain growth which was 2.0, 1.35, and 0.58 μm for annealing pressures of 0.1 MPa, 2 GPa and 6 GPa, respectively. Since the HPT sample consisted of the austenitic phase no phase transformation occurred during annealing under the atmospheric or increased hydrostatic pressures.

3.3. The Impact of High Hydrostatic Pressure Annealing on Precipitate Size, Shape, and Distribution

It should be noted that precipitates were evident in all of the HPT-processed samples annealed at various pressures, as presented in **Figure 5**. They formed at grain boundaries as well as inside grains. However, the pressure had affected their size, shape, and distribution, as summarized in **Table 1**. Firstly, one can notice that the higher the pressure, the lower the precipitate size. After annealing under 0.1 MPa, the average precipitate size is 131 nm whereas it becomes slightly smaller, 119 nm, after annealing under 2 GPa. A further increase in annealing pressure to 6 GPa leads to a reduction in precipitate size to 36 nm. In contrast, CV(d_2) parameter, which quantifies the size diversity, increases slightly with increased pressure, from approximately 0.43 for pressures 0.1 MPa and 2 GPa to 0.56 for 6 GPa. The precipitates are slightly elongated, as expressed in the value of d_{max}/d_2, which varies from 1.24 for 0.1 MPa to 1.40 for 6 GPa. Moreover, the density of the precipitate distribution, shown by the value of Av, is similar when pressures of 0.1 and 2 GPa are applied (3.11 μm^2 for 0.1 MPa and 3.95 μm^2 for 2 GPa). The precipitates are more densely distributed – Av equals 0.28 μm^2–when the pressure is increased to 6 GPa. The heterogeneity of the spatial distribution of elements, described by CV(Av), increases when high hydrostatic pressure is applied, from 0.31 after annealing under 0.1 MPa to 0.63 and 0.57 after annealing under 2 and 6 GPa, respectively.

In the EDS spectra presented in **Figure 6**, one can notice significantly higher peaks of Cr and Mo for the spectra taken from regions containing precipitates when compared to the spectra taken from the matrix. It indicates that precipitates rich in Mo and also Cr are present in the samples, irrespective of the pressure applied. Cr-rich precipitates are particularly hazardous, as their formation reduces chromium content in the area close to the grain boundaries, which induces inter-granular corrosion. In order to verify whether the precipitates present in the samples after annealing could deteriorate the corrosion resistance to inter-granular corrosion, corrosion tests were performed.

3.4. The Impact of High Hydrostatic Pressure Annealing on Inter-Granular Corrosion Resistance

Before commencing the corrosion tests, the surfaces of the samples were observed. They were totally free of dimples or

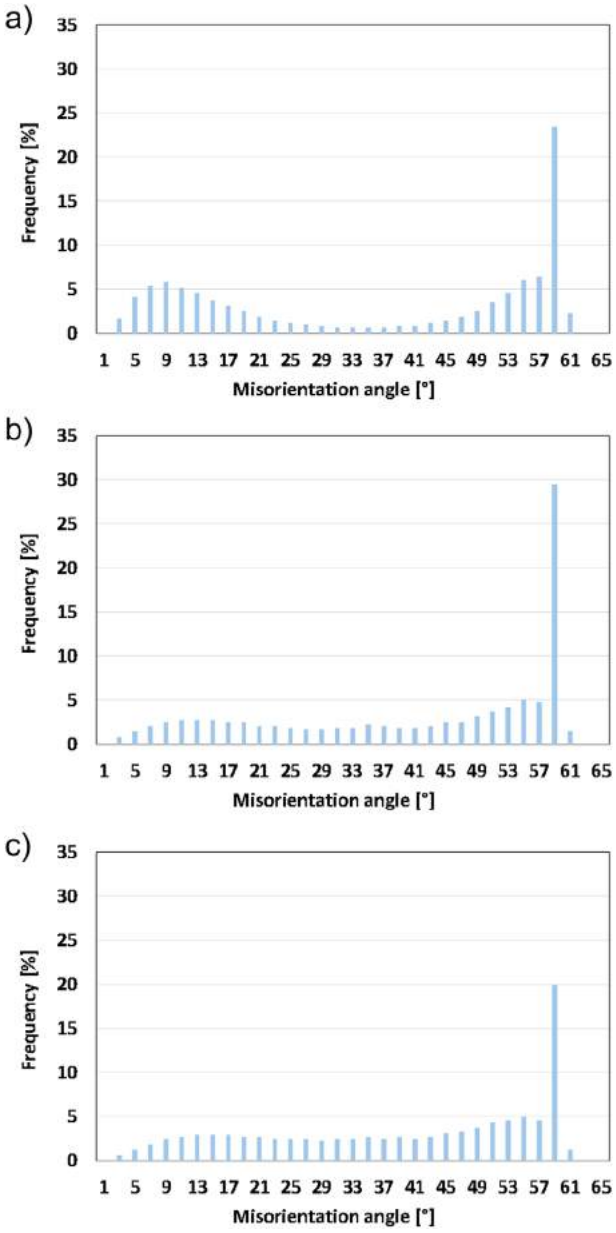

Figure 4. Misorientation angle distribution from EBSD measurements of samples annealed under a) 0.1 MPa, b) 2 GPa, and c) 6 GPa.

scratches, as indicated in **Figure 7**a–c. The surfaces after the corrosion tests are shown in Figure 7d–g. In the case of the HPT_0.1 MPa and HPT_2 GPa, dimples seldom appear on the sample surfaces. The HPT_6 GPa behaves differently, having dimples uniformly distributed across the surface. These dimples could be the effect of corrosion of the areas surrounding the Cr-precipitates resulting from the reduced chromium content. The etched dimples did not form etched lines along grain boundaries characteristic for the advanced intergranular corrosion. Therefore, it is highly probable that in the HPT_6 GPa sample inter-granular corrosion is at the initial stage. The average size of the etched dimples was 250 nm and the average size of the Voronoi cell area was 1.51 μm^2. The latter is larger than that calculated for the precipitates (0.28 μm^2), which suggests that not all the precipitates in the HPT_6 GPa sample are $Cr_{23}C_6$ carbides.

4. Discussion

4.1. The Impact of High Hydrostatic Pressure Annealing on the Character of Grain Boundaries

Our discussion must include the effect of pressure on the percentage of low-angle grain boundaries. It was noticed that samples annealed under high hydrostatic pressure showed approximately half the number of low-angle grain boundaries (12%) than the sample annealed under atmospheric pressure (27%). This observation suggests that a pressure of 2–6 GPa hinders the movement/creation of low-angle grain boundaries. It must be pointed out that, after HPT, high-angle grain boundaries that possess specific non-equilibrium structures prevail. They are characterized by increased free energy density, increased width, high density of dislocations, and large residual microstrain.[33–35] Apart from these, there are also general high-angle grain boundaries whose structure is similar to those of relaxed high-angle grain boundaries, highly-defected twin boundaries, and low-angle boundaries. One may, therefore, assume that, during annealing under high hydrostatic pressure, it is mainly the high-angle grain boundaries that migrate, and that, while in motion, they probably engulf areas with low-angle grain boundaries. For this reason, their percentage is higher in the samples annealed under 2 and 6 GPa than in those annealed under 0.1 MPa. As suggested in the literature, low-angle grain boundaries are well ordered and can migrate only by the vacancy migration mechanism, which is strongly limited under high pressure annealing because vacancy concentration decreases with increased pressure.[19] Therefore, during higher pressure annealing the migration of high-angle grain boundaries may be the reason of the disappearance of low-angle grain boundaries and it seems to be the deterministic factor.

Another issue that the authors would like to address is the impact of high hydrostatic pressure on the evolution of privileged orientations. There are many factors that have an impact on the texture created during annealing, namely prior grain size and texture, strain, time, annealing temperature, and the rate of heating. The results obtained indicate that the high hydrostatic pressure annealing must be added to this list. In fcc metals after deformation, one usually observes the occurrence of the cube ({001}<100>) texture. The orientation <100> prevails in the as-received material.[36] However, in this study in a HPT_0.1 MPa sample the orientation <111> dominates. It might be due to the fact that in metals after large deformation, the network of high-angle grain boundaries prevails. During annealing those grain boundaries change to conventional ones. Subsequently recrystallization occurs by small-scale boundary migration.[37] Since it is established that certain misorientations meaning 40° <111> result in high mobility boundaries, the prevailing orientation <111> is an effect of such a phenomenon.

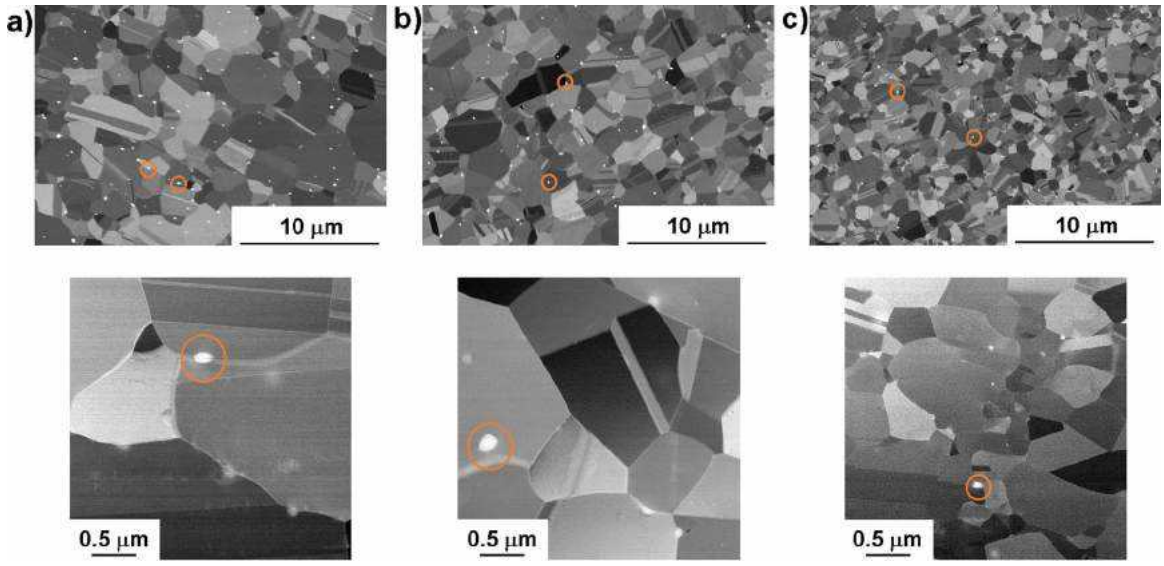

Figure 5. Microstructures of HPT-processed austenitic stainless steel annealed under hydrostatic pressure of a) 0.1 MPa, b) 2 GPa, c) 6 GPa; exemplary precipitates, indicated in orange circles, are visible as bright dots in the BSE-SEM mode and ZC-STEM mode.

Table 1. Parameters of precipitate size, shape (d_{2av}, SD (d_2), CV(d_2), d_{max}/d_2) and distribution (Av_{av}, SD(Av), CV(Av)) after annealing under 0.1 MPa, 2 GPa, and 6 GPa.

	d_{2av} [nm]	SD (d_2)	CV(d_2)	d_{max}/d_2	Av_{av} [μm^2]	SD(Av)	CV(Av)
0.1 MPa	131	57	0.43	1.24	3.11	0.60	0.31
2 GPa	119	50	0.42	1.29	3.95	2.49	0.63
6 GPa	36	20	0.56	1.40	0.28	0.16	0.57

Within the present study, two main orientations <111> and <100> were analyzed. One can notice that, during annealing under high hydrostatic pressure, the orientation <100> appears apart from the dominant <111>, suggesting that the high pressure supports the coexistence of these two orientations, whereas atmospheric pressure supports mainly <111>.This phenomenon might be explained in the following way. During annealing under the atmospheric pressure high-angle grain boundaries migrate easily in a HPT-processed steel. As a result a microstructure consisting of <111> oriented grains is created (It was proved experimentally that <111> boundaries show the highest mobility).[38] In contrast, under the increased pressure the movement of boundaries is more limited. For this reason, the delivered energy during heating may enable nucleation of new recrystallized grains of the orientation <100>. The fact that newly recrystallized grains gain the orientation <100> might be explained in the following way: the cube component has the lowest possible Taylor factor and consumes the higher Taylor factor texture components.[38] It seems that this issue was neglected in previous studies on the impact of high hydrostatic pressure annealing on microstructure. This could be due to the fact that higher pressure slows down recrystallization and grain growth. For this reason, even after 240 min of annealing an Al–2%Mg alloy under 10 MPa, the rolling texture remained stable with no significant reduction in intensity.[39]

In contrast to the visible impact of pressure on the amount of low-angle boundaries and texture, high hydrostatic pressure during annealing has a negligible effect on twinning frequency. The similarity in the twinning frequencies among the HPT_0.1

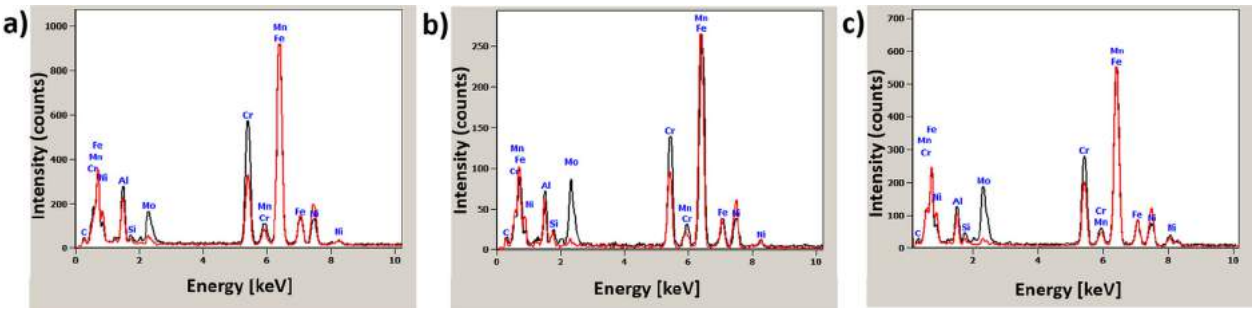

Figure 6. Exemplary spectra collected from matrix (red line) and from precipitates (black line) of an austenitic stainless steel annealed under hydrostatic pressure of a) 0.1 MPa, b) 2 GPa, and c) 6 GPa.

MPa, HPT_2 GPa, and HPT_6 GPa samples may be due to the fact that the probability of twin appearance is a function of the rate of boundary motion, and it has been shown that it is a function of the grain size ratio of D/D_0, where D is the grain size after annealing and D_0 is the original grain size before annealing.[40,41] It has been observed that the frequency of annealing twins rapidly increases at the beginning of grain growth and attains a maximum at a ratio of D/D_0 around 2.5, then steadily decreases. Considering the fact that the average grain size after HPT is approximately 100 nm and in all samples the annealed grain size is many times greater, the impact of the D/D_0 is negligible on twinning frequency.

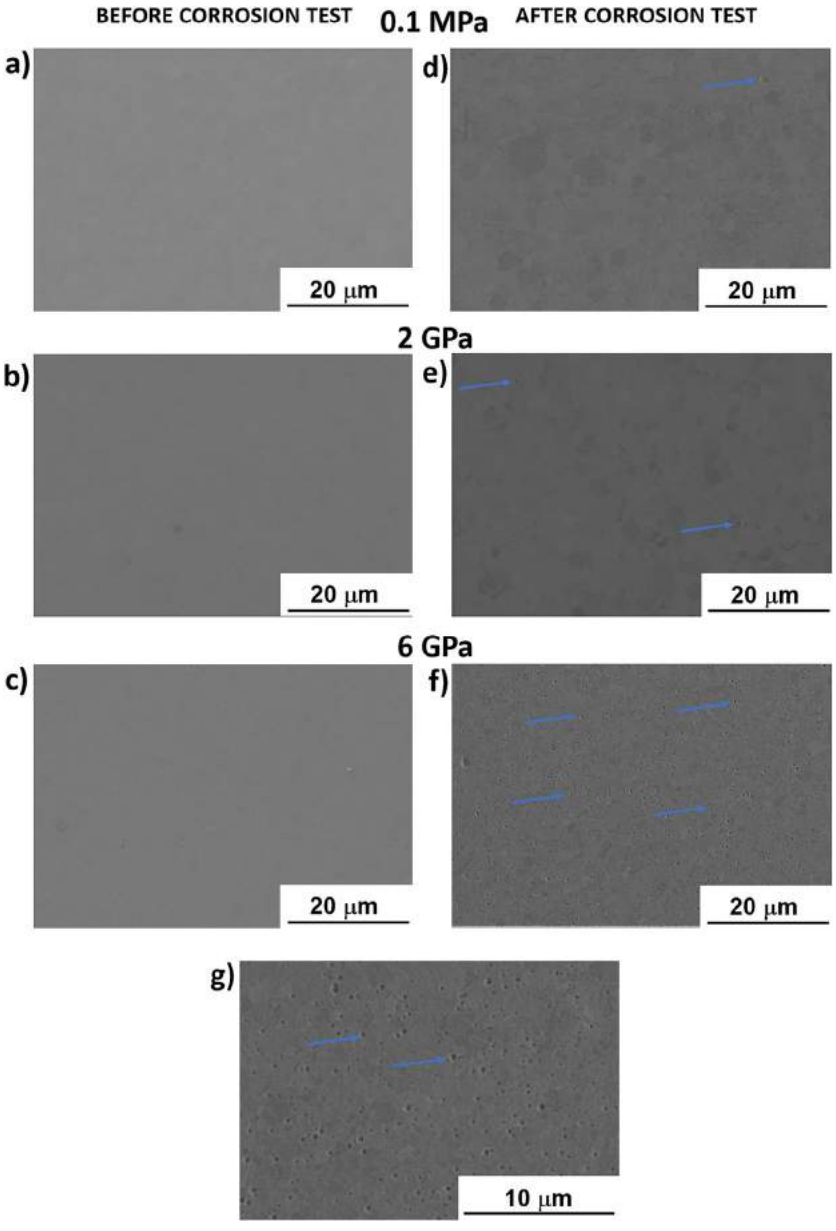

Figure 7. Surfaces of annealed samples before corrosion tests, a) HPT_0.1 MPa, b) HPT_2 GPa, c) HPT_6 GPa; surfaces of annealed samples after corrosion tests, d) HPT_0.1 MPa, e) HPT_2 GPa, f and g) HPT_6 GPa; blue arrows indicate corrosion dimples.

4.2. The Impact of High Hydrostatic Pressure Annealing on Precipitate Rate, Chemical Composition, and Intergranular Corrosion Resistance

On the one hand, SPD enhances the precipitation rate after the deformation process and subsequent annealing.[42–44] This is due to enhanced diffusion owing to the presence of an artificially high, deformation-induced vacancy content.[25,26,33] The excess vacancy concentration in pure Cu and Ni samples processed by HPT can achieve values of $(0.9–20)^*10\wedge(-4)$, whereas in α'-martensite processed by HPT the equivalent values are $(5.2 \pm 3.6)^*10\wedge(-4)$.[45–47] On the other hand, it is well know that high pressure annealing slows down diffusion processes.[19] In this experiment, it was proved that the high hydrostatic pressure applied during annealing did not completely block the precipitation processes. It only impeded the growth of precipitates under 6 GPa. However, their number increased. The increase in their number may be the consequence of the fact that annealing under high hydrostatic pressure reduces both the climb and glide rates of a dislocation.[48] Therefore, probably more dislocations are present at the beginning of the annealing process in a sample annealed under the pressure of 6 GPa than under 0.1 MPa. Generally, solute atoms migrate to dislocations and segregate along dislocation lines which leads to the formation of solute-enriched regions, which subsequently promotes nucleation and growth of precipitates. In addition, to dislocation-induced segregation, dislocation cores also act as fast paths for diffusing atoms since the disorder in the core region facilitates diffusion.[49,50] These two facts meaning: 1) higher dislocation density at the beginning of annealing under high hydrostatic pressure than under the atmospheric pressure; 2) dislocation induced segregation, are responsible for a higher number of precipitates created during annealing at 900 °C at 6 GPa than under 0.1 MPa.

These results can be compared with those obtained for an austenitic stainless steel 316LVM deformed by hydrostatic extrusion (HE) and subsequently annealed at the same conditions as in the present study, where no precipitates appeared.[17] It seems that the deformation technique plays a significant role as exactly the same material and annealing treatment were used in both experiments. HPT in comparison to HE was performed to higher equivalent strain and as a consequence it introduced higher vacancy concentration. Hence, as suggested above probably vacancies facilitated diffusion during annealing enabling precipitation of carbides.

Moreover, the applied pressure had an impact on the chemical composition of carbides meaning that more $Cr_{23}C_6$ carbides appeared

with the increase in pressure to 6 GPa leading to the susceptibility to the intergranular corrosion of this sample. This is an interesting fact as it underlines that does the high hydrostatic pressure not only slow down diffusion processes characteristic for a particular temperature but it also makes possible of phenomena that can happen at lower temperature. In the case of austenitic stainless steel the appearance of $Cr_{23}C_6$ carbides responsible for the intergranular corrosion is observed far below 900 °C. These results provide evidence that annealing under high hydrostatic pressure is potentially an efficient way to design and control the microstructure of nano-grained materials.

5. Conclusions

1) Annealing austenitic stainless steel 316LVM under high hydrostatic pressure:
   a) leads to a higher percentage of high-angle grain boundaries (88%) than annealing under atmospheric pressure (73%),
   b) promotes the coexistence of two orientations <111> and <100>, whereas atmospheric pressure supports mainly <111> (approximately 0.9%, 6.4%, and 4.2% for annealing under 0.1 MPa, 2 GPa, and 6 GPa, respectively),
   c) promotes the nucleation of precipitates and hinders their growth, thereby resulting in a higher number of $Cr_{23}C_6$ carbides during annealing under 6 GPa, making this sample susceptible to inter-granular corrosion.

2) The current study indicates that annealing under high hydrostatic pressure makes it possible to produce austenitic stainless steel 316LVM having a different microstructure than results from conventional annealing, while considering low-angle grain boundary fraction, texture, precipitate size, and chemical composition.

Acknowledgements

This work was supported by Polish National Science Center project SONATA No.UMO-2014/15/D/ST8/00532 and FWF Austrian Science fund No: T512-N20.

Conflict of Interest

The authors declare no conflict of interest.

Keywords

annealing, austenitic stainless steel, intergranular corrosion resistance, nanostructured materials

Received: January 31, 2018
Revised: April 22, 2018
Published online:

[1] S. V. Dobatkin, O. V. Rybalchenko, N. A. Enikeev, A. A. Tokar, M. M. Abramova, *Mater. Lett.* **2016**, *166*, 276.
[2] R. Z. Valiev, Y. Estrin, Z. Horita, T. G. Langdon, M. J. Zehetbauer, Y. Zhu, *JOM* **2016**, *68*, 1216.
[3] Y. Estrin, A. Vinogradov, *Acta Mater.* **2013**, *61*, 782.
[4] M. El-Tahawy, P. H. R. Pereira, Y. Huang, H. Park, H. Choe, T. G. Langdon, J. Gubicza, *Mater. Lett.* **2018**, *214*, 240.
[5] M. Kumar, A. J. Schwartz, W. E. King, *Acta Mater.* **2002**, *50*, 2599.
[6] X. H. An, S. D. Wu, Z. F. Zhang, R. B. Figueiredo, N. Gao, T. G. Langdon, *Scr. Mater.* **2012**, *66*, 227.
[7] R. Z. Valiev, A. V. Sergueeva, A. K. Mukherjee, *Scr. Mater.* **2003**, *49*, 669.
[8] L. Xiong, Z. S. You, L. Lu, *Scr. Mater.* **2016**, *119*, 55.
[9] E. S. Machlin, *J. Appl. Phys.* **1959**, *30*, 1109.
[10] J. W. Park, H. J. Jeong, S. W. Jin, M. J. Kim, K. Lee, J. J. Kim, S. T. Hong, H. N. Han, *Mater. Charact.* **2017**, *133*, 70.
[11] C. Li, S. Jiang, K. Zhang, *Int. J. Adv. Manuf. Technol.* **2012**, *63*, 931.
[12] J. Magargee, F. Morestin, J. Cao, *J. Eng. Mater. Technol.* **2013**, *135*, 41003.
[13] H. Conrad, N. Karam, S. Mannan, *Scr. Metall.* **1983**, *17*, 411.
[14] H. Conrad, N. Karam, S. Mannan, A. F. Sprecher, *Scr. Metall.* **1988**, *22*, 235.
[15] Z. S. Xu, Z. H. Lai, Y. X. Chen, *Scr. Metall.* **1988**, *22*, 187.
[16] M. J. Kim, M. G. Lee, K. Hariharan, S. T. Hong, I. S. Choi, D. Kim, K. H. Oh, H. N. Han, *Int. J. Plast.* **2017**, *94*, 148.
[17] A. T. Krawczynska, T. Brynk, S. Gierlotka, E. Grzanka, S. Stelmakh, B. Palosz, M. Lewandowska, K. J. Kurzydlowski, *Mech. Mater.* **2013**, *67*, 25.
[18] A. Vorhauer, S. Kleber, R. Pippan, *Mater. Sci. Eng. A* **2005**, *410-411*, 281.
[19] V. Sursaeva, S. Protasova, W. Lojkowski, J. Jun, *Textures Microstruct.* **1999** *32*, 175.
[20] W. Lojkowski, D. A. Molodov, G. Gottstein, L. S. Shvidlerman, *Mater. Sci. Forum* **1996**, *207*, 537.
[21] L.E. Tanner, S. V Radcliffe, *Acta Metall.* **1962**, *10*, 1161.
[22] W. Kuhlein, H. P. Stuwe, *Acta Metall. Mater.* **1988**, *36*, 3055.
[23] A. T. Krawczynska, M. Gloc, K. Lublinska, *J. Mater. Sci.* **2013**, *45*, 17.
[24] Y. Zhou, Y. Liu, X. Zhou, C. Liu, J. Yu, Y. Huang, H. Li, W. Li, *J. Mater. Sci. Technol* **2017**, *33*, 1448.
[25] N. A. Enikeev, X. Sauvage, M. M. Abramova, M. Y. Murashkin, R. Z. Valiev, *Conf. Ser.: Mater. Sci. Eng.*, **2014**, *63*, 012127.
[26] M. M. Abramova, N. A. Enikeev, R. Z. Valiev, A. Etienne, B. Radiguet, Y. Ivanisenko, X. Sauvage, *Mater. Lett.* **2014**, *136*, 349.
[27] S. Gierlotka, E. Grzanka, A. Krawczynska, S. Stelmakh, B. Palosz, M. Lewandowska, C. Lathe, K. J. Kurzydlowski, *Z. Kristallogr.* **2011**, *1*, 281.
[28] T. Wejrzanowski, W. Spychalski, K. Różniatowski, K. Kurzydłowski, *Int. J. Appl. Math. Comput. Sci.* **2008**, *18*, 33.
[29] T. Wejrzanowski, M. Lewandowska, K. J. Kurzydlowski, *IAS* **2010**, *29*, 1.
[30] S. Scheriau, Z. Zhang, S. Kleber, R. Pippan, *Mater. Sci. Eng. A* **2011**, *528*, 2776.
[31] R. Pippan, S. Scheriau, A. Taylor, M. Hafok, A. Hohenwarter, A. Bachmaier, *Ann. Rev. of Mater. Res.* **2010**, *40*, 319.
[32] A. T. Krawczynska, S. Gierlotka, P. Suchecki, D. Setman, B. Adamczyk-Cieslak, M. Lewandowska, M. Zehetbauer, *J. Mater Sci.* https//doi.org/10.1007/s10853-018-2459-1
[33] X. Sauvage, G. Wilde, S. V. Divinski, Z. Horita, R. Z. Valiev, *Mater. Sci. Eng. A* **2012**, *540*, 1.
[34] R. Z. Valiev, R. K. Islamgaliev, I. V. Alexandrov, *Prog. Mater. Sci.* **2000**, *45*, 103.
[35] Z. Horita, D. J. Smith, M. Furukawa, M. Nemoto, R. Z. Valiev, T. G. Langdon, *J. Mater. Res.* **1996**, *11*, 1880.
[36] A. T. Krawczynska, W. Chrominski, E. Ura-Binczyk, M. Kulczyk, M. Lewandowska, *Mater. Des.* **2017**, *136*, 34.

[37] A. Belyakov, T. Sakai, H. Miura, R. Kaibyshev, K. Tsuzaki, *Acta Mater.* **2002**, *50*, 1547.
[38] R. D. Doherty, D. A. Hughes, F. J. Humphreys, J. J. Jonas, D. Juul Jensen, M. E. Kassner, W. E. King, T. R. McNelley, H. J. McQueen, A. D. Rollett, *Mater. Sci. Eng. A* **1997**, *238*, 219.
[39] M. Winning, C. Schäfer, *Mater. Sci. Eng. A* **2006**, *419*, 18.
[40] M. Odnobokova, M. Tikhonova, A. Belyakov, R. Kaibyshev, *J. Mater. Sci*. **2017**, *52*, 4210.
[41] M. Tikhonova, Y. Kuzminova, X. Fang, W. Wang, R. Kaibyshev, A. Belyakov, *Philos. Mag*. **2014**, *94*, 4181.
[42] K. Oh-ishi, Y. Hashi, A. Sadakata, K. Kaneko, Z. Horita, T. G. Langdon, *Mater. Sci. Forum* **2002**, *396*, 333.
[43] W. Chrominski, M. Lewandowska, *Acta Mater.* **2016**, *103*, 547.
[44] Y. Huang, J. D. Robson, P. B. Prangnell, *Acta Mater.* **2010**, *58*, 1643.
[45] D. Setman, E. Schafler, E. Korznikova, M. J. Zehetbauer, *Mater. Sci. Eng. A* **2008**, *493*, 116.
[46] M. J. Zehetbauer, G. Steiner, E. Schafler, A. Korznikov, E. Korznikova, *Mater. Sci. Forum* **2006**, *503*, 57.
[47] M. El-Tahawy, Y. Huang, T. Um, H. Choe, J. L. Lábár, T. G. Langdon, J. Gubicza, *J. Mater. Res. Technol*. **2017**, *6*, 339.
[48] J. E. Hilliard, J. M. Lommel, J. B. Hudson, D. F. Stein, J. D. Livingston, *Acta Metall*. **1961**, *9*, 787.
[49] J. Huang, M. Meyer, V. Pontikis, *Phys. Rev. Lett*. **1989**, *63*, 628.
[50] J. Rabier, M. P. Puls, *Philos. Mag. A* **1989**, *59*, 533.

Materials Science & Engineering A 767 (2019) 138381

Contents lists available at ScienceDirect

Materials Science & Engineering A

journal homepage: www.elsevier.com/locate/msea

Influence of high hydrostatic pressure annealing on the recrystallization of nanostructured austenitic stainless steel

Agnieszka Teresa Krawczynska*, Przemyslaw Suchecki, Boguslawa Adamczyk-Cieslak, Barbara Romelczyk-Baishya, Malgorzata Lewandowska

Warsaw University of Technology, Faculty of Materials Science and Engineering, Woloska 141, 02-507, Warsaw, Poland

ARTICLE INFO

Keywords:
Nanocrystalline materials
Electron microscopy
Hardness
X-ray analysis

ABSTRACT

The aim of this study was to investigate recrystallization in 316LVM nanostructured austenitic stainless steel annealed under high hydrostatic pressure. The nanostructured austenitic stainless steel was obtained by caliber rolling to a total strain of 3.4. This process resulted in a microstructure consisting of nanotwins and elongated bands. Nanostructured austenitic stainless steel is thermally stable up to 700 °C and shows a measurable "hardening by annealing" effect after annealing at 500 °C. The deformed samples were annealed at 900 °C for 10 min under atmospheric or hydrostatic pressures of 2 and 6 GPa. The resulting microstructures were examined using transmission scanning electron microscopy techniques. Moreover, the development of the texture during annealing was analyzed by means of orientation distribution functions. It was established that, apart from promoting the appearance of new texture components, annealing under hydrostatic pressure supports the nucleation of precipitates.

1. Introduction

316L austenitic stainless steel is widely applied in numerous industrial sectors, from medicine through petrochemistry to nuclear power, due to its corrosion resistance and favourable ductility. Its exceptional corrosion resistance is an effect of its low carbon content, which minimizes the sensitization effect, and of its high chromium content, which leads to the formation of a stable chromium oxide (III) passive layer. Moreover, corrosion resistance is further improved by the addition of Mo. Additionally, Mo in solid solution reduces dislocation mobility which results in a high work hardening. In industry, many products are fabricated through various manufacturing processes, among which rolling is considered to be the most common.

A further optimization of various properties is possible by means of annealing [1–4]. The degree of deformation, annealing temperature and time are the most important factors that affect the texture, microstructure and mechanical properties of 316L stainless steels. It is well known that texture is an inherent characteristic of metals and has a significant impact on their strength-ductility balance and electrical conductivity. The design of well-tailored textures with respect to certain desired anisotropic properties of the final product is still a challenge. Annealing temperature and time can significantly change the texture of cold-rolled austenitic stainless steels. For example, the typical rolling texture of AISI 300 austenitic steel is generally Brass type $\{110\} < 112 >$, along with a scatter towards an S orientation $\{123\} < 634 >$ and Goss orientation $\{011\} < 100 >$ [5]. Some authors note that as the % of cold rolling increases, a development of the S and Goss texture components is observed [6]. However, after recrystallization, major components are centred on Goss and Cu $\{112\} < 111 >$ as well as the BR component $\{236\} < 385 >$. With an increase in annealing temperature the textural evolution shows the emergence of weak texture along with another new component $\{197\} < 211 >$ [5]. Grain orientation distribution affects the mechanical parameters [7]. In the case of pipeline steel, texture components had the biggest impact on toughness [8]. For applications, what is most important is to obtain, through annealing, a product having the desired strength and plasticity. A good strength-ductility combination can be gained through high-strain cold rolling (rolling strain > 90%) and subsequent annealing (σ_{UTS} = 1385 MPa and At = 5.5%) [9]. Moreover, further deformation, known as severe plastic deformation (SPD) or dynamic plastic deformation (DPD), when combined with annealing, may lead to an even better strength-plasticity balance. Quite remarkable results - an ultimate tensile strength of 1 GPa and an elongation-to-failure of 27%, were obtained in 316L stainless steel refined by DPD and

* Corresponding author.
E-mail addresses: agnieszka.krawczynska@pw.edu.pl, akrawczynska@wp.pl (A.T. Krawczynska), przemyslawsuchecki@gmail.com (P. Suchecki), boguslawa.cieslak@pw.edu.pl (B. Adamczyk-Cieslak), barbara.romelczyk.dokt@pw.edu.pl (B. Romelczyk-Baishya), malgorzata.lewandowska@pw.edu.pl (M. Lewandowska).

https://doi.org/10.1016/j.msea.2019.138381
Received 19 March 2019; Received in revised form 2 September 2019; Accepted 3 September 2019
Available online 05 September 2019
0921-5093/

additionally annealed at 750 °C, due to the creation of a specific microstructure consisting of recrystallized grains embedded within nano-sized twin bundles and nano-grains [10]. In another work it was found that annealing at 723 °C after high pressure torsion (HPT) led to a remarkably good combination of yield strength 1330 MPa and elongation to failure 43% [11]. However, the industrial application of these techniques is still quite limited due to the small dimensions of steels processed in this way, and rolling techniques remain the most popular. It should be emphasized that rolling techniques such as asymmetric flat rolling (AFR) [12,13], continuous repetitive corrugation and straightening (CRCS) [14], and caliber rolling (CaR) [15–17], can also lead to ultrafine-grained (UFG) or nanograined structures (NS), and therefore to high strength. For example, in 304-type nitrogen-bearing stainless steel subjected to CaR, the grain size was reduced to 50 nm [18]. Nevertheless, there is little information available on the CaR of 316LVM austenitic stainless steel.

One can have the impression that a lot is known about the rolling and annealing of austenitic stainless steel. However, according to the authors, there is still room for improvement in optimizing texture, microstructure and mechanical properties. This can be achieved when one applies unconventional annealing techniques such as, for example, high hydrostatic pressure annealing. This method is proposed because it is an effective way to control grain growth and produce microstructures that could not be obtained under atmospheric pressure due to fast and uncontrollable grain growth, whereas high pressure during annealing slows down the diffusion processes taking place and, as a consequence, grain boundary mobility [17,19–28]. It has been proved that annealing austenitic stainless steel after deformation by hydrostatic extrusion (HE) under high hydrostatic pressure led to an unprecedented strength-plasticity balance, meaning an ultimate tensile strength of almost 1250 MPa combined with a uniform elongation of 7.7% and a total elongation of 24% [19]. Furthermore, the high hydrostatic pressure annealing of austenitic stainless steel deformed by HPT had an impact on grain growth, the volume fraction of high-angle grain boundaries, preferable grain orientations, precipitate size distribution, and chemical composition in comparison with atmospheric annealing [17,28]. It was discovered that an increase in hydrostatic pressure hindered grain growth, led to a higher percentage of high-angle grain boundaries than annealing under atmospheric pressure, and promoted the coexistence of two orientations $< 111 >$ and $< 100 >$, whereas atmospheric pressure supported mainly $< 111 >$ and hindered the growth of carbides. The effect of high hydrostatic pressure annealing on recrystallization and grain growth was even more profound in the case of austenitic stainless steel deformed by rolling [17].

In view of recent publications, one may expect that, in the case of austenitic stainless steel deformed by CaR, the impact of high hydrostatic pressure annealing on texture, precipitate size distribution and chemical composition in comparison with atmospheric annealing should be more significant than in the case of austenitic stainless steel deformed by HPT. Additionally, the thermal stability of CaR austenitic stainless steel was investigated to verify its behavior as a nanomaterial. An investigation of those factors is the aim of the present study.

2. Materials and methods

316LVM austenitic stainless steel, supplied by Sandvik in the form of 50 mm diameter annealed rods, was used in this study. This steel is also designated as UNS: S31673, DIN: X 2 CrNiMo 18 15 3 and ASTM F138. The chemical composition of this steel is shown in Table 1.

The samples were conventionally deformed using room temperature, multi-pass, longitudinal CaR with a total reduction in cross section of 23.8, which corresponds to a strain value of approximately 3.4 [29,30]. The strain was calculated according to the equation $\epsilon = 2\ln(d_1/d_2)$, where d_1 ($\varphi = 12$ mm) is the initial diameter and d_2 ($\varphi = 2.2$ mm) the final diameter. It must be pointed out that this calculation is only an approximation, since the cross section is not actually a circle. During the deformation process, the geometry of the transverse section of a material changes from circular to polygonal to nearly circle. The CaR was performed at the Faculty of Materials Science and Engineering, Warsaw University of Technology, Poland.

Table 1
Chemical composition (wt.%) of austenitic stainless steel 316LVM.

	C	Si	Mn	P	S	Cr	Ni	Mo	Cu	N
316LVM	0.025	0.6	1.7	0.025	0.003	17.5	13.5	2.8	0.1	< 0.1

After CaR, samples were subsequently annealed at 400, 500, 600, 700 and 900 °C for 10 min. The values of Vickers microhardness, Hv, were recorded along a diameter with a separation of 0.1 mm. These measurements were made using a Zwick microhardness tester under a load of 200 g. Uniaxial tensile tests were carried out at room temperature using an Zwick/Roell Z005 universal machine. Tensile tests were conducted under the displacement control mode at an initial strain rate of 10-3 1/s. Samples of a 1 mm-gauge section length and 0.3x0.4 cross-section were used for each test. For the strain measurements the digital image correlation method was applied.

After CaR, samples 3 mm in height were cut from a CaR rod, and then annealed at 900 °C for 10 min, either at atmospheric pressure (0.1 MPa) or at a hydrostatic pressure of 2 or 6 GPa. The high hydrostatic pressure annealing was performed in a toroidal high-pressure cell [31,32] whereas atmospheric pressure annealing in a conventional furnace. From here on in this text, those samples will be referred to as CaR, CaR_0.1 MPa, CaR_2 GPa, CaR_6 GPa.

The microstructure of the samples was investigated using scanning electron microscopes a Hitachi SU 8000, a Hitachi HD2700 and a transmission electron microscope JEOL JEM TEM1200 working at 5, 200 and 120 kV, respectively. For the examination on the Hitachi SU 8000, the samples were prepared by electropolishing: Struers A3 electrolyte, voltage −15V, time - 15 s. For the examination on the Hitachi HD2700 and the JEOL JEM TEM1200, the samples were mechanically polished to a disk thickness of approximately 100 µm and afterwards thinned by electropolishing using Struers A2 electrolyte. The microstructure was analyzed in the centre of the samples. Microstructures were observed in the BSE (back scattered electron), BF-STEM (bright field) and TEM modes, using the Hitachi SU 8000, the Hitachi HD2700 the JEOL JEM TEM1200, respectively.

The global texture investigations were performed using a Bruker D8 X-ray diffractometer applying filtered radiation Co Kα (Kα1 = 0.1789 nm). The texture was measured over an area of approximately 1.5 mm^2 (the beam diameter was 1 mm) in the center of the sample on the cross section. The measurements were recorded within a 5° × 5° mesh and a beam intensity at 5 s intervals. Three incomplete X-ray pole figures ({111},{200} and {311}) were used to evaluate complete Orientation Distribution Functions (ODFs) by spherical harmonics method and the Gauss model functions proposed by the Schultz reflection method [33]. The Labotex 2.1 software [34] was used to calculate volume fraction of the main texture components. It should be pointed out that a tolerance angle of 10° was used when the volume fractions were calculated.

Quantitative investigation of the precipitates was performed using stereological and image analysis methods [35,36]. To determine their size, variation of their size, spatial distribution and the uniformity of spatial distribution, parameters as equivalent diameter d_2, variation coefficient of equivalent diameter CV(d_2), Voronoi cell area Av, cells surrounding each particle and variation coefficient of Voronoi cell area CV(Av), describing the uniformity of the spatial distribution of particles, were applied.

3. Results

3.1. Texture analysis and microstructure observation after CaR

Texture analysis after CaR was performed, as shown in Fig. 1 and Table 2. A previous X-ray study revealed after CaR the presence of only

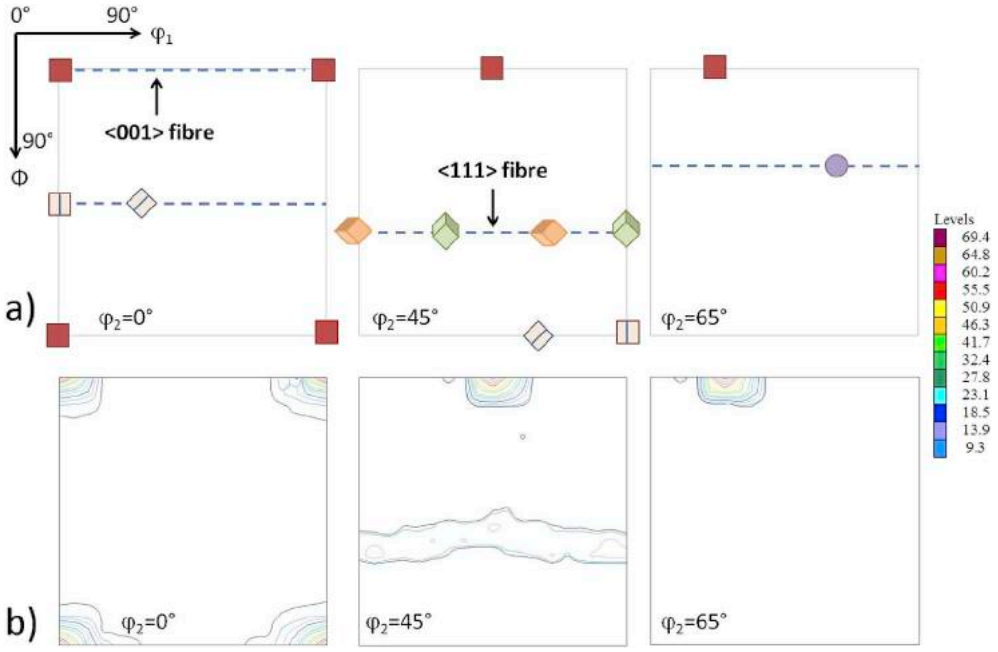

Fig. 1. a) ODFs at ϕ2 = 0, 45 and 65° for some ideal orientations and for b) CaR sample.

an austenitic phase [17]. Quantitative texture analysis indicates that the main texture component is {001} < 100 > − cube component, which volume fraction is 33%. In addition, the < 111 > fiber with local maxima corresponding to {111} < 1$\bar{1}$0 > and {111} < 11$\bar{2}$ > components were formed. Their volume fraction is 10 and 6%, respectively. In addition to the texture analysis, a microstructure characterization was performed, as shown in Fig. 2. The microstructure after CaR is severely refined (Fig. 2a). This fact is also confirmed by the diffraction pattern, which consists of segmented rings. The main microstructure features are elongated deformation bands locally divided into subgrains and deformation nanotwins. Texture components can be linked with characteristic microstructural features. Areas in the < 100 > orientation illustrate grains deformed by dislocation slip (Fig. 2b). The local maximum{111} < 11$\bar{2}$ > can be assigned to a pure shear texture [37,38]. The texture {111} < $\bar{1}$ $\bar{1}$2 > might be also attributed to deformation twins marked in Fig. 2c. The local maximum {111} < 1$\bar{1}$0 > is connected with the appearance of a lamellar-like nanostructure [39] also found after CaR as presented in Fig. 2d.

3.2. Thermal stability after CaR

To verify whether the 316LVM steel produced by CaR behaves like a typical nanostructural material during annealing, that is, whether it exhibits the hardening by annealing phenomenon, the samples after deformation were annealed for 10 min at a temperature range of from 400 °C to 900 °C. Microhardness measurements made after plastic deformation and annealing at the diameter of a given CaR sample are presented in Fig. 3. After CaR, the average value of microhardness was 425 Hv0.2 with a standard deviation of 28 Hv0.2. Annealing at 500 °C for 10 min led to the highest increase in microhardness, to a value of 465 Hv0.2 with a standard deviation of 23 Hv0.2. This result confirms the occurrence of the phenomenon of hardening by annealing. Further annealing did not contribute to a further increase in microhardness. After annealing at 900 °C, the microhardness declined to about 170 Hv0.2. The hardening by annealing phenomenon was also confirmed in the tensile tests performed on those samples annealed in a temperature range of from 400 to 700 °C, as shown in Fig. 4 as tensile tests better reflect changes in mechanical properties of bulk materials. After CaR, the ultimate tensile strength increased to a value of 1477 MPa, and the uniform and total elongation were 1.3% and 26%, respectively. After annealing at 500 °C, the ultimate tensile strength increased to a highest value of 1584 MPa, and the uniform and total elongation were 1.8% and 23.0%, respectively.

Table 2
Volume fraction of texture components and fibers after CaR.

Texture component	Volume fraction of the main texture components [%]
{001} < 100 >	33
{111} < 11$\bar{2}$ >	6
{111} < 1$\bar{1}$0 >	10
< 111 > fibre	16
< 001 > fibre	2
Background	*33*

Annealing under high hydrostatic pressure makes it possible to maintain quite high microhardness values in comparison with conventional annealing at the same temperature, as shown in Fig. 5. The microhardness of the CaR_6 GPa sample is like that of the sample annealed at 700 °C for 10 min. The microhardness of the CaR_2 GPa sample is comparable with that after annealing at approximately 750 °C for 10 min.

3.3. Texture analysis after CaR and high hydrostatic pressure annealing

A texture analysis was performed for CaR_0.1 MPa, CaR_2 GPa and CaR_6 GPa, as shown in Fig. 6 and Table 3.

In the case of CaR_0.1 MPa, the character of the texture components and fibers is similar to that for CaR, however there are no {111} < 1$\bar{1}$0 > and {111} < 11$\bar{2}$ > components. The {001} < 100 > texture component, which was predominant in CaR sample has undergone a significant sharpening in CaR_0.1 MPa and its volume fraction increased to 75%. One can also notice the same fibers as after deformation, < 111 > and < 001 > , which fractions are 7% and 12%, respectively. The low level of background denotes the formation of strongly oriented components in a significant volume. The sharp texture is a result of the presence of micron-sized grains of an inconsiderable misorientation in the analyzed plane.

CaR_2 GPa and CaR_6 GPa maintain the texture components characteristic for CaR. The cube component which was predominant in CaR and CaR_0.1 MPa has undergone a significant broadening and weakening in CaR_2 GPa and CaR_6 GPa samples and decreased to the volume fraction of 17% and 21%, respectively. Moreover, in samples annealed under high hydrostatic pressure {111} < 1$\bar{1}$0 > and {111} < 11$\bar{2}$ >

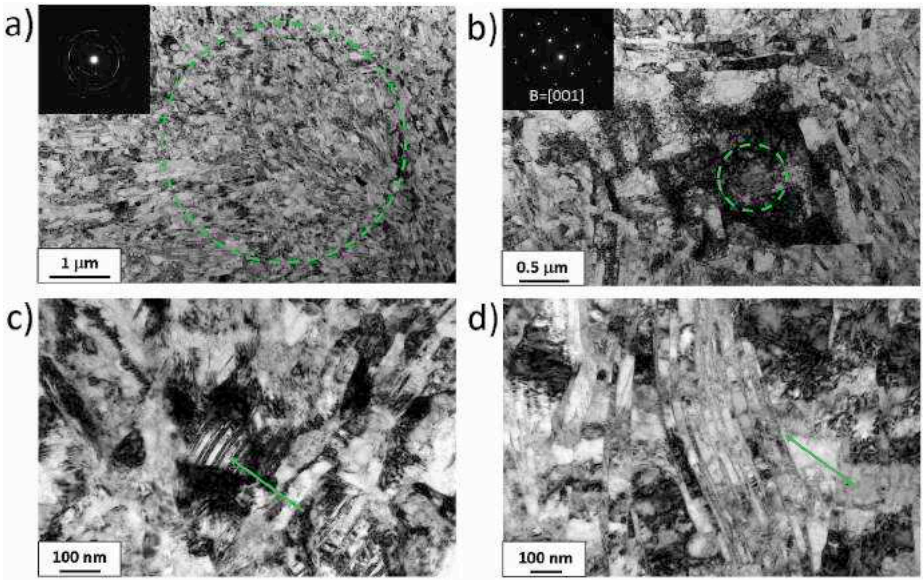

Fig. 2. Microstructures of the CaR sample – a cross-section a) a global view with a selected area diffraction pattern (SAED), b) areas in the < 001 > orientation with SAED from a region in the circle, c) nanotwins, shown by the arrow, d) lamellar-like nanostructure, shown by the arrow.

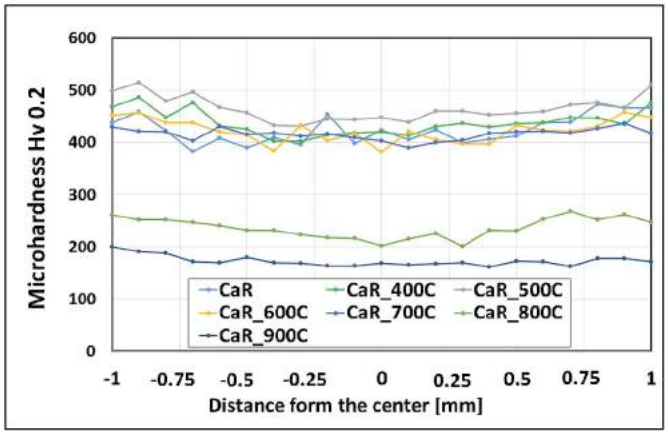

Fig.3. Microhardness measurements after CaR and annealing for 10 min at the diameter of CaR samples.

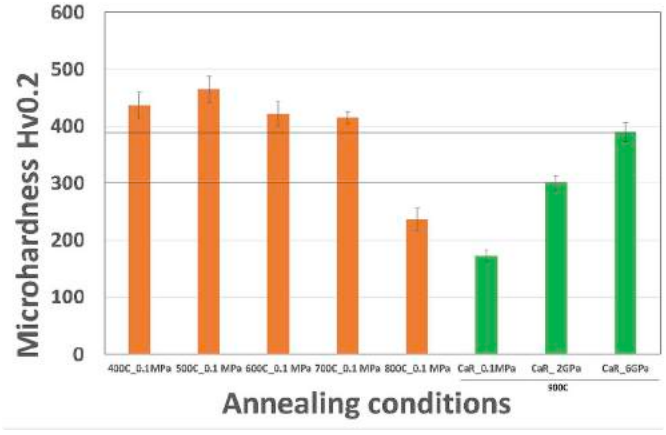

Fig. 5. Microhardness measurements after CaR and annealing under various annealing conditions.

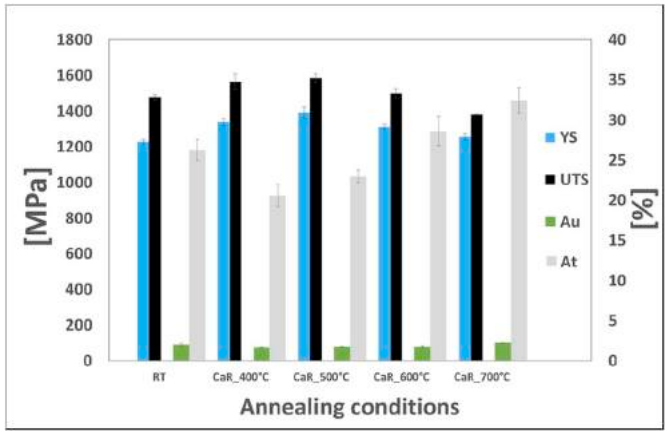

Fig.4. Room temperature mean values and standard deviation of ultimate tensile strength, (UTS); yield stress, (YS); total elongation, (At); uniform elongation (Au) of CaR samples.

texture components, recognized in the CaR sample are still present. In CaR_2 GPa, the volume fraction of $\{111\} < 11\bar{2} >$ texture components is 20%. In CaR_6 GPa the volume fraction of $\{111\} < 1\bar{1}0 >$ and $\{111\} < 11\bar{2} >$ texture components is 14 and 23%, respectively. The volume fraction of < 111 > and < 001 > fibers is the highest in CaR_2 GPa from all annealed samples and collectively constitutes 43%. The novelty in the texture and fiber components of the samples annealed under high hydrostatic pressure in comparison with the sample annealed under atmospheric pressure is the significant emergence of local maxima on the < 111 > fiber close to $\{111\} < \bar{1}\,\bar{1}2 >$ in a great volume fraction of approximately 20% in each sample.

3.4. Microstructure observations after high hydrostatic pressure annealing

The origin of texture components in each sample after annealing might be explained by the TEM investigations. In CaR_0.1 MPa, which is fully recrystallized, areas in the predominant < 100 > orientation represent recrystallized grains as shown in Fig. 7. The fact that after conventional annealing cube texture prevails was previously described in the literature [2]. In the CaR_2 GPa sample microstructure consists of both recrystallized and deformed regions (Fig. 8a). The diffraction taken directly from the recrystallized area shows that the ring pattern is highly segmented, which indicates a textured microstructure and that the signal comes mainly from the {100} planes. This analysis well-corresponds with the texture analysis, since the < 001 > fiber dominates after annealing

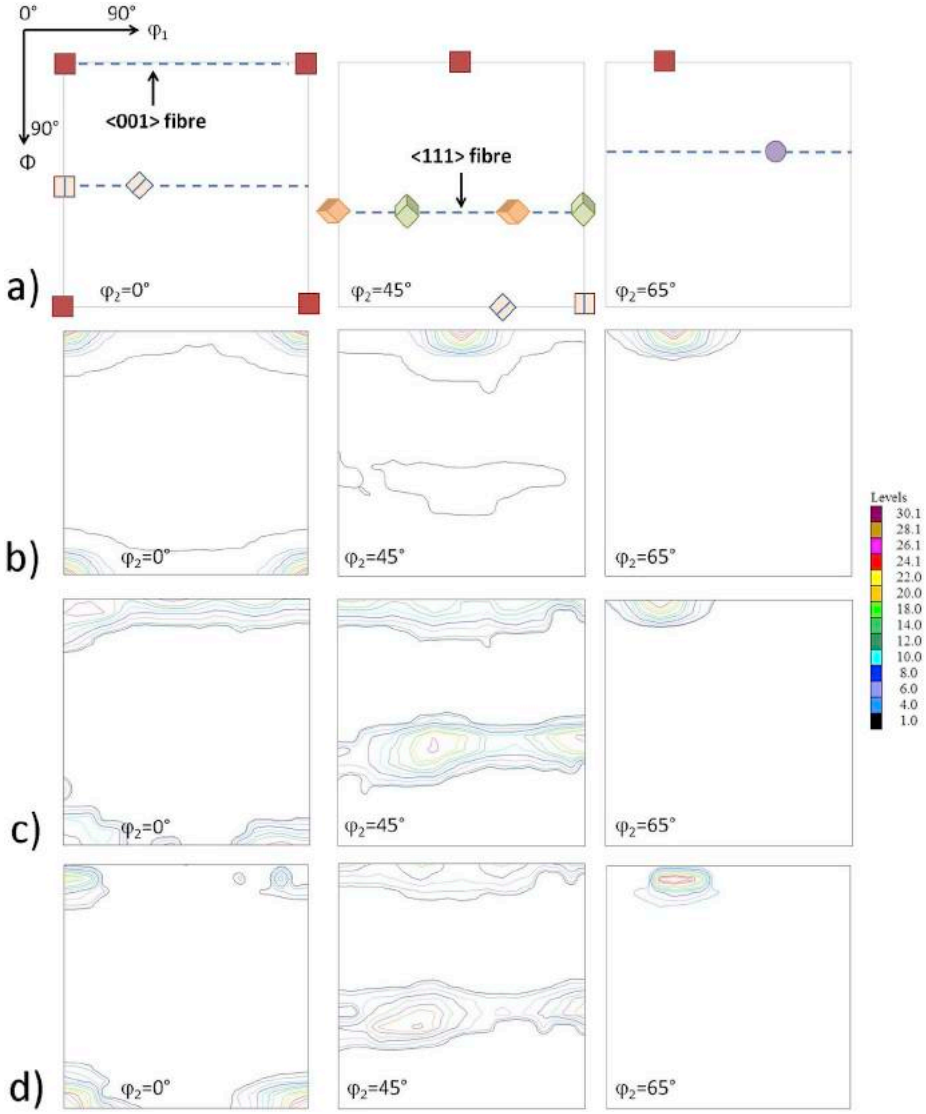

Fig. 6. a) ODFs at ϕ2 = 0, 45 and 65° for some ideal orientations b) CaR_0.1 MPa c) CaR_2 GPa, and d) CaR_6 GPa samples.

Table 3
Volume fraction of texture components and fibers after CaR and annealing.

Texture component	Volume fraction of the main texture components in the investigated materials [%]		
	CaR_0.1 MPa	CaR_2 GPa	CaR_6 GPa
{001} < 100 >	75	17	21
{111} < 11$\bar{2}$ >	0	20	23
{111} < 1$\bar{1}$0 >	0	0	14
< 111 > fibre	7	22	7
< 001 > fibre	12	21	0
Background	*6*	*20*	*35*

under 2 GPa. The detailed observations of the deformed areas reveal the presence of twins representing a {111} < $\bar{1}\,\bar{1}$2 > texture as shown in Fig. 8b. Deformation twins were created during CaR. It is highly probable that slight lattice rotations during annealing under high hydrostatic pressure might have enabled the higher volume fraction of {111} < $\bar{1}\,\bar{1}$2 > than after CaR. The fact that areas with twins are not recrystallized is in good agreement with previous finding about diffusivities of grain boundaries, which underline that twin boundaries, especially relaxed ones, show low diffusivity. Under high hydrostatic pressure, which retards diffusion, their mobility may be further suppressed. As a consequence, they remain as unrecrystallized areas.

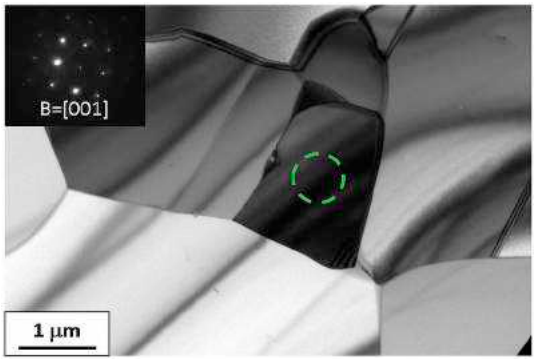

Fig. 7. Microstructure of the CaR_0.1 MPa sample with a SAED from an area indicated in the circle – a cross section.

In CaR_6 GPa, the microstructure is partially recrystallized (Fig. 9). The diffraction pattern shows that the strongest signal comes from {001} planes (Fig. 9a). The observation in the dark field reveals that this orientation is characteristic for nanosized grains (Fig. 9d and e). Twins representing {111} < $\bar{1}\,\bar{1}$2 > texture component are also visible as marked in Fig. 9b. Apart from twins one can distinguish a lamellar-like nanostructure (Fig. 9c). As earlier proved, this morphology is

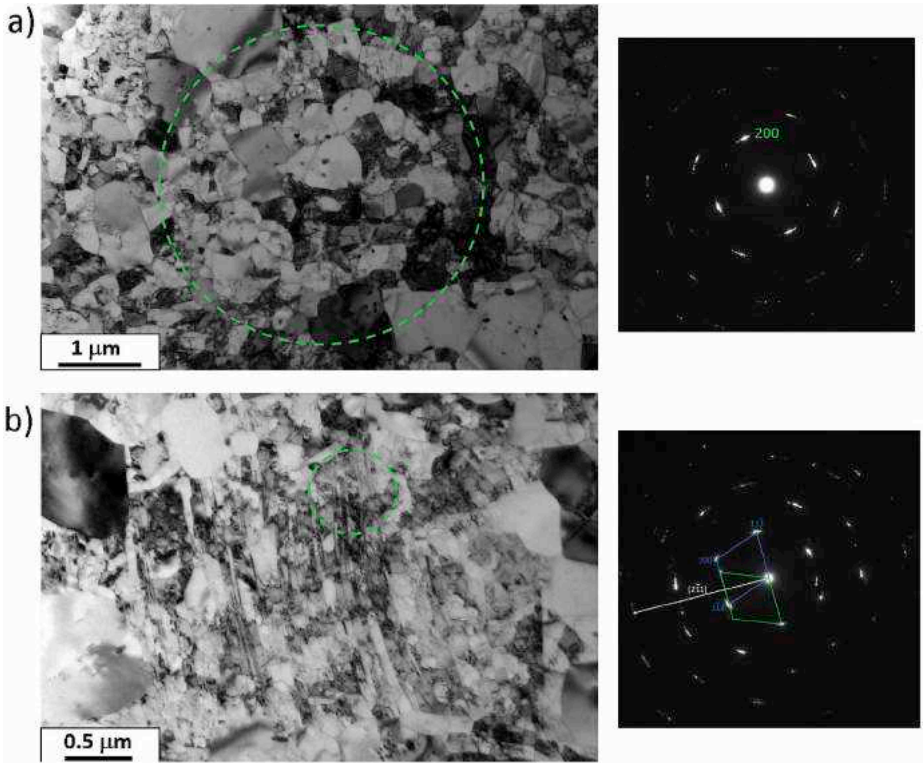

Fig. 8. Microstructures of the CaR_2 GPa sample – a cross section a) an area with recrystallized grains with a SAED from a region in the circle, b) a non-recrystallized area with SAED in the orientation [011] of the matrix and [$0\bar{1}\,\bar{1}$] of twins from an area in the circle.

characteristic for {111} < $1\bar{1}0$ > texture components.

The impact of annealing under a pressure of 0.1 MPa, 2 GPa and 6 GPa at 900 °C for 10 min on recrystallized grain size and shape has been previously explored [17]. The main conclusion that can be drawn is that the pressure retards recrystallization and grain growth. The grain sizes were approximately 4.3 μm, 0.42 μm and 0.087 μm for annealing pressures of 0.1 MPa, 2 GPa and 6 GPa, respectively.

Apart from grain growth, high hydrostatic pressure annealing also affects precipitate size and distribution. It should be noted that precipitates are present in the CaR-processed and annealed samples, as identified in Fig. 10 and Fig. 11. They precipitated at grain boundaries and inside grains. In the CaR_0.1 MPa and CaR_2 GPa, the precipitates are round, but in the CaR_6 GPa they are elongated and can mainly be found at triple-points. The pressure affected their size, and distribution, as summarized in Table 4. Firstly, the conclusion can be drawn that the increase in pressure causes the reduction in the precipitate size. In CaR_0.1 MPa, the average precipitate size is 195 nm, whereas it is four times smaller in CaR_2 GPa, and that size is further reduced to 12 nm when the pressure increased to 6 GPa. Secondly, the pressure has the impact on CV(d_2) parameter, which quantifies size diversity. This

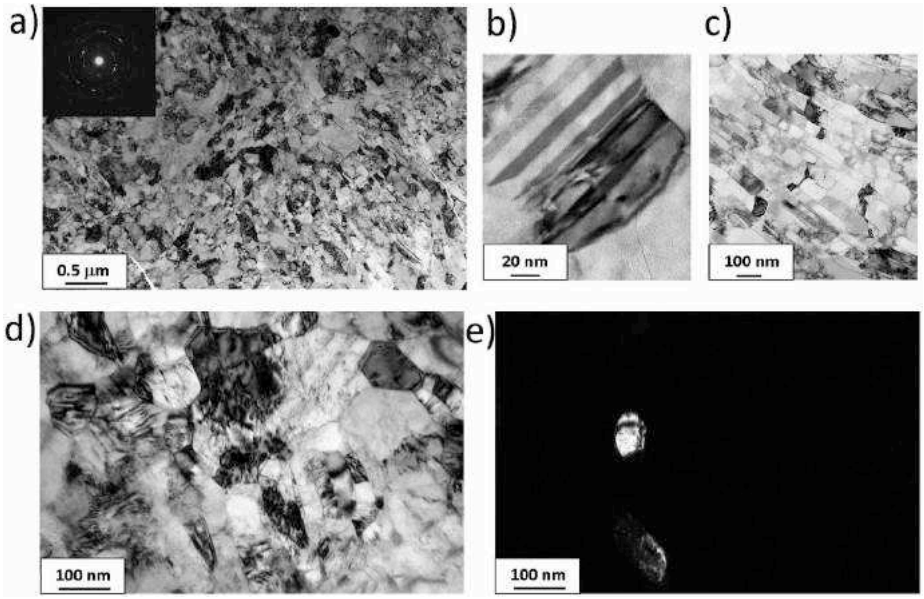

Fig. 9. Microstructures of the CaR_6 GPa sample – a cross-section a) a global view with a SAED from an area indicated in the circle, b) nanotwins, c) a lamellar-like nanostructure, nanograins observed in d) a bright, and e) dark field – the signal from (002) planes was selected.

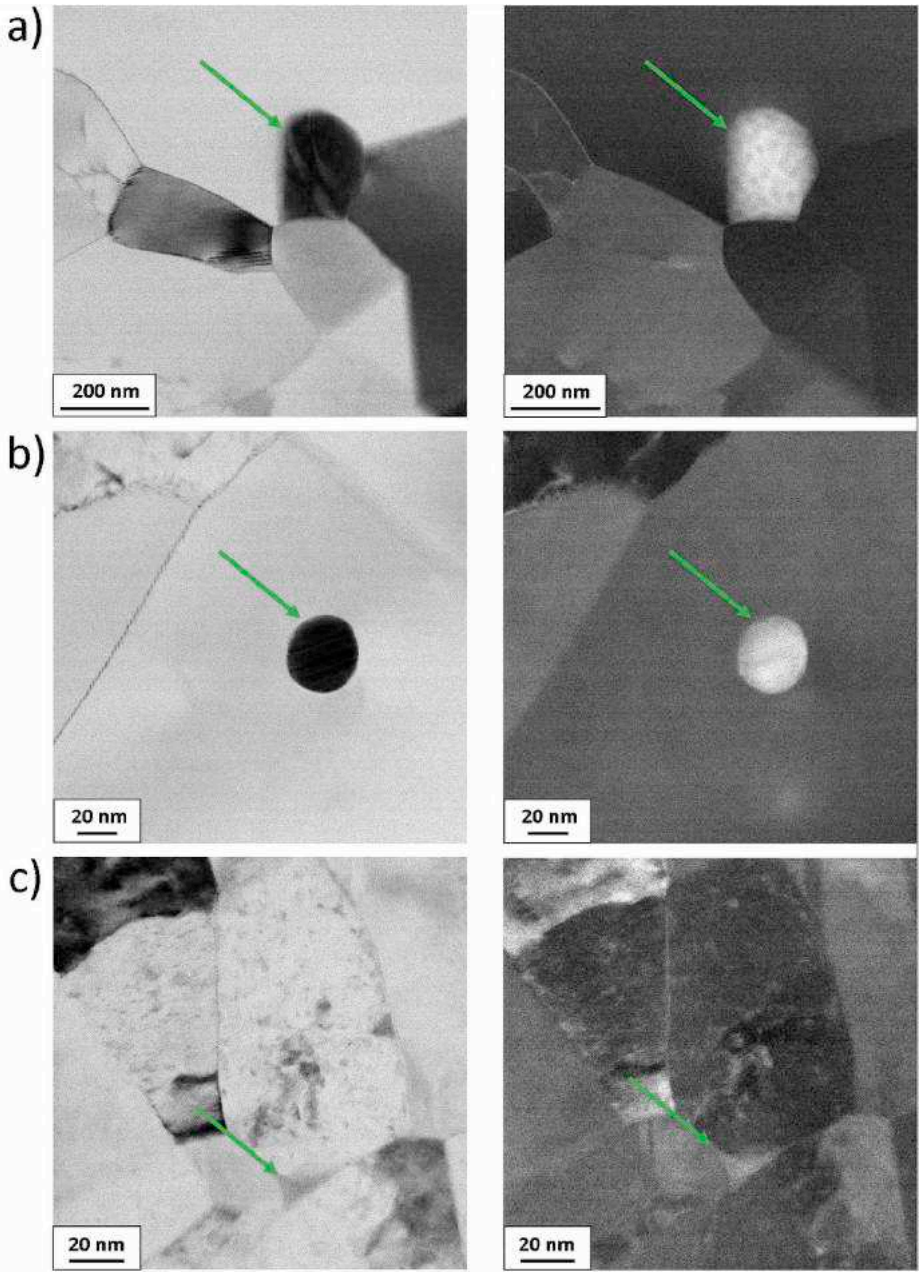

Fig. 10. Microstructures of a) CaR_0.1 MPa, b) CaR_2 GPa, c) CaR_6 GPa; exemplary CaR precipitates, indicated by green arrows in the BF-STEM and ZC-STEM modes. (For interpretation of the references to colour in this figure legend, the reader is referred to the Web version of this article.)

parameter has a tendency to increase slightly with increased pressure, from approximately 0.28 at a pressure of 0.1 MPa and 0.32 for 2 GPa to 0.46 for 6 GPa. Finally, it can be noted that the higher the pressure the more densely precipitates are distributed. The density of precipitate distribution, quantified by the value of Av, is the lowest at atmospheric pressure - 75.2 μm^2 - and the highest for 6 GPa - 0.14 μm^2. All annealing conditions lead to the comparable uniformity of spatial distribution of precipitates, which is expressed in the value of CV(Av), approximately 0.8 for all annealing conditions.

4. Discussion

4.1. Effect of CaR on microstructure, mechanical properties and texture in austenitic stainless steel

The microstructure after CaR consists of nanotwins and elongated bands, as described in detail in the authors' work [17]. The grain size of 1.3 μm in CaR steel reported elsewhere refers to low-carbon steel, not to austenitic stainless steel [18].

The mechanical properties after cold rolling depend on the degree of deformation, and it has been observed that, for 50% cold rolled austenitic stainless steel, the YS reached 990 MPa, and for 90% 1200 MPa [40]. Cold rolling performed to a high strain of 3 results in a high UTS of 1830 MPa, comparable to that obtained after SPD [15]. The mechanical properties obtained here, meaning a UTS of 1477 MPa and At of 26%, can be compared with those resulting after HE process of an austenitic stainless steel to a true strain of 1.4, UTS of 1470 MPa and At of 8% (sample geometry: a diameter of 2 mm and a gauge length of 18 mm) [41]. The quite remarkable At of 26% is higher than that after HE, and much higher than that for austenitic steel after HPT and conventional annealing at 450 °C, that is, a UTS of 1500 MPa and At of 10% (sample geometry: a cross section of 0.7 × 0.4 mm and a gauge length of 2.5 mm) [42]. This quite high total elongation can be attributed to the presence of nano-scale twins. Nanotwin boundaries are effective in

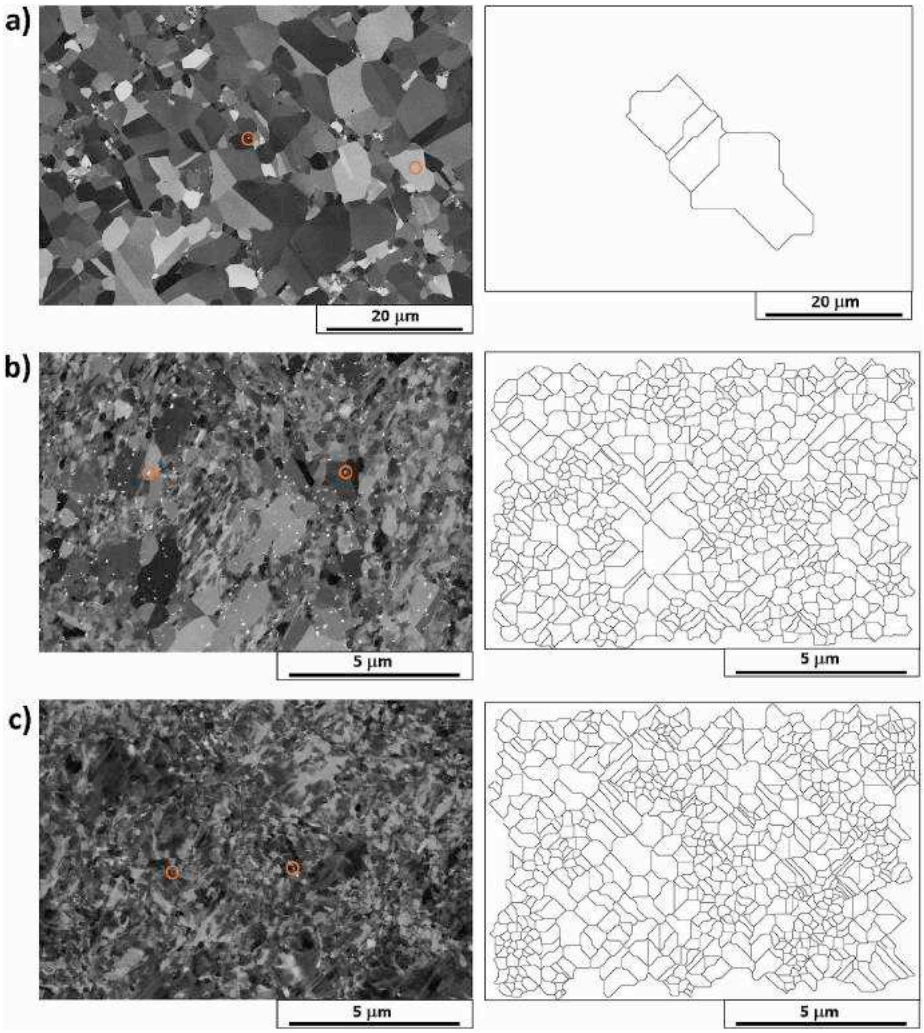

Fig. 11. Microstructures of CaR_0.1 MPa, b) CaR_2 GPa, c) CaR_6 GPa; exemplary precipitates, indicated in orange circles, are visible as bright dots in the BSE-SEM mode and corresponding area division around the precipitates – Voronoi tesselation

Table 4
Parameters of precipitate size, shape (d_{2av}, SD (d_2), CV(d_2)) and distribution (Av_{av}, SD(Av), CV(Av)) after annealing under 0.1 MPa, 2 GPa and 6 GPa.

	d_{2av} [nm]	SD (d_2) [nm]	CV(d_2)	Av_{av} [µm^2]	SD(Av) [µm^2]	CV(Av)
0.1 MPa	195	54	0.28	75.2	56	0.74
2 GPa	54	18	0.32	0.17	0.12	0.73
6 GPa	12	6	0.46	0.14	0.11	0.81

blocking dislocation motion, and at the same time act as slip planes that accommodate dislocations [43,44].

The texture after deformation mainly depends on the crystal structure of the metal, the deformation technique, and its magnitude. Textures of various materials after CaR are not well-ascertained. They have mainly been studied for dual-phase steels and magnesium alloys [45,46], which have different crystal structures from austenitic stainless steel. The texture of austenitic stainless steel after CaR has little in common with its texture after cold rolling. The typical rolling texture of AISI 300 austenitic steel is generally Brass $\{110\} < 112 >$, along with a scatter towards the $S\{123\} < 634 >$ and Goss $\{011\} < 100 >$ [5,46,47]. However, in this study, the main texture component is the cube component, whose volume fraction is 33%; there are also $< 111 >$ and $< 001 >$ fibers and local maxima on the $< 111 >$ fiber corresponding to $\{111\} < 1\bar{1}0 >$ and $\{111\} < 11\bar{2} >$ components. For this reason, this texture might be better compared with that after HE [41,48]. HE is a deformation technique resulting in rods whose main orientations in austenitic stainless steel are $< 111 >$ and $< 100 >$ [41,49].

4.2. Thermal stability and hardening by annealing phenomenon in CaR austenitic stainless steel

It is well-known that, during annealing, nanomaterials exhibit different behavior than their coarse-grained counterparts. It has been observed that the processes of recovery and recrystallization start in nanomaterials at lower temperatures than in their micrograined counterparts. This is due to a high volume fraction of grain boundaries, an enhanced atomic mobility of grain boundaries and a lower activation energy of grain boundary diffusion. In this work, the austenitic steel exhibited thermal stability up to 700 °C, which is the same as that of nanostructured austenitic stainless steels obtained by HPT and annealed for 10 min at various temperatures [50].

One peculiarity is the phenomenon known as “hardening by annealing”. It was firstly reported for a nanostructured aluminum produced by accumulative roll bonding (ARB) and subsequently annealed at 150 °C for 30 min [51]. It was suggested that annealing nanostructured materials at a relatively low temperature leads to the disappearance of free dislocations and dislocation sources without recrystallization or grain growth. This change in the dislocation density is responsible for the increase in strength and decrease in elongation. This phenomenon was further confirmed in an aluminium alloy [52]. The

issue of hardening by annealing was also raised in the case of nanograined austenitic steel. The reason for the phenomenon has been the subject of a number of publications [53,54]. One group of researchers suggested that the formation of Mo–Cr–Si rich grain boundary segregations in the steel led to a significant enhancement in yield stress after low-temperature annealing [53]. Another proposed the same explanation as earlier suggested for aluminium, underlying that solute segregation is not the origin of the phenomenon [54].

Other factors that may also be responsible for hardening by annealing in a CaR sample include a decreased dislocation density in grains that could have led to the annihilation of some dislocation sources and the creation of recrystallized nanograins, free of dislocations, as presented in Fig. 12. This latter factor well corresponds with the literature, since recrystallized nanograins form areas free of dislocation sources.

4.3. The impact of high hydrostatic pressure annealing on texture development

The recrystallization textures developed in cold-rolled austenitic steels have been the subject of extensive study. Most of that research has focused on the impact of strain, starting texture, and particularly annealing time and temperature, on the recrystallization texture [5,46]. It has been observed that, up to 700 °C, there are few changes in texture components in comparison with the texture developed during rolling. There is a significant change in the evolution of texture at 800 °C, when the Brass $\{110\} < 112 >$ and S $\{123\} < 634 >$ components disappear, mainly in favour of Goss $\{110\} < 100 >$, Cu $\{001\} < 100 >$ and BR $\{236\} < 385 >$ components. A further increase in temperature is responsible for the emergence of a small number of new components.

Little is known, apart the author's own work, about the impact of high hydrostatic pressure applied during annealing on recrystallization textures. It has been proved that high hydrostatic pressure annealing supports the emergence of other orientations than those formed during conventional annealing [17,28]. In the case of the high hydrostatic pressure annealing of austenitic steel deformed by HPT, an increased fraction of orientation $< 100 >$ appeared apart from the mainly $< 111 >$ found after conventional annealing under the same time and temperature conditions. In this work, it has been confirmed that high hydrostatic pressure annealing supports the appearance of other orientations ($\{111\} < 1\bar{1}0 >$, $\{111\} < 11\bar{2} >$) apart from those existing after conventional annealing ($\{001\} < 100 >, < 111 >, < 001 >$). However, texture components $\{111\} < 1\bar{1}0 >$, $\{111\} < 11\bar{2} >$ have been found in a CaR sample. This seems to be an interesting issue, since it leads to the conclusion that pressure retards the evolution of texture, meaning that, at a higher annealing pressure, the texture becomes more similar to that obtained directly after CaR. It should be also underlined that the moderate pressure of 2 GPa supports the axial texture as $< 111 >$ and $< 001 >$ fibers represent together 43% of texture components.

4.4. The impact of high hydrostatic pressure annealing on precipitate rate and distribution

It has been proved that, in the case of austenitic stainless steel deformed by HPT and high hydrostatic pressure annealed at 900 °C under 2 and 6 GPa, the high hydrostatic pressure made the growth of carbides difficult but facilitated their precipitation and, as a consequence, contributed to an increase in their number with an increase in applied pressure [17]. The same tendency was also observed in this work for austenitic stainless steel deformed by CaR and annealed under the same annealing conditions. However, there are some differences, which derive from the different deformation techniques that led to the creation of the different microstructures. Firstly, in the CaR_6 GPa sample, the average precipitate size was smaller - 12 nm - than in the HPT sample annealed under 6 GPa, where it was 20 nm. Moreover, after annealing at 2 and 6 GPa, the precipitates were more densely distributed in the austenitic stainless steel deformed by CaR than HPT. This phenomenon is represented in the values of Av_{av}, which are, for the CaR-deformed sample and the sample annealed under 2 and 6 GPa, 0.17 and 0.14 μm^2, respectively, and for the HPT-processed sample 3.95 and 0.28, respectively. It must be underlined that the precipitate rate during annealing under high hydrostatic pressure is much more accelerated for the CaR-processed sample and the HPT-process in comparison with annealing at the atmospheric pressure since, in the case of the CaR-processed sample at atmospheric pressure, precipitates are rarely noticed.

As mentioned earlier, these differences must come from various deformation techniques that affect the microstructure and vacancy concentration. The higher the deformation, the higher the concentration of vacancies, as investigated in Refs. [55–57]. Vacancies facilitate the movement of dislocations during annealing. During high hydrostatic pressure annealing, their movement is slowed down, as demonstrated in Ref. [20]. However, if there is a high concentration of vacancies, they will still climb, as in HPT-processed steel annealed at 2 and 6 GPa, where no dislocations were present in the recrystallized grains. If the vacancy concentration is much lower due to a lower deformation degree, as in the case of CaR, dislocations will exist at 900 °C during annealing at 2 and 6 GPa. As a result, these dislocations induce a segregation of solute atoms and contribute to the creation of precipitates.

4.5. Possible application of obtained results

Obtained in the present study nanostructured austenitic stainless steel of the ultimate tensile strength of 1477 MPa and after additional annealing of almost 1600 MPa is a promising result from the perspective of future applications especially when one realises that the commercially available austenitic stainless steel by Sandvic reaches the maximum ultimate tensile strength of 1400 MPa. One must underline that calliber rolling is an easy technique to apply in practise in comparison with much more energy consuming HE and HPT, which also result with high ultimate strength of austenitic stainless steels [41,42]. In our study high ultimate tensile strength is combined with satisfactory elongation (sample geometry: a cross-section of 0.4 × 0.3 mm and a gauge length of 1 mm) of above 20%, whereas other techniques like HE (sample geometry: a diameter of 2 mm and a gauge length of 18 mm) or HPT (sample geometry: a cross-section of 0.7x0.4mmand a gauge length of 2.5 mm) assure total elongation far beyond 10%. This provides opportunities for manufacturing fixing elements in various

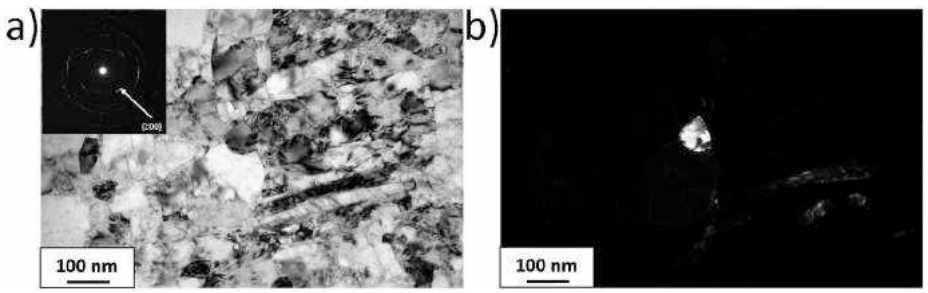

Fig. 12. Nanograins observed in a CaR sample after annealing at 500 °C for 10 min in a) a bright, and b) dark field – the signal from (200) planes was selected.

industrial branches such as medicine or marine [48]. Another issue important from the industrial point of view is the fact that the high pressure annealing may enable optimizing microstructure features for selective goals. It is especially important from the formability point of view since the high pressure annealing gives the opportunity to tailor the crystallographic texture. Moreover, the fact that high pressure annealing promotes the nucleation of precipitates might be wider applied for precipitate strengthened alloys.

5. Conclusions

1. After caliber rolling to a true strain of 3.4, 316LVM austenitic stainless steel reaches an ultimate tensile stress of 1470 MPa and a total elongation of 26%. It is thermally stable up to 700 °C and exhibits the "hardening by annealing effect", well visible after annealing at 500 °C. The main texture components directly after deformation are cube $\{001\} < 100 >$, with a volume fraction of 33% and $< 111 >$ and $< 001 >$ fibers.
2. Annealing austenitic steel under high hydrostatic pressure after caliber rolling:
   a) supports the appearance of other texture components, $\{111\} < 11\bar{2} >$, apart from those existing after conventional annealing such as $\{001\} < 100 >$, $< 111 >$, $< 001 >$.
   b) promotes the nucleation of precipitates and hinders their growth.

Data availability

The raw/processed data required to reproduce these findings cannot be shared at this time due to technical or time limitations.

Acknowledgements

This work was supported by Polish National Science Center project SONATA No. UMO-2014/15/D/ST8/00532.

References

[1] B.R. Kumar, S. Sharma, B.P. Kashyap, N. Prabhu, Ultrafine-grained microstructure tailoring in austenitic stainless steel for enhanced plasticity, Mater. Des. 68 (2015) 63–71 https://doi.org/10.1016/j.matdes.2014.12.014.
[2] R.D. Doherty, D.A. Hughes, F.J. Humphreys, J.J. Jonas, D. Juul Jensen, M.E. Kassner, W.E. King, T.R. McNelley, H.J. McQueen, A.D. Rollett, Current issues in recrystallization: a review, Mater. Sci. Eng. A 238 (1997) 219–274, https://doi.org/10.1016/S0921-5093(97)00424-3.
[3] A. Belyakov, A. Kipelova, M. Odnobokova, I. Shakhova, R. Kaibyshev, Development of ultrafine-grained austenitic stainless steels by large strain deformation and annealing, Mater. Sci. Forum 783 (2014) 651–656 https://doi.org/10.4028/www.scientific.net/MSF.783-786.651.
[4] C. Donadille, R. Valle, P. Dervin, R. Penelle, Development of texture and microstructure during cold-rolling and annealing of FCC alloys: example of an austenitic stainless steel, Acta Metall. 37 (1989) 1547–1571 https://doi.org/10.1016/0001-6160(89)90123-5.
[5] S.G. Chowdhury, P. Sahu, B. Mahato, P.K. De, Evolution of recrystallization texture in AISI300 series austenitic stainless steels after cold rolling to large strain, in: A. Haldar, S. Suwas, D. Bhattacharjee (Eds.), Microstructure and Texture in Steels, Springer, London, 2009, pp. 361–378.
[6] M. Mineur, P. Villechaise, J. Mendez, Influence of the crystalline texture on the fatigue behavior of a 316L austenitic stainless steel, Mater. Sci. Eng. A 286 (2000) 257–268 https://doi.org/10.1016/S0921-5093(00)00804-2.
[7] M.R. Bache, W.J. Evans, Impact of texture on mechanical properties in an advanced titanium alloy, Mater. Sci. Eng. A 319 (2001) 409–414 https://doi.org/10.1016/S0921-5093(00)02034-7.
[8] P.K.C. Venkatsurya, R.D.K. Misra, M.D. Mulholland, M. Manohar, J.E. Hartmann, Effect of microstructure on the mechanical properties and texture in high strength 560 MPa linepipe steels, Mater. Sci. Eng. A 575 (2013) 5–14 https://doi.org/10.1016/j.msea.2013.03.040.
[9] M. Eskandari, A. Zarei-Hanzaki, H.R. Abedi, An investigation into the room temperature mechanical properties of nanocrystalline austenitic stainless steels, Mater. Des. 45 (2013) 674–681 https://doi.org/10.1016/j.matdes.2012.08.042.
[10] F.K. Yan, G.Z. Liu, N.R. Tao, K. Lu, Strength and ductility of 316L austenitic stainless steel strengthened by nano-scale twin bundles, Acta Mater. 60 (2012) 1059–1071 https://doi.org/10.1016/j.actamat.2011.11.009.
[11] M. El-Tahawy, P.H.R. Pereira, Y. Huang, H. Park, H. Choe, T.G. Langdon, J. Gubicza, Exceptionally high strength and good ductility in an ultrafine-grained 316L steel processed by severe plastic deformation and subsequent annealing, Mater. Lett. 214 (2018) 240–242 https://doi.org/10.1016/j.matlet.2017.12.040.
[12] A.T. Krawczynska, T. Brynk, S. Gierlotka, E. Grzanka, S. Stelmakh, B. Palosz, M. Lewandowska, K.J. Kurzydlowski, Mechanical properties of nanostructured 316LVM stainless steel annealed under pressure, Mech. Mater. 67 (2013) 25 https://doi.org/10.1016/j.mechmat.2013.07.017.
[13] X. Guo, Y. Deng, Y. Zhang, J. Zhang, X. Zhang, Microstructure and microtexture evolution of shear bands in Al–Cu single crystal during asymmetric rolling, Mater. Char. 128 (2017) 37–42 https://doi.org/10.1016/j.matchar.2017.03.022.
[14] S. Ucuncuoglu, A. Ekerim, G.O. Secgin, O. Duygulu, Effect of asymmetric rolling process on the microstructure, mechanical properties and texture of AZ31 magnesium alloys sheets produced by twin roll casting technique, J. Magnes. Alloy. 2 (2014) 92–98 https://doi.org/10.1016/j.jma.2014.02.001.
[15] J. Huang, Y.T. Zhu, D.J. Alexander, X. Liao, T.C. Lowe, R.J. Asaro, Development of repetitive corrugation and straightening, Mater. Sci. Eng. A 371 (2004) 35–39 https://doi:10.1016/S0921-5093(03)00114-X.
[16] M. Tikhonova, I. Shakhova, R. Kaibyshev, A. Belyakov, Effect of SPD processing technique on grain refinement and properties of an austenitic stainless steel, Mater. Sci. Forum 879 (2016) 1957–1962 https://doi:10.4028/www.scientific.net/MSF.879.1957.
[17] Z. Yanushkevich, S.V. Dobatkin, A. Belyakov, R. Kaibyshev, Hall-Petch relationship for austenitic stainless steels processed by large strain warm rolling, Acta Mater. 136 (2017) 39–48 https://doi:10.1016/j.actamat.2017.06.060.
[18] A.T. Krawczynska, S. Gierlotka, P. Suchecki, D. Setman, B. Adamczyk-Cieslak, M. Lewandowska, M. Zehetbauer, Recrystallization and grain growth of a nano/ultrafine structured austenitic stainless steel during annealing under high hydrostatic pressure, J. Mater. Sci. 53 (2018) 11823–11836 https://doi:10.1007/s10853-018-2459-1.
[19] T. Lee, Ch H. Park, S.-Y. Lee, I.-H. Son, D.-L. Lee, Ch S. Lee, Mechanisms of tensile improvement in caliber-rolled high-carbon steel, Met. Mater. Int. 18 (2012) 391–396 https://doi: 10.1007/s12540-012-3002-6.
[20] J.E. Hillard, J.M. Lommel, J.B. Hudson, D.F. Stein, J.D. Livingston, Effect of annealing under high pressure on dislocations in lithum fluoride, aluminium, copper and iron, Acta Metall. 9 (1961) 787–794 https://doi.org/10.1016/0001-6160(61)90108-0.
[21] L.E. Tanner, S.V. Radcliffe, Effect of hydrostatic pressure on the kinetics of recrystallization in high purity copper, Acta Metall. 10 (1962) 1161–1169 https://doi.org/10.1016/0001-6160(62)90169-4.
[22] W. Lojkowski, D.A. Molodov, G. Gottstein, L.S. Shvidlerman, The mechanism of grain boundary migration in aluminium bicrystals, Mater. Sci. Forum 207–209 (1996) 537–540 https://doi.org/10.4028/www.scientific.net/MSF.207-209.537.
[23] L.S. Shvindlerman, U. Czubayko, G. Gottstein, D.A. Molodov, High pressure effect on grain boundary migration and mechanism of grain boundary migration, Mater. Sci. Forum (1996) 45–54 204–206 https://doi.org/10.1063/1.46492.
[24] A.F. Syrenko, G.P. Klinishev, V.T. Khôi, Recrystallization of copper under hydrostatic pressure up to 15 kbar, J. Mater. Sci. 8 (1973) 765–769 https://doi.org/10.1007/BF00553726.
[25] W. Kühlein, H.P. Stüwe, The influence of high hydrostatic pressure on recrystallization of α-brass, Acta Metall. 36 (1988) 3055–3059 https://doi.org/10.1016/0001-6160(88)90188-5.
[26] W. Lojkowski, On the effect of high pressures on the mobility of atoms in grain boundaries, J. Phys.-Paris 49 (1988) 545–549 https://doi.org/10.1051/jphyscol:1988566.
[27] V. Sursaeva, S. Protasova, W. Lojkowski, J. Jun, Microstructure evolution during normal grain growth under high pressure in 2-D aluminium foils, Textures Microstruct. 32 (1999) 175–185 https://doi.org/10.1155/TSM.32.175.
[28] A.T. Krawczynska, S. Gierlotka, P. Suchecki, D. Setman, B. Adamczyk-Cieslak, M. Gloc, W. Chrominski, M. Lewandowska, M. Zehetbauer, Phenomena occurring in nanostructured stainless steel 316LVM during annealing under high hydrostatic pressure, Adv. Eng. Mater. 21 (2019) 1800101 https://doi.org/10.1002/adem.201800101.
[29] T. Inoue, F. Yin, Y. Kimura, Strain distribution and microstructural evolution in multi-pass warm caliber rolling, Mater. Sci. Eng. A 466 (2007) 114–122, https://doi.org/10.1016/j.msea.2007.02.098.
[30] T. Krzysztof, H. Garbacz, Manufacturing of nanostructured titanium Grade 2 using caliber rolling, Mater. Sci. Eng. A 739 (2019) 277–288 https://doi.org/10.1016/j.msea.2018.10.011.
[31] L.G. Khvostantsev, A verkh-niz (up-down) toroid device for generation of high pressure, High. Temp. - High. Press. 16 (1984) 165–169.
[32] L.G. Khvostantsev, V.N. Slesarev, V.V. Brazhkin, Toroid type high-pressure device: history and prospects, High Press. Res. 24 (2004) 371–383 https://doi.org/10.1080/08957950412331298761.
[33] L.G. Schulz, A direct method of determining preferred orientation of a flat reflection sample using a Geiger Counter X-ray spectrometer, J. Appl. Phys. 20 (1997) 1030–1033 https://doi.org/10.1063/1.1698268.
[34] Labotex, http://www.labosoft.com.pl.
[35] T. Wejrzanowski, W. Spychalski, K. Rozniatowski, K. Kurzydłowski, Image based analysis of complex microstructures of engineering materials, Int. J. Appl. Math. Comput. Sci. 18 (2008) 33–39 https://doi.org/10.2478/v10006-008-0003-1.
[36] T. Wejrzanowski, M. Lewandowska, K.J. Kurzydlowski, Stereology of nano-materials, Image Anal. Stereol. 29 (2010) 1–12 https://doi.org/10.5566/ias.v29.p1-12.
[37] A. Khalajhedayati, T.J. Rupert, Disruption of thermally-stable nanoscale grain structures by strain localization, Sci. Rep. 5 (2015) 10663 https://doi.org/10.1038/srep10663.
[38] H.T. Jeong, S.D. Park, T.K. Ha, Evolution of shear texture according to shear strain ratio in rolled fcc metal sheets, Met. Mater. Int. 12 (2006) 21–26 https://doi.org/

10.1007/BF03027518.
[39] A. Tripathi, S.V.S.N. Murty, P.R. Narayanan, Microstructure and texture evolution in AZ31 magnesium alloy during caliber rolling at different temperatures, J. Magnes. Alloy 5 (2017) 340–347 https://doi.org/10.1016/j.jma.2017.07.001.
[40] B.R. Kumar, Influence of crystallographic textures on tensile properties of 316L austenitic stainless steel, J. Mater. Sci. 45 (2010) 2598–2605 https://doi.org/10.1007/s10853-010-4233-x.
[41] A.T. Krawczynska, W. Chrominski, E. Ura-Binczyk, M. Kulczyk, M. Lewandowska, Mechanical properties and corrosion resistance of ultrafine-grained austenitic stainless steel processed by hydrostatic extrusion, Mater. Des. 136 (2017) 34–44 https://doi.org/10.1016/j.matdes.2017.09.050.
[42] A. Vorhauer, S. Kleber, R. Pippan, Influence of processing temperature on microstructural and mechanical properties of high-alloyed single-phase steels subjected to severe plastic deformation, Mater. Sci. Eng. A 410–411 (2005) 281–284 https://doi.org/10.1016/j.msea.2005.08.119.
[43] W.S. Zhao, N. R Tao, J.Y. Guo, Q.H. Lu, K. Lu, High density nano-scale twins in Cu induced by dynamic plastic deformation, Scr. Mater. 53 (2005) 745–749 https://doi.org/10.1016/j.scriptamat.2005.05.022.
[44] M. Dao, L. Lu, Y.F. Shen, S. Suresh, Strength, strain-rate sensitivity and ductility of copper with nanoscale twins, Acta Mater. 54 (2006) 5421–5432 https://doi.org/10.1016/j.actamat.2006.06.062.
[45] X.J. Shen, S. Tang, Y.J. Wu, X.L. Yang, J. Chen, Z.Y. Liu, R.D.K. Misra, G.D. Wang, Evolution of microstructure and crystallographic texture of microalloyed steel during warm rolling in dual phase region and their influence on mechanical properties, Mater. Sci. Eng. A 685 (2017) 194–204, https://doi.org/10.1016/j.msea.2016.12.108.
[46] A.F. Padilha, R.L. Plaut, P.R. Rios, Annealing of cold-worked austenitic stainless steels, ISIJ Int. 43 (2003) 135–143 https://doi.org/10.2355/isijinternational.43.135.
[47] M. Odnobokova, A. Belyakov, R. Kaibyshev, Grain refinement and stengthening of austenitic stainless steel during large strain cold rolling, Phylos. Mag. 99 (2018) 531–556 https://doi.org/10.1080/14786435.2018.1546961.
[48] W. Pachla, J. Skiba, M. Kulczyk, S. Przybysz, M. Przybysz, M. Wróblewska, Nanostructurization of 316L type austenitic stainless steels by hydrostatic extrusion, Mater. Sci. Eng. A 615 (2014) 116–127, https://doi.org/10.1016/j.msea.2014.07.069.
[49] S. Gierlotka, E. Grzanka, A. Krawczynska, S. Stelmakh, B. Palosz, M. Lewandowska, C. Lathe, K.J. Kurzydlowski, Strain relaxation and grain growth in 316LVM stainless steel annealed under pressure, Z. Kristallogr. Proc. 1 (2011) 281–286.
[50] A. Etienne, B. Radiguet, C. Genevois, J.M. Le Breton, R. Valiev, P. Pareige, Thermal stability of ultrafine-grained austenitic stainless steels, Mater. Sci. Eng. A 527 (2010) 5805–5810 https://doi.org/10.1016/j.msea.2010.05.049.
[51] X. Huang, N. Hansen, N. Tsuji, Hardening by annealing and softening by deformation in nanostructured metals, Science 312 (2006) 249–251 https://doi.org/10.1126/science.1124268.
[52] D. Terada, H. Houda, N. Tsuji, Effect on "hardening by annealing and softening by deformation" phenomena in ultrafine-grained aluminium, J. Mater. Sci. 43 (2008) 7331–7337 https://doi.org/10.1007/s10853-008-2809-5.
[53] M.M. Abramova, N.A. Enikeev, R.Z. Valiev, A. Etienne, B. Radiguet, Y. Ivanisenko, X. Sauvage, Grain boundary segregation induced strengthening of an ultrafine-grained austenitic stainless steel, Mater. Lett. 136 (2014) 349–352 https://doi.org/10.1016/j.matlet.2014.07.188.
[54] O. Renk, A. Hohenwarter, K. Eder, K.S. Kormout, J.M. Cairney, R. Pippan, Increasing the strength of nanocrystalline steels by annealing: is segregation necessary? Scr. Mater. 95 (2015) 27–30 https://doi.org/10.1016/j.scriptamat.2014.09.023.
[55] D. Setman, E. Schafler, E. Korznikova, M.J. Zehetbauer, The presence and importance of vacancy type defects in SPD nanometals, Mater. Sci. Eng. A 493 (2008) 116–122 https://doi.org/10.1016/j.msea.2007.06.093.
[56] M.J. Zehetbauer, G. Steiner, E. Schafler, A. Korznikov, E. Korznikova, Deformation induced vacancies in SPD Cu, measurements & modelling, Mater. Sci. Forum 503–504 (2006) 57–64 https://doi.org/10.4028/www.scientific.net/MSF.503-504.57.
[57] M. El-Tahawy, Y. Huang, T. Um, H. Choe, J.L. Lábár, T.G. Langdon, J. Gubicza, Stored energy in ultrafine-grained 316L stainless steel processed by high-pressure torsion, J. Mater. Res. Technol. 6 (2017) 339 https://doi.org/10.1016/j.jmrt.2017.05.001.

Materials Science & Engineering A 808 (2021) 140913

Contents lists available at ScienceDirect

Materials Science & Engineering A

journal homepage: http://www.elsevier.com/locate/msea

The impact of the stacking fault energy of nanostructured metals on phenomena during annealing at the high hydrostatic pressure

Agnieszka Teresa Krawczynska [a,*], Michael Kerber [b], Przemyslaw Suchecki [a], Barbara Romelczyk-Baishya [a], Malgorzata Lewandowska [a], Daria Setman [b]

[a] Warsaw University of Technology, Faculty of Materials Science and Engineering, Woloska 141, 02-507, Warsaw, Poland
[b] University of Vienna, Faculty of Physics, Boltzmanngasse 5, A, 1090, Vienna, Austria

ARTICLE INFO

Keywords:
Stacking fault energy
Nanomaterials
Microstructure
Severe plastic deformation
Annealing

ABSTRACT

The present study investigates the impact of stacking fault energy on the microstructure evolution and mechanical properties of nanostructured metals that differ in stacking fault energy, annealed under high hydrostatic and atmospheric pressure. Ag and Ni were selected as materials of low and high stacking fault energy, respectively. To this end, nanostructured metals were obtained by high pressure torsion and subsequently annealed by high hydrostatic pressure annealing, performed under 2 GPa at 0.4 homologous temperature for 1h. For comparison, similar experiments at the same temperature and time were performed under atmospheric pressure. After deformation and annealing, the microstructures were examined using transmission and scanning electron microscopy, and further analysed in terms of grain size, coefficient of grain size variation, and twinning frequency. The stored energy and peak temperatures were measured by differential scanning calorimetry. The mechanical properties were evaluated from microhardness measurements and tensile tests. It is demonstrated that the pressure applied during annealing leads to a more profound retardation of microstructure evolution in the low stacking fault energy material, mainly due to a higher deformation nanotwin density. The twinning deformation mechanism generates a higher dislocation density and a lower grain size than those achieved by dislocation slip.

1. Introduction

When applied to metallic materials, severe plastic deformation (SPD) results in grain size reduction down to the nanoscale [1–4]. The grain refinement is achieved by the activation of deformation mechanisms such as dislocation glide and/or deformation twinning. One of the essential parameters that has an impact on the deformation mechanisms and, as a consequence, on the nanostructure created during deformation, is stacking fault energy (SFE). In principle, in closed-packed structures, the SFE determines the extent of dislocation dissociation. In materials with a high SFE, the separation between two partial dislocations is negligible, and so cross-slip prevails as a deformation mechanism. A decrease in SFE leads to a change in deformation behaviour such that deformation twinning starts to play a crucial role. As a result, the deformation mechanism has a profound impact on: (i) the efficiency of grain refinement, (ii) microstructural homogeneity, and (iii) strength-ductility synergy after SPD [5]. (I) The grain refinement mechanism through nanotwin fragmentation enables greater grain refinement than deformation by slip. This was confirmed in previous studies, e.g. on Cu (SFE = 78 mJm^{-2}) and Cu–Zn (SFE = 35 mJm^{-2}) deformed by high pressure torsion (HPT) [6]. A decrease in SFE due to the addition of Zn atoms caused a reduction in grain size from 75 to 25 nm. (II) There is no simple relation between nanostructure homogeneity and the deformation mechanism. Experiments show that homogenous nanostructures are easily achieved for materials of both low and high SFE, while in medium SFE materials there is competition between deformation mechanisms that results in higher microstructure non-homogeneity [7]. (III) Nanotwins created in low-SFE materials play a significant role in achieving a satisfactory strength-ductility balance because they act as strengthening elements. As a consequence, deformation nano-twinning may increase uniform elongation, as proved in experiments on HPT-processed Cu and Cu-8% at. Al (SFE = 8 mJm^{-2}) alloys, where the alloy showed a 1% higher uniform elongation [8]. However, the suggestion that with a decrease in SFE the

* Corresponding author.
E-mail addresses: agnieszka.krawczynska@pw.edu.pl (A.T. Krawczynska), michael.kerber@univie.ac.at (M. Kerber), przemyslaw.suchecki@gmail.com (P. Suchecki), bromelczyk@gmail.com (B. Romelczyk-Baishya), malgorzata.lewandowska@pw.edu.pl (M. Lewandowska), daria.setman@univie.ac.at (D. Setman).

https://doi.org/10.1016/j.msea.2021.140913
Received 10 November 2020; Received in revised form 2 February 2021; Accepted 5 February 2021
Available online 13 February 2021

strength-plasticity balance is improved is a simplification, since it has been proved that there exists an optimal SFE below which uniform elongation decreases. The reverse behaviour below a certain SFE is due to the small grain size achieved during deformation, which makes the storage of dislocations during subsequent tensile tests impossible [9].

Apart from having a significant impact on deformation mechanisms, SFE is also an essential parameter influencing nanostructure evolution during annealing and nanostructure thermal stability. In micrograined materials, the role of SFE has been well described [10]. In high SFE micrograined materials it is mainly recovery that is observed, while in low SFE materials recovery is limited due to dissociated dislocations, and it is mainly nucleation and recrystallization that occur. This issue is definitely much more complex in nanostructured materials. A general model has been proposed for nanostructure evolution during annealing [11,12]. According to this model, firstly, the recovery of non-equilibrium grain boundaries is to be expected. Here, recovery should be understood as a partial annihilation of defects at grain boundaries; it is followed by a migration of grain boundaries that may lead to abnormal grain growth. In the end, there is a normal grain growth. This model suggests that, even in low SFE nanostructured materials, recovery should occur rather than recrystallization. The term recovery is, indeed, used for the evolution of an Ag nanostructure in some papers [13]. However, recrystallization is also observed in nanostructured Ag, especially after a large number of equal channel angular (ECAP) passes, when there is a reduced dislocation/twin density ratio. Strongly nano-twinned regions become sites for the nuclei of recrystallized grains [13].

In the case of nanostructured metals, SFE influences their thermal stability. The lowest thermal stability, and even self-annealing, are exhibited by low SFE, high-purity nanostructured metals such as Au, Cu and Ag processed by HPT and ECAP [14–18]. Very high dislocation densities and nanotwins contribute to an increase in the driving force for subsequent recovery and grain growth.

As may be expected, SFE has an impact on the strength-ductility balance of annealed nanostructured materials. During the annealing of Cu-8at.%Al (SFE = 28 mJ/m^2) and Cu-5at.%Al (SFE = 17 mJ/m^2), an obvious trend was observed whereby strength decreased at the expense of ductility. Nevertheless, a better strength-ductility balance was measured for an alloy with a lower SFE [19]; this can be explained similarly to the case of nanostructured materials, by a hindered cross slip in low-SFE materials that makes the strain hardening more efficient. Moreover, in low-SFE metals, the SFs contribute significantly to plasticity before any deformation twinning [20].

Considering the available results, one might expect that, if any kind of unconventional annealing is applied to nanostructured materials, the SFE may have a considerable impact on the resulting microstructures and properties. There are various unconventional annealing techniques, such as heating by an electric current [21,22], electric current pulses [23], and high hydrostatic pressure annealing (HPA) [23–34]. In the present work, HPA was applied, since, unlike other techniques, it makes it possible to gain control over the evolution of a material's microstructure. That evolution is retarded, since the high hydrostatic pressure applied during annealing supresses diffusion processes [24,25]. Consequently, HPA not only affects the rate of grain growth, but also the volume fraction of high-angle grain boundaries, texture, precipitate size, distribution, and chemical composition [27–29]. Furthermore, the diffusion mechanism changes from a vacancy diffusion mechanism to an interstitial diffusion mechanism along with the increase in pressure applied during annealing. As measured by DSC in low-SFE materials processed by HPT, only vacancy agglomerates were found, whereas in high-SFE materials single/double vacancies were also present, leading one to expect that their behaviour should vary during HPA [35]. The fact that HPA retards recrystallization and grain growth was found during experiments on low- [23,26–29], medium- [32,33] and high-SFE [24, 34] materials. However, in the case of nanostructured materials, this was proved only on the example of an austenitic steel [23,26–29].

Even though the behaviour of materials of various SFE was investigated during HPA in the past, never before has a comparison been made between nanostructures of various SFE deformed to the same degree of plastic deformation. The aim of this paper is to show the impact of SFE on the microstructure evolution and mechanical properties of nanostructured metals of different SFE annealed under HPA.

2. Experimental

2.1. Material and experiments

In the present study, two pure metals of different SFE were investigated, namely, Ni and Ag. The SFE, purity, melting temperatures (T_m) and annealing temperatures of these metals are presented in Table 1. The annealing temperatures were selected in a way that corresponded to about 0.4 T_m. From these materials, disks of 0.8 mm in thickness and 10 mm in perimeter were cut by spark erosion; the disks were then annealed at 873K for 2 h in order to obtain well-recrystallized materials.

The HPT experiments were carried out at the Faculty of Physics at the University of Vienna. The disks were processed at room temperature using an HPT device at a constant pressure of 6.0 GPa and a speed of 0.2 rpm. The disks were torsionally strained to 5 revolutions. The strain was well defined as simple shear, γ, and was calculated according to the equation $\gamma = 2\pi \times r \times n/t$, where r, n and t are the distance from the torsion axes, the number of applied revolutions and the mean thickness of the sample, respectively. The equivalent strains $\epsilon eq = \gamma/\sqrt{3}$, calculated at 3.5 mm from the central point of the sample after 5 revolutions, were equal to 79.

After deformation, the samples were annealed at the same homologous temperatures under a pressure of 2 GPa in a HPT device for 1 h, and conventionally in differential scanning calorimetry (DSC) using a PerkinElmer DSC7. The pressure - 2 GPa - applied during HPA has been selected basing on previous experiments performed on a SPD-processed austenitic stainless steel [26–28] and initial HPA experiments performed on Ni while 2, 4 and 6 GPa were applied. It was proved that only under 2 GPa the changes in microhardness between HPT-processed and HPA samples were significant. The heating rates during high hydrostatic pressure and conventional annealing were 1200 and 100 K/min, respectively, and the cooling rates were 50 and 15 K/min, respectively. Although the heating and cooling rates differ between applied techniques their impact on the microstructure transformation should be negligible since the annealing time, 1h, is much longer than the processes of heating and cooling. Moreover, heating and cooling in the case of HPA was done under 2 GP to eliminate the possible impact of the atmospheric pressure on microstructure transformation during HPA. This study is the first one where HPT was applied for high hydrostatic pressure annealing; previous experiments were performed in a toroidal high-pressure cell [40,41]. Further on in this text, these annealing techniques are referred to as CA – conventional annealing - and HPA – high hydrostatic pressure annealing, and the samples are referred to as Ni_HPT, Ag_HPT, Ni_CA, Ag_CA, Ni_HPA and Ag_HPA.

2.2. Analysis methods

After deformation and annealing, the microhardness was measured using an MHT-4 microhardness tester manufactured by Paar equipped with a Zeiss microscope. The indentation force was 1 N, the rate 0.1 N/s

Table 1
Melting temperature T_m, SFE, purity, wt.%, annealing temperature T_{an}.

	Ni	Ag
T_m [K] [36,37]	1728	1234
SFE [mJ/m^{-2}] [38,39]	125	16
Purity, wt. %	99.99%	99.95%
T_{an} (0.39 T_m) [K] for 1 h	627	479

and the holding time 10 s. The indentations were performed on the diameter, with a distance of 0.5 mm between them. The uniaxial tensile tests were carried out at room temperature using a Zwick/Roell Z005 machine. The tensile tests were conducted under the displacement control mode at an initial strain rate of 10^{-3} 1/s. The dimensions of the samples were as follows: a gauge section length of 2 mm and a cross section of 0.3 mm × 0.4 mm. The strain measurements were performed using the digital image correlation method (DIC).

The annealing of deformation-induced defects was registered by the occurrence of exothermic peaks during DSC heating, where the area of a peak is related to the total enthalpy of the annealing defects. During the DSC measurements, the heating rate was 10 K/min.

The samples after the HPT experiments were cut 1.5 mm from the sample edge, parallel to the radius and the sample surface by a focused ion beam FiB/SEM NB5000, as presented in Fig. 1. Subsequently, the samples were observed by transmission electron microscopy using a JEOL 1200 TEM at 120 kV. The samples after HPT and annealing were cut by spark erosion so that an area 1.5 mm from the edge parallel to the radius and sample surface was polished by ion milling system IM 4000 and subsequently observed using an SU 8000 scanning electron microscope at 5kV in the BSE mode. The microstructures obtained were further characterized by stereological and image analysis methods that are well-developed at the Warsaw University of Technology [42,43]. Calculations were then made of the average grain size (calculated as the equivalent diameter MV(d_2)), the standard deviation of the equivalent diameter SD(d_2), and the variation coefficient of the equivalent diameter CV(d_2). Moreover, the grain boundary area in the unit volume Sv was determined by counting the intersection points of the test lines with the grain boundary network. The Sv was calculated for twin boundaries and twin and grain boundaries, marked S_{VTB} and S_{VTB+GB}, respectively.

3. Results

3.1. Microhardness measurements

After the HPT, the microhardness of both metals increased by more than 200%, as presented in Fig. 2. The increase was 30% higher for Ni than Ag. A comparison of the microhardness values between metals after HPT and HPT combined with annealing is presented in Fig. 2. After CA, the most significant decrease in microhardness was observed for Ni, 62%, whereas in the case of Ag microhardness decreased by approximately 44%. HPA did not cause as profound a decrease in microhardness as CA did. The microhardness values decreased by 45 and 25% for Ni and Ag, respectively. The drop in microhardness was larger in the case of Ni than Ag, both after CA and after HPA. If one correlates the changes in microhardness between the two annealing conditions (by subtracting the percentage of the microhardness drop after HPA and CA), it can be seen that the difference is comparable for both metals - 17% and 19% for Ni and Ag, respectively.

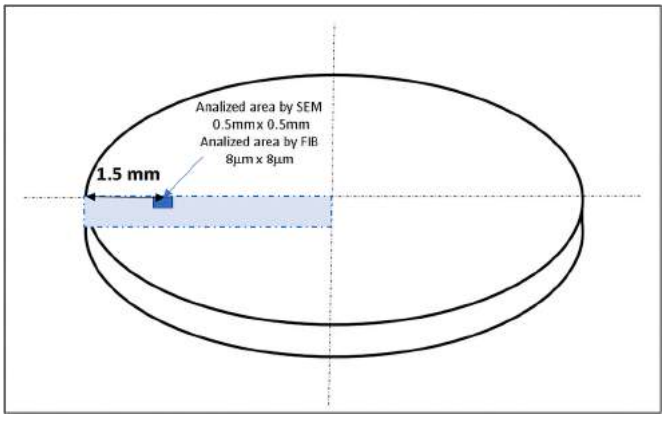

Fig. 1. HPT disk with marked area of microstructure observations.

3.2. Microstructure characterisation after HPT

Before the HPT experiments, the metals were annealed at 873K for 2 h to homogenize their microstructures, as presented in Fig. 3. As a result, coarse-grained microstructures of 31 and 23 µm in average equivalent diameter were obtained for Ni and Ag, respectively. Subsequently, the HPT processes were performed. The microstructures cut from cross sections (Fig.1) of the HPT-processed metals varying in SFE are highly refined, as shown in Fig.4. However, they vary in grain size and nanotwin density. The average grain size in Ni was slightly larger than in Ag: 140 nm in comparison with 120 nm in Ag. It is reported in the literature that, after HPT with similar processing parameters, the average grain size in Ni reached 170 nm [44], and in Ag 200 nm [45]. These differences in grain size might come from differences in the HPT processing parameters, what sections were selected for observation, and how the grain size was calculated. They were no nanotwins observed in Ni, whereas in the case of Ag, deformation nanotwins were present in numerous grains. Their average thickness was approximately 10 nm.

3.3. DSC measurements after HPT

The DSC measurements, shown in Fig. 5, revealed two peaks in the Ni and Ag. In the case of Ni, the first peak is exothermic at T_{peak} 519K, which is 0.3 of T_{hom}. This peak is called a "dislocation peak" [35] and consists of two subpeaks: one from dislocations and one from vacancy agglomerates. The second peak at T_{peak} 632K corresponds to the Curie temperature. In the case of Ag, the first exothermic peak temperature, as in Ni, is at $0.3T_{hom.}$ However, here it is composed of three subpeaks coming from dislocations, vacancy agglomerates and SFs. The second peak of T_{peak} 647K is also exothermic and can be assigned to grain growth. Considering the stored energy of the first peak in both metals, there is 49% more stored energy in the Ag.

3.4. Microstructure characterisation after annealing

The microstructures of the samples after annealing are shown in Fig. 6. The MV(d_2), SD (d_2), CV(d_2) and S_{VTB}, S_{VTB}/S_{VTB+GB} are presented in the form of charts in Fig. 7. An analysis of the microstructures permits the observations that (i) the samples are fully recrystallized; (ii) HPA inhibits grain growth in comparison with CA, and the degree of retardation depends on the SFE of a given material; and (iii) HPA and CA affect twin density differently.

HPA inhibits grain growth so that the grain size after HPA in comparison with CA reaches approximately 70% and 13% of the grain size after CA for Ni and Ag, respectively. It has also an impact on the homogeneity of the microstructures. HPA significantly increases CV(d_2) in the case of Ni, and decreases it in the case of Ag in comparison with CA. One can observe in Fig.7 c) the expected trend that, with a decrease in SFE, the S_{VTB} increases. However, if one compares the ratio of S_{VTB}/S_{VTB+GB}, it can be noticed that there is an increase only for CA. The HPA stabilises the S_{VTB}/S_{VTB+GB} ratio for various SFE metals at a level of 0.4.

3.5. Tensile tests and Hall-Petch plots

The stress–strain curves obtained during the room temperature tensile tests for Ni, both HPT-processed and annealed under various conditions, are presented in Fig. 8. The mean values (MV) and standard deviation (SD) of ultimate tensile strength (UTS), yield stress (YS), uniform elongation (Au), and total elongation (At) are summarized in Table 2.

The results indicate that HPT increases the UTS from 349 to 1015 MPa. However, in the literature, a higher value of 1270 MPa has been reported [46]. The difference may come from the fact that, in this study, the tensile mini-samples have different dimensions – a smaller width and

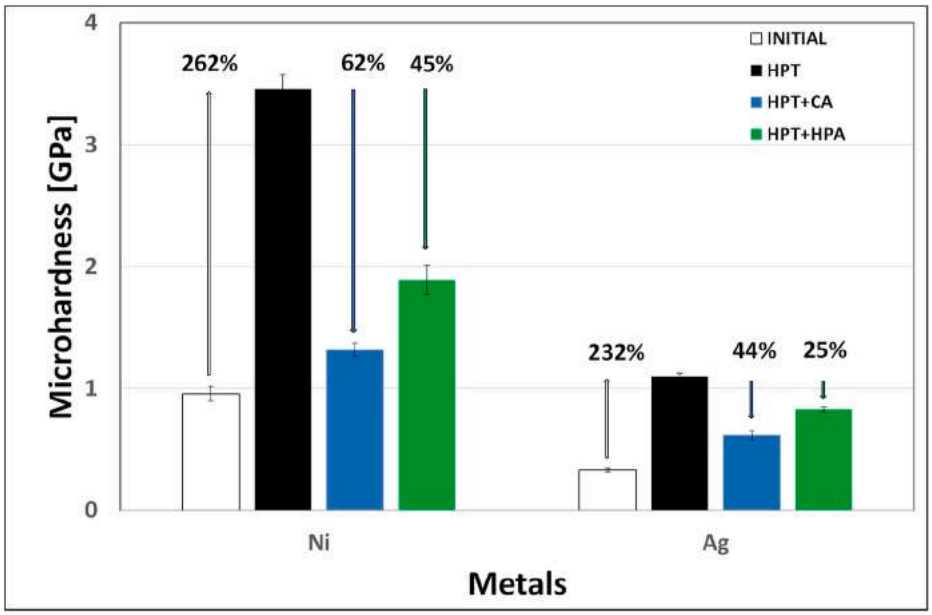

Fig. 2. Comparison of microhardness between HPT processed and annealed metals at various conditions.

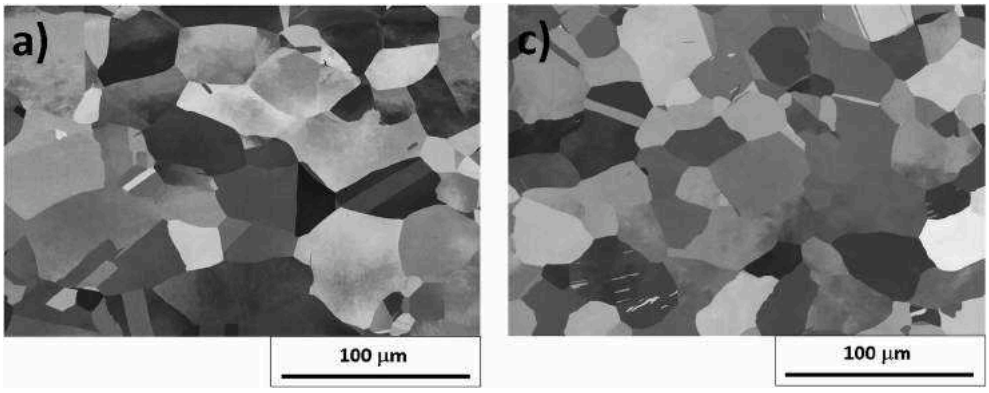

Fig. 3. Microstructures of a) Ni and b) Ag after annealing at 873K for 2 h – cross sections; in BSE-mode SEM.

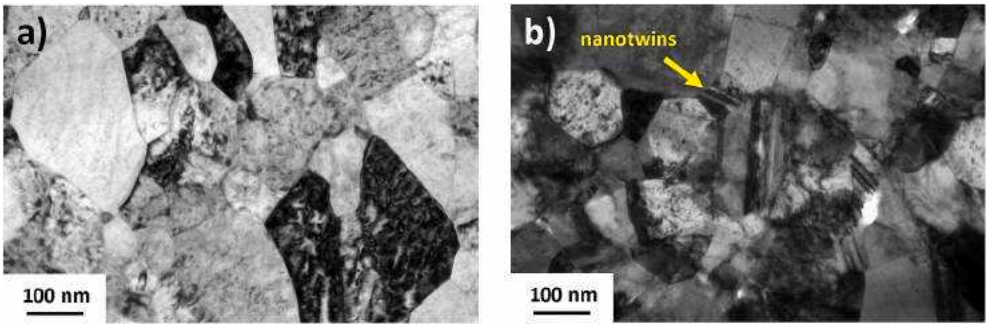

Fig. 4. Microstructures of HPT-processed materials varying in SFE: a) Ni, b) Ag with nanotwins indicated by the yellow arrow – cross sections; bright field TEM. (For interpretation of the references to colour in this figure legend, the reader is referred to the Web version of this article.)

thickness (0.4 × 03 mm) than those reported elsewhere (1.5 × 1.5 mm) [46] – and so there is a much larger volume of sample recrystallized during the cutting by the spark erosion process. These observations inclined the authors to perform tensile tests only on the Ni samples since, as is well-known, Ag has a lower thermal stability, meaning that the recrystallized volume changed by spark erosion cutting would have been greater. The results gathered clearly show that the samples after annealing at 627K have a similar plasticity, but the Ni HPA has higher strength. If one compares the result applying the factor YS*At, it is clearly visible that the greatest value is obtained for Ni_HPA, which therefore looks promising for obtaining a desirable strength-ductility balance for HPA materials.

The fact that HPA can produce unique microstructures is clearly visible in Fig. 9a), which presents a Hall-Petch plot with reference data

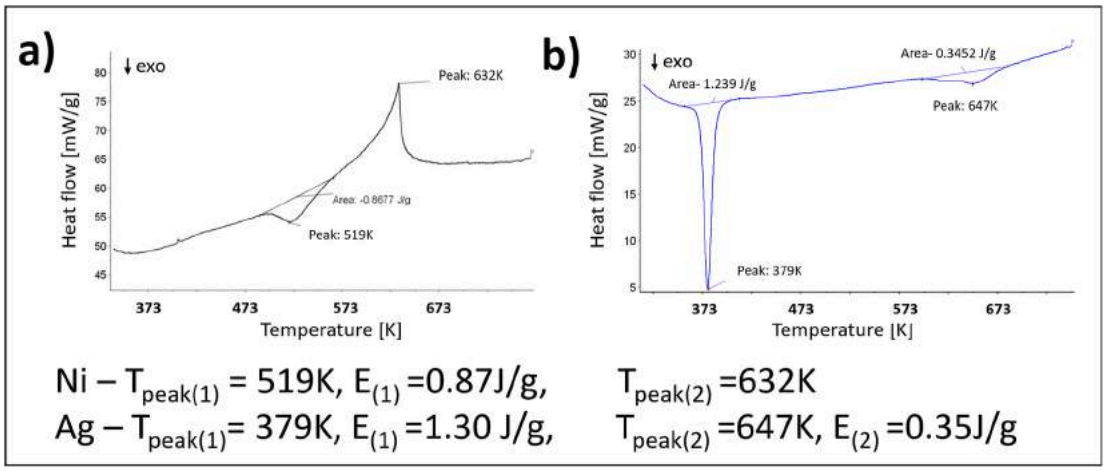

Fig. 5. Heat flow curves as a function of temperature for a) Ni and b) Ag, exhibiting peaks with marked peak temperatures and stored energy calculated from the integrated areas of the peaks.

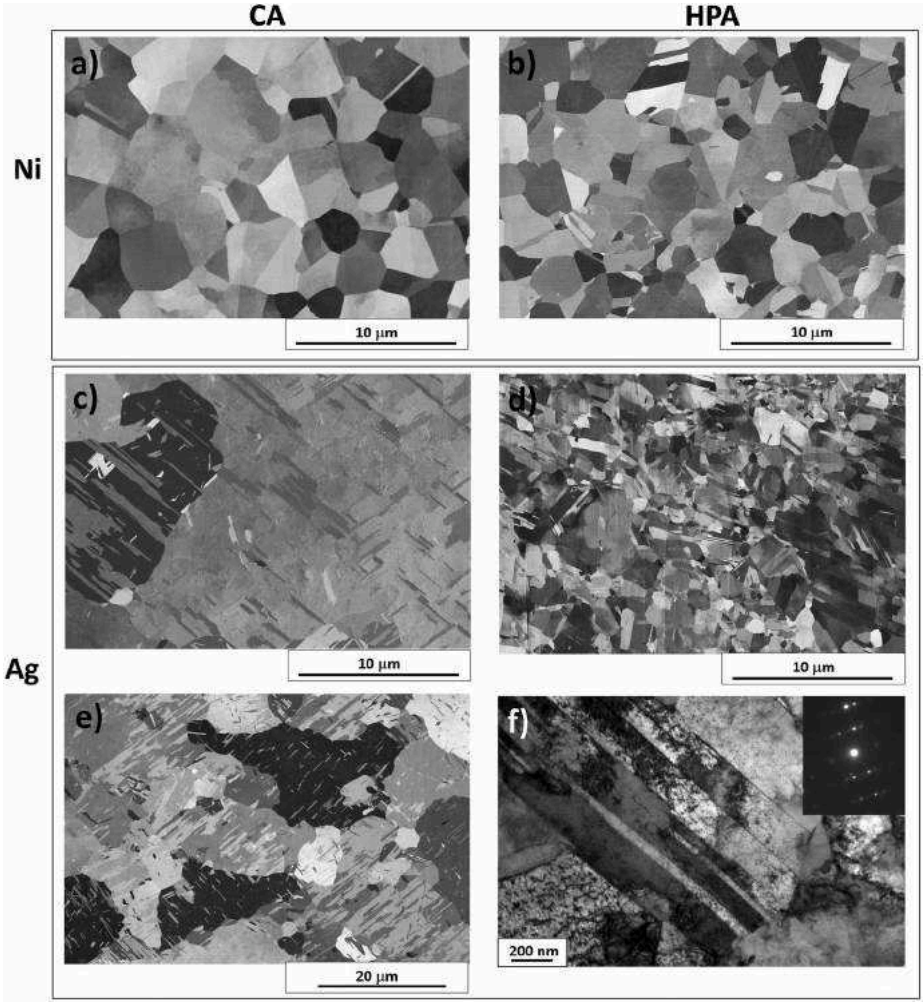

Fig. 6. Microstructures of HPT-processed and annealed materials - cross sections: a), b) Ni, c)-f) Ag; microstructures after CA: a), c), e); microstructures after HPA: b), d), f); a)-e) in BSE-mode SEM, f) TEM) with a selected area electron diffraction (SAED) pattern in the orientation [011].

from the literature. One can notice that the Ni_HPA does not lie on the trend line for conventionally annealed Ni when compared with the data from this article or from the literature. This phenomenon may be the result of differences in texture, the percentage of high-angle grain boundaries, or the misorientation angles between the HPA and CA samples, and demands further research.

In the case of Ag, Ag_HPA does not lie on the trend line for conventionally annealed Ag when one considers the grain size (d_2) as a d parameter in the Hall-Petch equation or the size of an area surrounded by twin boundaries or/and grain boundaries (d_2+t), as presented in

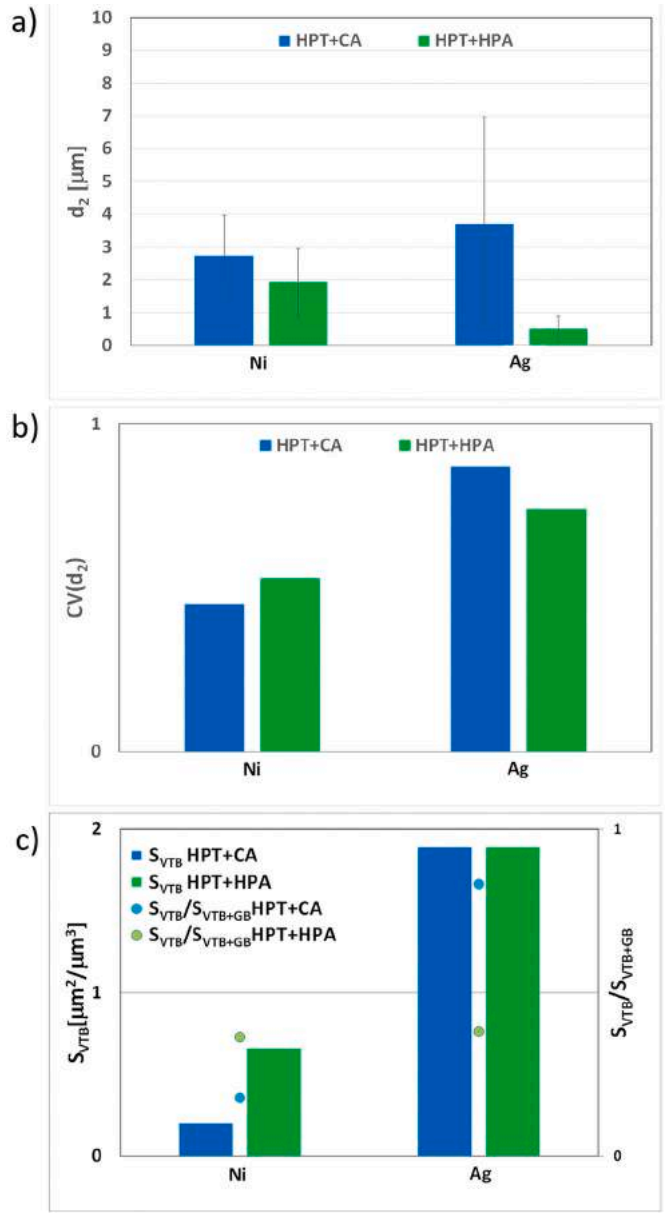

Fig. 7. Comparison of a) the average d_2, b) CV(d_2), and c) S_{VTB} and S_{VTB}/S_{VTB+GB} of HPT-processed and annealed materials varying in SFE.

Fig. 9b). However, if one considers the latter method as a d assessment, the Ag_HPA seems to be much closer to the Hall-Petch trend line. This might be because the volume fraction of the twin boundaries is high in Ag_HPA and Ag_CA. The second assessment method seems to be much more appropriate for silver, since in this material twin boundaries play a significant strengthening role at room temperature [47].

4. Discussion

The results clearly show that the application of a hydrostatic pressure of 2 GPa at 0.4 T_{hom} retards recovery, recrystallization and grain growth of nanostructured metals that differ in SFE. This fact is in agreement with previous studies, since the retardation of a microstructure rearrangement was noticed in the case of a high-SFE material – rolled aluminium, annealed under a pressure of 1.2 GPa [34] at 773K, and of a low SFE material – HPT-processed austenitic stainless steel annealed under 2 GPa and 6 GPa at 1173K [27,28].It must be underlined, however, that in this study materials that differ in SFE were deformed to the same deformation degree (using the same technique, temperature and pressure) and subsequently annealed at the same T_{hom}.

4.1. The impact of HPA on recovery, recrystallization and grain growth on nanostructured metals that differ in SFE

Based on the microhardness measurements and microstructure observations, it can be stated that HPA most significantly slows down the microstructure evolution of the low SFE material - Ag. This is in contrast with CA, where the greatest grain size is achieved in Ag. (An interesting fact is that, although after conventional annealing the greatest grain size is achieved for Ag, the greatest reduction in microhardness in comparison with the microhardness after HPT is achieved for Ni. This may come from the strengthening mechanisms of twin boundaries in Ag, which contribute to a higher yield stress and microhardness of Ag than may be simply estimated basing on the grain size [49].) It seems, therefore, that it is necessary to focus firstly on the impact of atmospheric pressure on microstructure evolution, and consider the factors that trigger changes in the microstructure. Those factors combine with the microstructural features formed during HPT. Low-SFE nanostructured metals, in comparison with high-SFE nanostructured metals obtained by HPT, are distinguished by Ref. [50]:

a) higher deformation nanotwin density.
b) higher dislocation density - deformation twins caused by lowering the SFE may serve as locations for an accumulation of dislocations,
c) lower grain size – a higher volume fraction of grain boundaries due to the twin deformation mechanism.

The high dislocation density and high volume fraction of grain boundaries enhance the diffusion rate at elevated temperatures and contribute to a high rate of recovery by climb, which is less sensitive to the splitting distance between two partials than cross-slip is. In addition to recovery, recrystallization is promoted in highly twinned regions, as these sites act as nuclei for recrystallized grains [13]. As a consequence, these factors constitute a large driving force for the microstructure evolution leading to fast grain growth. Even a self-annealing phenomenon can be observed in Ag after HPT. The DSC measurements confirm that the stored energy for Ag is higher than for Ni. Apart from the microstructural features, the physical properties of these materials, such as thermal diffusivity, should be taken into consideration. Ag features the highest thermal diffusivity ($D_{Ag} = 1.72*10^{-4}$ m^2/s, $D_{Ni} = 0.22*10^{-4} m^2/s$), supplying yet another factor for the fastest grain growth in Ag under atmospheric pressure [51]. However, it must be underlined that, in metals, all these processes also depend on the level of impurity. For this reason, in this study the purity of the selected metals was comparable.

If high pressure is applied during annealing, the microstructure evolution is retarded the most significantly in the lowest-SFE material. Despite the fact that in low-SFE materials the dislocation density is higher than in high-SFE metals, which may facilitate grain growth during conventional annealing, the vacancy concentration is lower [35]. It is the result of two processes - vacancy generation and annihilation. Since the migration enthalpy of vacancies for Ag is much lower than for Ni, it must be concluded that the concentration of vacancies after HPT should be the highest for Ni. During HPA, the movement of vacancies is hindered, and along with it processes such as recovery and grain growth. The movement of vacancies is hindered since high hydrostatic pressure has an impact on the enthalpy of vacancy migration. Consequently, vacancy migration influences annihilation of edge dislocations climbing. Therefore, under a certain hydrostatic pressure p applied, an extra work $p\Omega$, where Ω is the atomic volume, is necessary when a vacancy migrates through the lattice, which increases the vacancy migration enthalpy as $dHeff = dH + p\Omega$ [52,53]. During HPA at a given T, the effective vacancy migration enthalpy dHeff is correlated with the diffusivity by a formula $D = D_0 \exp(-dHeff/kT)$ where D_0 is the core diffusion coefficient [54].

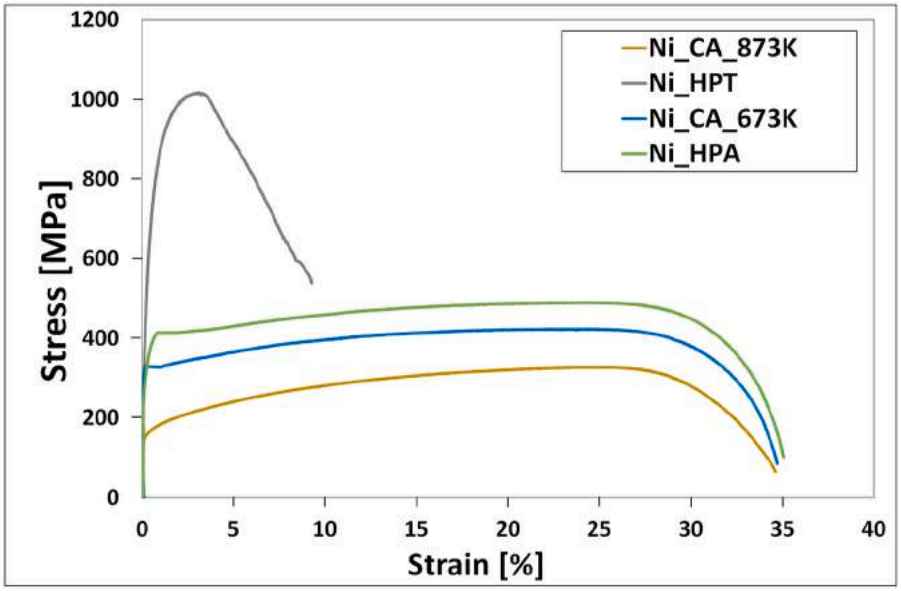

Fig. 8. Stress–strain curves obtained during room temperature tensile tests for Ni HPT-processed and annealed under various conditions.

Table 2
MV and SD of UTS, YS, Au, and At.

Parameter Sample indication	YS [MPa]		UTS [MPa]		Au [%]		At [%]		YS*At
	MV	SD	MV	SD	MV	SD	MV	SD	[MPa*%]
Ni_873K_CA	171	15	349	21	26.0	0.6	35.2	0.6	6045
Ni_HPT	757	32	1015	2	2.1	0.3	9.4	0.1	7147
Ni_673K_CA	341	13	440	16	24.7	0,9	36.4	0.7	12456
Ni_400K_HPA	401	13	479	11	25.2	0.6	37.3	2.3	15087

Another factor which may contribute to the retardation of recovery and grain growth is the high density of nanotwin boundaries. The most distinctive feature of low-SFE metals is the nanotwin boundaries formed during HPT. These boundaries are viewed as 60° <111> twin boundaries or, less commonly, marked as 70.5°<110> tilt boundaries. Since tilt boundaries <110> move by a cooperative motion of several atoms, while <100> and <111> tilt boundaries do so by a single atom mechanism, it can be estimated that twin boundaries movement will be more retarded than <100> and <111> tilt boundaries as the vacancy mobility decreases with increasing pressure during annealing. The fact that a high density of twin boundaries may significantly slow down recovery and grain growth was also observed in a nanostructured austenitic stainless steel refined by hydrostatic extrusion (HE) and profile rolling (PR) after annealing at 1173K under 6 GPa for 10 min [26,27,29].

4.2. The impact of HPA on twinning frequency in nanostructured metals that differ in SFE

Annealing twin boundaries - which are understood as a special kind of coherent high-angle grain boundaries with the lowest interfacial energy [55] - have an impact on various properties of materials. They can improve corrosion resistance by, e.g., accelerating the formation of a homogeneous [56] and/or less defective [57] film in the twinned areas, and can also improve the material's mechanical properties by acting as obstacles to dislocations [49,58]. On the other hand, twins can be detrimental to fatigue resistance, as they may accelerate the crack initiation process [59]. Moreover, they can be disadvantageous to electrical conductivity, as proved in nano-twinned copper: the contribution to resistivity in nanotwinned Cu of twin widths of 15 nm and 90 nm is $8.5*10^{-2}$ and $1.2*10^{-2}$ μΩcm, respectively [60]. According to Gleiter's theory [61], still in development [62,63] – the so-called growth accident model – annealing twin boundaries are created when a migrating grain boundary encounters an SF. The highest density of SFs is in Ag, and for this reason Ag has the highest S_{VTB}. In comparison with CA, HPA has an impact on twinning creation, although the trend is different in Ni and Ag. The phenomenon observed in Ni can be easily justified if one assumes that HPA slows down the processes of recrystallization and grain growth. Then, the microstructure obtained during HPA may be treated as that obtained by CA but after a shorter annealing time. If so, and knowing that annealing twin density decreases during grain growth, the results obtained in the case of Ni remain in agreement with the prediction from the literature [63,64]. If one tries to apply the same theory to Ag, it should be expected that HPA will result in a much higher S_{VTB}. In order to find the reasons for the different behavior of Ag, the factors that affect annealing twin generation must be considered. Those factors are as follows: grain boundary velocity, which is considered as the most essential; grain size; grain boundary energy; and twin boundary energy. As previously stated, HPA retards grain growth - in other words, it decreases grain boundary velocity. This can be the main reason for the comparable S_{VTB} in Ag_HPA and Ag_CA. The fact that a low grain growth rate results in a lower twinning frequency than a high rate was previously observed in Ag stocked at room temperature [65]. However, that kind of treatment precludes any control over the number of twin boundaries, unlike HPA, which the authors believe may be useful in grain engineering to obtain desirable microstructures for various applications.

Another important factor that demands further investigation in the future is the impact on HPA of unloading after HPT. This process may lead to an annihilation/recombination of dislocations which are hindered under high pressure [54,66]. This could be essential for materials of low thermal stability - in this study Ag - since for this material the

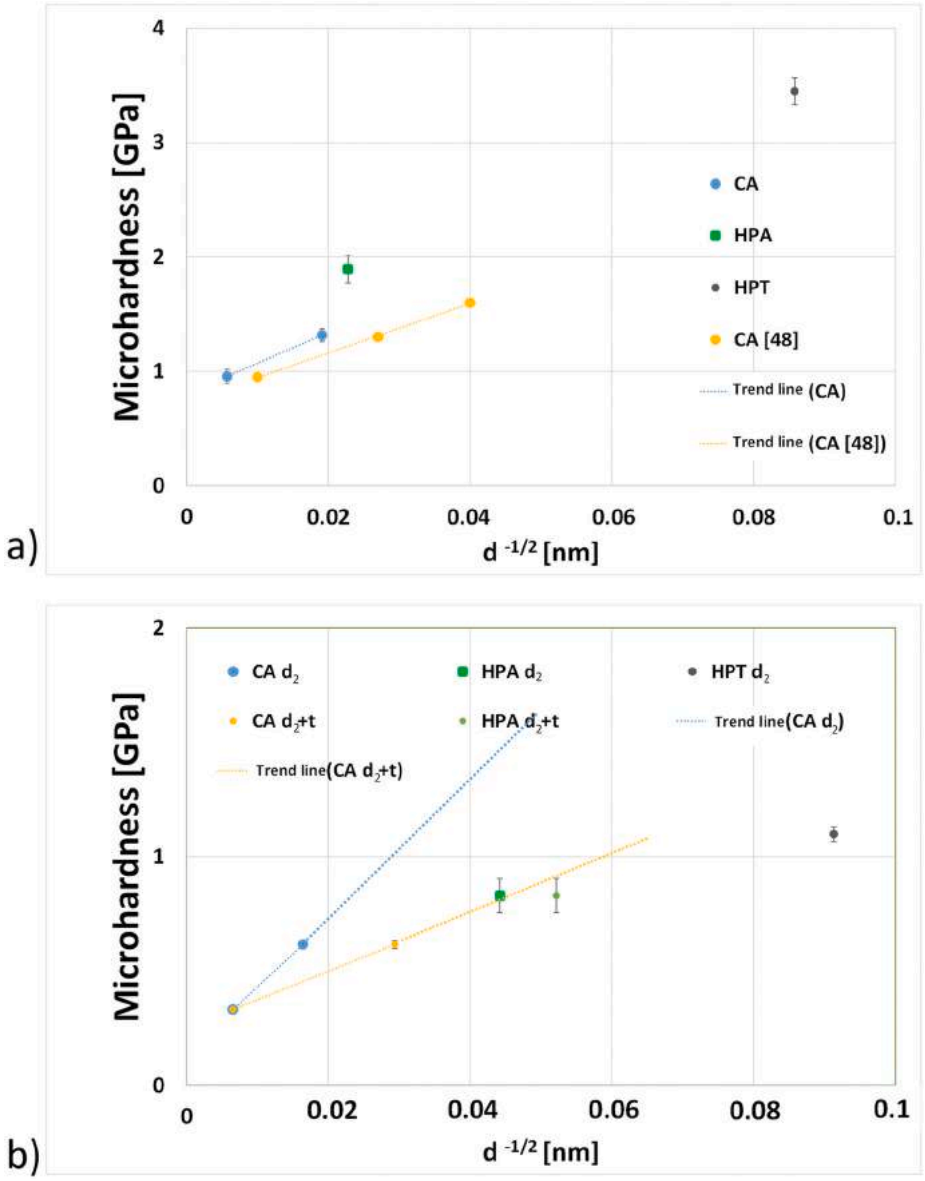

Fig. 9. Hall-Petch plot for HPT-processed and annealed a) Ni and b) Ag [48].

diffusivity at RT is the highest. Yet even Ni, which is considered to have high vacancy migration enthalpy [66], was significantly affected by unloading.

5. Conclusions

a) High pressure torsion leads to the microstructure refinement of both low- (Ag) and high– (Ni) stacking fault energy metals. The microstructures obtained differ in grain size and twin density, with a smaller grain size and greater twin density is observed in Ag.

b) High hydrostatic pressure annealing retards the microstructure evolution of Ag more than that of Ni. This is contrary to conventional annealing, which results in a greater grain size in Ag than in Ni.

c) The lower grain growth rate during high hydrostatic pressure annealing in the case of Ag (in comparison with Ni) was attributed to a higher frequency of deformation twins during deformation and a lower vacancy concentration.

d) Unlike conventional annealing, high pressure annealing leads to a smaller twin boundary area per unit volume than that expected for the determined grain size, since high pressure annealing decreases the rate of boundary motion. The magnitude of this phenomenon is greater for Ag than Ni, since in Ag grain growth is more retarded.

Data availability statement

The raw/processed data required to reproduce these findings cannot be shared at this time due to technical or time limitations.

CRediT authorship contribution statement

Agnieszka Teresa Krawczynska: Conceptualization, Investigation, Writing - original draft, Funding acquisition, Formal analysis. **Michael Kerber:** Methodology, Validation, Investigation. **Przemyslaw Suchecki:** Investigation. **Barbara Romelczyk-Baishya:** Investigation, Formal analysis. **Malgorzata Lewandowska:** Supervision, Conceptualization, Investigation, Supervision, Funding acquisition, On behalf of all authors, Agnieszka.

Declaration of competing interest

The authors declare that they have no known competing financial interests or personal relationships that could have appeared to influence the work reported in this paper.

Acknowledgement

This work was supported by the Austrian Federal Ministry of Education, Science and Research WTZ PL 11/2018 and the Polish Ministry of Science and Higher Education scientists exchange programme 2018–2020.

References

[1] T.C. Lowe, R.Z. Valiev, The use of severe plastic deformation techniques in grain refinement, JOM (2004), https://doi.org/10.1007/s11837-004-0295-z.
[2] R. Valiev, Y. Estrin, Z. Horita, T.G. Langdon, M.J. Zehetbauer, Y.T. Zhu, Producing bulk ultrafined grained materials by severe plastic deformation, Jom (2006), https://doi.org/10.1007/s11837-006-0213-7.
[3] J. Zrnik, S. Dobatkin, I. Mamuzic, Processing of Metals by Severe Plastic Deformation (SPD)-structure and Mechanical Properties Respond, Metal, 2008.
[4] R.Z. Valiev, R.K. Islamgaliev, I.V. Alexandrov, Bulk nanostructured materials from severe plastic deformation, Prog. Mater. Sci. (2000), https://doi.org/10.1016/S0079-6425(99)00007-9.
[5] X.H. An, S.D. Wu, Z.G. Wang, Z.F. Zhang, Significance of stacking fault energy in bulk nanostructured materials: insights from Cu and its binary alloys as model systems, Prog. Mater. Sci. (2019), https://doi.org/10.1016/j.pmatsci.2018.11.001.
[6] Y.H. Zhao, Y.T. Zhu, X.Z. Liao, Z. Horita, T.G. Langdon, Influence of stacking fault energy on the minimum grain size achieved in severe plastic deformation, Mater. Sci. Eng. A. (2007), https://doi.org/10.1016/j.msea.2006.08.119.
[7] X.H. An, Q.Y. Lin, S.D. Wu, Z.F. Zhang, R.B. Figueiredo, N. Gao, T.G. Langdon, Significance of stacking fault energy on microstructural evolution in Cu and Cu-Al alloys processed by high-pressure torsion, Philos. Mag. A (2011), https://doi.org/10.1080/14786435.2011.577757.
[8] X.H. An, Q.Y. Lin, S.D. Wu, Z.F. Zhang, R.B. Figueiredo, N. Gao, T.G. Langdon, The influence of stacking fault energy on the mechanical properties of nanostructured Cu and Cu-Al alloys processed by high-pressure torsion, Scripta Mater. (2011), https://doi.org/10.1016/j.scriptamat.2011.01.041.
[9] Y.H. Zhao, X.Z. Liao, Z. Horita, T.G. Langdon, Y.T. Zhu, Determining the optimal stacking fault energy for achieving high ductility in ultrafine-grained Cu-Zn alloys, Mater. Sci. Eng. A. (2008), https://doi.org/10.1016/j.msea.2007.11.074.
[10] A. Rollett, F. Humphreys, G.S. Rohrer, M. Hatherly, Recrystallization and Related Annealing Phenomena, second ed., 2004, https://doi.org/10.1016/B978-0-08-044164-1.X5000-2.
[11] N.M. Amirkhanov, J.J. Bucki, R.K. Islamgaliev, K.J. Kurzydlowski, R. Valiev, Thermal evolution of structure of ultrafine grained copper, processed by severe plastic deformation, J. Metastable Nanocryst. Mater. (2001). https://doi.org/10.4028/www.scientific.net/jmnm.9.21.
[12] H. Jiang, Y.T. Zhu, D.P. Butt, I.V. Alexandrov, T.C. Lowe, Microstructural evolution, microhardness and thermal stability of HPT-processed Cu, Mater. Sci. Eng., A (2000), https://doi.org/10.1016/S0921-5093(00)00919-9.
[13] J. Gubicza, N.Q. Chinh, J.L. Lábár, Z. Hegedus, T.G. Langdon, Principles of self-annealing in silver processed by equal-channel angular pressing: the significance of a very low stacking fault energy, Mater. Sci. Eng. A. (2010), https://doi.org/10.1016/j.msea.2009.08.071.
[14] O.V. Mishin, A. Godfrey, Microstructure of ECAE-processed copper after long-term room-temperature storage, Metall. Mater. Trans. A Phys. Metall. Mater. Sci. (2008), https://doi.org/10.1007/s11661-008-9658-3.
[15] J. Gubicza, S.V. Dobatkin, E. Khosravi, A.A. Kuznetsov, J.L. Lábár, Microstructural stability of Cu processed by different routes of severe plastic deformation, Mater. Sci. Eng. A. (2011), https://doi.org/10.1016/j.msea.2010.11.026.
[16] H. Matsunaga, Z. Horita, Softening and microstructural coarsening without twin formation in FCC metals with low stacking fault energy after processing by high-pressure torsion, Mater. Trans. (2009), https://doi.org/10.2320/matertrans.MF200921.
[17] Z. Hegedus, J. Gubicza, M. Kawasaki, N.Q. Chinh, Z. Fogarassy, T.G. Langdon, The effect of impurity level on ultrafine-grained microstructures and their stability in low stacking fault energy silver, Mater. Sci. Eng. A. (2011), https://doi.org/10.1016/j.msea.2011.08.034.
[18] X.K. Zhang, X.Y. Yang, W. Chen, J. Qin, J.P. Fouse, Effect of stacking fault energy on mechanical properties and annealing behavior of brasses, J. Alloys Compd. (2016), https://doi.org/10.1016/j.jallcom.2016.04.083.
[19] X.H. An, S. Qu, S.D. Wu, Z.F. Zhang, Effects of stacking fault energy on the thermal stability and mechanical properties of nanostructured Cu-Al alloys during thermal annealing, J. Mater. Res. (2011), https://doi.org/10.1557/jmr.2010.39.
[20] Y.Z. Tian, L.J. Zhao, S. Chen, A. Shibata, Z.F. Zhang, N. Tsuji, Significant contribution of stacking faults to the strain hardening behavior of Cu-15%Al alloy with different grain sizes, Sci. Rep. (2015), https://doi.org/10.1038/srep16707.
[21] J.W. Park, H.J. Jeong, S.W. Jin, M.J. Kim, K. Lee, J.J. Kim, S.T. Hong, H.N. Han, Effect of electric current on recrystallization kinetics in interstitial free steel and AZ31 magnesium alloy, Mater. Char. (2017), https://doi.org/10.1016/j.matchar.2017.09.021.
[22] A.T. Krawczynska, M. Lewandowska, R. Kuziak, K.J. Kurzydłowski, Recrystallization and grain growth in nano-structured austenitic stainless steel under electric current heating, Phys. Status Solidi (2010), https://doi.org/10.1002/pssc.200983377.
[23] A.T. Krawczynska, T. Brynk, M. Rosioski, A. Michalski, S. Gierlotka, E. Grzanka, S. Stelmakh, B. Pałosz, M. Lewandowska, K.J. Kurzydłowski, Improving mechanical properties of nanometals by annealing. Proceedings of the 33rd Risoe International Symposium on Materials Science:Nanometals - Status and Perspective, 2012, pp. 279–286.
[24] B.J. Buescher, R.M. Emrick, Pressure effect on defect migration in aluminum, Phys. Rev. B (1970), https://doi.org/10.1103/PhysRevB.1.3922.
[25] M. Büscher, C. Herzig, U. Köhler, H. Mehrer, W. Lojkowski, Pressure dependence of Zr diffusion in the equiatomic B.C.C. TiZr alloy, Phys. Status Solidi (1992), https://doi.org/10.1002/pssb.2221740205.
[26] A.T. Krawczynska, T. Brynk, S. Gierlotka, E. Grzanka, S. Stelmakh, B. Palosz, M. Lewandowska, K.J. Kurzydlowski, Mechanical properties of nanostructured 316LVM stainless steel annealed under pressure, Mech. Mater. (2013), https://doi.org/10.1016/j.mechmat.2013.07.017.
[27] A.T. Krawczynska, S. Gierlotka, P. Suchecki, D. Setman, B. Adamczyk-Cieslak, M. Lewandowska, M. Zehetbauer, Recrystallization and grain growth of a nano/ultrafine structured austenitic stainless steel during annealing under high hydrostatic pressure, J. Mater. Sci. (2018), https://doi.org/10.1007/s10853-018-2459-1.
[28] A.T. Krawczynska, S. Gierlotka, P. Suchecki, D. Setman, B. Adamczyk-Cieslak, M. Gloc, W. Chrominski, M. Lewandowska, M. Zehetbauer, Phenomena occurring in nanostructured stainless steel 316LVM during annealing under high hydrostatic pressure, Adv. Eng. Mater. (2018), https://doi.org/10.1002/adem.201800101.
[29] A.T. Krawczynska, P. Suchecki, B. Adamczyk-Cieslak, B. Romelczyk-Baishya, M. Lewandowska, Influence of high hydrostatic pressure annealing on the recrystallization of nanostructured austenitic stainless steel, Mater. Sci. Eng. A. (2019), https://doi.org/10.1016/j.msea.2019.138381.
[30] W. Lojkowski, D.A. Molodov, G. Gottstein, L.S. Shvidlerman, The mechanism of grain boundary migration in aluminium bicrystals, Mater. Sci. Forum (1996) 537–540, 207–209.
[31] L.S. Shvindlerman, U. Czubayko, G. Gottstein, D.A. Molodov, High pressure effect on grain boundary migration and mechanism of grain boundary migration, Mater. Sci. Forum (1996) 45–54, 204–206.
[32] A.F. Syrenko, G.P. Klinishev, V.T. Khoi, Recrystallization of copper under hydrostatic pressure up to 15kbar, J. Mater. Sci. 8 (1973) 765–769.
[33] L.E. Tanner, S.V. Radcliffe, Effect of hydrostatic pressure on the kinetics of recrystallization in high-purity copper, Acta Metall. Mater. 10 (1962) 1161–1169.
[34] V. Sursaeva, S. Protasova, W. Lojkowski, J. Jun, Microstructure evolution during normal grain growth under high pressure in 2-D aluminium foils, Textures Microstruct. (2008), https://doi.org/10.1155/tsm.32.175.
[35] D. Setman, E. Schafler, E. Korznikova, M.J. Zehetbauer, The presence and nature of vacancy type defects in nanometals detained by severe plastic deformation, Mater. Sci. Eng. A. (2008), https://doi.org/10.1016/j.msea.2007.06.093.
[36] A. Buch, Short Handbook of Metal Elements Properties and Elastic Properties of Pure Metals, third ed., Krzysztof Biesaga, Warsaw, 2005.
[37] A. Buch, Pure Metals Properties, Scientific-Technical Handbook, Metals Park/London and Tel-Aviv, ASM International/Freund Publishing House, 1999.
[38] L.E. Murr, Interfacial Phenomena in Metals and Alloys, Addison-Wesley, Reading, MA, 1975.
[39] P.C.J. Gallagher, The influence of alloying, temperature and related effects on thestacking fault energy, Metall. Trans. 1 (1970) 2429–2461.
[40] L.G. Khvostantsev, L.F. Vereshchagin, A.P. Novikov, A verkh-niz (up-down) toroid device for generation of high pressure 9, High Temp-High Press, 1997, p. 637.
[41] L.G. Khvostantsev, V.N. Slesarev, V.V. Brazhkin, Toroid type high-pressure device: history and prospects 24, High Press Res, 2004, pp. 371–383.
[42] T. Wejrzanowski, W.L. Spychalski, K. Różniatowski, K.J. Kurzydłowski, Image based analysis of complex microstructures of engineering materials, Int. J. Appl. Math. Comput. Sci. (2008), https://doi.org/10.2478/v10006-008-0003-1.
[43] T. Wejrzanowski, K.J. Kurzydlowski, Stereology of grains in nano-crystals, Solid State Phenom. 94 (2003) 221–228.
[44] A.P. Zhilyaev, S. Lee, G.V. Nurislamova, R.Z. Valiev, T.G. Langdon, Microhardness and microstructural evolution in pure nickel during high-pressure torsion, Scripta Mater. (2001), https://doi.org/10.1016/S1359-6462(01)00955-1.
[45] Z. Hegeds, J. Gubicza, M. Kawasaki, N.Q. Chinh, Z. Fogarassy, T.G. Langdon, Microstructure of low stacking fault energy silver processed by different routes of severe plastic deformation, J. Alloys Compd. (2012), https://doi.org/10.1016/j.jallcom.2011.10.070.
[46] N. Krasilnikov, W. Lojkowski, Z. Pakiela, R. Valiev, Tensile strength and ductility of ultra-fine-grained nickel processed by severe plastic deformation, Mater. Sci. Eng. A. (2005), https://doi.org/10.1016/j.msea.2005.03.001.
[47] X. Liu, L. Sun, L. Zhu, J. Liu, K. Lu, J. Lu, High-order hierarchical nanotwins with superior strength and ductility, Acta Mater. (2018), https://doi.org/10.1016/j.actamat.2018.01.047.
[48] M.C. Iordache, S.H. Whang, Z. Jiao, Z.M. Wang, Grain growth kinetics in nanostructured nickel, Nanostruct. Mater. (1999), https://doi.org/10.1016/S0965-9773(00)00427-X.
[49] M. Schneider, E.P. George, T.J. Manescau, T. Záležák, J. Hunfeld, A. Dlouhý, G. Eggeler, G. Laplanche, Analysis of strengthening due to grain boundaries and annealing twin boundaries in the CrCoNi medium-entropy alloy, Int. J. Plast. (2019), https://doi.org/10.1016/j.ijplas.2019.08.009.

[50] J. Gubicza, N.Q. Chinh, J.L. Lábár, Z. Hegedus, T.G. Langdon, Principles of self-annealing in silver processed by equal-channel angular pressing: the significance of a very low stacking fault energy, Mater. Sci. Eng. A. (2010), https://doi.org/10.1016/j.msea.2009.08.071.
[51] https://thermtest.com/materials-database.
[52] M.J. Zehetbauer, H.P. Stüwe, A. Vorhauer, E. Schafler, J. Kohout, The role of hydrostatic pressure in severe plastic deformation, Adv. Eng. Mater. (2003), https://doi.org/10.1002/adem.200310090.
[53] E. Schafler, G. Steiner, E. Korznikova, M. Kerber, M.J. Zehetbauer, Lattice defect investigation of ECAP-Cu by means of X-ray line profile analysis, calorimetry and electrical resistometry, Mater. Sci. Eng. A. (2005), https://doi.org/10.1016/j.msea.2005.08.070.
[54] E. Schafler, Effects of releasing the hydrostatic pressure on the nanostructure after severe plastic deformation of Cu, Scripta Mater. (2010), https://doi.org/10.1016/j.scriptamat.2009.12.004.
[55] J.W. Christian, S. Mahajan, Deformation twinning, Prog. Mater. Sci. (1995), https://doi.org/10.1016/0079-6425(94)00007-7.
[56] G. Zou, Q. Peng, Y. Wang, B. Liu, The effect of extension twinning on the electrochemical corrosion properties of Mg-Y alloys, J. Alloys Compd. (2015), https://doi.org/10.1016/j.jallcom.2014.08.115.
[57] G. Meng, Y. Shao, T. Zhang, Y. Zhang, F. Wang, Synthesis and corrosion property of pure Ni with a high density of nanoscale twins, Electrochim. Acta (2008), https://doi.org/10.1016/j.electacta.2008.03.070.
[58] K.J.H. Al-Fadhalah, C.M. Li, A.J. Beaudoin, D.A. Korzekwa, I.M. Robertson, Microplastic processes developed in pure Ag with mesoscale annealing twins, Acta Mater. (2008), https://doi.org/10.1016/j.actamat.2008.07.050.
[59] G.M. Castelluccio, D.L. McDowell, Effect of annealing twins on crack initiation under high cycle fatigue conditions, J. Mater. Sci. (2013), https://doi.org/10.1007/s10853-012-7021-y.
[60] X.H. Chen, L. Lu, K. Lu, Electrical resistivity of ultrafine-grained copper with nanoscale growth twins, J. Appl. Phys. (2007), https://doi.org/10.1063/1.2799087.
[61] H. Gleiter, The formation of annealing twins, Acta Metall. (1969), https://doi.org/10.1016/0001-6160(69)90004-2.
[62] J.R. Cahoon, Q. Li, N.L. Richards, Microstructural and processing factors influencing the formation of annealing twins, Mater. Sci. Eng. A. (2009), https://doi.org/10.1016/j.msea.2009.07.021.
[63] Y. Jin, B. Lin, M. Bernacki, G.S. Rohrer, A.D. Rollett, N. Bozzolo, Annealing twin development during recrystallization and grain growth in pure nickel, Mater. Sci. Eng. A. (2014), https://doi.org/10.1016/j.msea.2014.01.018.
[64] Y. Jin, M. Bernacki, G.S. Rohrer, A.D. Rollett, B. Lin, N. Bozzolo, Formation of annealing twins during recrystallization and grain growth in 304L austenitic stainless steel, Mater. Sci. Forum (2013). https://doi.org/10.4028/www.scientific.net/MSF.753.113.
[65] H. Matsunaga, Z. Horita, Softening and microstructural coarsening without twin formation in FCC metals with low stacking fault energy after processing by high-pressure torsion, Mater. Trans. (2009), https://doi.org/10.2320/matertrans.MF200921.
[66] E. Schafler, Strength response upon pressure release after high pressure torsion deformation, Scripta Mater. (2011), https://doi.org/10.1016/j.scriptamat.2010.09.026.

Załącznik 8

Umowa nr UMO-2014/15/D/ST8/00532

o realizację i finansowanie projektu badawczego który uzyskał finansowanie w ramach konkursu „SONATA 8"

zawarta w dniu ..... w Krakowie pomiędzy:

Narodowym Centrum Nauki w Krakowie, ul. Królewska 57, 30-081 Kraków, NIP 6762429638, REGON 121361537, zwanym dalej "Centrum"
reprezentowanym przez Dyrektora .....

a

Politechniką Warszawską
pl. Politechniki 1, 00-661 Warszawa
NIP: 5250005834 REGON: 000001554

zwaną(ym) dalej "Jednostką", którą reprezentuje(ą):

prof. dr hab. **Rajmund Bacewicz**, Prorektor ds. Nauki,

oraz

dr inż. Agnieszką Teresą Krawczyńską
[redacted]

zwaną(ym) dalej "Kierownikiem projektu"

na podstawie decyzji Dyrektora Narodowego Centrum Nauki Nr DEC-2014/15/D/ST8/00532 z dnia 2015-05-11.

§ 1. Przedmiot umowy

Umowa określa warunki realizacji, finansowania oraz rozliczania projektu badawczego pt.
Rekrystalizacja i rozrost ziaren w silnie odkształconej stali austenitycznej, zwanego dalej „projektem", przyjętego do finansowania w ramach konkursu „SONATA 8" na projekty badawcze, realizowane przez osoby rozpoczynające karierę naukową posiadające stopień naukowy doktora, ogłoszonego w dniu 15 września 2014 r. Projekt będzie realizować **Politechnika Warszawska, Wydział Inżynierii Materiałowej**.

§ 2. Termin realizacji projektu

1. Dzień rozpoczęcia realizacji projektu strony ustalają na dzień zawarcia umowy, a zakończenia realizacji projektu na dzień .....
2. Okres realizacji projektu wynosi **36** miesięcy/miesiące.

MINISTERSTWO
NAUKI I SZKOLNICTWA WYŻSZEGO
Departament Współpracy Międzynarodowej

DWM.WKE.183.10.2018/AM

Warszawa, 24 stycznia 2018 r.

Dr inż. Agnieszka Krawczyńska
Politechnika Warszawska
Wydział Inżynierii Materiałowej

Szanowna Pani,

uprzejmie informuję, że w dniu 15 grudnia 2017 r. Polsko-Francuska Komisja dokonała wyboru projektów spośród przedłożonych w ramach Programu Wymiany Osobowej na lata 2018-2019. Uprzejmie informuję, że decyzją Komisji, Pani projekt pt. *Badanie plastyczności tlenku aluminium w różnej skali podczas eksperymentów in situ w mikroskopach elektronowych* został przyjęty do realizacji.

Z wyrazami szacunku,

Dyrektor
Departamentu
Współpracy Międzynarodowej
Juliusz SZYMCZAK-GAŁKOWSKI

ul. Wspólna 1/3, 00-529 Warszawa
tel. (22) 52 92 266, faks: (22) 50 17 130, e-mail: sekretariat.DWM@nauka.gov.pl, www.nauka.gov.pl

Współpraca polsko-austriacka

Dziedzic Wojciech <Wojciech.Dziedzic@mnisw.gov.pl>

Śr 09.05.2018 10:06

Do:akrawczy@inmat.pw.edu.pl <A.Krawczynska@inmat.pw.edu.pl>;

DW:Calak Jan <Jan.Calak@mnisw.gov.pl>; Agnieszka Stefaniak-Hrycko <agnieszka.stefaniak@nawa.gov.pl>; researchers@nawa.gov.pl <researchers@nawa.gov.pl>; 'Magdalena Kachnowicz' <Magdalena.Kachnowicz@nawa.gov.pl>;

Szanowna Pani,

chciałbym nawiązać do złożonego przez Panią zgłoszenia do udziału w polsko-austriackim konkursie wymiany osobowej naukowców (edycja 2018-2020) pt.: "Wpływ energii błędu ułożenia nanomateriałów na zjawiska zachodzące podczas wyżarzania pod wysokim ciśnieniem / The impact of the stacking fault energy of nanomaterials on phenomena during annealing at high hydrostatic pressure".

Uprzejmie informuję, że dnia 26 kwietnia 2018 r. odbyło się w Wiedniu posiedzenie polsko-austriackiej grupy roboczej do spraw współpracy naukowo-technicznej, w trakcie którego dokonano oceny złożonych wniosków.
Pragnę Panią poinformować, że ww. zgłoszenie zostało zaakceptowane do realizacji w okresie od 1 maja 2018 r. do 30 kwietnia 2020 r.

Życzę powodzenia w realizacji zamierzonej współpracy i załączam wyrazy szacunku
Wojciech Dziedzic
naczelnik wydziału

Wydział Spraw Europejskich
Departament Współpracy Międzynarodowej
Ministerstwo Nauki i Szkolnictwa Wyższego

tel. 22 50 17 119

Zał. Nr 3

POROZUMIENIE
w sprawie realizacji grantu wewnętrznego wspierającego prowadzenie działalności naukowej w dyscyplinie Inżynieria Materiałowa

pt. **Kształtowanie nanostruktury stopu aluminium w procesie starzenia pod wysokim ciśnieniem hydrostatycznym** opisanego we wniosku z dnia 14.03.2022 r.

zawarte w dniu **14.04.2022 r.** pomiędzy:

prof. dr hab. inż. Jarosławem Mizerą, dziekanem Wydziału Inżynierii Materiałowej, w którym jest realizowana praca, zwanym dalej „Kierownikiem jednostki" oraz

Kierownikiem grantu **dr inż. Agnieszką Krawczyńską**, zwanym dalej „Kierownikiem pracy".

1. Kierownik pracy zobowiązuje się wykonać wszystkie prace objęte wnioskiem o grant, zgodnie z harmonogramem oraz *Regulaminem przyznawania i rozliczania grantów wewnętrznych wspierających prowadzenie działalności naukowej w dyscyplinie Inżynieria Materiałowa.*
2. Harmonogram pracy i kalkulacja kosztów stanowią załączniki do porozumienia.
3. Na sfinansowanie realizacji pracy przyznana została kwota w wysokości **34 800,00 zł**

(słownie zł : trzydzieści cztery tysiące osiemset złotych)

4. Termin zakończenia realizacji pracy ustala się na dzień **31.12.2023 r.**
5. Kierownik jednostki, w której jest realizowana praca, udostępni składniki mienia jednostki niezbędne do realizacji pracy oraz obsługę realizacji pracy przez administrację jednostki.
6. Niewykorzystane w czasie realizacji pracy środki, Kierownik pracy przekazuje do dyspozycji Przewodniczącego Rady Naukowej Dyscypliny Inżynieria Materiałowa.
7. Porozumienie sporządzono w czterech jednobrzmiących egzemplarzach po jednym dla każdej ze stron oraz jeden dla pełnomocnika kwestora w jednostce zatrudniającej Kierownika pracy oraz Przewodniczącego Rady Naukowej Dyscypliny Inżynieria Materiałowa.

Przewodniczący Rady Naukowej Dyscypliny

PRZEWODNICZĄCA
Rady Naukowej Dyscypliny
INŻYNIERIA MATERIAŁOWA

prof. dr hab. Małgorzata Lewandowska

.....
(data i podpis)

Kierownik jednostki, w której jest realizowana praca

DZIEKAN
WYDZIAŁU INŻYNIERII MATERIAŁOWEJ

Prof. dr hab. inż. Jarosław Mizera

.....
(data i podpis)

Kierownik pracy

K I E R O W N I K
PROJEKTU BADAWCZEGO

dr inż. Agnieszka Krawczyńska

.....
(data i podpis)

Pełnomocnik Kwestora w jednostce, w której jest realizowana praca

z up. Głównego Księgowego

Wiesława Skomorowska

(data i podpis)

Umowa nr UMO-2021/42/E/ST5/00118
o realizację i finansowanie projektu badawczego,
który uzyskał finansowanie w ramach konkursu „SONATA BIS-11"

zawarta w Krakowie w dniu podpisania przez Dyrektora Narodowego Centrum Nauki, pomiędzy stronami, którymi są:

Narodowe Centrum Nauki,
ul. Twardowskiego 16, 30-312 Kraków,
NIP: 6762429638, REGON: 121361537,
zwane dalej „Centrum" lub „NCN",
reprezentowane przez Zbigniewa Błockiego - Dyrektora Narodowego Centrum Nauki,
zwanego dalej „Dyrektorem"

Politechnika Warszawska
zwana(y) dalej „Podmiotem"

Adres siedziby:
pl. Politechniki 1, 00-661 Warszawa

Adres korespondencyjny:
pl. Politechniki 1, 00-661 Warszawa

Wydział Inżynierii Materiałowej

NIP: 5250005834, REGON: 000001554
którą(y) reprezentuje(ą):
prof. dr hab. inż. Mariusz Malinowski, Prorektor ds. Nauki

oraz

dr inż. Agnieszka Teresa Krawczyńska
[redacted], zwana(y) dalej „Kierownikiem projektu"

na podstawie decyzji Dyrektora nr **DEC-2021/42/E/ST5/00118** z dnia **2022-02-24**.

§ 1. Informacje ogólne

1. Umowa określa warunki realizacji, finansowania oraz rozliczenia projektu badawczego pt. **Kształtowanie mikrostruktury materiałów metalicznych w celu poprawy ich właściwości antybakteryjnych**, objętego wnioskiem zarejestrowanym w systemie ZSUN/OSF (Zintegrowany System Usług dla Nauki/Obsługa Strumieni Finansowania) administrowanym przez OPI (Ośrodek Przetwarzania Informacji) pod numerem **2021/42/E/ST5/00118** i przyjętego do finansowania w ramach ogłoszonego przez Centrum konkursu „SONATA BIS-11", zwanego dalej „projektem".
2. Projekt będzie realizować **Politechnika Warszawska, Wydział Inżynierii Materiałowej**.
3. Na realizację projektu przyznano Podmiotowi środki finansowe w wysokości **2 042 493,00** zł (słownie: **dwa miliony czterdzieści dwa tysiące czterysta dziewięćdziesiąt trzy złote**).
4. Dzień rozpoczęcia realizacji projektu strony ustalają na dzień zawarcia umowy.

Umowa nr UMO-2021/03/Y/ST5/00253

o realizację i finansowanie projektu badawczego, który uzyskał finansowanie w ramach konkursu „Weave-UNISONO"

zawarta w dniu podpisania przez Dyrektora Narodowego Centrum Nauki w Krakowie, pomiędzy stronami, którymi są:

Narodowe Centrum Nauki w Krakowie,
ul. Twardowskiego 16, 30-312 Kraków,
NIP: 6762429638, REGON: 121361537, zwane dalej „Centrum" lub „NCN",
reprezentowane przez Zbigniewa Błockiego - Dyrektora Narodowego Centrum Nauki,
zwanego dalej „Dyrektorem",

Politechnika Warszawska
zwana(y) dalej „Podmiotem"

Adres siedziby:
pl. Politechniki 1, 00-661 Warszawa

Adres korespondencyjny:
pl. Politechniki 1, 00-661 Warszawa

Wydział Inżynierii Materiałowej

NIP: 5250005834, REGON: 000001554,

którą(y) reprezentuje(ą):
prof. dr hab. inż. **Mariusz Malinowski**, Prorektor ds. Nauki

oraz

dr inż. Agnieszka Teresa Krawczyńska
[redacted]
zwana(y) dalej „Kierownikiem projektu"

na podstawie decyzji Dyrektora nr **DEC-2021/03/Y/ST5/00253** z dnia **2022-04-04**.

§ 1. Informacje ogólne

1. Umowa określa warunki realizacji, finansowania oraz rozliczenia projektu badawczego pt. **Kształtowanie nanomateriałów w wyniku wyżarzania pod wysokim ciśnieniem**, objętego wnioskiem zarejestrowanym w systemie ZSUN/OSF (Zintegrowany System Usług dla Nauki/Obsługa Strumieni Finansowania) administrowanym przez OPI (Ośrodek Przetwarzania Informacji) pod numerem **2021/03/Y/ST5/00253** i przyjętego do finansowania w ramach ogłoszonego przez Centrum konkursu „Weave-UNISONO", zwanego dalej „projektem".

Załącznik 9

UMOWA nr 1820/38/Z09/2023
NA FINANSOWANIE MOBLINOŚCI O CHARAKTERZE MIĘDZYNARODOWYM
W RAMACH PROGRAMU MOBILITY PW

zawarta w dniu 10 MAR. 2023 w Warszawie pomiędzy

Politechniką Warszawską z siedzibą w Warszawie (00-661), Plac Politechniki 1, NIP 5250005834, REGON 000001554, reprezentowaną przez kierownika zespołu zarządzającego projektu „ Inicjatywa doskonałości-uczelnia badawcza", prof. dr hab. inż. Małgorzatę Lewandowską, działającą na podstawie pełnomocnictwa BR-P-674/2020 z dn. 01.09.2020 r., zwaną dalej „Uczelnią",
a
Krawczyńska Agnieszka [redacted]
zamieszkałą/-ym przy [redacted]
zwany dalej „Uczestnikiem Programu"

Strony ustaliły następujące warunki Umowy:

§ 1 – PRZEDMIOT UMOWY

1. Przedmiotem umowy jest określenie warunków finansowania mobilności o charakterze międzynarodowym w ramach programu Mobility PW, realizowanego w ramach i ze środków programu „Inicjatywa doskonałości – uczelnia badawcza", zwanego dalej „Programem IDUB", na podstawie art. 389 ust. 1 i 2 ustawy z dnia 20 lipca 2018 r. Prawo o szkolnictwie wyższym i nauce oraz w związku z umową nr 04/IDUB/2019/94 z dnia 30 grudnia 2019 r.
2. Uczestnik Programu oświadcza, że zapoznał się i akceptuje warunki umowy oraz zapisy regulaminu konkursu w ramach programu Mobility PW., stanowiący załącznik do decyzji nr 217/2021 Rektora Politechniki Warszawskiej z dnia 1 września 2021r. w sprawie uruchomienia Mobility PW oraz ogłoszenia I konkursu w ramach tego programu zwany dalej regulaminem konkursu w ramach programu Mobility PW.
3. Uczelnia zapewni Uczestnikowi Programu finansowanie mobilności o charakterze międzynarodowym „zbadanie przy użyciu metody anihilacji pozytronów: koncentracji, wielkości i rozmieszczenia defektów w próbkach Cu i CuZn poddanych obróbce HPT w temperaturze pokojowej oraz podczas izochronicznego wyżarzania do 250°C." do HZDR, Dresden, Niemcy na okres 6 dni, zwanej dalej „mobilnością".
4. Uczestnik Projektu przyjmuje finansowanie i zobowiązuje się zrealizować mobilność, o której mowa w ust. 3.

§ 2 – CZAS TRWANIA UMOWY

1. Umowa wchodzi w życie w dniu jej zawarcia, tj. po podpisaniu przez ostatnią ze Stron.
2. Mobilność rozpocznie się w dniu 13.06.2023 r. a zakończy w dniu 18.06.2023 r.

§ 3 – FINANSOWANIE MOBILNOŚCI

1. Na pokrycie kosztów związanych z mobilnością Uczestnik Programu otrzymuje ryczałt w wysokości 6420 zł (słownie: sześć tysięcy czterysta dwadzieścia złotych zero groszy). Na powyższą kwotę składa się kwota przeznaczona na koszty podróży, ubezpieczenia zdrowotnego, OC, NNW,

koszty opłat wizowych lub związanych z legalizacją pobytu w wysokości 2000 zł oraz kwota przeznaczona na koszty utrzymania w wysokości 4420 zł zgodnie z informacją dodatkową dotyczącą finansowania mobilności zawartą w Ogłoszeniu konkursowym Mobility PW.

2. Skierowanie za granicę w celu realizacji mobilności odbywa się na zasadach określonych w Zarządzenia nr 97/2021 Rektora PW z dnia 25 października 2021 r. w sprawie kierowania za granicą pracowników, doktorantów i studentów Politechniki Warszawskiej w celach naukowych, dydaktycznych i szkoleniowych.
3. W przypadku nie rozpoczęcia realizacji mobilności, o której mowa w § 1 ust. 3 Uczestnik zobowiązany jest do zwrotu kwoty ryczałtu, o której mowa w ust. 1 w terminie 14 od wezwania do zwrotu przez Uczelnię.
4. W przypadku przerwania realizacji mobilności, o której mowa § 1 ust. 3 z powodu siły wyższej, Uczestnik zobowiązany jest do zwrotu kwoty ryczałtu , o której mowa w ust. 1 proporcjonalnie do niewykorzystanej kwoty ryczałtu, w terminie 14 od wezwania do zwrotu przez Uczelnię.
5. Świadczenia wynikające z umowy na finansowanie mobilności z programu IDUB, zgodnie z art.21 ust. 1 pkt.16 ustawy o podatku dochodowym od osób fizycznych są zwolnione z opodatkowania do wysokości określonej w Rozporządzeniu Ministra Pracy i Polityki Społecznej z dnia 29 stycznia 2013 r. w sprawie należności przysługujących pracownikowi zatrudnionemu w państwowej lub samorządowej jednostce sfery budżetowej z tytułu podróży służbowej (Dz.U. 2013 poz. 167).
6. W związku z powyższym Uczestnik Programu zobowiązany jest dostarczyć potwierdzenia poniesionych kosztów związanych z wyjazdem. Kwota ryczałtu przekraczająca udokumentowane koszty i przysługujące diety za podróż podlega opodatkowaniu podatkiem dochodowym od osób fizycznych.

§ 4 – INFORMACJA O PRZETWARZANIU DANYCH OSOBOWYCH

Zgodnie z art. 13 Rozporządzenia Parlamentu Europejskiego i Rady (UE) 2016/679 z dnia 27 kwietnia 2016 r. w sprawie ochrony osób fizycznych w związku z przetwarzaniem danych osobowych i w sprawie swobodnego przepływu takich danych oraz uchylenia dyrektywy 95/46/WE (Dz. U. UE L 119/1 z dnia 4 maja 2016 r.), zwanym dalej „RODO", Politechnika Warszawska informuje, że:

1) Administratorem danych osobowych Uczestnika Programu jest Politechnika Warszawska z siedzibą przy Pl. Politechniki 1, 00-661 Warszawa.
2) Administrator wyznaczył w swoim zakresie Inspektora Ochrony Danych (IOD) nadzorującego prawidłowość przetwarzania danych osobowych. Można skontaktować się z nim, pod adresem mailowym: iod@pw.edu.pl.
3) Administrator będzie przetwarzać dane osobowe w zakresie danych osobowych zawartych w niniejszej umowie.
4) Dane osobowe Uczestnika Programu przetwarzane będą przez Administratora w celu sfinansowania Uczestnikowi mobilności o charakterze międzynarodowym – podstawą do przetwarzania danych osobowych Doktoranta jest art. 6 ust. 1 lit. b) RODO.
5) Politechnika Warszawska nie zamierza przekazywać danych osobowych Uczestnika Programu poza Europejski Obszar Gospodarczy.
6) Uczestnik Programu ma prawo dostępu do treści swoich danych osobowych oraz prawo ich sprostowania, prawo żądania usunięcia, ograniczenia przetwarzania, prawo wniesienia sprzeciwu wobec przetwarzania danych osobowych. Ze względu na fakt, że przesłanką przetwarzania danych osobowych nie jest zgoda nie przysługuje prawo do przenoszenia danych osobowych.

7) Dane osobowe Uczestnika Programu nie będą udostępniane innym podmiotom (administratorom), za wyjątkiem podmiotów upoważnionych na podstawie przepisów prawa.
8) Dostęp do danych osobowych Uczestnika Programu mogą mieć podmioty (podmioty przetwarzające), którym Politechnika Warszawska zleca wykonanie czynności mogących wiązać się z przetwarzaniem danych osobowych.
9) Politechnika Warszawska nie wykorzystuje w stosunku do Uczestnika Programu zautomatyzowanego podejmowania decyzji, w tym nie wykonuje profilowania Uczestnika Programu.
10) Podanie przez Uczestnika Programu danych osobowych jest dobrowolne, jednakże ich niepodanie uniemożliwia Uczestnikowi Programu otrzymania finansowania w ramach programu Mobility PW.
11) Dane osobowe Uczestnika Programu przetwarzane będą przez okres trwania Umowy oraz na potrzeby wieczystej archiwizacji.
12) Doktorant ma prawo do wniesienia skargi do organu nadzorczego - Prezesa Urzędu Ochrony Danych Osobowych, gdy uzna, iż przetwarzanie Pani/Pana danych osobowych narusza przepisy RODO.

§ 5 - WARUNKI KOŃCOWE

1. Sądem właściwym dla rozstrzygania wszelkich sporów wynikłych z realizacji Umowy, będzie Sąd właściwy dla Uczelni.
2. Niniejszą umowę sporządzono w dwóch jednobrzmiących egzemplarzach, po jednym dla każdej ze Stron.

Załączniki:
Załącznik nr 1 Wniosek o finansowanie mobilności

Uczelnia POLITECHNIKA WARSZAWSKA
Biuro Projektu
"Inicjatywa Doskonałości - Uczelnia Badawcza"
ul. Rektorska 4 lok. 4.23, 00-614 Warszawa
tel. (22) 234 1337, NIP: 525-000-58-34
-2-

.....
(pieczęć Biura projektu IDUB)

Uczestnik Programu

A. Krawczyńska
.....
(podpis Uczestnika Programu)

Kierownik Zespołu Zarządzającego Projektu IDUB
prof. dr hab. inż. Małgorzata Lewandowska

.....
(pieczęć i podpis Kierownika IDUB)

z up. Głównego Księgowego
mgr Wioletta Gustaw-Baranowska

.....
(pieczęć i podpis Pełnomocnika Kwestora)

Fundacja na rzecz
Nauki Polskiej

Warszawa, 27 maja 2019 r.

ZAŚWIADCZENIE

Niniejszym zaświadczam, że Pani Dr Agnieszka Krawczyńska w 2015 roku uczestniczyła w programie SKILLS Fundacji na rzecz Nauki Polskiej, w ramach którego odbyła 2-miesięczny staż w National Physical Laboratory w Wielkiej Brytanii.

Michał Pietras

Dyrektor ds. Działalności Programowej FNP

ul. I. Krasickiego 20/22
02-611 Warszawa
tel.: 22 845 95 00, fax: 22 845 95 05
fnp@fnp.org.pl, www.fnp.org.pl

Organizacja pożytku publicznego
KRS: 0000109744
Konto dla darowizn i 1% odpisów podatkowych na cele statutowe:
29 1500 1272 1212 7004 4667 0000

Délégation Midi-Pyrénées
16, av Edouard Belin -BP 24367
31055 Toulouse Cedex 4

CONTRAT DE TRAVAIL

N ° : 380943

ENTRE :

Le Président du Centre National de la Recherche Scientifique (CNRS),

d'une part,

ET

Madame Agnieszka ~~KRAWCZINSKA~~ KRAWCZYNSKA
Domicilié(e) : 29 rue J. Marvig 31 400 TOULOUSE
[redacted]
Agent n° 111514 N° INSEE : 2 82 07 99 122 999
ci-après dénommé(e) "le bénéficiaire",

d'autre part,

Vu la loi n° 83-634 du 13 juillet 1983 modifiée portant droits et obligations des fonctionnaires

Vu la loi n° 84-16 du 11 janvier 1984 modifiée portant dispositions statutaires relatives à la fonction publique de l'Etat, notamment son article 4-2°

Vu le décret n° 82-993 du 24 novembre 1982 modifié portant organisation et fonctionnement du Centre National de la Recherche Scientifique

Vu le décret n° 86-83 du 17 janvier 1986 modifié relatif aux dispositions applicables aux agents non titulaires de l'Etat pris pour l'application de l'article 7 de la loi 84-16 du 11 janvier 1984 portant dispositions statutaires relatives à la fonction publique de l'Etat

Vu, le contrat n° 045482, signé avec l'Agence Nationale de la Recherche relatif au projet MINIC

IL A ETE CONVENU CE QUI SUIT :

ARTICLE 1 : OBJET

Madame Agnieszka KRAWCZYNSKA est recruté(e), en qualité d'agent contractuel au Centre national de la recherche scientifique à compter du 01 décembre 2012 au titre du 2ème alinea de l'article 4 de la loi du 11 janvier 1984 susvisée pour exercer les fonctions de chercheur en microscopie élec tronique .

A compter de cette même date, l'intéressé(e) est affecté(e) à l'unité UPR8011 CEMES lieu de travail TOULOUSE et placé(e) sous l'autorité hiérarchique de Monsieur ALAIN CLAVERIE.

ARTICLE 2 : DUREE DU CONTRAT

Sous réserve des dispositions prévues à l'article 7, le présent contrat est conclu pour une durée de 7 mois du 01 décembre 2012 au 30 juin 2013.

Il est précisé que le présent contrat ne constitue pas un engagement à caractère permanent et ne confère en aucun cas le droit à une intégration dans le cadre des personnels statutaires du CNRS.

ARTICLE 3 : REMUNERATION

Le bénéficaire perçoit, pour un travail à Temps plein une rémunération mensuelle brute de 2 296,62 euros exclusive de toutes primes et indemnités.

Cette rémunération, indexée sur la valeur du point indiciaire de la fonction publique, est payable à terme échu.

ARTICLE 4 : COUVERTURE SOCIALE

Le bénéficiaire est soumis aux dispositions prévues dans le décret du 17 janvier 1986 susvisé.

A ce titre, il est affilié et se voit appliquer le régime général de Sécurité Sociale pour ce qui concerne les prestations d'assurances sociales, notamment de l'assurance maladie, et le régime de IRCANTEC pour ce qui concerne la retraite complémentaire.

Il bénéficie de la législation relative aux accidents du travail et aux maladies professionnelles.

ARTICLE 5 : HORAIRES - CONGES - CUMUL D'ACTIVITE - FRAIS DE DEPLACEMENTS

En ce qui concerne l'horaire de travail, la durée du congé annuel et les frais de déplacement, le bénéficiaire est soumis aux règles applicables aux agents titulaires du CNRS.

Les congés annuels doivent être pris pendant la durée du contrat : aucune indemnité ne sera due pour compenser les congés non utilisés du fait du bénéficiaire.

Le bénéficiaire du présent contrat est soumis à la réglementation sur les cumuls.

ARTICLE 6 : OBLIGATION DE RESERVE ET PROPRIETE INTELLECTUELLE

6-1 Obligation de réserve et obéissance hiérarchique

Le bénéficiaire du présent contrat est soumis aux obligations incombant à l'ensemble des agents publics, notamment celle d'obéissance hiérarchique et à l'obligation de réserve. Il est également tenu au secret professionnel à l'égard des tiers en ce qui concerne les activités exercées au CNRS.

6-2 Propriété Intellectuelle

Les missions confiées au bénéficiaire au titre du présent contrat de travail comportent une mission inventive permanente.

En conséquence et conformément à la législation en vigueur en matière de propriété intellectuelle (articles L. 611-7 et R. 611-11 à R. 611-14 notamment), les inventions faites par le bénéficiaire appartiennent au CNRS.

Le bénéficiaire reconnaît que le CNRS est propriétaire de tout autre résultat valorisable, protégeable ou non par un titre de propriété intellectuelle.

Ainsi, les logiciels créés par le bénéficiaire dans le cadre du présent contrat appartiennent au CNRS en application de l'article L.113-9 du code de la propriété intellectuelle.

En outre, le bénéficiaire s'engage à céder au CNRS, par le biais de cessions de droits particuliers, la propriété pleine et entière des résultats protégés par le droit d'auteur qu'il pourrait obtenir ou pourrait contribuer à obtenir.

Le CNRS dispose seul du droit de déposer les titres de propriété intellectuelle correspondants aux résultats précités.

Le CNRS s'engage à ce que le nom du bénéficiaire, s'il est considéré comme inventeur, soit mentionné dans les demandes de brevets, à moins que le bénéficiaire ne s'y oppose.

Le bénéficiaire s'engage à donner toutes signatures et à prêter son entier concours au CNRS pour les procédures de protection de ces résultats (notamment pour le dépôt éventuel d'une demande de brevet, son maintien en vigueur et sa défense) ainsi que pour leur exploitation et ce tant en France qu'à l'étranger.

L'ensemble de ces dispositions demeure valable à l'expiration du contrat.

6-3 Confidentialité

Le bénéficiaire s'engage à considérer comme strictement confidentielles les informations de toute nature, communiquées par tous moyens, dont il pourrait avoir connaissance à l'occasion de l'exécution du présent contrat.

Cette obligation de confidentialité reste en vigueur pendant la durée du contrat et après son expiration.

6-4 Publications

Le bénéficiaire du présent contrat doit solliciter de manière expresse de l'autorité hiérarchique, l'autorisation de publier.

Toute publication ou communication du bénéficiaire doit explicitement mentionner le nom de l'unité et du CNRS.

Ces dispositions demeurent en vigueur pendant la durée du contrat et après son expiration.

ARTICLE 7 : RESILIATION DU CONTRAT - PREAVIS

Le présent contrat pourra être résilié :
- sans préavis, à l'initiative de l'une ou l'autre des parties pendant une période de 14 Jours suivant l'entrée en fonctions et constituant une période d'essai ou passé ce délai, en cas de faute grave, par décision unilatérale du président du CNRS.

- avec préavis,
  - à l'initiative du bénéficiaire du présent contrat
  - à l'initiative du président du CNRS passé la période d'essai fixée par le présent article, pour des motifs réels et sérieux. En ce cas, le bénéficiaire sera informé des griefs portés contre lui et mis en mesure de présenter ses observations sur les faits qui lui sont reprochés.

Hormis le cas de faute grave, pour lequel le licenciement sans indemnités ni préavis peut être prononcé, la durée du préavis à respecter par l'une ou l'autre des parties est la suivante :

- huit jours si le bénéficiaire a moins de 6 mois de service,
- un mois, s'il a au moins 6 mois de service et moins de 2 ans,
- deux mois s'il a au moins 2 ans de service.

ARTICLE 8 : IMPUTATION DE LA DEPENSE

La dépense sera imputée au budget du CNRS, agrégat 1 "activité conduite par les unités de recherche" nature B1 "dépenses de personnel non limitatives", compte comptable 646322.

Fait à Toulouse, le 28 novembre 2012 en deux exemplaires.

Pour le Délégué Régional Empêché

Le Président du CNRS

par délégation le Délégué Régional

Ingrid BONET

Patrick MOUNAUD

Le bénéficiaire

(signature, précédée de la mention "lu et approuvé")

A. Krawczyńska lu et approuvé

KMM.VIN EUROPEAN VIRTUAL INSTITUTE ON KNOWLEDGE-BASED MULTIFUNCTIONAL MATERIALS AISBL

KMM-VIN Research Fellowship Agreement

I. Details of the Fellowship Holder

Name (first, last): **Agnieszka Krawczyńska**
e-mail: akrawczynska@wp.pl
Sending institution (name, address):

Politechnika Warszawska (Warsaw University of Technology)
Wydział Inżynierii Materiałowej (Faculty of Materials Science and Engineering)
Wołoska 141, 02-507 Warszawa, Poland

Contact person in the sending institution (name, function, phone, e-mail):

Prof. M. Lewanowska, vice-Dean,
+48 (22) 2348399, malew@inmat.pw.edu.pl

II. Details of the Host

Host institution (name, address):

Materials Center Leoben Forschung GmbH (MCL)
Roseggerstraße 12, 8700 Leoben, Austria

Contact person in the host institution (name, function, phone, e-mail):

Prof. R. Pippan, Univ. Prof. Dr.
+ 43 (0) 3842 804 311, reinhard.pippan@oeaw.ac.at

III. Start and end date of the Fellowship period:

September 11. 2010 – November 13. 2010

IV. Fellowship

After having received this Fellowship Agreement duly signed by the Fellowship Holder the KMM-VIN will transfer the fellowship of the amount of:

3000,- €

directly to the bank account of the Fellowship Holder.

This amount is to be reported as a foreign income in the personal annual tax return of the Fellowship Holder according to the national regulations that apply to the Fellowship Holder.

V. Resignation from the Fellowship or shortening the Fellowship period

In case of resignation from the Fellowship or shortening of its duration period the Fellowship Holder commits herself/himself to pay back to the KMM-VIN bank account, respectively, the whole amount received or a part of it equal to the fraction of the Fellowship received corresponding to the period by which the stay was shortened.

VI. Reporting of the Fellowship's results

The Grant Holder commits herself/himself to provide to the Chair of the KMM-VIN Mobility Programme, Prof. J. Eberhardsteiner (ej@mail.tuwien.ac.at) within a month after the Research Fellowship stay a scientific report including all scientific results gained during the research stay (data, tables, experimental results, ...).

VII. Commitment of the Parties involved

By signing this document the Fellowship Holder, KMM-VIN and the Host Institution confirm that they will abide by the principles of this Fellowship Agreement

Fellowship Holder's signature: ..... A. Krawczyńska .....

Place and date: ..... 04.08.2010 .....

KMM-VIN Representative

We confirm that **Agnieszka Krawczyńska** was awarded the KMM-VIN Research Fellowship as stated above

On behalf of KMM-VIN: .....

Signature: Michal Basista
Chief Executive Officer
KMM-VIN-AISBL

Place and date: Warszawa, 13.08.2010

Host institution representative:

We confirm that **Agnieszka Krawczyńska** stayed at our institution from 11. Sept. 2010 to 13. Nov. 2010 as KMM-VIN research fellow

Signature of the Host:

Place and date:

Leoben, 20. 9. 2010

Materials Center Leoben
Forschung GmbH
8700 Leoben, Roseggerstraße 12
Tel: 03842 / 45922